INFORMATION TO USERS

This manuscript has been reproduced from the microfilm master. UMI films the text directly from the original or copy submitted. Thus, some thesis and dissertation copies are in typewriter face, while others may be from any type of computer printer.

The quality of this reproduction is dependent upon the quality of the copy submitted. Broken or indistinct print, colored or poor quality illustrations and photographs, print bleedthrough, substandard margins, and improper alignment can adversely affect reproduction.

In the unlikely event that the author did not send UMI a complete manuscript and there are missing pages, these will be noted. Also, if unauthorized copyright material had to be removed, a note will indicate the deletion.

Oversize materials (e.g., maps, drawings, charts) are reproduced by sectioning the original, beginning at the upper left-hand corner and continuing from left to right in equal sections with small overlaps. Each original is also photographed in one exposure and is included in reduced form at the back of the book.

Photographs included in the original manuscript have been reproduced xerographically in this copy. Higher quality 6" x 9" black and white photographic prints are available for any photographs or illustrations appearing in this copy for an additional charge. Contact UMI directly to order.

UMI

A Bell & Howell Information Company
300 North Zeeb Road, Ann Arbor MI 48106-1346 USA
313/761-4700 800/521-0600

UNIVERSITÉ D'OTTAWA
UNIVERSITY OF OTTAWA

INTERPLAY OF SPIN STRUCTURES, HYPERFINE MAGNETIC FIELD DISTRIBUTIONS AND CHEMICAL ORDER-DISORDER PHENOMENA IN FACE CENTERED CUBIC FE-NI ALLOYS STUDIED BY MÖSSBAUER SPECTROSCOPY MEASUREMENTS AND MONTE CARLO SIMULATIONS

By

Mei Zhen Dang

A thesis submitted to
the School of Graduate Studies and Research
in partial fulfillment of the requirements
for the degree of Doctor of Philosophy

Department of Physics

University of Ottawa
Ottawa, Ontario
May 28, 1996

Abstract

The magnetic properties of fcc Fe-Ni alloys are studied by Mössbauer spectroscopy and Monte Carlo (MC) simulations. Both macroscopic (magnetization, paraprocess susceptibility, Curie points, etc.) and microscopic properties (hyperfine fields) are used to test simple local moment models under various assumptions.

A non-linear composition dependence of the average hyperfine field is observed by Fe-57 Mössbauer spectroscopy. A microscopic vector hyperfine field model is proposed and used to model the measured average hyperfine fields and hyperfine field distributions (HFDs) in the collinear ferromagnetic Fe-Ni alloys ($y \leq 0.45$ in Fe_yNi_{1-y}). Modeling the liquid helium temperature average hyperfine fields and HFDs resolves the coupling parameters in the proposed hyperfine field model:

$$< \vec{H}_k >_T = A < \vec{\mu}_k >_T + B \sum_j < \vec{\mu}_j >_T .$$

To the extent that chemical short range order can be neglected in our rapidly quenched samples, the coupling parameters are $A = A_0 + A_1 y$ (A_0 = 89 kOe/μ_B, A_1 = -20 kOe/μ_B) and $B = B_0 + B_1 y$ (B_0 = 4.4 kOe/μ_B, B_1 = 3.2 kOe/μ_B).

MC simulations show the success and the limits of a simple local moment model, in characterizing the bulk magnetic properties of Fe-Ni. A new approach for simulating HFDs is developed. It combines MC simulation for the spin structure and the above phenomenological hyperfine field model for the site-specific hyperfine field values. Using this method, we calculated spin structures and HFDs in Fe-Ni alloys at different compositions and temperatures.

Finally, interplay between the magnetic and the atomic ordering phenomena is studied in $FeNi_3$, FeNi and Fe_3Ni, by considering the magnetic and chemical interactions simultaneously using MC simulations. Serveral new features that are not predicted by mean-field theory or MC simulations with chemical interactions only arise: (1) chemical order can be induced where using chemical interactions only

leads to the prediction of no chemical order (2) chemical segregation can be induced where using chemical interactions only leads to the prediction of no chemical segregation, (3) $FeNi_3$ and Fe_3Ni are found to have significantly different chemical ordering temperatures where chemical interactions only lead to equal ordering temperatures, (4) chemical ordering temperatures are significantly shifted from their chemical interactions only values, even when the chemical ordering temperature is larger than the magnetic ordering temperature, (5) abrupt steps can occur in the spontaneous magnetization at the chemical ordering temperature, when the latter is smaller than the magnetic ordering temperature, and (6) nonlinear relations arise between the chemical ordering temperature and the chemical exchange parameter U $\equiv 2U_{FeNi} - U_{FeFe} - U_{NiNi}$, where the U_{ij} are the near-neighbour pair-wise chemical bonds.

Acknowledgements

I would like first to thank my supervisor Dr.Denis Rancourt for what he has input for me to accomplish this Ph.D project: offering the opportunity of being a Ph.D student, presenting interesting Fe-Ni research topics, leading me to the Mössbauer spectroscopy and its application field, guidance to solve the research problems, advices for being precise and accurate, careful reviewing of the thesis manuscript, and generous financial support.... I am in debt of him for all of these.

I want to thank Dr. R. A. Dunlap at Dalhousie University for making splat quenched and roller quenched Fe-Ni samples which made the research possible.

Thanks to André Lalonde for letting me learn and practice on X-Ray diffraction and Rietveld method.

Thanks to NSERC and the University of Ottawa for the financial support for my first two year study of this program.

I want to thank Myriam Dubé for her initial Monte Carlo work, which becomes a starting point of some important parts of this thesis. Thanks to Iain Christie for teaching me how to use liquid helium cryostat. Thanks to Claude Plante for all his help since he worked in Mössbauer laboratory. Thanks to Patric Mercier, Ken Lagarec for sharing office and useful discussions. Thanks to Zi Cong Zhou, Lixin Dou for their explaination to my questions about the physics. Thanks to all fellow graduate students, professors, support staff and technical staff in electronic and mechanical shop for making Physics Department existing.

Finally I would like to express my sincere appreciation for my husband and son for being with me here. Also the support from my family in China is very much appreciated, their support is always the important motivation of my progress. Thank you all!

List of Abbreviations

bcc	body centered cubic
CS	Center shift.
CSD	Center shift distribution
EFG	Electric field gradient.
fcc	Face centered cubic
FWHM	Full width at half maximum.
hcp	hexagonal close packed
HFD	Hyperfine field distribution
LNT	Liquid nitrogen temperature
LHT	liquid helium temperature
LROP	Long range order parameter
MC	Monte Carlo
MFT	Mean field theory
NN	neaarest neighbour
PDF	Probability density function
QS	Quadrupole splitting.
QSD	Quadrupole splitting distribution.
RQ	Roller quenched
RT	Room temperature
SROP	Short range order parameter
SOD	Second order Doppler shift.
SQ	Splat quenched
VBF	Voigt Based HFD Fitting
XRD	X-Ray diffraction

Contents

List of Tables

List of Figures

Chapter 1. INTRODUCTION

1.1 Fe-Ni alloys and the Invar Problem

Face centered cubic (fcc) Fe-Ni alloys, as a fundamentally and practically important class of materials, have been by far the most studied binary transition metal alloys. The most well known distinctive property is that at the composition 65 at.% Fe, its thermal expansion coefficient is near zero at room temperature [1]. This alloy is named Invar for its volume or length invariability. Virtually, every measured quantity of Invar is anomalous. Some of the more notable Invar anomalies include a large spontaneous volume magnetostriction [2, 3], a large pressure effect on both the intensity of the magnetization [4] and the Curie temperature [5, 6], a sudden drop of the saturation magnetization from the Slater-Pauling curve [7], an unusually low mean lattice parameter of the fcc structure [8, 9], and a low ferromagnetic ordering temperature T_C [7] compared to the Curie points of bcc iron, fcc nickel, and non-Invar fcc Fe-Ni alloys. The problem of solving the origin of the "Invar anomalies" is called the "Invar problem".

1.2 Main Proposed Models

Many models have been proposed to solve the "Invar problem". Besides earlier incorrect models, the most popular candidates have been: the 2γ state model [10, 11, 12], the weak itinerant ferromagnetism model [13, 14, 15], and the latent antiferromagnetism model [16].

In the 2γ state model, Weiss extended Kaufmann's [17] 2γ state model of fcc pure iron to fcc Fe-Ni alloys. It assumes that an Fe atom in the fcc lattice can exist in two different states. The first state γ_1, called low spin state, has low spin and small volume, the second state γ_2, called high spin state, has a larger magnetic

moment and large volume. The energy difference between these two states is small (0.035 eV). The Invar effects were ascribed to the change in proportion of these two states due to thermal excitation of one to the other. The related electronic charge transfer due to the thermal excitation which can be easily recognized by various spectroscopic techniques has never been observed.

The weak itinerant ferromagnetism model requires that weak itineracy be present ad hoc in the Invar region of Fe-Ni. The observed drop in saturation magnetization occurring at 65 at.% Fe is interpreted as a drop in local atomic magnetic moment. However, neutron magnetic disorder scattering studies [18, 19] have shown that the moments are preserved at all concentrations.

The latent antiferromagnetism or mixed exchange model is a strong local moment model in which it is proposed that the magnetic exchange interactions in Fe-Fe pairs are antiferromagnetic while that of Fe-Ni and Ni-Ni pairs are ferromagnetic. Due to the ferromagnetic coupling, the magnetic moments align ferromagnetically in the Ni rich alloys. On increasing the iron content, the average moment first increases following the Slater-Pauling curve. Because of the antiferromagnetic coupling between Fe atoms, further increase in Fe concentration induces local antiferromagnetic spin alignment in some parts of the alloy. This antiferromagnetism leads to decreases of both the average magnetic moment and the Curie temperature. The model leads to an understanding of many Invar anomalies and is not in contradiction with any experimental evidence.

Theoretical calculations have also been developed to solve the Invar problem. There are ground state electronic structure calculations [20, 21, 22] from electronic band structure perspective and finite temperature calculations based on spin fluctuation theory [23, 24, 25, 26]. However, a fully self-consistent theory has not yet been developed.

For a more complete view of the Invar-related experimental and theoretical works, there are several review papers available (e.g. [27, 29, 30, 31, 38]).

1.3 Perspective and Approach

Despite numerous experimental and theoretical efforts, there are still many problems which are not well understood. In other words, work on the Invar problem remains inconclusive up to today. In order to eventually solve the Invar problem, we try to understand the magnetism of Fe-Ni alloys as a first step. As mentioned above, among the main proposed models latent antiferromagnetism is the simplest and it has no contradictions with any known experimental evidence yet. It has never been applied systematically and compared quantitatively to the measured properties of Fe-Ni alloys. In this work, we model and explain the magnetic behaviors of Fe-Ni alloys within the frame work of the latent antiferromagnetism model (i.e. using simple interacting local moment models) and we investigate the extent to which such models are valid.

1.4 Thesis Overview

The thesis consists of four parts.

Part I deals with the Mössbauer study of fcc Fe-Ni alloys from low to high iron concentration (from y = 0.05 to 0.75 in Fe_yNi_{1-y}). The spectra were taken at three temperatures (liquid helium temperature, LHT, liquid nitrogen temperature, LNT, and room temperature, RT). A new phenomenological model that relates the site-specific hyperfine field to the magnetic moments of the alloy is proposed and examined. Composition dependent coupling parameters are proposed and obtained by fitting the new phenomenological model to the average hyperfine fields and to the hyperfine field distributions (HFDs) at LHT. Then, the model is tested at higher temperatures.

Part I includes Chapters 2 to 9. Chapter 2 is the background of Mössbauer spectroscopy. Chapter 3 contains a description of the hyperfine field phenomenological model. Chapter 4 is about experimental and data analysis methods. Chapter 5 is about the sample synthesis and characterization. Chapter 6 covers the Mössbauer study of the splat quenched (SQ) alloys and the hyperfine field phenomenological

model. Chapter 7 gives the Mössbauer results for roller quenched (RQ) samples, and the examination of the proposed model. In Chapter 8, the phenomenological model is extended to LNT and RT to obtain the average magnetic moments of the Fe and Ni atoms. Conclusions for Part I are given in Chapter 9.

Part II is about Monte Carlo (MC) simulations of the magnetic properties of random fcc Fe-Ni alloys. With Ising approximation of the latent antiferromagnetism model we investigate how the magnetic properties in fcc Fe-Ni change with the near neighbor exchange constants J_{FeFe}, J_{FeNi}, and J_{NiNi}. The best exchange coupling parameters are obtained from comparison of the calculated results to the measurements.

Part II includes Chapters 10 to 13. Chapter 10 gives a brief introduction to the MC method and its application in fcc random Fe-Ni alloys. In Chapter 11, the simulation algorithms are given. Chapter 12 presents the simulation results and discussion. Chapter 13 concludes the work of Part II.

In Part III, HFDs are simulated by combining the hyperfine field phenomenological model given in Part I and the MC simulation results in Part II. Part III includes Chapters 14 to 18. Chapter 14 is a short introduction of Part III. Chapter 15 introduces the HFD simulation method. Chapter 16 is about ground state spin structure calculations and Chapter 17 is the HFD and the atomic moment distributions at higher temperatures. Discussion and conclusion are given in Chapter 18.

Part IV is the study of simutaneous magnetic and chemical order-disorder phenomena in fcc $FeNi_3$, FeNi and Fe_3Ni alloys. It contains Chapters 19 to 23. Chapter 19 is an introduction to magnetic and chemical ordered-disordered $FeNi_3$, FeNi and Fe_3Ni alloys. Chapter 20 is about the method used for HFD calculation. Chapter 21 covers the results for (1) magnetic interactions only, (2) chemical interactions only and (3) with simultaneous magnetic and chemical interactions. Chapter 22 is the general predictions with combined chemical and magnetic interations. Chapter 23 gives the conclusions for Part IV.

The final chapter (Chapter 24) gives an overall summary and conclusion for the thesis. Proposals for further work are pointed out.

Part I

MÖSSBAUER STUDY OF FCC Fe-Ni ALLOYS

Chapter 2. BACKGROUND OF MÖSSBAUER SPECTROSCOPY

Mössbauer spectroscopy is a nuclear spectroscopic technique. It relies on the "Mössbauer effect": that a γ-ray can be emitted or absorbed by a nucleus in a solid without recoil. Its unique feature is in the production of narrowly defined γ-ray energy spectra with Heisenberg natural line widths in the range of 10^{-6} to 10^{-9} eV. Basic concepts of Mössbauer spectroscopy can be found in many books [32, 33]. In this chapter we briefly introduce some of the Mössbauer parameters that will be used in the thesis in application to Fe-Ni.

2.1 Hyperfine Interactions

Interactions between the nucleus and its external electronic environment are called hyperfine interactions. These may alter the energy levels of the nuclear states. Such alternations are quite small in comparison with the typical γ-ray energy which is of the order of 10^4 to 10^5 eV. With Mössbauer spectroscopy we are able to detect such minute energy changes and resolve the hyperfine structures of nuclear levels. Information about local electronic, magnetic and crystallographic states of the studied material can be then extracted from the spectra.

Three hyperfine interactions can be studied in ^{57}Fe Mössbauer spectroscopy. They are the electric monopole, electric quadrupole, and magnetic dipole interactions. These three manifest themselves in the spectrum as an isomer shift, a quadrupole splitting and a magnetic Zeeman splitting, respectively.

First, the isomer shift arises from the electrostatic monopole interaction between the nuclear charge and electron density within nuclear volume. The effect of this interaction causes the nuclear energy levels (ground state energy level and excited state energy level) to shift by different amounts. Consequently, the resonant energy

between the two levels is changed, in comparison to that of some source (or of some standard absorber), by amount:

$$IS = \frac{2}{3}piZe^2(R_e^2 - R_g^2)(\mid \psi(0)_a \mid^2 - \mid \psi(0)_s \mid^2) \tag{2.1}$$

where R_e and R_g are nuclear radii in the excited and ground states. $e \mid \psi(0)_a \mid^2$ is the charge density at the nucleus in the absorber, and $e \mid \psi(0)_s \mid^2$ is the charge density at the nucleus in the source. In the absence of other hyperfine interactions, the corresponding absorption spectrum is a singlet (illustrated in Fig.2.1(a)).

The isomer shift is one of the most important hyperfine parameters in Mössbauer spectroscopy. It is directly related to the electron density at the nucleus. Therefore, it provides very useful chemical information of the resonant absorber.

In addition to the isomer shift, the second order Doppler (SOD) effect [33] that originates from the thermal motion of the nuclei, also alters the line position. The sum of the isomer shift and the SOD effect shift is the measured center shift (CS), δ, of the spectrum:

$$\delta = IS + SOD \tag{2.2}$$

The second hyperfine interaction is quadrupole interaction is due to the non-spherical charge distribution of the nucleus and the non-symmetric electronic environment. A nuclear state with a spin number greater than I = 1/2 has a non zero quadrupole moment eQ. When electric charges are distributed asymmetrically around the atomic nucleus, the nucleus is subjected to an electric field gradient (EFG). The EFG is a tensor whose elements are defined by second order derivatives of the electrostatic potential V:

$$V_{ij} = \partial^2 V / \partial x_i \partial x_j \tag{2.3}$$

where $x_i, x_j = x, y, z$. When selecting a coordinate system such that eq $\equiv V_{zz}$ is the maximum value of the EFG, only two independent parameters are needed to specify the EFG completely. These are eq and η, and the asymmetry parameter η defined by:

$$\eta = (V_{xx} - V_{yy})/V_{zz} \tag{2.4}$$

where x is the orthogonal direction of the next largest EFG. Then, the Hamiltonian of the quadrupole interaction for the relevant state can be expressed as:

$$\mathcal{H} = \frac{e^2qQ}{4I(2I-1)}(3\hat{I_z}^2 - I(I+1) + \eta(\hat{I_x}^2 - \hat{I_y}^2)) \tag{2.5}$$

where I is the nuclear spin number of the state. After the Hamiltonian matrix is diagnoalized, the energy levels are given directly by

$$E_Q = \frac{e^2qQ}{2I(2I-1)}[3I_z^2 - I(I+1)](1+\eta^2/3)^{1/2} \tag{2.6}$$

The electric quadrupole interaction causes a splitting of the (2I+1) fold degenerate energy level. Consequently, in the absence of a hyperfine field, one observes two resonance lines in the ^{57}Fe spectrum. These two lines are called a quadrupole doublet. The distance between the two lines seen in Fig.2.1(b), is called the quadrupole splitting (QS). It is an important hyperfine parameter that contains information about the chemical bond properties and the molecular and electronic structures of the studied materials.

The third hyperfine interaction is the magnetic hyperfine interaction. It is the interaction between the magnetic moment of the nucleus and the total effective magnetic field at the position of the nucleus. It causes magnetic hyperfine splitting or Zeeman splitting. The Hamiltonian for this interaction is described as:

$$\mathcal{H} = -\vec{\mu} \bullet \vec{H} = -g\mu_N(\hat{I}_xH_x + \hat{I}_yH_y + \hat{I}_zH_z) \tag{2.7}$$

where H is the effective magnetic field felt by the nucleus, $\hat{I}$ is the nuclear spin operator of the particular nuclear level, g is the gyromagnetic factor of this nuclear level, and μ_N is the nuclear magneton. Assigning H to be along the z-axis, the eigenvalues of Eq.2.7 are given by

$$E_m = -g\mu_N H m_I \tag{2.8}$$

where m_I is the magnetic quantum number of the nuclear spin state with the spin number I. In the absence of an EFG interaction, the magnetic hyperfine interaction splits the nuclear state with spin number I into 2I+1 equally spaced and non-degenerate substates, which are characterized by the sign and the magnitude of the

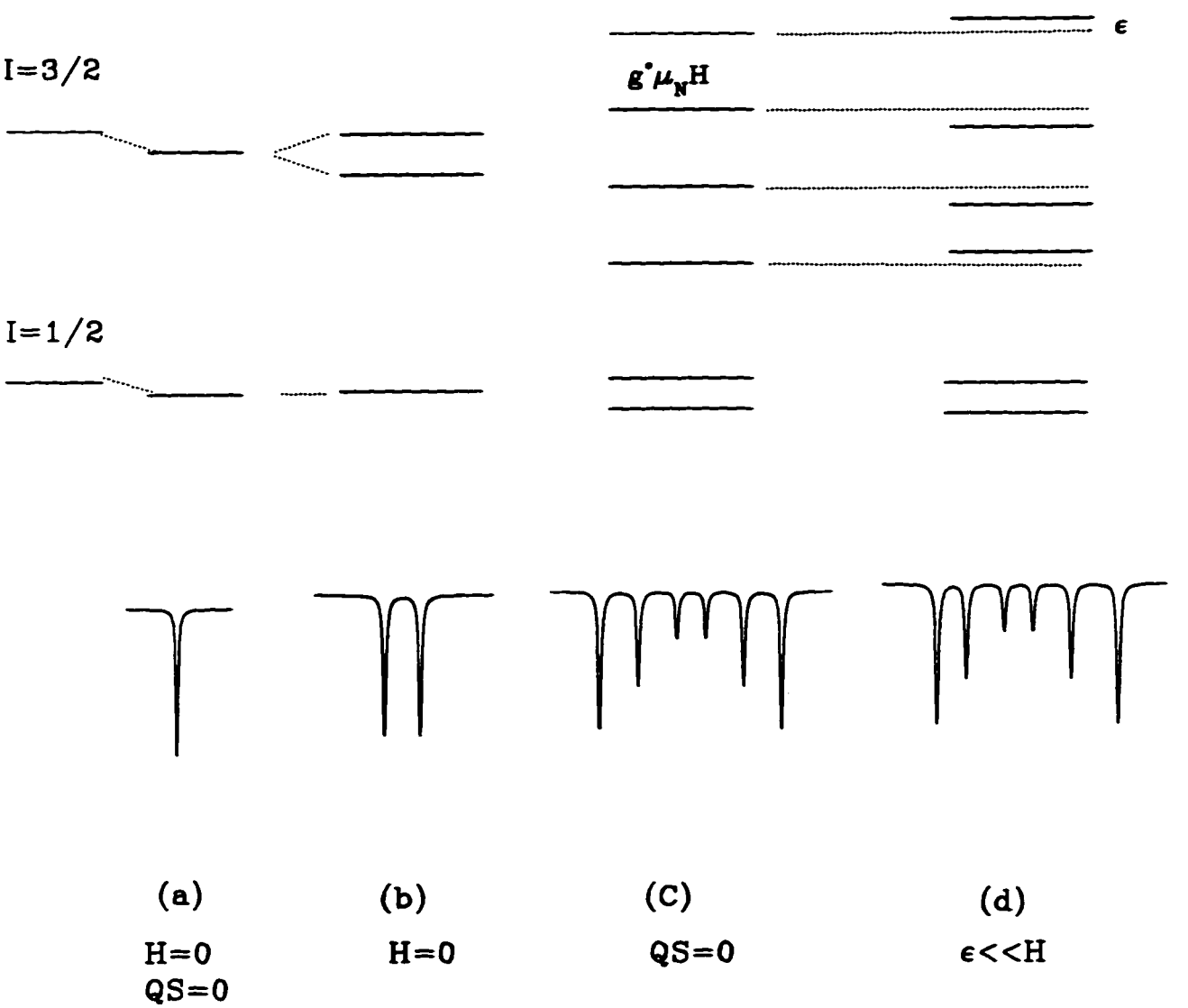

Figure 2.1 : Schematic hyperfine interactions diagram and the corresponding Mössbauer absorption spectra.

m_I. Fig.2.1(c) shows schematically the effect of this interaction in ^{57}Fe, where the I = 3/2 level is split into four sublevels and the ground state with I = 1/2 into two. The allowed transitions between the sublevels of the excited state and those of the ground state are found to be six in number following the selection rules.

In the case of mixed hyperfine interactions, the general treatment is more complicated. Several authors have worked on analytical solutions for the eigenvalues and eigenvectors of the I = 3/2 excited state of Fe-57 [35, 36, 57]. In the simple case where $e^2qQ \ll g^*\mu_N H$ and the EFG tensor is axially symmetric, a perturbation treatment shows that the energy levels are shifted from their e^2qQ = 0 positions by an amount ϵ:

$$\epsilon = (-1)^{|m_I|+1/2}\frac{e^2qQ}{4}[1 - \frac{sin^2\theta(3 - \eta cos2\phi)}{2}] \tag{2.9}$$

where θ and ϕ are the polar and azimuthal angles of magnetic field H in the coordinate system defined by the principal axes of EFG. The corresponding local diagram and spectrum is illustrated in Fig.2.1(d).

2.2 Unit Conversion

In Mössbauer spectroscopy, the unit for energy or splitting is given in mm/s, that can be converted to energy units by the Doppler effect formula:

$$E = \frac{E_0}{(1 - v/c)} \tag{2.10}$$

where E is the observed γ-ray energy for the source at velocity v with respect to the absorber, E_0 is the emmited γ-ray energy when the source is stationary, equal to 14.4130 keV for ^{57}Fe. c is the speed of light. For $v << c$, we have:

$$E = E_0(1 + v/c). \tag{2.11}$$

In the case where there is a hyperfine field splitting in the spectrum, one often uses the Zeeman splitting $z = g^*\mu_N H$ in mm/s to get the H in Tesla (or kOe). There is a simple relationship for this conversion. The derivation is given as follows. If $g^*\mu_N$ is known, then H can be obtained from $z/(g^*\mu_N)$. Here g^* is the first excited

state nuclear g-factor, equal to -0.10355 [37]. μ_N is the nuclear magneton, given by 3.15245×10^{-8} eV T^{-1}. Therefore:

$$\begin{aligned} g^*\mu_N &= 0.10355 \times 3.15245 \times 10^{-8} eVT^{-1} \\ &= 3.2628 \times 10^{-9} eVT^{-1}. \end{aligned}$$

Next, we need to convert the eV into mm/s. From Eq.2.11, a given energy splitting , ΔE, is equivalent to the corresponding velocity splitting, Δv, as:

$$\Delta E = E_0 \frac{\Delta v}{c} \tag{2.12}$$

which , for the transition from the first excited state in Fe-57, is

$$\begin{aligned} \Delta E &= \frac{14.4130 \times 10^3 eV}{2.99792 \times 10^8 m/s} \Delta v \\ &= (4.80767 \times 10^{-8} \text{eV per mm/s}) \Delta v. \end{aligned} \tag{2.13}$$

Having 1 eV = 0.2080 $\times10^8$ mm/s from Eq.2.13, we obtain $g^*\mu_N = 6.787 \times 10^{-2}$ mm/s T^{-1}. Therefore, from the Zeeman splitting in mm/s, dividing this factor, we obtain the H in Tesla. Otherwise, from the H in kOe, we can derive back to get the zeeman splitting in mm/s.

It is worth mentioning that the magnitude of g^* has changed during the last ten years. The factor $g^*\mu_N = 6.787 \times10^{-2}$ mm/s T^{-1} is calculated from the updated g^*. However, throughout this thesis, $g^*\mu_N$ is taken as 6.757×10^{-2} mm/s T^{-1} from the previous g^* value published in in 1979.

2.3 Transmission Integral

Quantum mechanics predicts that when the interaction between the nucleus and its surroundings is static the intrinsic resonance absorption cross-section is a Lorentzian line centered on E_0:

$$\sigma_a(E) = \frac{\sigma_0 \Gamma_0^2/4}{(E - E_0)^2 + \Gamma_0^2/4} \tag{2.14}$$

in which σ_0 is the cross-section at resonance, Γ_0 is the natural full width at half maximum (FWHM) of the emission, given by $\Gamma_0 = \hbar/\tau$ where $\hbar$ is the Plank's constant and τ is the decay time of the excited state.

Instead of observing the intrinsic Lorentzian, the measured Mössbauer absorption lineshape is determined by:

$$\begin{aligned} N(\psi) &= \eta_0 + \eta_m(1 - f_s) \\ &+ \frac{\eta_m f_s 2}{\pi\Gamma_0}\int dE \frac{\Gamma_0^2/4}{(E-E_0)^2+\Gamma_0^2} e^{-t_a\sigma_a(E)/\sigma_0} \end{aligned} \tag{2.15}$$

where $N(\psi)$ is the number of counts per unit time in the channel centered at ψ, η_0 is the count rate per channel from all sources excluding the Mössbauer γ-rays, η_m is the count rate per channel from the Mössbauer γ-rays, including both recoilless and non recoilless events, f_s is the Mössbauer recoilless fraction of the source given by $f_s = exp(-k^2 < x^2 >)$, with the wave number k for the Mössbauer γ-ray, and $< x^2 >$ is the mean square displacement of the emitting nucleus. t_a is the dimensionless thickness parameter defined as $t_a = f_a n_a \sigma_0$, where f_a is the recoilless fraction of the absorber and n_a is the number of Mössbauer isotope atoms per area of the absorber. $\sigma_a(E)$ is the intrinsic resonance absorption cross-section of the Mössbauer nucleus.

When an absorber is in the thin limit where $t_a \ll 1$, it can be proved that if $\sigma_a(E)$ is a Lorentzian with natural FWHM Γ_0, the observed lineshape is still a Lorentzian but the FWHM changes to $2\Gamma_0$.

2.4 Hyperfine Parameter Distributions

We now consider the case where only the magnetic hyperfine field is distributed while the CS and the ϵ are constants. In the thin absorber limit [38], given a set of hyperfine parameters: a CS (δ), quadrupole splitting shift (ϵ), and a hyperfine magnetic field H where $e^2qQ \ll g^*\mu_N H$, six lorentzian lines would be observed. This six line pattern is called the elemental sextet and is written as:

$$E(H;v) = \sum_i^6 h_i L(v_i(\delta,\epsilon,H) - v) \tag{2.16}$$

where the sum is over 6 Lorentzians, each of them centered at position v_i which is determined by δ, ϵ, and H. v is the velocity or energy, h_i is the i-dependent Lorentzian height.

If there are N nonequivalent Mössbauer nuclei, each of them experiences different hyperfine fields $H_i(i = 1, ...N)$. The resulting observed spectrum will be the superposition of all the elemental Lorentzian sextets:

$$M(v) = \sum_{i}^{N} E(H_i; v) = \sum_{k} g(k) E(H_k; v) \tag{2.17}$$

where the first sum is over all nuclei, the second sum is over all the different values of the hyperfine field, $g(k)$ is the weight factor for the nuclei having the hyperfine field H_k. If the electronic and magnetic environment changes continuously from atom to atom, for instance in solid solutions or amorphous alloys, the hyperfine parameters will spread over a certain range. The second sum in Eq.2.17 can be replaced by an integral:

$$M(v) = \int E(H; v) P(H) dH \tag{2.18}$$

where $P(H)$ is the probability density distribution function with respect to the elemental lineshape $E(H; v)$. Resolving it from the spectrum is an important aspect of the spectral analysis in Mössbauer spectroscopy.

Various methods have been developed to extract the hyperfine parameter distributions from Mössbauer spectra. For example, there are: the Fourier transform method [39], the damped histogram method [40] and a new Voigt-based HFD method (VBF) [41]. The one used in this work is the VBF method.

Chapter 3. PHENOMENOLOGICAL MODEL OF THE HYPERFINE FIELD

3.1 Electronic Origin of the Hyperfine Field

In Chapter 2, the magnetic hyperfine field has occurred in the hyperfine magnetic interaction of Eq.2.7, and we know how to calculate the spectra with it. The hyperfine field H in Eq.2.7 is an effective field (H^{eff}). It may consist of many terms since it originates within the atom itself, and within the crystal via exchange interactions, or as a result of placing the compound in an externally applied magnetic field. A general expression is written as:

$$\vec{H}^{eff} = \vec{H}^{ext} + \vec{H}^{int}. \tag{3.1}$$

Here, the internal component consists of three parts:

$$\vec{H}^{int} = \vec{H}^{L} + \vec{H}^{d} + \vec{H}^{d-d} + \vec{H}^{c}. \tag{3.2}$$

where $\vec{H}^{L}$ is the contribution from the orbital motion of the electrons written as

$$\vec{H}^{L} = -2\mu_B < r^{-3} >_L \vec{L}_P. \tag{3.3}$$

It is negligible for 3d transition metals where the orbital momentum is quenched by the crystal field. $\vec{H}^{d}$ arises from the dipolar interactions between the nuclear moment and the electron spin moments of the atom and is called the dipolar term:

$$\vec{H}^{d} = -2\mu_B < 3\vec{r}(\vec{s}.\vec{r})r^{-5} - \vec{s}r^{-3} > . \tag{3.4}$$

It is thought to be negligible for 3d transition metals [33].

$\vec{H}^{d-d}$ is the dipole-dipole magnetic interaction between the nuclear moments. It is a long distance interaction, and comparatively weak. The last term $\vec{H}^{c}$ is the

contribution of the spin polarization at the nucleus and is called the Fermi contact contribution. It can be written as

$$\vec{H}^c = 8/3\pi\mu_B \sum_n [(|\uparrow \psi(0)_{ns}|^2 - |\downarrow \psi(0)_{ns}|^2)] \tag{3.5}$$

with $|\uparrow \psi(0)_{ns}|^2$ and $|\downarrow \psi(0)_{ns}|^2$ being the spin up and spin down densities at the nucleus, respectively. It is the most important contribution and it is proportional to the net electron spin density at the nuclear site. To understand the spin polarization mechanism of the hyperfine field, $\vec{H}^c$ is decomposed into the core polarization contribution H_{cp} and the conduction electron polarization contribution H_{cep} [45]. H_{cp} is contribution due to the inner s-electrons that are polarized by the magnetic moment of the atom itself (i.e. the local d electrons). H_{cep} is further considered as a sum of two terms: one due to polarization of the conduction electrons by the probe atomic moment, the other due to the sum of the conduction electron polarization caused by all the neighbour moments [43].

Alternatively, it is useful to divide the $\vec{H}^c$ into two different terms: a "local" term that includes H_{cp} and the part of the conduction electron polarization that is caused by the local (on-site or probe) moment and a "transferred" term that includes only the part of H_{cp} that is due to moments other than the local moment [44].

From these contributions we see that magnetic hyperfine field is related to a many-body problem. A quantitative analysis of the different contributions to the hyperfine field is a difficult task. It requires an exact evaluation of the electron densities for both spin directions. Therefore it is often studied by using phenomenological models. Recently, the theory of hyperfine field interactions in metallic system has become an active field for electronic structure calculations [46]. This should provide a theoretical basis for our understanding of the hyperfine and its phenomenological models.

3.2 Previous Mössbauer Studies of Fe-Ni and Related Alloys

Mössbauer spectroscopy has been applied to study magnetism of iron metal and metallic iron alloys almost since its discovery. Many works on Fe-Ni alloys were undertaken. The majority of studies focus near the Invar composition (65 at. % Fe), which includes studies at different temperatures (e.g.[42, 47, 48, 54], with applied field [49, 50], and using polarized γ-rays [51], and high pressure [6, 52, 53].

The purpose of these studies are to understand the magnetic anomalies of the Invar alloys. The spectra are mainly interpreted in terms of HFDs [48, 54, 55, 56, 62]. Independent of fitting method, at low temperature (T = 4.2 K) the HFD of the Invar alloy contains a high field peak, and low and intermediate field components. It is agreed that the high field component arises from the ferromagnetic Fe atoms. But for the low and intermediate field values, it is still ambiguous whether they originate from the low moment iron in Weiss's 2γ-state model [58] or from the latent antiferromagnetic high moment Fe [59, 60]. These are the two main interpretations. Attempts have been made to test the validity of these two models [48, 51]. It remains one of the open questions in Invar problem study.

Mössbauer studies of chemically ordered and disordered Ni_3Fe alloys provided information on how the hyperfine parameters are related to atomic structure [65]. Working with single crystals of Ni_3Fe, Cranshaw identified components in the Mössbauer spectrum from Fe sites and Ni sites of the ordered structure and reported evidence of anisotropic hyperfine parameters contributions [66, 67]. Note that, Cranshaw's isotropic parameters for ordered Ni_3Fe do not lead to a correct predicted HFD for a random alloy of the same bulk composition.

Studies at different compositions of fcc Fe-Ni have also been reported [61, 62, 64]. Such studies are aimed at (1)understanding the magnetic properties of the Invar alloy by understanding that of the whole alloy system (2)obtaining the information about the core and conduction electron polarization, that would contribute to a general understanding of the cause of the hyperfine field in other alloy systems.

3.3 Previous Phenomenological Models of the Hyperfine Fields in Alloys

To understand the large amount of the measured hyperfine field data, attempts have been made to find phenomenological relationships with other measured quantities such as the bulk magnetization. The very first experiment on pure iron [68] has shown that the hyperfine internal field has the same temperature dependence as the saturation magnetization. This similarity was seen later in the Fe-Ni alloys [7, 64]. These observations led to a natural assumption that the hyperfine field at 57-Fe nuclei is proportional to the average magnetic moment not only for pure iron but also for its alloys with the other elements. The experimental verification showed that the average hyperfine field varies in a way that is not directly proportional to the average magnetic moment [64]. An attempt was first made by the same authors to fit the average hyperfine field data as:

$$H = a\mu_{Fe} + b\bar{\mu} \tag{3.6}$$

where $\bar{\mu}$ is the (saturation) moment per atom of the alloy and μ_{Fe} is the (saturation) moment on an Fe atom in the alloy. Parameters a and b are proportionality constants. The physical meaning of a and b were not clearly given at first. Later this model was successfully used in ^{57}Fe and ^{61}Ni hyperfine field study of Fe-Ni alloys [69, 70]. It was often referred to as an empirical formula.

Some other variations about the model have also been proposed [71, 72, 73, 74] and compared [75]. But they are not as widely used as the one above.

The phenomenological model works approximately by connecting the average hyperfine field to the average atomic magnetic moments. It does not gives a microscopic perspective of the physical origin of the hyperfine field.

3.4 Proposed Phenomenological Model

In fact, the average hyperfine field is only part of the available information. The HFD contains more microscopic information about each iron nucleus in the absorber. It

can be resolved from the spectra by various HFDs methods. A microscopic relationship between the hyperfine field for a given site and the moments surrounding it is desired for extracting the magnetic moments and their local environments from the measured HFDs. Such a model, once we know the spin structure at any composition and temperature, gives both the average hyperfine field and the HFDs.

Based on the polarization mechanism of the hyperfine field (that the magnitude of the hyperfine field is proportional to the spin density at the nucleus), we propose a microscopic model of the hyperfine field. It can be stated that the thermal average hyperfine field at temperature T for a given site k is a vector sum of the local term and the transferred term. This is expressed as

$$< \vec{H}_k >_T = A < \vec{\mu}_k >_T + B \sum_j < \vec{\mu}_j >_T \tag{3.7}$$

where the first term on the right is proportional to the on-site thermal average moment $< \vec{\mu}_k >_T$ and is called the local term. A is the coupling parameter between the local moment and the on-site hyperfine field. The local term reflects how the s-electron spin density at the nucleus is affected by the local moment. It contains the core s-electrons (1s, 2s, 3s) and the conduction (4s-like) electron's polarization due to the local moment. The second term is the transferred field. It is related to the part of the spin density at the nucleus that is caused by near neighbor moment polarization of the conduction electrons. It sums over all the near neighbor moments $< \vec{\mu}_j >_T$. The parameter B is the coupling between the near neighbor moments and the on site hyperfine field. It is called the transferred coupling parameter.

This model, in comparison with the previous phenomenological model given by Eq.3.6, presents four important modifications: (1) Instead of taking an average hyperfine field, we use a site-specific hyperfine field H_k (for site-k). (2) Instead of dealing only with saturation (i.e. T = 0 K) values, we use thermal average local moments and thermal average site-specific hyperfine fields. (3) We take H_k and the local magnetic moments to be vector quantities rather than scalars. (4) Finally, we replace $\bar{\mu}$ by a vector sum of near neighbour local moments.

Later (Chapters 6 and 7) we will apply the model to the hyperfine field data of fcc Fe-Ni alloys. Then we will use it to simulate the HFDs of the alloys as a function

of temperature and composition (Part III).

3.5 Case of Perfect Randomness

When a binary alloy is perfectly random, the populations of local environments distribute binomially. The probability of finding a given Fe atom surrounded by k Fe atoms (k = 0 to 12) in the near neighbor shell is:

$$P_k(y) = y^k(1-y)^{12-k}\frac{12!}{k!(12-k)!} \tag{3.8}$$

where y is the concentration of Fe in Fe_yNi_{1-y}.

In the collinear ferromagnets, all spins align in the same direction. The vector sum in Eq.3.7 becomes a scalar operation. For an Fe atom with k Fe atoms in the near neighbor shell, the hyperfine field is written as

$$\begin{aligned} H_k &= A < \mu_{Fe} > +B\sum_{jnn} < \mu_{jnn} > \\ &= A < \mu_{Fe} > +12B < \mu_{Ni} > +kB(< \mu_{Fe} > - < \mu_{Ni} >) \end{aligned} \tag{3.9}$$

Here for simplicity, we dropped the $<>_T$ in Eq.3.10 and used <> from now on to denote both the space and the thermal average of physical properties. With the binomial distribution, the average hyperfine field $< H >$ can be predicted as:

$$\begin{aligned} < H > &= \sum_{k=0}^{12} P_k(y) < H_k > \\ &= A < \mu_{Fe} > +12B < \mu_{Ni} > +12yB(< \mu_{Fe} > - < \mu_{Ni} >) \end{aligned} \tag{3.10}$$

On the other hand, the HFDs can be obtained from the binomial distribution P_k at each field value H_k. To compare with the HFD from the spectra, the probability density often used in the text is defined as:

$$P(H_k) = \frac{P_k(y)}{dH_k/dk} = \frac{P_k(y)}{B(< \mu_{Fe} > - < \mu_{Ni} >)} \tag{3.11}$$

where $P(H_k)$ is the probability density, $P_k(y)$ is the binomial probability, and $\frac{dH_k}{dk}$ is the derivative of H_k with respect to k.

Chapter 4. EXPERIMENTAL AND SPECTRAL ANALYSIS METHODS

4.1 Experimental Aspects

Conventional transmission Mössbauer spectra of fcc Fe-Ni alloys were taken with 25 to 50 mCi sources of Co-57 in rhodium matrix. The spectrometer was operated in a constant acceleration mode. Data was accumulated in 1024 channels. The Doppler velocity was calibrated with an α-Fe spectrum at RT. The spectra were folded to ensure flat background.

The spectra were taken at RT, LNT and LHT in cryostat in which temperature is measured within 1 K accuracy. In our case, RT is 295 K, LNT is 78 K and LHT is from 4.2 K to 5 K. All absorbers were prepared by cutting a uniform piece of 99.9995% Al foil to cover the 0.5" diameter cryogenic sample holder. Sample thickness was typically from 40 μm to 80 μm.

4.2 Spectral Analysis Method

Various HFD methods have been developed to extract the information from the Mössbauer spectra. The one used in this work is the VBF method [41]. It assumes that the arbitrary shaped HFD can be represented as a sum of Gaussians as follows:

$$P(p) = \sum_{i}^{N} w_i G_i(p_{0i}, \sigma_{pi}; p) \tag{4.1}$$

where

$$G_i(p_{0i}, \sigma_{pi}; p) = \frac{1}{\sigma_{pi}\sqrt{2\pi}} exp[-\frac{(p - p_{0i})^2}{2\sigma_{pi}^2}] \tag{4.2}$$

and w_i is the weight, p_{0i} is the position, and σ_{pi} is the width of the ith Gaussian component.

The spectral lineshape in this method can be expressed as a sum of Voigt lines. The Voigt function is a convolution of a Gaussian and a Lorentzian. Our spectra could be fitted with only two Gaussian components to obtain a good fit ($\chi^2_{red} \sim 1$).

The applicability of the method in Fe-Ni alloys has been demonstrated previously [62]. At most, three Gaussian components were required to obtain convergence to unique HFDs corresponding to ideal fits.

Each Gaussian component of a HFD needs three parameters: a weight factor p_i, a centroid H_{0i}, and a width σ_{0i}, where i labels the particular component. Additional parameters are: the background, BG, the total spectral area, A_T, the elemental height ratios of line-1 to line-3, $h1/h3$, and of line-2 to line-3, $h2/h3$, and the Lorentzian FWHM, Γ. The center shift δ and the quadrupole shift (ϵ) are assumed to be linearly coupled to the hyperfine field with four coupling parameters ($\delta_0, \delta_1, \epsilon_0, \epsilon_1$):

$$\delta = \delta_0 + \delta_1 H \tag{4.3}$$

and

$$\epsilon = \epsilon_0 + \epsilon_1 H \tag{4.4}$$

This amounts to 8 + 3N parameters when N Gaussian components are used.

Chapter 5. SAMPLE SYNTHESIS AND CHARACTERIZATION

5.1 Sample Synthesis

There are two groups of fcc Fe-Ni alloys made by different methods by Dr. R.A.Dunlap at Dalhousie University. The first group is made by splat quenching (SQ) and the other is made by roller quenching (RQ).

SQ Fe_yNi_{1-y} samples with $y = 0.70, 0.68, 0.65, 0.60, 0.55, ..., 0.05$ were prepared as described elsewhere [63] and they have been previously studied at RT temperature [62].

The RQ samples with $y = 0.60, 0.55, 0.50, 0.45, 0.35, 0.25, 0.15, 0.05$ were prepared as follows. Ingots of the composition Fe_yNi_{1-y} with $(0.05 \leq y \leq 0.60)$ were prepared by melting elemental components (99.98 wt.% Fe and 99.97 wt.% Ni) in an argon arc furnace. Portions of the ingots of 600-700 mg were rapidly quenched from the melt utilizing the twin roller method [76, 77]. Samples were induction melted under He in a quartz tube with a 2.0 mm diameter orifice and were injected by a small overpressure. The rollers were hardened steel with a diameter of 5.0 cm. Samples of all compositions were prepared with a roller speed of 3000 revolutions per minute (rpm) and a force between rollers of 200 N. As well, samples with y = 0.25 were prepared as a function of roller speed between 2000 to 3000 rmp and forces between about 69 and 200 N in order to investigate the effect of different quenching rates. Typical foil dimensions were about 1 cm wide by a few cm long. The typical thickness is about 60 to 100 μm. Quench rates obtained by this method have been estimated at between 10^5 to 10^6 K/s [78]. For the y = 0.25 samples, relative quench rate for different samples has been estimated on the basis of relative foil thickness.

5.2 Lattice Parameters From X-ray Diffraction

The lattice parameter of fcc Fe-Ni alloys is an important parameter. It is related to the stability of the fcc structure and to magneto-striction and Invar effects. It has been measured as a function of the composition and temperature (e.g. [3, 8]) using X-ray diffraction (XRD). Their studies show an important feature: that the lattice parameter increases linearly with the iron content (Vegard's law [79]) at low iron concentrations, and deviates from the straight line from y = 0.60 at T = 0 K. In contrast, the spontaneous magnetization deviates from the Slater-Pauling curve at $y \geq 0.45$ [7]. There is a similarity between the drop in the lattice parameter and the magnetic moment and a dissimilarity that the drop starts at different compositions.

To check the lattice parameter in our samples, and characterize the samples more completely, we measured all lattice parameters of SQ Fe_yNi_{1-y} foils ($0.05 \leq y \leq 0.75$) at RT using a Philips-PW3020 diffractometer with $Cu\ K_\alpha$ radiation. All the samples with $y \leq 0.7$ were flattened by polishing on sand paper. It is known that polishing samples at $y \geq 0.68$ can induce the bcc phase. A flat piece at y = 0.75 is used without polishing.

Typical XRD patterns with Rietveld fits are shown in Fig.5.1 and Fig.5.2. Lattice parameters are obtained from fitting the diffraction profile by the Rietveld method [80]. Different fittings with different numbers of free parameters have been performed to give the uncertainty in the final lattice parameters. The errors are the maximum error calculated from the different fits, all of which give rise to approximately equal goodness of the fit. The obtained lattice parameters are listed in Table 5.1, and shown in Fig.5.3.

The result is in agreement with the previous measurements. The lattice parameter increases following the Vegard's law till it reaches a maximum at y = 0.60, then it deviates continuously.

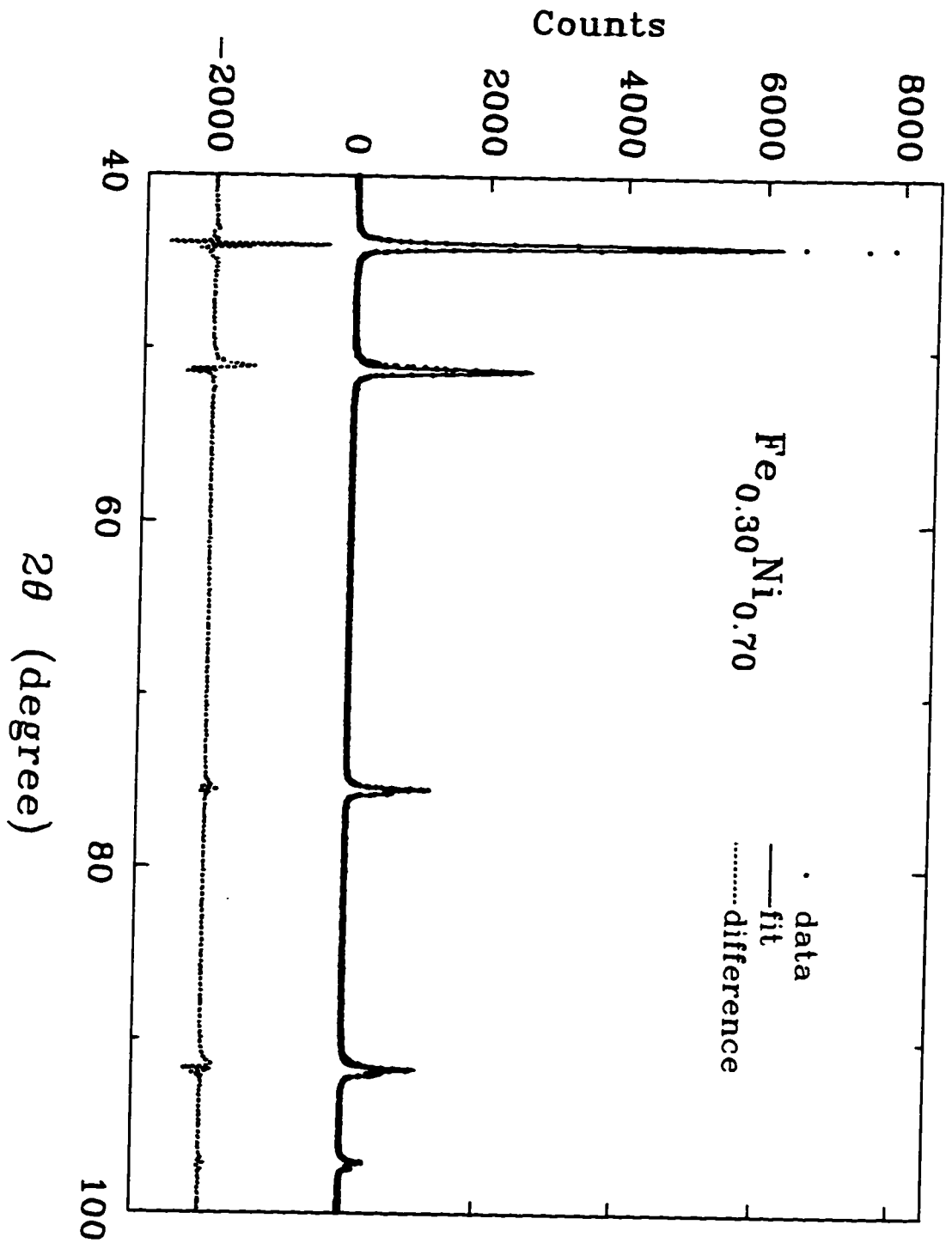

Figure 5.1: XRD pattern with Rietveld fit for $Fe_{0.30}Ni_{0.70}$.

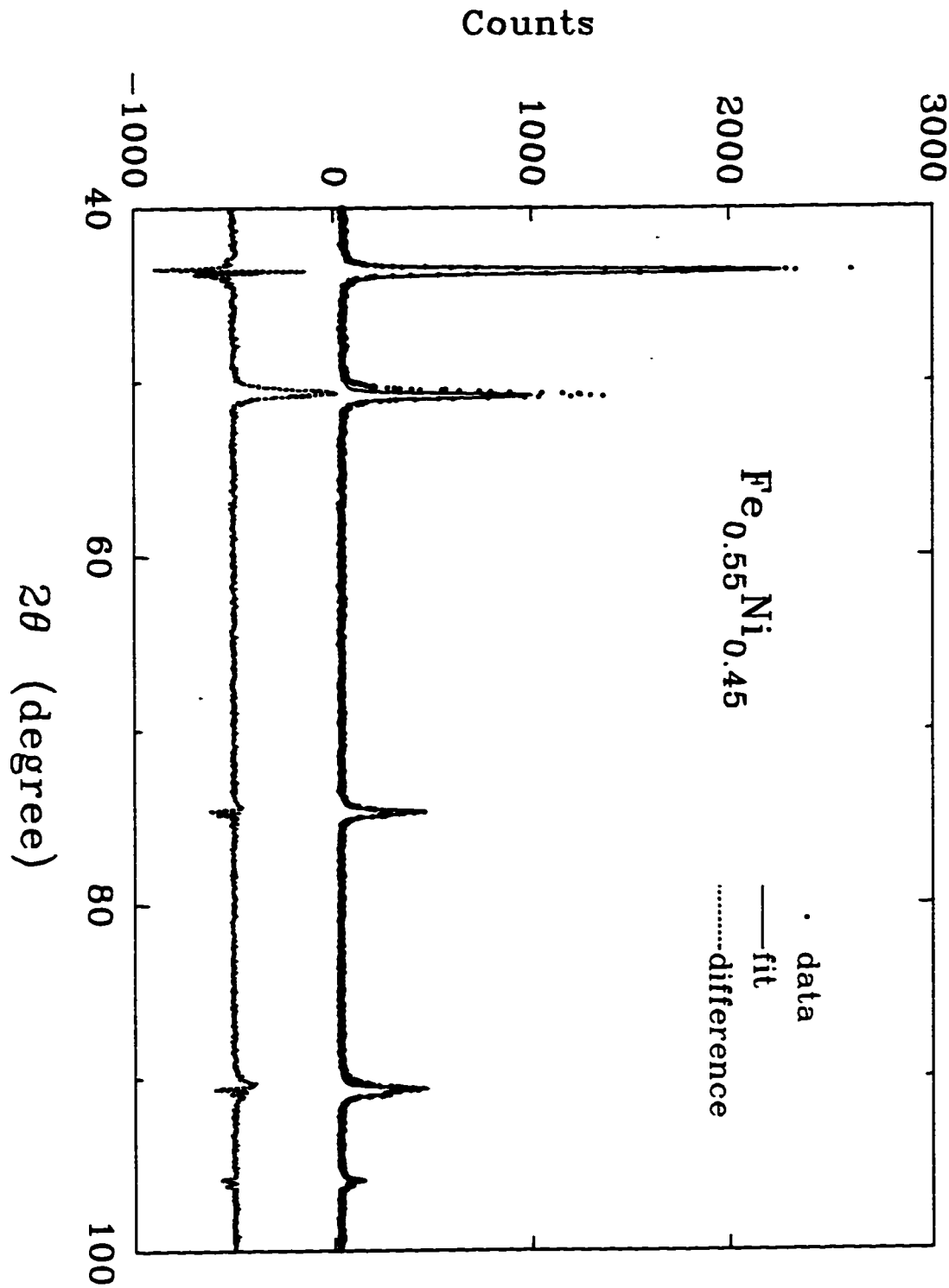

Figure 5.2: XRD pattern with Rietveld fit for $Fe_{0.55}Ni_{0.45}$.

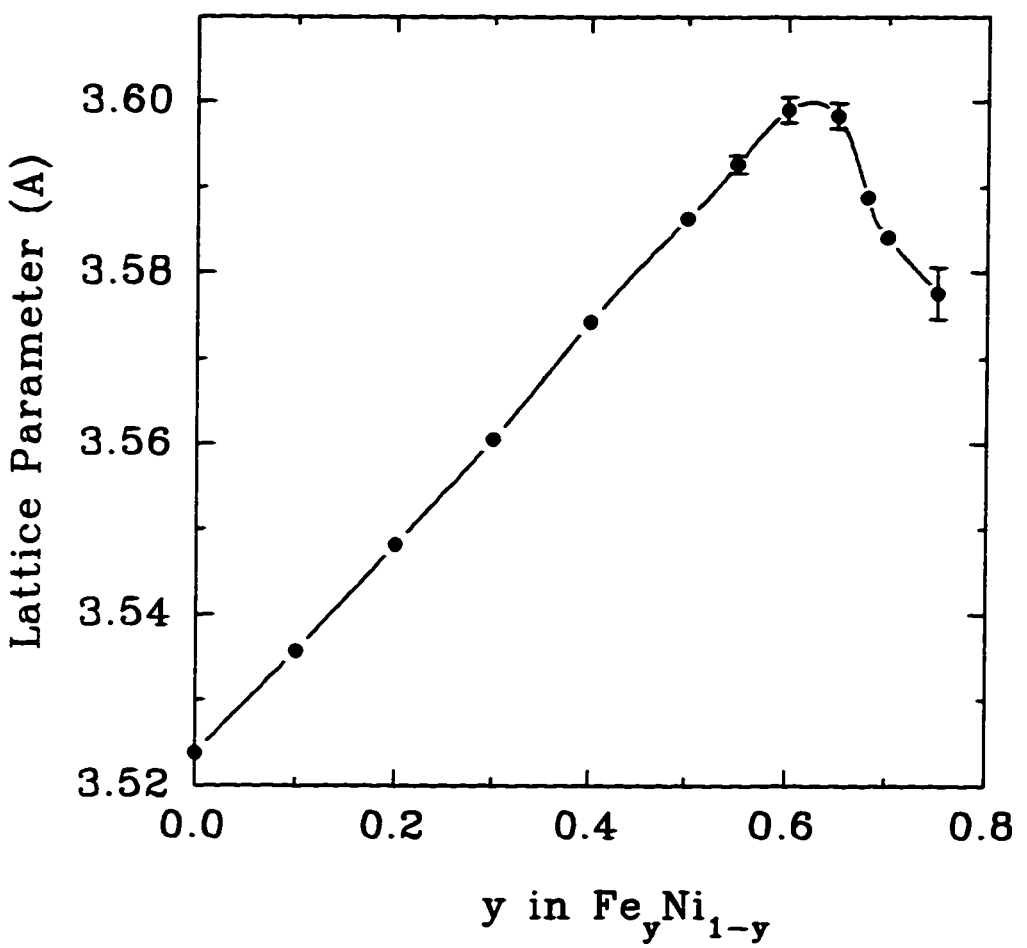

Figure 5.3: RT Lattice parameters of SQ samples.

Table 5.1: Lattice parameters of SQ Fe-Ni alloys.

y in Fe_yNi_{1-y}	a ($\AA$)	$\Delta a(\AA)$
0.10	3.5357	0.0005
0.20	3.5483	0.0005
0.30	3.5605	0.0005
0.40	3.5843	0.0005
0.45	3.5786	0.0005
0.50	3.5863	0.0005
0.55	3.5927	0.0010
0.60	3.5990	0.0015
0.65	3.5983	0.0015
0.68	3.5888	0.0005
0.70	3.5841	0.0005
0.75	3.5776	0.0030

5.3 XRD Line Width

Another interesting feature is noticed from the RT X-ray diffraction peaks of the alloys. The full width at half maximum (FWHM) of each peak changes with the composition. As shown in Fig.5.4, a general trend is seen that the FWHM increases with the increase of the iron concentration till the maximum width near the Invar composition (y $\simeq$ 0.60), then it drops very rapidly at y = 0.68, and broadens slightly after that. Here, the peaks are labeled as follows: P1 = (111) at $2\theta \sim 44^0$, P2 = (200) at $2\theta \sim 51^0$, P3 = (220) at $2\theta \sim 75^0$, P4 = (311) at $2\theta \sim 91^0$, and P5 = (222) at $2\theta \sim 97^0$. These are the first five reflections, in order of increasing 2θ angle from P1 to P5.

The initial broadening up to y = 0.65 may be due to the magneto-volume effect and magnetic inhomogeneity (the frustrated magnetic Fe-Fe bonds). The drop that occurs between y = 0.65 and y = 0.68 is probably due to a concomitant drop in the Curie point such that, at RT, the spontaneous average moment drops significantly between these compositions.

Arai [81] studied XRD line width for the Invar alloy at different temperatures.

His measured XRD line widths were much broader at $T<T_C$ than at $T>T_C$. He also proposes that the line broadening is due to the internal stress through the spontaneous volume magnetostriction depending on the magnetic moments.

A systematic study on the breadth of the X-ray diffraction lines in Fe_yNi_{1-y} at low temperature would be helpful to understand the change in the FWHM as a function of the composition.

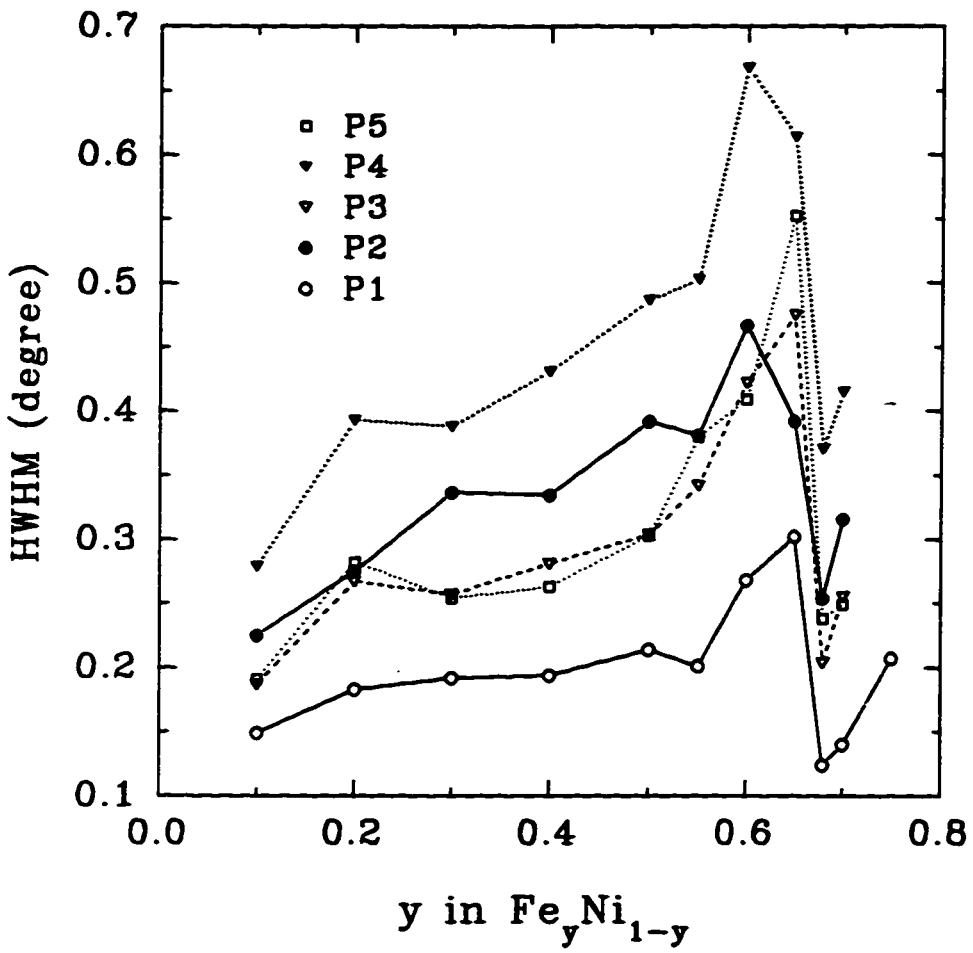

Figure 5.4: XRD FWHM at RT for SQ samples.

Chapter 6. MÖSSBAUER RESULTS FOR SQ SAMPLES

6.1 Results for LNT Spectra of SQ Samples

SQ fcc Fe_yNi_{1-y} alloys are studied by Mössbauer spectroscopy at RT and LNT, and LHT in our laboratory. The RT results were reported previously [62]. Here we first focus on the Mössbauer study of the spectra at LNT. All the LNT spectra were fitted by the VBF method with 2 Gaussian components, except three components are required to obtained good fits ($\chi^2_{red} \sim 1$) for y = 0.65 and 0.68. The spectrum for y = 0.70 at LNT shows only a bcc phase, that indicates a martensitic phase transition undergone when the temperature decreases from RT to LNT in this Fe-rich sample.

Fig.6.1 shows some of the fitted spectra, and the corresponding HFDs. The final fitting parameters are given in Table 6.1. Notice that the unit of the hyperfine splitting ($g^*\mu_N H$) is in mm/s whereas the unit of the hyperfine field (H) is in kOe. Given the splitting in mm/s, we can obtain H in kOe by dividing out the factor $g^*\mu_N$ (= 6.757 $\times 10^{-3}$ mm/s per kOe given in section 2.2). Here Γ is left as a free parameter as an effective way to take thickness broadening into account. For comparison, the true value of Γ is $2\Gamma_0$ = 0.197 mm/s.

All the spectra at LNT are interpreted by HFDs. As seen in Fig.6.1, HFDs for y $\leq$ 0.60 have no low field or intermediate field contributions, only one main peak is present even though two Gaussian components are used in most cases. This can also be noticed in the spectra themselves where the background over the whole velocity range is not depressed below its off-resonance value. Whereas in the spectra of y = 0.65 and 0.68, the HFDs have low field bumps which cause the spectra to have depressed effective background levels between the main absorption lines.

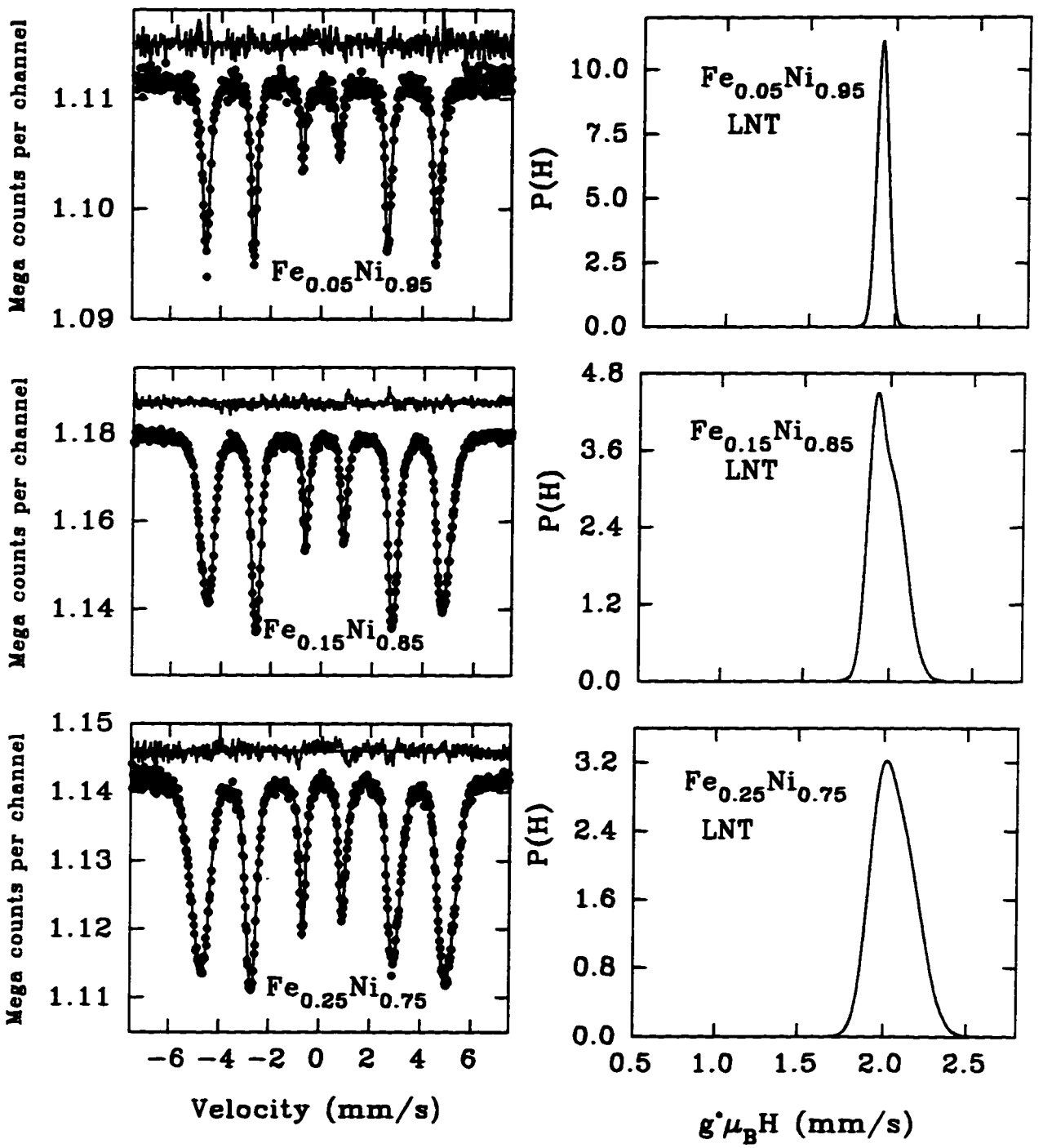

Figure 6.1 : Mössbauer spectra of selected SQ samples at LNT and corresponding HFDs.

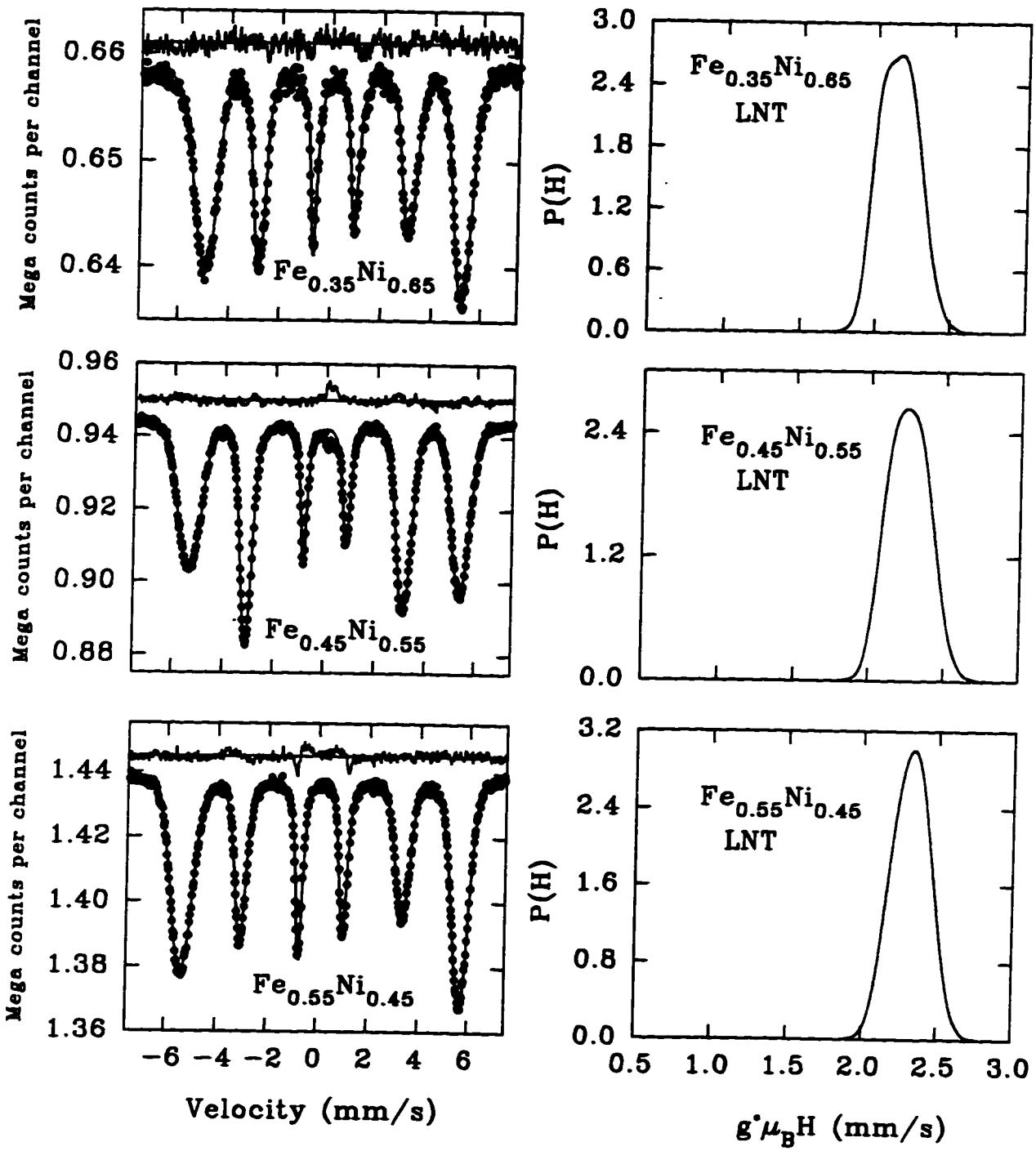

Fig.6.1 continued...

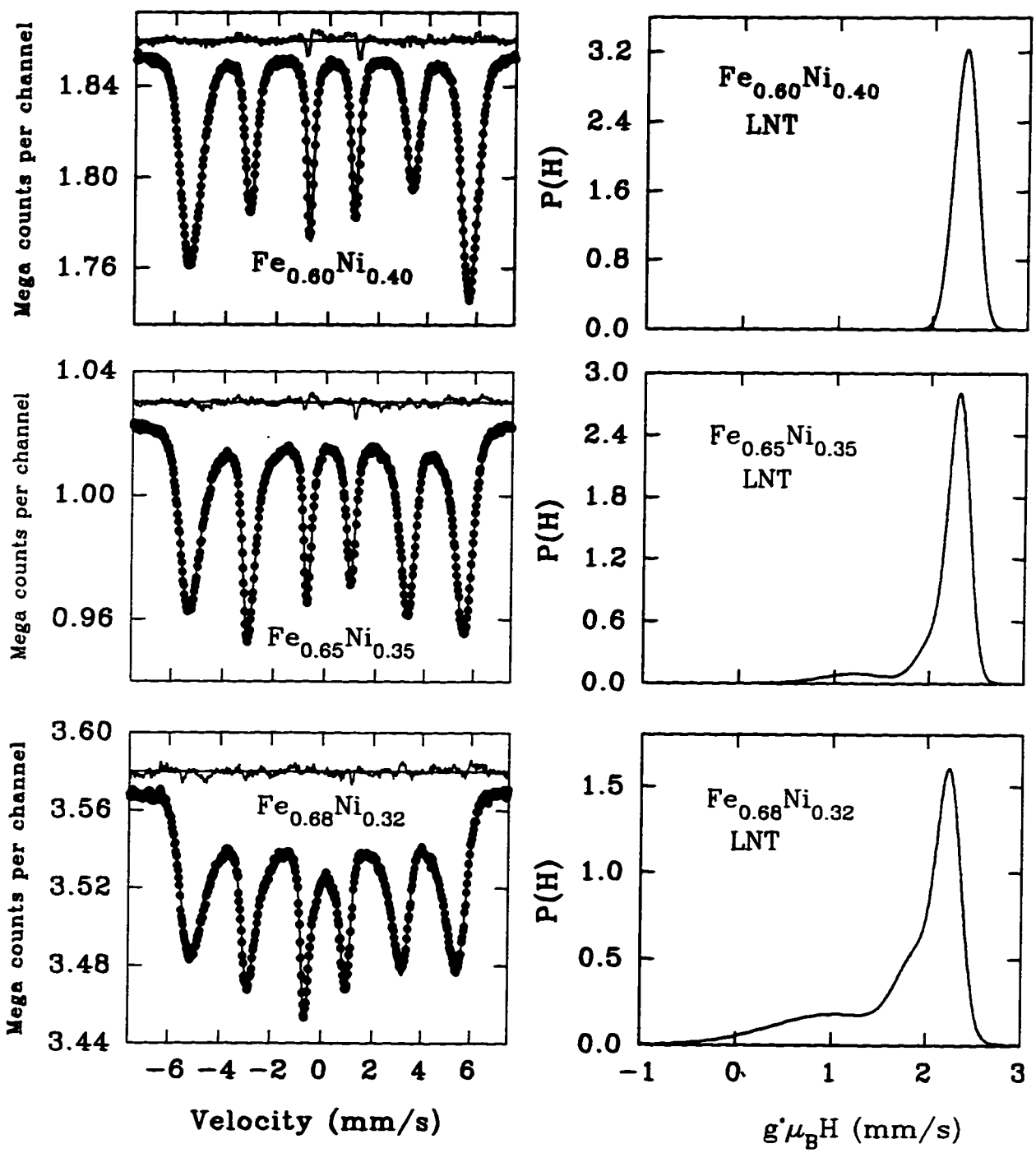

Fig.6.1 continued...

Table 6.1: LNT spectral fitting parameters for SQ samples.

y	$h3_1$	$h3_2$	$h3_3$	HF_1 (kOe)	HF_2 (kOe)	HF_3 (kOe)	σ_1 (kOe)	σ_2 (kOe)	σ_3 (kOe)
0.05	7538	-	-	283.97	-	-	5.30	-	-
0.15	18616	9167	-	297.55	281.86	-	12.76	6.75	-
0.25	15266	8906	-	311.82	291.52	-	16.70	11.17	-
0.30	25634	11454	-	316.83	294.65	-	17.52	10.90	-
0.35	14369	3264	-	321.49	297.42	-	18.29	9.62	-
0.40	35261	11286	-	331.19	306.53	-	18.14	11.87	-
0.45	27167	13549	-	342.02	315.97	-	17.04	12.79	-
0.50	42514	4685	-	340.96	313.07	-	18.25	10.03	-
0.55	36622	21049	-	350.93	327.93	-	15.25	14.29	-
0.60	37429	46106	-	353.46	335.56	-	14.49	16.11	-
0.65	42883	12813	4781	340.08	306.39	180.7	16.12	26.93	49.77
0.68	54392	39112	37726	330.42	151.57	287.1	18.21	97.96	34.51

y	δ_0 (mm/s)	δ_1 (mm/s)	ε_0 (mm/s)	ε_1 (mm/s)	h1/h3	h2/h3	BG	Γ (mm/s)	χ^2_{red}
0.05	-0.142	0.068	0.210	-0.110	2.77	2.40	1111676	0.236	1.06
0.15	0.138	-0.007	0.150	-0.075	3.08	2.53	1180104	0.236	1.34
0.25	0.0797	0.029	0.320	-0.153	2.97	2.09	1142447	0.262	1.33
0.30	0.127	0.007	0.402	-0.190	2.89	1.73	1003192	0.282	1.70
0.35	0.186	-0.019	0.518	-0.241	2.78	1.63	658743	0.303	1.42
0.40	0.178	-0.012	0.513	-0.233	2.78	1.61	1101610	0.299	2.21
0.45	0.202	-0.024	0.495	-0.220	2.78	1.72	1867629	0.312	1.76
0.50	0.219	-0.028	0.483	-0.212	2.69	1.86	1068765	0.315	2.31
0.55	0.228	-0.033	0.542	-0.235	2.60	1.35	1440029	0.313	2.44
0.60	0.204	-0.023	0.543	-0.234	2.60	1.21	1855358	0.312	3.07
0.65	0.182	-0.013	0.469	-0.205	2.45	1.77	1024128	0.364	2.75
0.68	0.199	-0.022	0.226	-0.101	2.76	1.76	3572206	0.322	2.53

In Table 6.1, $h3_i$ is the line-3 peak height for the ith Gaussian component, HF_i is the center of the ith HF Gaussian distribution, σ_i is the hyperfine field Gaussian distribution width for the component-i, where i = 1, 2, 3.

An interpretation of the HFDs of the Fe-rich alloys in terms of both the latent antiferromagnetism model and the spin structure from MC simulation is given in part III, along with a comparison with the binomial distribution in the collinear ferromagnetic region (section 6.3).

More information can be obtained from the fitting parameters. We first examine the distribution widths of hyperfine parameters. As mentioned in section 4.2, both the CS and the QS shift are linearly coupled with the hyperfine field. From the HFD we can easily obtain the corresponding QS shift distribution (QSD) and CS distribution (CSD). Therefore, we have three hyperfine parameter distributions (CSD, QSD, HFD) for each of the spectra.

For most of the spectra we use two Gaussian components to fit the HFDs. Each component has its a centroid, and a Gaussian width. To represent the HFD width properly, we choose the standard deviation $\sigma_H = (< H^2 > - < H >^2)^{1/2}$ to describe the overall HFD width. The standard deviation is related to the component-wise Gaussian width in such a way that if there are two Gaussian components used in the fit, then standard deviation is:

$$\sigma_H^2 = A_1(H_{01}^2 + \sigma_{H_1}^2) + (1 - A_1)(H_{02}^2 + \sigma_{H_2}^2) - < H >^2 \qquad (6.1)$$

where A_1 is the fraction for the first Gaussian component, H_{01}, and H_{02} are the centroids for the first and second Gaussian components and σ_{H_1} and σ_{H_2} are their Gaussian widths.

In this way the standard deviations of the CSD, the QSD and the HFD, represented by σ_{CS}, σ_{QS} and σ_H, are all able to be obtained from the Gaussian widths of the components. In Fig.6.2, σ_{CS}, σ_{QS}, and σ_H are shown as functions of composition for both RT and LNT. As seen in Fig.6.2a, σ_H increases slightly as y increases from 0 to 0.60, then a dramatic increases occurs in σ_H at y > 0.60 for LNT results. This change, we believe is due to the spin structure change, since moment fluctuations do not play a role at LNT. The broadening arises from the local spin structure complexity when more Fe atoms are added in the near neighbor environments. Another information from the same figure is that the σ_Hs at LNT are larger than those at RT in all the spectra except at y = 0.60 and 0.65. We will try to understand

this from modeling the HFDs by binomial distributions and by a hyperfine field phonomenological model in Chapter 8.

In Fig.6.2b a fairly constant σ_{CS} is seen in samples $y \leq 0.65$ at LNT. Then similar to the hyperfine field width, it shoots up at y = 0.68. In Fig.6.2c the σ_{QS} increases at first up to y = 0.30, then stays at a plateau till y = 0.60 at both RT and LNT. For y = 0.65 and 0.68, however, there are very different results at RT and LNT. It increases abruptly at y = 0.65 and 0.68 at LNT whereas at RT it drops back to the same value it had at y = 0.05.

The observed CSD, QSD and HFD from the spectral study suggest unusual behavior occuring in Fe-rich Fe-Ni alloys. This may arise from a spin structure change, or the failure of the HFD fitting method (dynamics effects), or the coexistence of both. The influence of the spin structure and thermal average effects on the spectra will be investigated later in Part III using MC simulations.

The average CSs at LNT are compared with those at RT in Fig.6.3. It increases continuously with the increase of y up to y = 0.45 at both RT and LNT. Both then have plateaus at y>0.45 except that at RT it drops suddenly at y>0.60. Such a dramatic change in the CS which is only observed at RT may be due to the failure of the fitting method, i.e. dynamic effects [62]. Otherwise, such a big change in CS is difficult to explain by an electronic density change as we only slightly change the concentration from y = 0.60 to y = 0.65 and to y = 0.68.

The average QSs and the corresponding component-wise average QSs are plotted in Fig.6.4. From y = 0.05 to y = 0.60, the component QSs at RT and LNT show the same character, and the average QSs at RT and LNT are scattered around a very small value (about 0.0 mm/s). But at y = 0.65 and y = 0.68, both the average and the components are different at RT and LNT. Since dynamic effects are not present at LNT, the average QS has a true increase at y>0.60.

The obtained average hyperfine fields for LNT are shown in Fig.6.5 in which they are compared with the results at RT for the same samples, at LNT the hyperfine field increases with the increases of Fe content upto y = 0.60 then drops significantly. The average hyperfine field at RT increases up to y = 0.50, then drops sooner than at LNT. It is noticed that the average hyperfine fields at RT and LNT are not

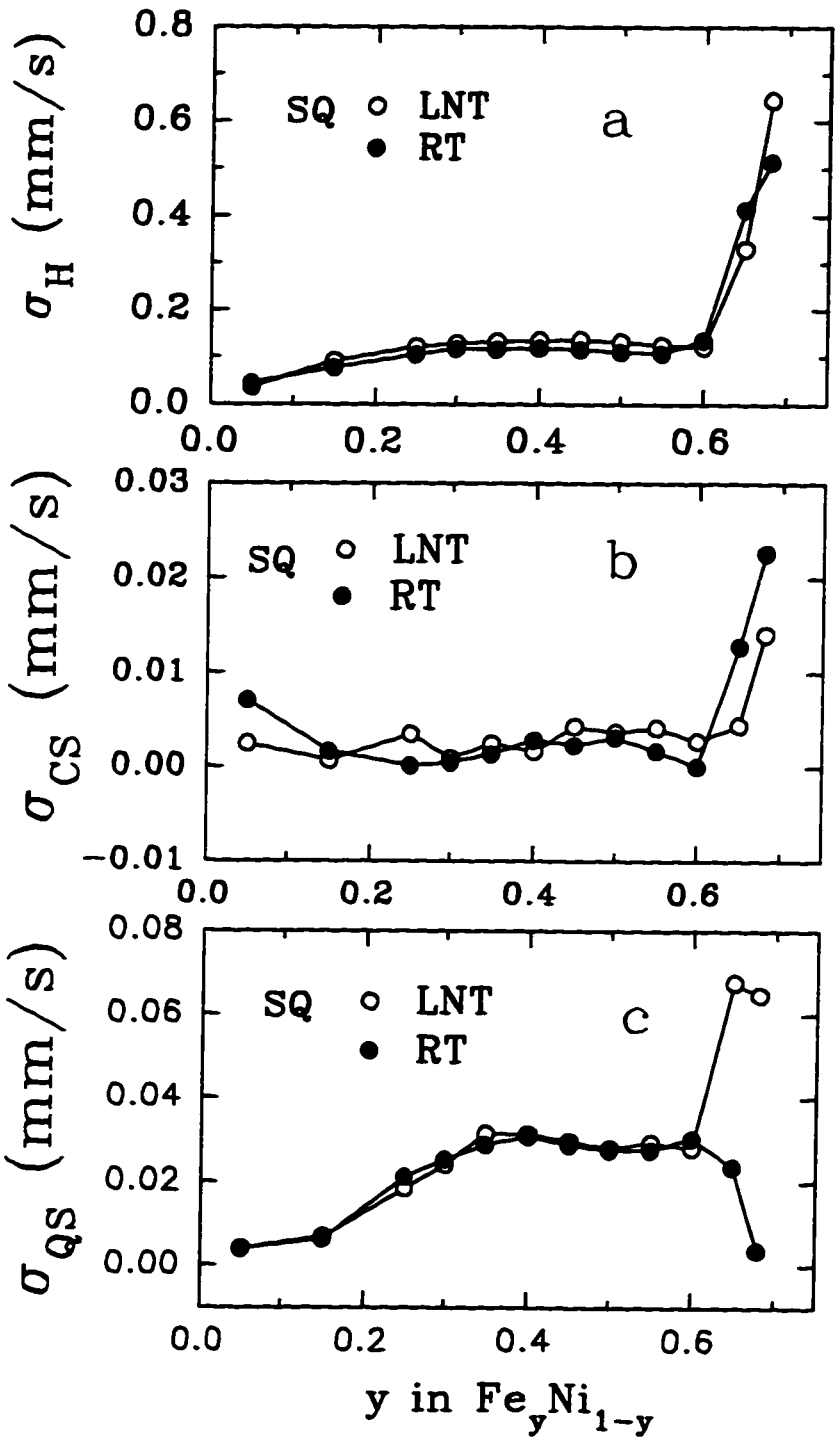

Figure 6.2 : Standard deviation of the hyperfine parameters for SQ samples.

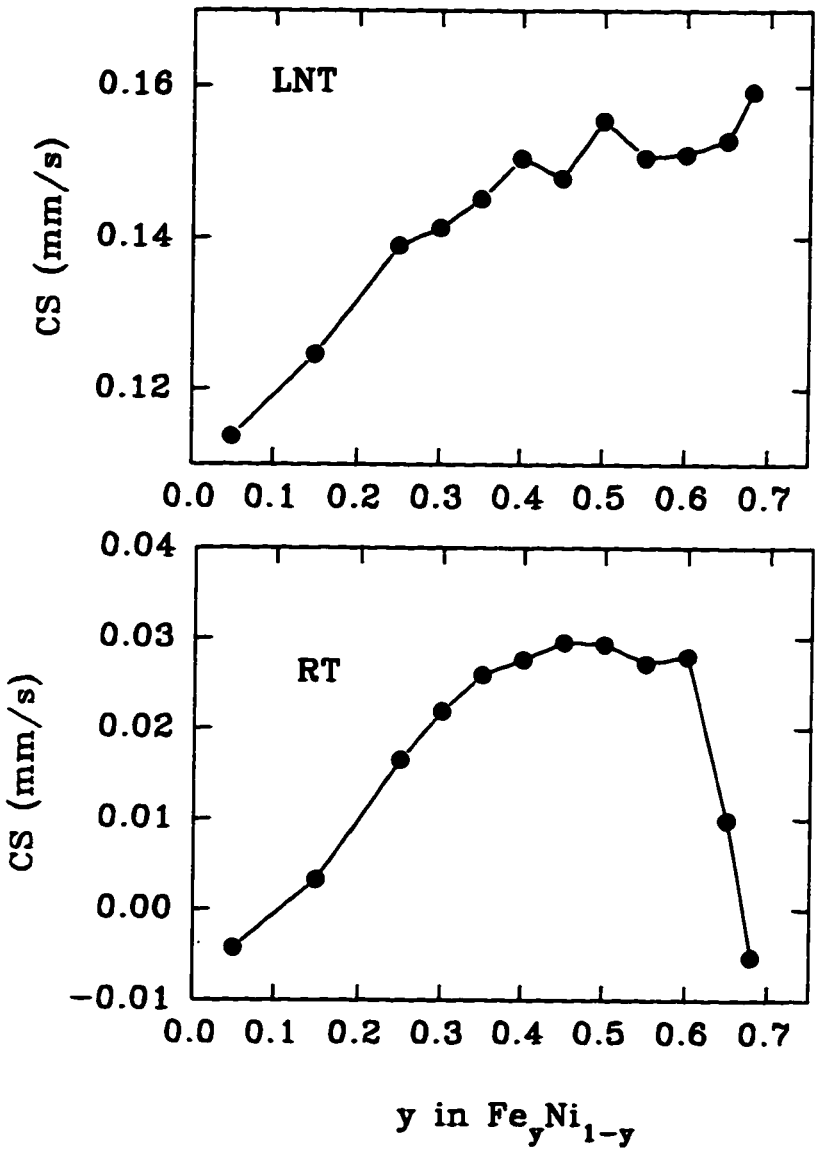

Figure 6.3 : CS at LNT and RT.

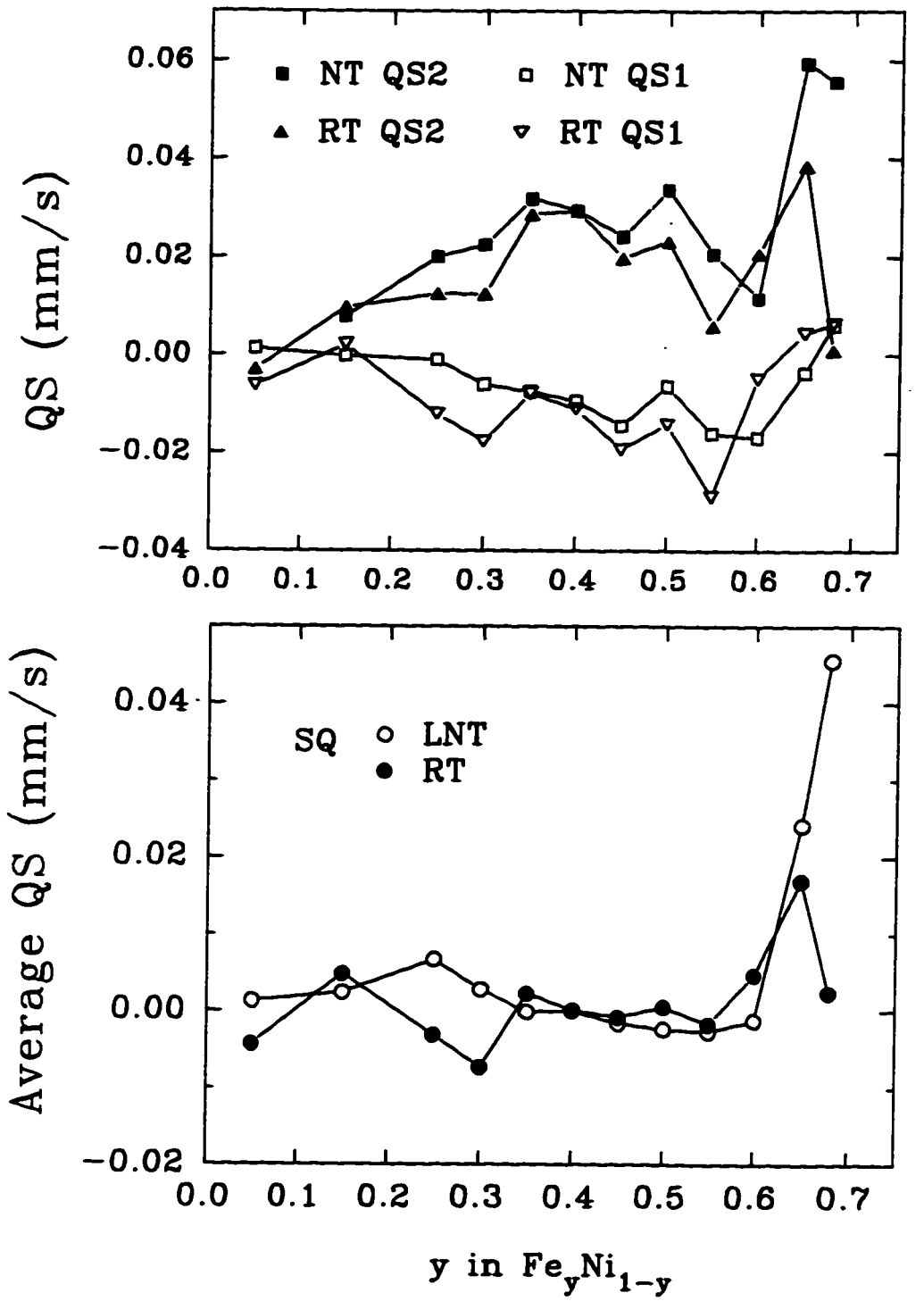

Figure 6.4 : QSs at LNT and RT.

straight lines as one may expect in the collinear ferromagnetic region ($y \leq 0.45$). A detailed consideration of this fact and study of the average hyperfine fields and the HFDs by comparison with a phenomenological model will be given in the rest of this chapter.

6.2 LHT Mössbauer Study of Collinear Ferromagnetic SQ Fe-Ni

In order to obtain the average hyperfine fields and the HFDs in Fe-Ni alloys at LHT, SQ samples at low iron concentration ($y = 0.05$, 0.10, 0.20 and 0.45) are rolled to about 20 μm, which is close to the ideal thickness - the thickness which optimizes the signal to noise ratio of the spectra. Running the as SQ samples at LHT would be too costly in liquid helium cryogen. Rolling is an effective way to get thin absorbers, however, it may induce changes such as precipitation, phase transformation and microstructural evolution. Therefore, careful comparisons are made for the spectra at RT and LNT for both rolled and as SQ samples. The rolling effects on the average hyperfine field are shown in Fig.6.6. It seems that rolling induces bigger increases in the average hyperfine fields in samples around $y = 0.30$ than at other concentrations.

Mössbauer spectra of the rolled SQ samples are measured at RT, LNT, and LHT and then fitted with the VBF method. The LHT spectra with the fits and the corresponding HFDs are shown in Figs.6.7, 6.8, 6.9, 6.10. The fitting parameters for LHT spectra are given in Table 6.2. The spectral fitting parameters for LNT and RT are given in Table 6.3 and Table 6.4, respectively.

The differences between the average hyperfine field at LNT and at LHT ($\Delta H_{LHT-LNT} = < H >_{LHT} - < H >_{LNT}$) in the rolled SQ samples are obtained from the spectral analysis. This difference is plotted as a function of concentration in Fig.6.11.

We have measured the average hyperfine fields at LHT in the rolled SQ samples only, not in the as SQ samples, however, we require the average hyperfine fields (and HFDs) at LHT for samples in the as SQ state. To obtain these quantities, we assume that, at each composition, the thermal and rolling effects are additive. For example, the required average hyperfine field at LHT in the as SQ state, $< H >_{LHT,as-SQ}$,

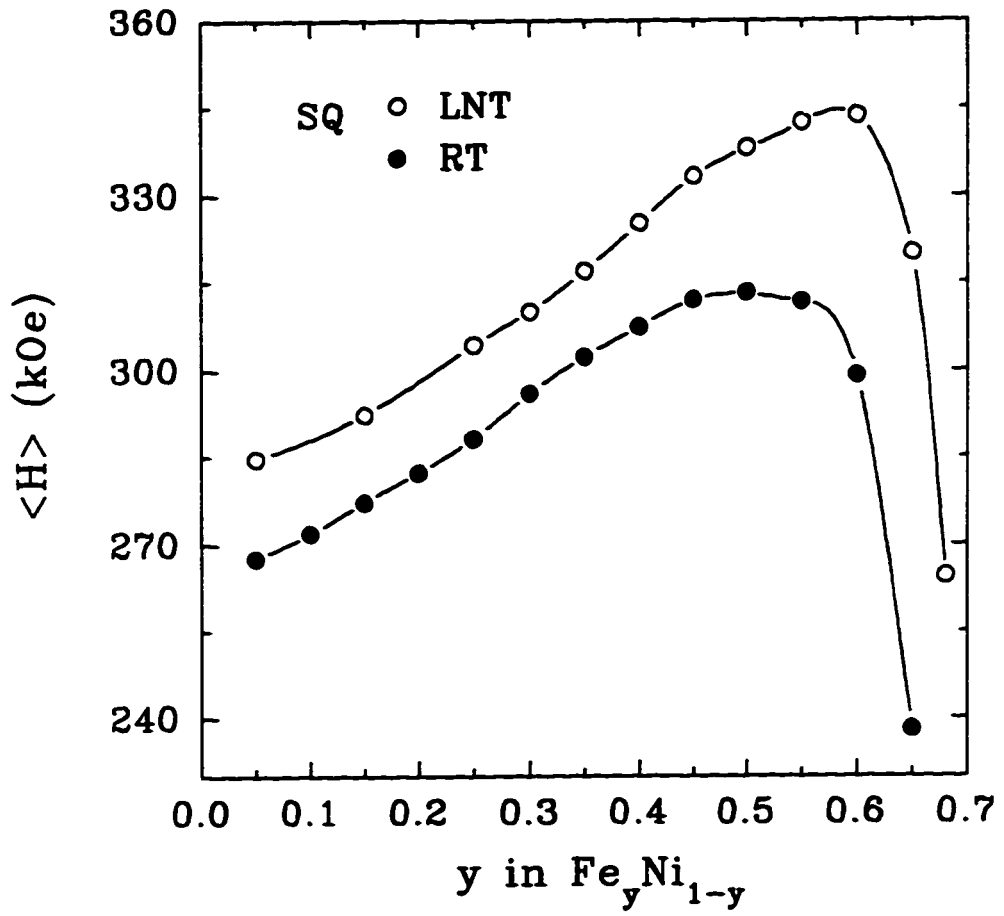

Figure 6.5 : Average hyperfine fields at RT and LNT for SQ samples.

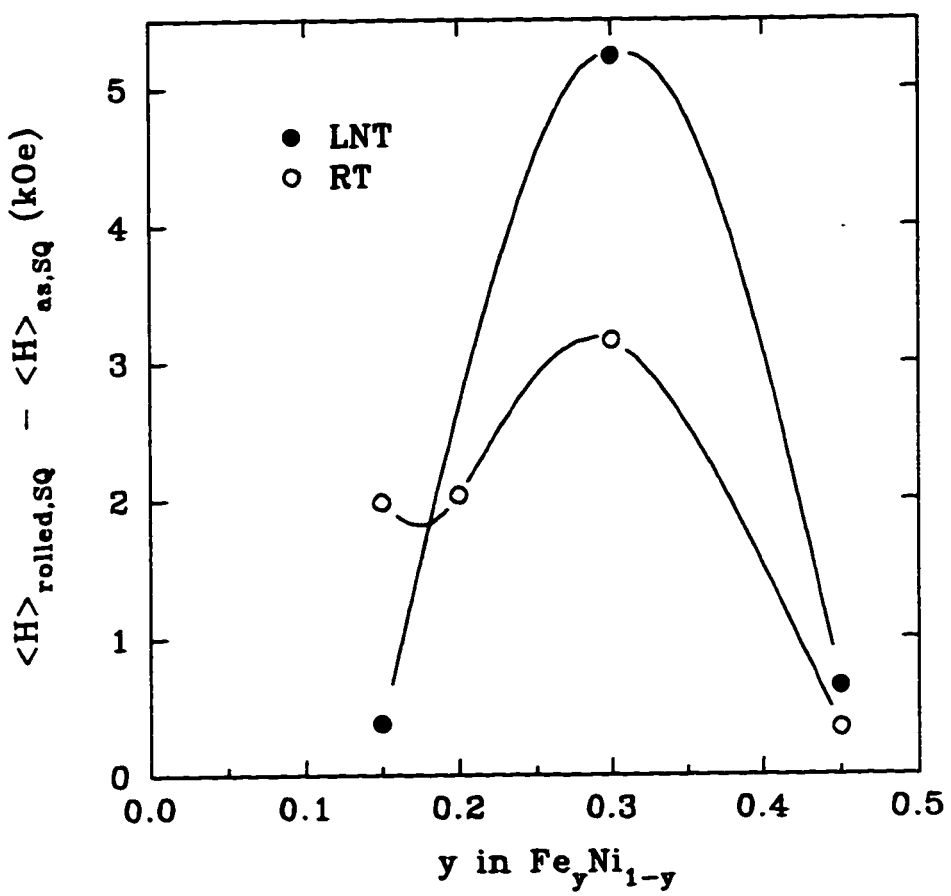

Figure 6.6 : Rolling effects on the average hyperfine fields at RT and LNT, for SQ samples.

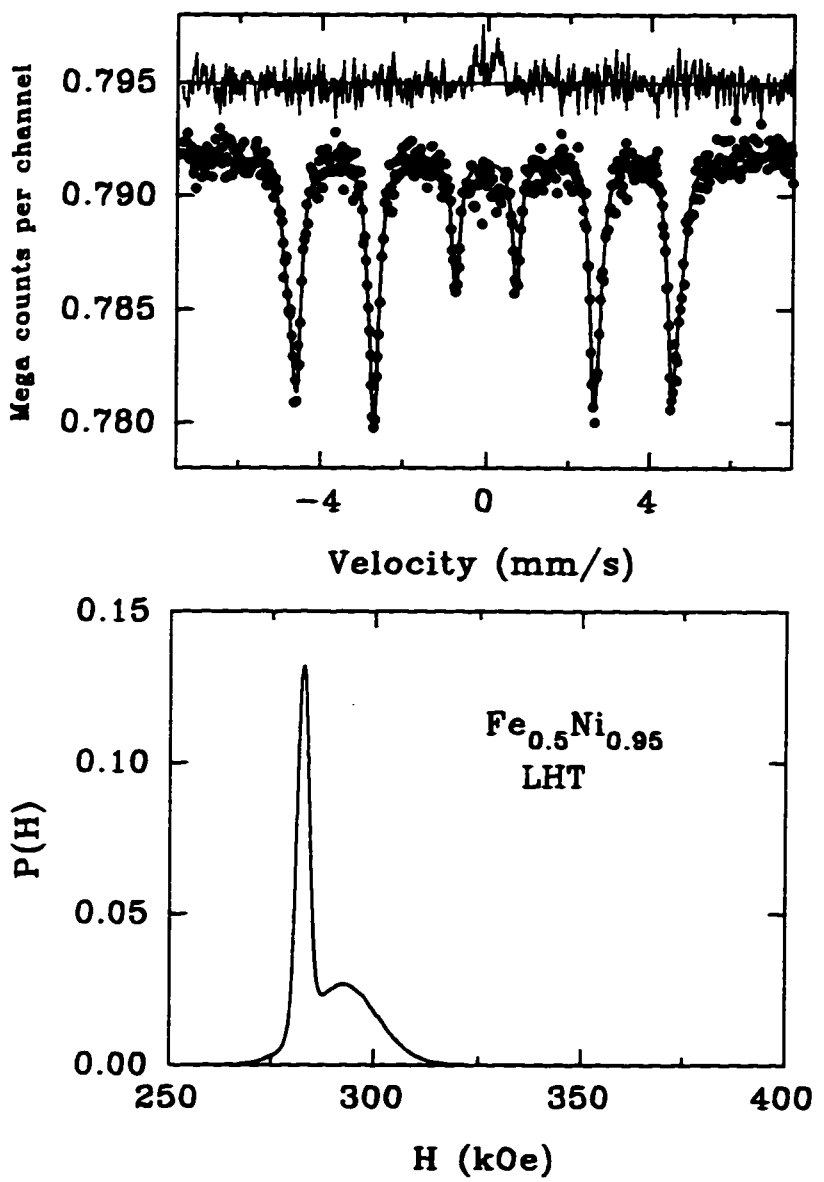

Figure 6.7 : The spectrum for rolled SQ $Fe_{0.05}Ni_{0.95}$ at LHT and the corresponding HFD.

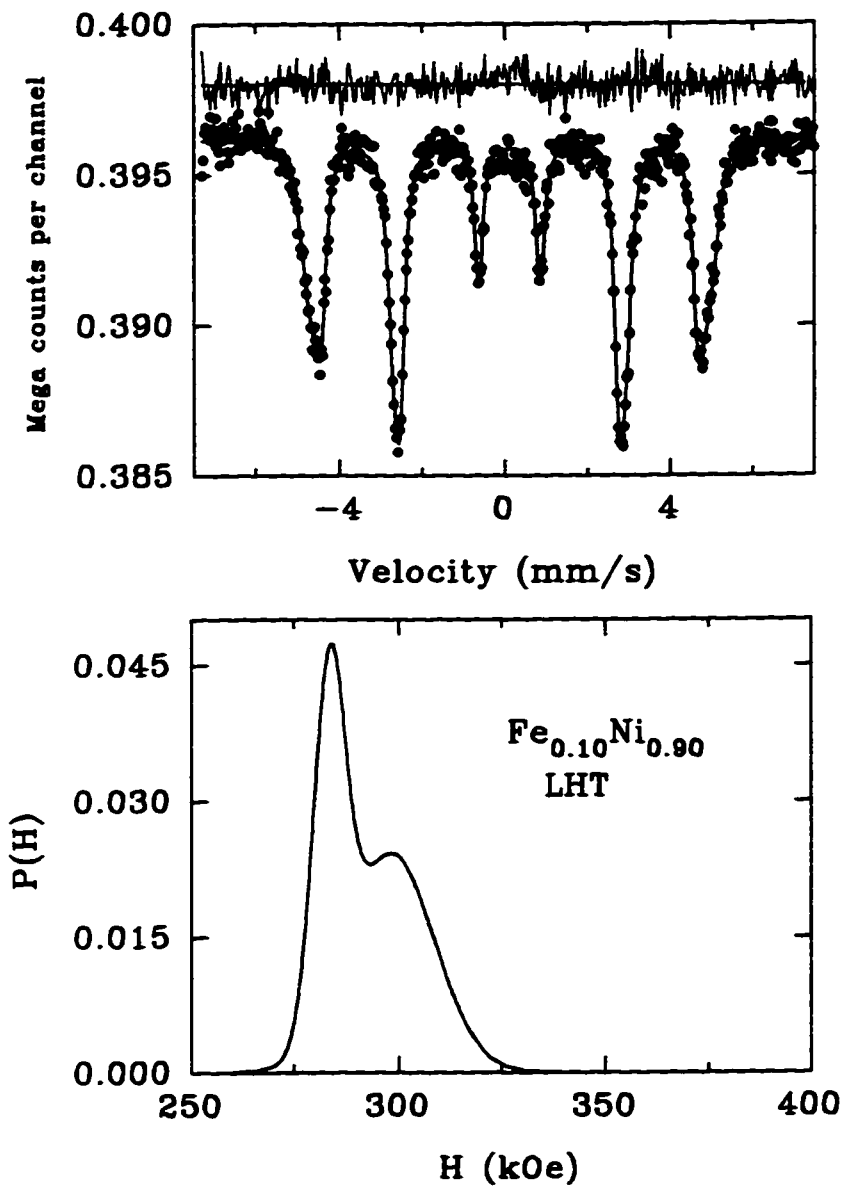

Figure 6.8 : The spectrum for rolled SQ $Fe_{0.10}Ni_{0.90}$ at LHT and the corresponding HFD.

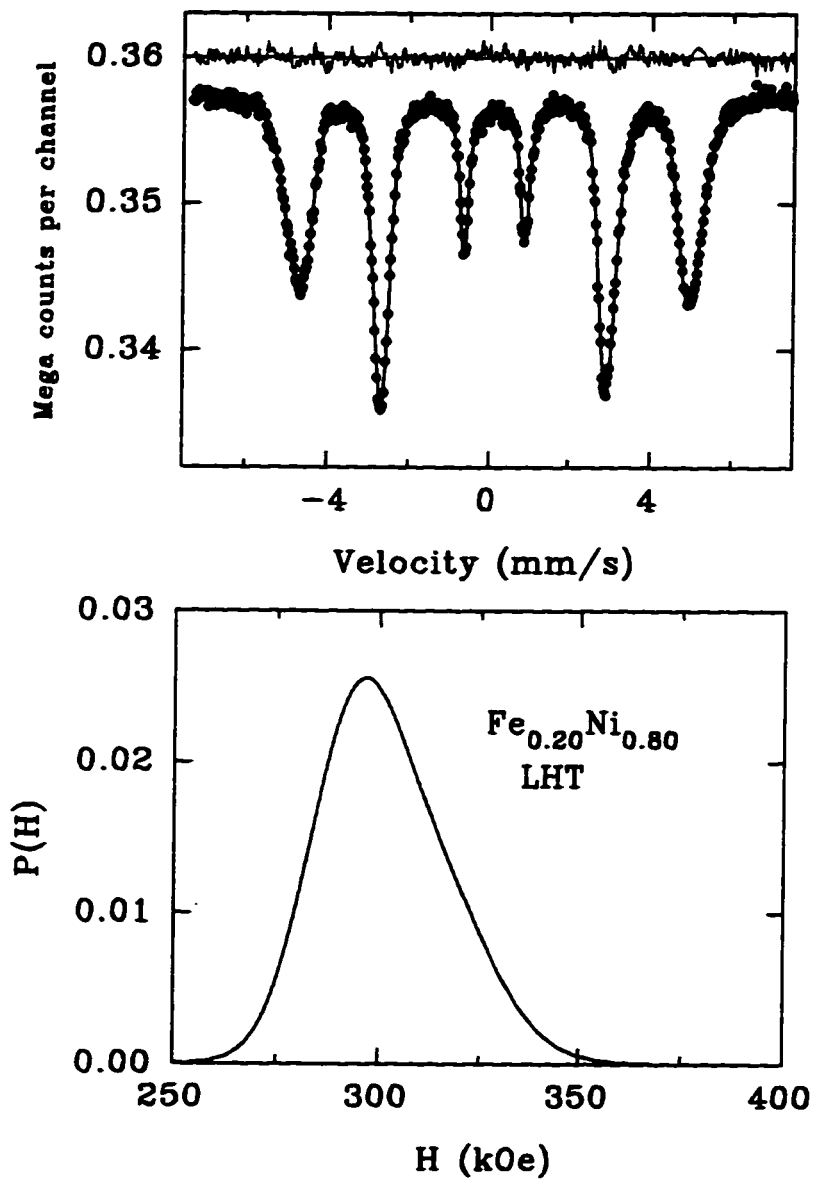

Figure 6.9 : The spectrum for rolled SQ $Fe_{0.20}Ni_{0.80}$ at LHT and the corresponding HFD.

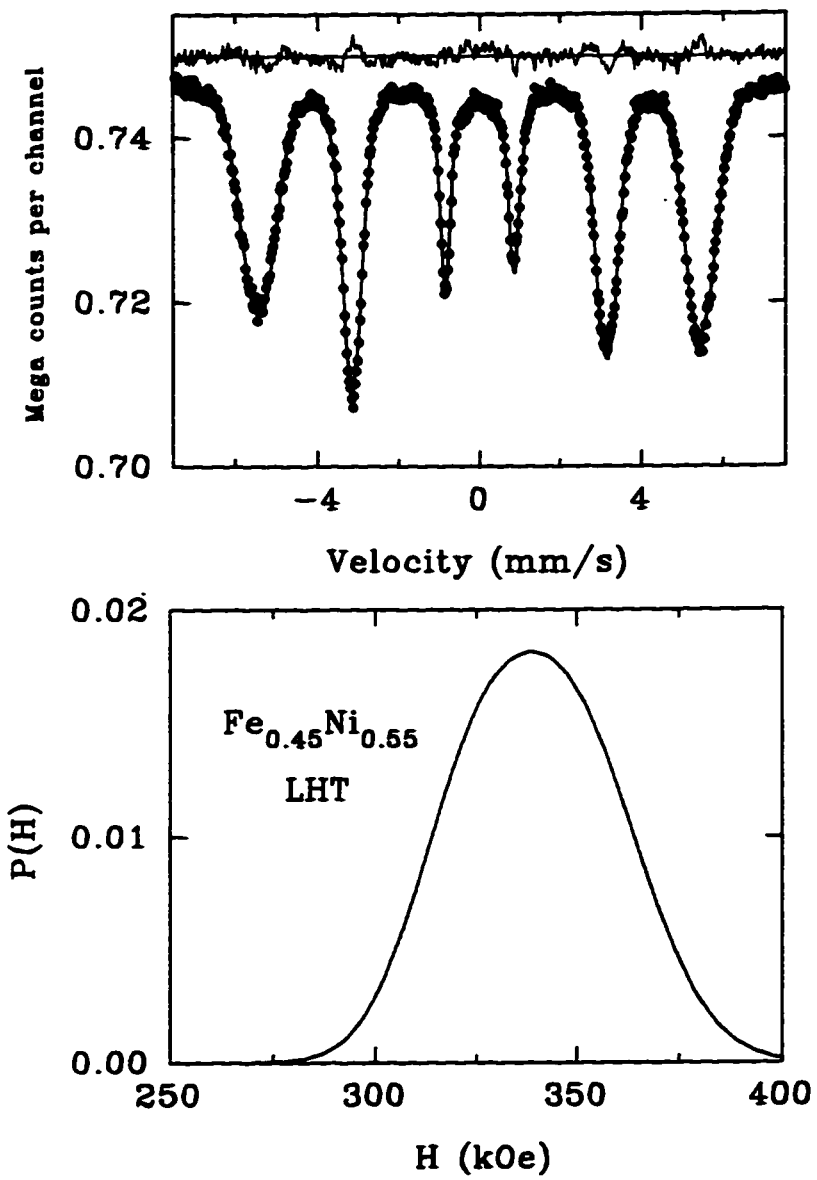

Figure 6.10 : The spectrum for rolled SQ $Fe_{0.45}Ni_{0.55}$ at LHT and the corresponding HFD.

Table 6.2: Fitting parameters for rolled SQ samples at LHT.

y	$h3_1$	$h3_2$	HF_1(kOe)	HF_2(kOe)	σ_1(kOe)	σ_2(kOe)	Γ(mm/s)
0.05	2616	3355	282.65	292.41	1.48	8.43	0.236
0.10	1786	3135	282.88	297.52	3.83	10.46	0.236
0.20	5853	5251	309.93	292.69	15.76	10.92	0.250
0.45	18320	8418	346.65	319.73	17.66	13.97	0.285

y	δ_0(mm/s)	δ_1	ε_0(mm/s)	ε_1	h1/h3	h2/h3	BG	χ_{red}^2
0.05	-0.012	-0.003	0.323	-0.166	2.63	2.40	111168	1.06
0.10	0.160	-0.018	0.015	-0.006	2.83	2.98	396171	0.80
0.20	0.015	-0.010	0.251	-0.121	2.87	3.11	357333	1.08
0.45	0.186	-0.014	0.518	-0.228	2.86	2.37	747031	1.22

In Table 6.2 $h3_i$ is the line-3 peak height for the ith Gaussian component, HF_i is the center of the ith HF Gaussian distribution, σ_i is the hyperfine field Gaussian distribution width for the component-i, where i = 1, 2.

Table 6.3: Fitting parameters for rolled SQ samples at LNT.

y	$h3_1$	$h3_2$	HF_1(kOe)	HF_2(kOe)	σ_1(kOe)	σ_2(kOe)	Γ(mm/s)
0.05	6307	5968	282.23	292.49	19.13	19.83	0.230
0.10	8541	4347	295.54	281.86	10.50	3.64	0.234
0.20	10464	13029	311.26	292.14	14.97	10.76	0.250
0.45	3091	3810	350.02	323.76	14.71	14.93	0.288

y	δ_0(mm/s)	δ_1	ε_0(mm/s)	ε_1	h1/h3	h2/h3	BG	χ^2_{red}
0.05	-0.021	0.002	0.117	-0.060	2.57	2.29	1610041	1.41
0.10	0.169	-0.023	0.084	-0.041	2.79	2.88	994996	1.24
0.20	0.140	-0.002	0.221	-0.105	2.86	3.07	767872	1.10
0.45	0.071	-0.026	0.513	-0.228	2.86	2.36	192502	0.96

In Table 6.3 $h3_i$ is the line-3 peak height for the ith Gaussian component, HF_i is the center of the ith HF Gaussian distribution, σ_i is the hyperfine field Gaussian distribution width for the component-i, where i = 1, 2.

Table 6.4: Fitting parameters for rolled SQ samples at RT.

y	$h3_1$	$h3_2$	HF_1(kOe)	HF_2(kOe)	σ_1(kOe)	σ_2(kOe)	Γ(mm/s)
0.05	7831	7106	272.94	266.07	9.03	1.55	0.230
0.10	1736	812	277.92	266.01	7.94	0.09	0.249
0.20	9477	11646	275.46	291.80	18.67	19.78	0.250
0.45	32729	13977	319.64	295.71	13.86	10.50	0.298

y	δ_0(mm/s)	δ_1	ε_0(mm/s)	ε_1	h1/h3	h2/h3	BG	χ_{red}^2
0.05	-0.002	-0.000	0.121	-0.065	2.90	2.60	311014	0.78
0.10	0.085	-0.048	0.059	-0.030	2.53	2.62	261177	0.93
0.20	0.009	0.003	0.262	-0.136	2.92	3.10	840555	1.90
0.45	0.072	-0.020	0.549	-0.259	2.78	2.91	1856855	1.82

In Table 6.4 $h3_i$ is the line-3 peak height for the ith Gaussian component, HF_i is the center of the ith HF Gaussian distribution, σ_i is the hyperfine field Gaussian distribution width for the component-i, where i = 1, 2.

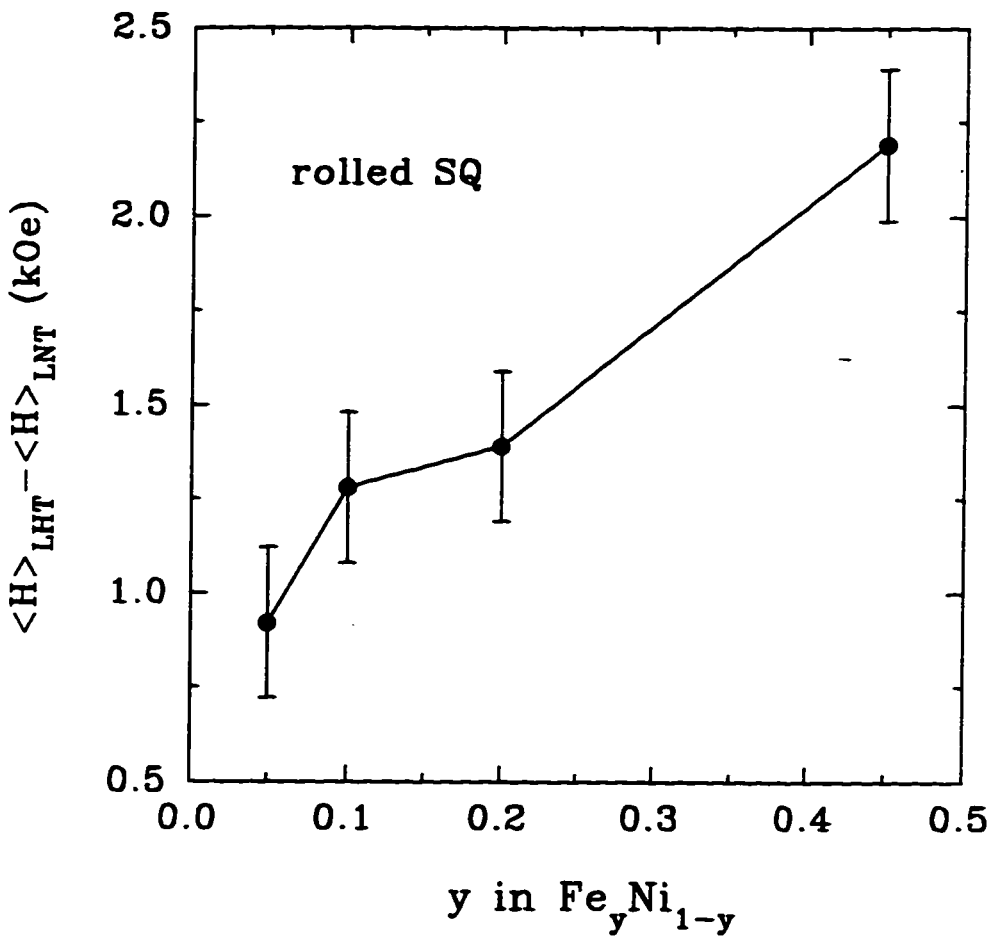

Figure 6.11 : Average hyperfine field difference between LHT and LNT for rolled SQ samples.

can be obtained as:

$$< H >_{LHT,as-SQ} = < H >_{LHT,rolled} - (< H >_{LNT,rolled} - < H >_{LNT,as-SQ}) \quad (6.2)$$

or, equivalently, as:

$$< H >_{LHT,as-SQ} = < H >_{LNT,as-SQ} + (< H >_{LHT,rolled} - < H >_{LNT,rolled}). \quad (6.3)$$

The derivation based on the latter equation is shown in Table 6.5, where the missing thermal increase data for some compositions is obtained by linear interpolation of the data shown in Fig.6.11.

The errors, by which we mean the Gaussian σ error in $< H >_{LHT,as-SQ}$, are estimated as follows. First, the uncertainty in the average hyperfine fields due to the fitting is negligible. The main error in the average hyperfine field is from the calibration which was used to set the velocity for each channel. This error is random with $\sigma \sim 0.5$ kOe. Such error exists in both $< H >_{LNT,rolled}$ and $< H >_{LHT,rolled}$. The total error in $\Delta H_{LHT-LNT}$ comes up to 0.7 kOe by the law of combination of errors [85]. Also, for f = ax + by, we have:

$$\sigma_f^2 = \left(\frac{df}{dx}\right)^2 \sigma_x^2 + \left(\frac{df}{dy}\right)^2 \sigma_y^2 \quad (6.4)$$

such that the error in $< H >_{LHT,as-SQ}$ is 0.86 kOe. This error is used later in least square fitting with various structural models.

The resulting average hyperfine field data for as-SQ samples are shown in Fig.6.12. Because the total error is smaller than the point size, it is not shown in the figure. The data for y = 0 at LHT is taken to be 281 kOe from the diluted Fe impurity in a Ni matrix work of Hesse and Buchal [83].

As shown in Fig.6.13 the HFDs at LNT and LHT for rolled SQ samples are almost exactly the same, except for the small shift of the distribution center. Therefore, we assume that the HFDs at LHT for as SQ samples are the same as those at LNT for as SQ samples, except that they are shifted by the difference shown in Fig.6.11. Thus the average hyperfine fields and the HFDs at LHT for as SQ samples are obtained. Next they will be modeled using the proposed hyperfine field phenomenological models (section 3.4) and binomial distributions of local environments, based on true atomic occupation randomness and ferromagnetic collinearity at $y \leq 0.45$.

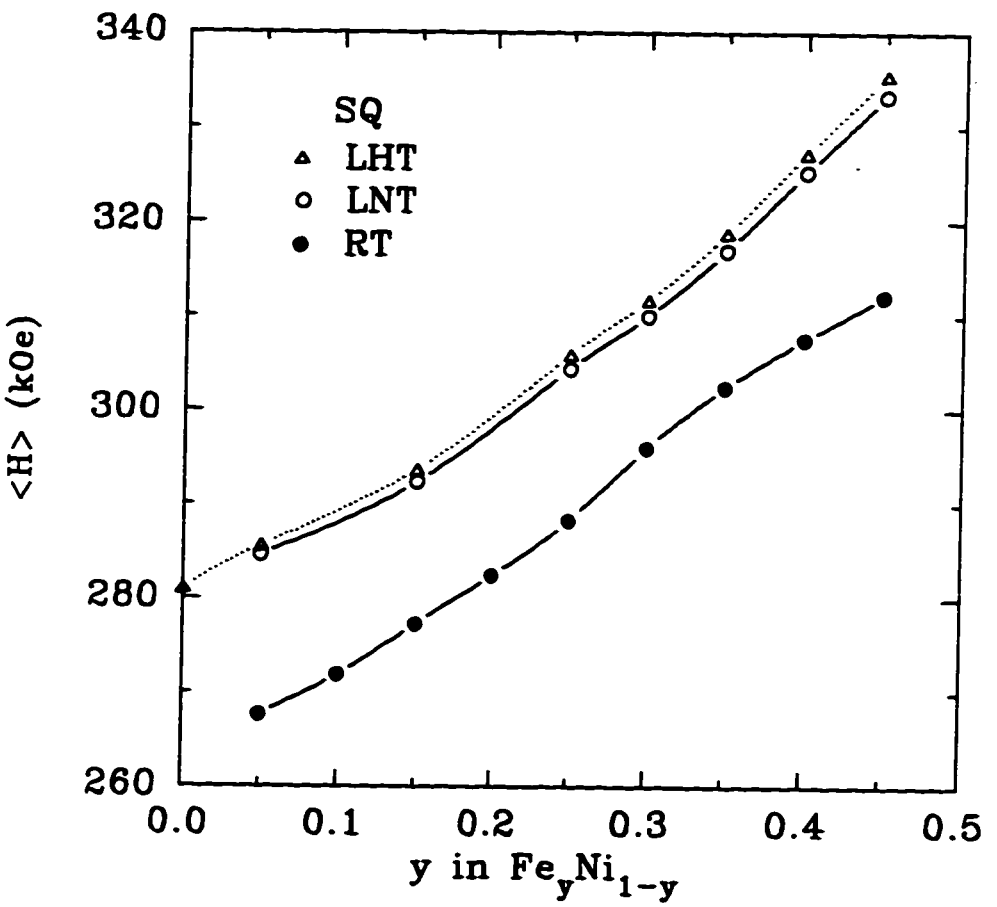

Figure 6.12 : Average hyperfine fields at RT, LNT and LHT for as SQ samples in the collinear ferromagnet region ($y \leq 0.45$).

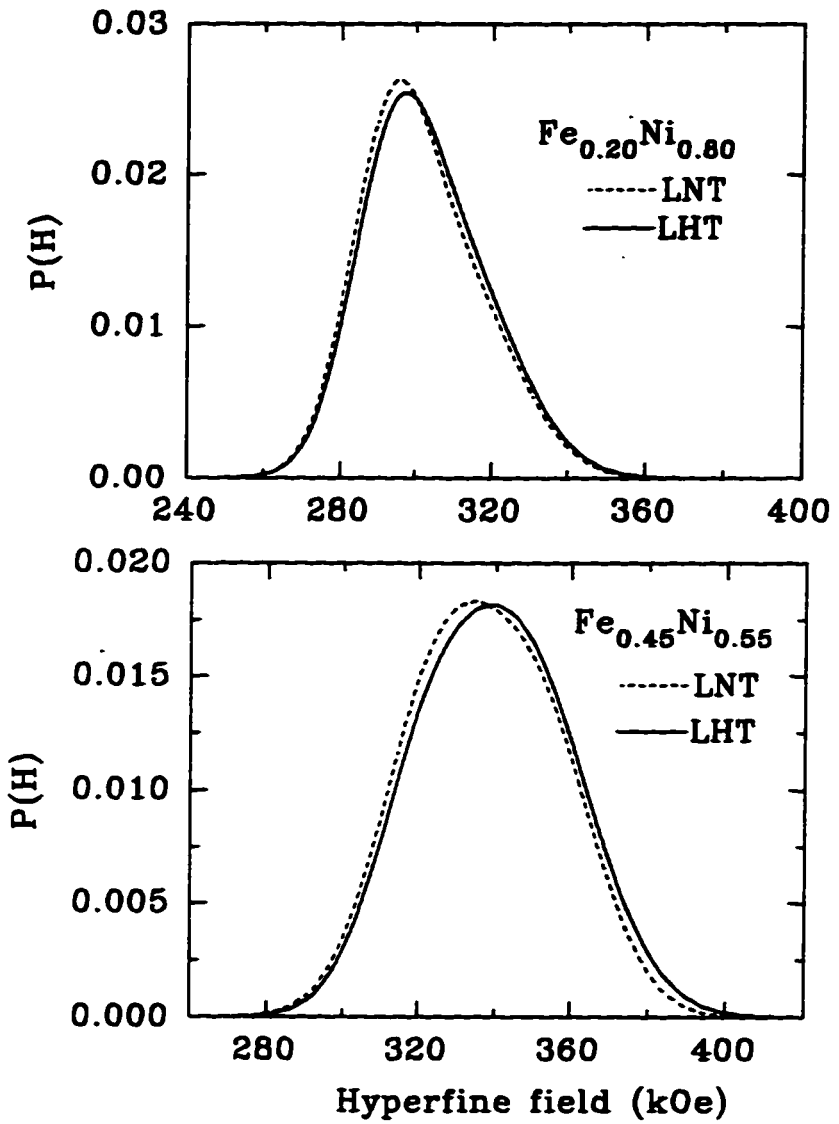

Figure 6.13 : HFDs at LHT and LNT for two rolled SQ samples.

Table 6.5: Average hyperfine field for as SQ samples at LHT.

y	$< H >_{LNT}$ kOe	$\pm \sigma_1$ kOe	$\Delta H_{LHT-LNT}$ kOe	$\pm \sigma_2$ kOe	$< H >_{LHT}$ kOe	$\pm \sigma_3$ kOe
0.05	284.65	0.5	0.93	0.7	285.57	0.87
0.15	292.37	0.5	1.30	0.7	293.67	0.87
0.25	304.34	0.5	1.50	0.7	305.84	0.87
0.30	309.98	0.5	1.65	0.7	311.63	0.87
0.35	317.04	0.5	1.80	0.7	318.84	0.87
0.40	325.21	0.5	2.00	0.7	327.21	0.87
0.45	333.35	0.5	2.18	0.7	335.53	0.87

6.3 Concentration Dependence of the Average Hyperfine Field

In ferromagnetic collinear Fe_yNi_{1-y} alloys ($y \leq 0.45$) the average hyperfine field from the phenomenological model is given by Eq.3.10:

$$< H >= A < \mu_{Fe} > +12B < \mu_{Ni} > +12yB(< \mu_{Fe} > - < \mu_{Ni} >)$$

where it is assumed that the average moment of every Fe site is the same and that the average moment on every Ni is the same (local environment effects on the thermal averages are ignored).

We first apply this model to the measured average hyperfine fields at LHT. The thermal average moments on Fe and Ni need to be known. At LHT, these are simply equal to the T = 0 K ground state saturation moments. The latter are taken to be 2.8 and 0.6 μ_B for Fe and Ni, respectively, as follows from the Slater-Pauling behavior of the alloys at $y \leq 0.45$ [7].

The least square method [84] is used to fit the model to the LHT hyperfine field data. χ^2 is the sum of the squared differences between the observed values and the theoretical values, suitably weighted by the errors in the measurements, written as:

$$\chi^2 = \Sigma_i^N \frac{[y_i - f(x_i)]^2}{\sigma_i^2}. \tag{6.5}$$

Table 6.6: χ^2 values (x_+) for various C.

	C = 90%	= 95%	98%	99%
$\nu = 1$	2.71	3.84	5.41	6.63
2	4.61	5.99	7.82	9.21
3	6.25	7.82	9.84	11.34
4	7.78	9.49	11.67	13.28
5	9.24	11.07	13.39	15.09
6	10.64	12.59	15.03	16.81

To make judgements and decisions about whether a particular model is acceptable, we use both the χ^2 probability distribution and the so called confidence [85]:

$$C = Prob(\chi^2 < x_+) = \int_{-\infty}^{x_+} P(\nu;\chi^2)d\chi^2 \qquad (6.6)$$

where $P(\nu;\chi^2)$ is the χ^2 probability distribution given by:

$$P(\nu;\chi^2) = \frac{2^{-\nu/2}}{\Gamma(\nu/2)}\chi^{\nu-2}e^{-\chi^2/2} \qquad (6.7)$$

in which ν is the number of degrees of freedom, equal to the number of the data points minus the number of parameters that are adjusted to minimise χ^2. $\Gamma(\nu/2)$ is the standard gamma function. When ν is large, the χ^2 distribution has mean ν and variance 2ν and tends to be Gaussian distribution. Some of the χ^2 distributions are shown in Fig.6.14 for $\nu = 1$, 3, 4 and 6. Some χ^2 values (x_+) for various confidence levels are listed in Table 6.6.

In attempts to obtain the coupling parameters for different assumptions (or models), that we next examine seperately, we expect that, if the model is correct, its corresponding particular value of χ^2 should be smaller than the x_+ corresponding to C = 95%.

Model-1: $A = A_0, B = B_0$

If the coupling parameters A and B are simply constants (independent of composition), Eq.3.10 leads to a linear relationship between the average hyperfine field

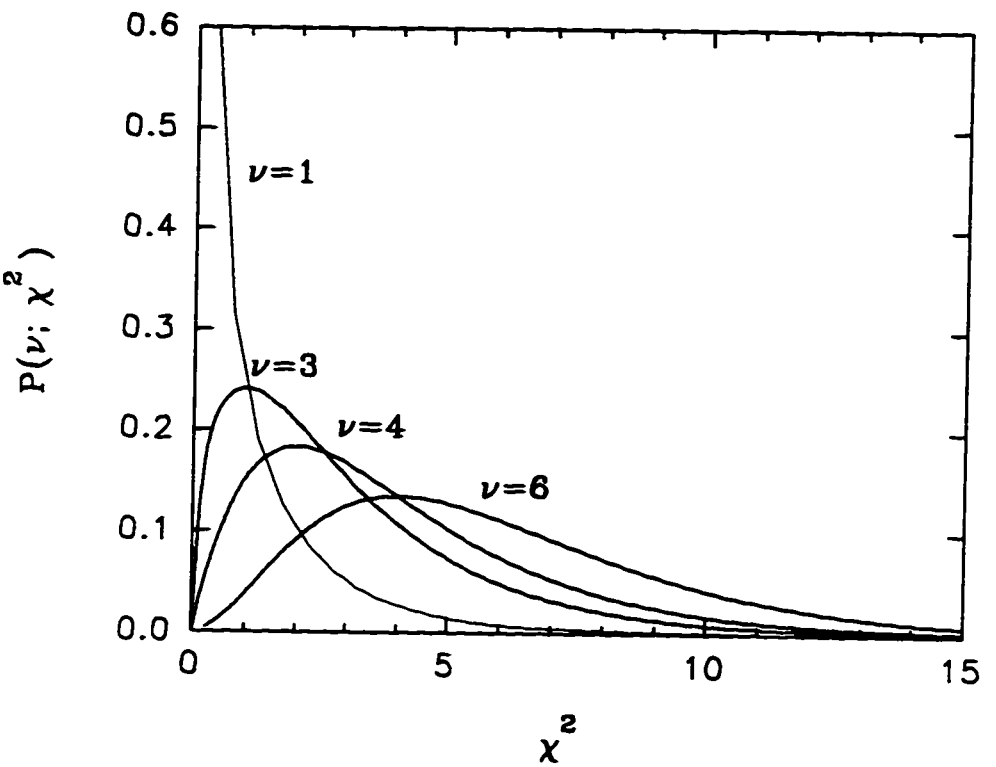

Figure 6.14 : χ^2 distributions for ν = 1, 3, 4 and 6, as indeicated.

and the iron concentration:

$$\begin{aligned} < H > &= A < \mu_{Fe} > +12B < \mu_{Ni} > +12yB(< \mu_{Fe} > - < \mu_{Ni} >) \\ &= A < \mu_{Fe} > +12B < \bar{\mu} > \end{aligned} \tag{6.8}$$

where $< \bar{\mu} >= y < \mu_{Fe} > +(1-y) < \mu_{Ni} >$. This is equivalent to the most often used empirical model (e.g. [64]). Fitting the model to the hyperfine field data leads to $A = 88.0\frac{kOe}{\mu_B}$, $B = 4.2\frac{kOe}{\mu_B}$, and the χ^2 is 56.

With Model-1, the number of degrees of freedom ν equals 6. The χ^2 distribution gives that for C = 95%, $x_+ = \chi^2 = 12.6$. In other words, the probability to find that the correct model gives a χ^2 larger than 12.6 is less than 5%. The obtained χ^2 = 56 is much larger than 12.6 and the probability of a correct model having $\chi^2 \geq$ 56 is effectively zero. This also is clearly shown in the χ^2 distribution for $\nu = 6$ of Fig.6.14. We conclude that the model with two constant couplings is impossible from the statistical point of view. Therefore, the model having average hyperfine field linearly dependent on the composition is not adequate to describe the measurements. The inadequacy is clearly shown in Fig.6.15 in which the deviations from the straight line at LHT, LNT and RT are plotted as a function of the concentration in (a) and the best straight line fit is given in (b). The model with constant couplings A and B needs to be improved for a better agreement with the experimental results.

Model-2: $A = A_0 + A_1 y, B = B_0$

When assuming A is composition dependent whereas B is a constant, the average hyperfine field can be written as:

$< H > = (A_0+A_1 y) < \mu_{Fe} >+12B_0 < \mu_{Ni} > +12yB_0(< \mu_{Fe} > - < \mu_{Ni} >)$.
The predicted average hyperfine field from this model is again linearly dependent on y. It is therefore rejected. The χ^2 of the fit is 56, and the resulting coupling parameters are: $A_0 = 92.9\frac{kOe}{\mu_B}$, $A_1 = 18.5\frac{kOe}{\mu_B}$, and $B_0 = 2.6\frac{kOe}{\mu_B}$.

Model-3: $A = A_0, B = B_0 + B_1 y$

When we substitute the $A = A_0$ and $B = B_0 + B_1 y$ into Eq.3.10, the average

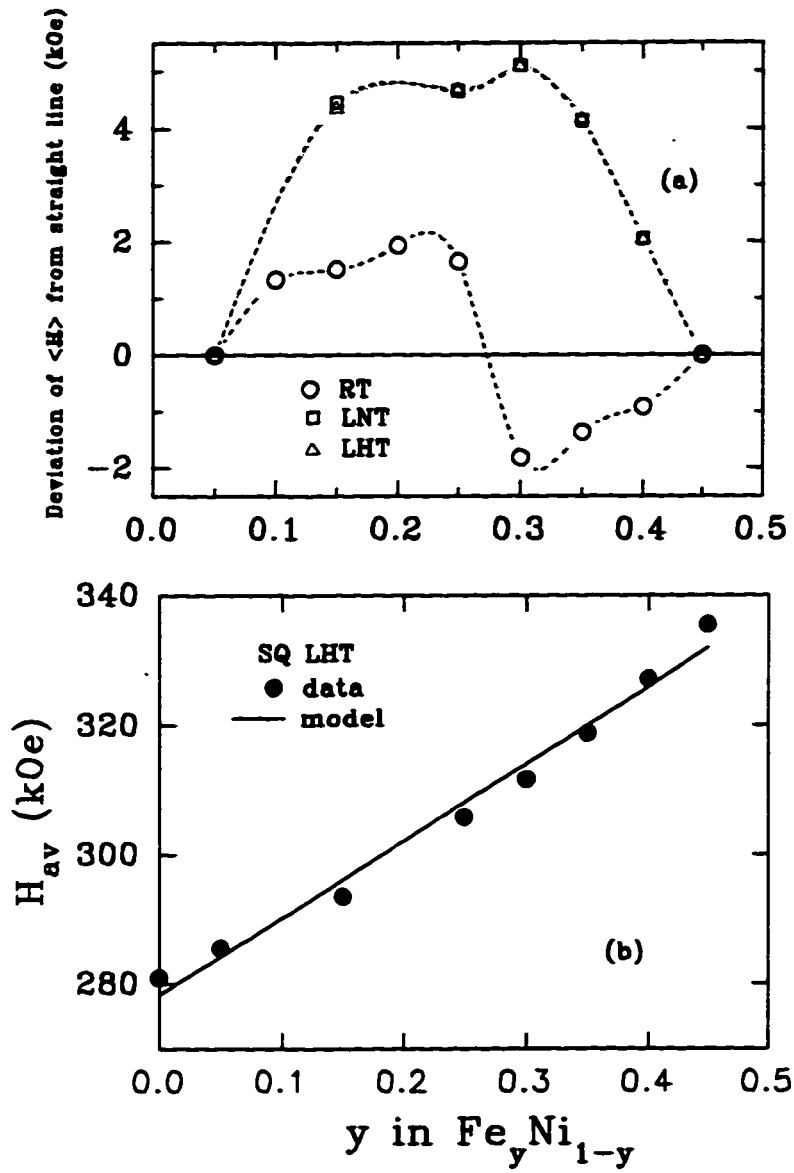

Figure 6.15 : (a)Average hyperfine field deviations from the straight line (model-1 and model-2) at RT, LNT and LHT in SQ samples. (b)The obtained best straight line compared with the experimental data at LHT.

hyperfine field now has a quadratic term in y:

$$\begin{aligned} < H > &= A_0 < \mu_{Fe} > +12B < \mu_{Ni} > \\ &+ 12y(B_0 + B_1 y)(< \mu_{Fe} > - < \mu_{Ni} >) \end{aligned} \tag{6.9}$$

With this model, we can fit the data successfully. We obtain $\chi^2 = 1.5$ and $A = 97.3\frac{kOe}{\mu_B}, B_0 = 1.2\frac{kOe}{\mu_B}$ and $B_1 = 4.6\frac{kOe}{\mu_B}$. Both the calculated and the measured hyperfine fields are shown in Fig.6.16. This model agrees well with the data of the average hyperfine fields.

On the other hand, the HFDs themselves, $P(H_k)$, can be calculated using the same hyperfine field model from the binomial distribution which was derived in section 3.4:

$$P(H_k) = \frac{P_k(y)}{B(< \mu_{Fe} > - < \mu_{Ni} >)}$$

At each composition of the alloy, thirteen discrete values of $P(H_k)$ are calculated with the obtained A and B for k = 0, 1,...12, which correspond to the thirteen calculated H_ks from the model. Such calculated HFDs are compared with the HFDs from the VBF of the spectra. Fig.6.17 shows the calculated HFDs with the best coupling parameters A_0, B_0 and B_1 and the experimental HFDs. They are significantly different. The HFDs from other values of B_1 (in the range 3.8-5.4 kOe/μ_B) which can fit the average HFs with acceptable χ^2 values are also examined for this model. But none of these agree with the measurements. The resulting HFDs from the two extreme values of B_1 (3.8 and 5.4 $\frac{kOe}{\mu_B}$) are shown in Fig.6.18. These results show that the assumption of $A = A_0$, $B = B_0 + B_1 y$ is not correct though it fits the average hyperfine field well.

Model-4: $A = A_0 + A_1 y, B = B_1 y$

Similarly, by assuming $A = A_0 + A_1 y$, and $B = B_1 y$ the model fits the average hyperfine field data as well as what we see in Fig.6.16, with $A_0 = 100.5\ \frac{kOe}{\mu_B}$, $A_1 = 11.6\ \frac{kOe}{\mu_B}$, $B_1 = 4.6\ \frac{kOe}{\mu_B}$ and the $\chi^2 = 1.5$. However, the HFDs calculated from the obtained coupling parameters are far away from the measured HFDs. This is shown

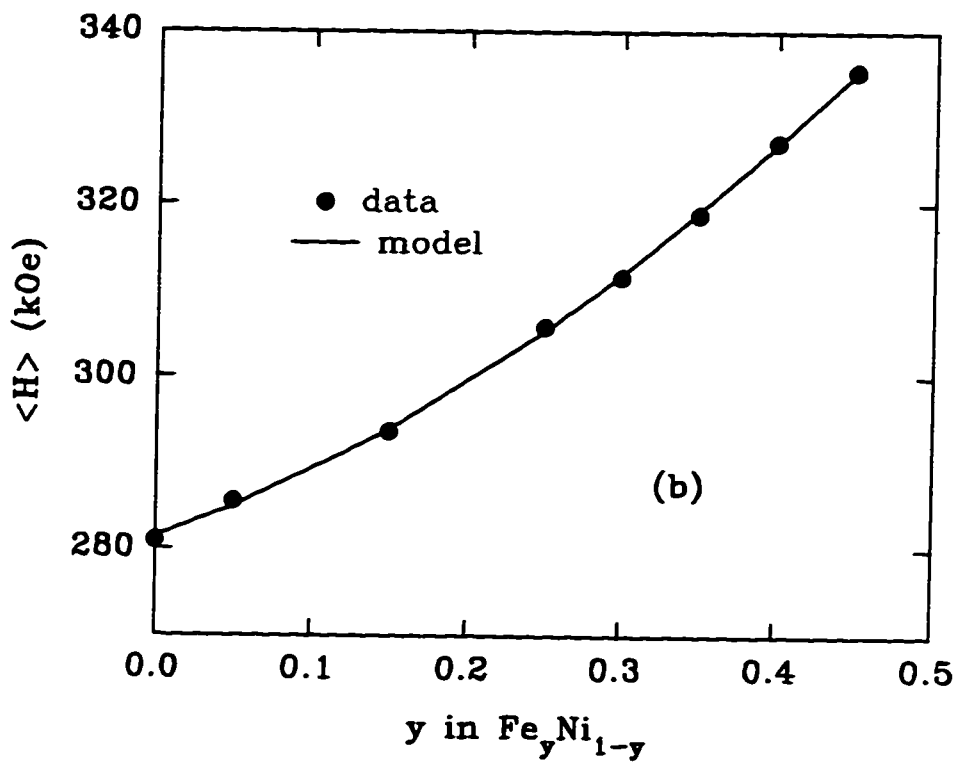

Figure 6.16 : The calculated average hyperfine fields using model-3, compared to the measured average hyperfine fields.

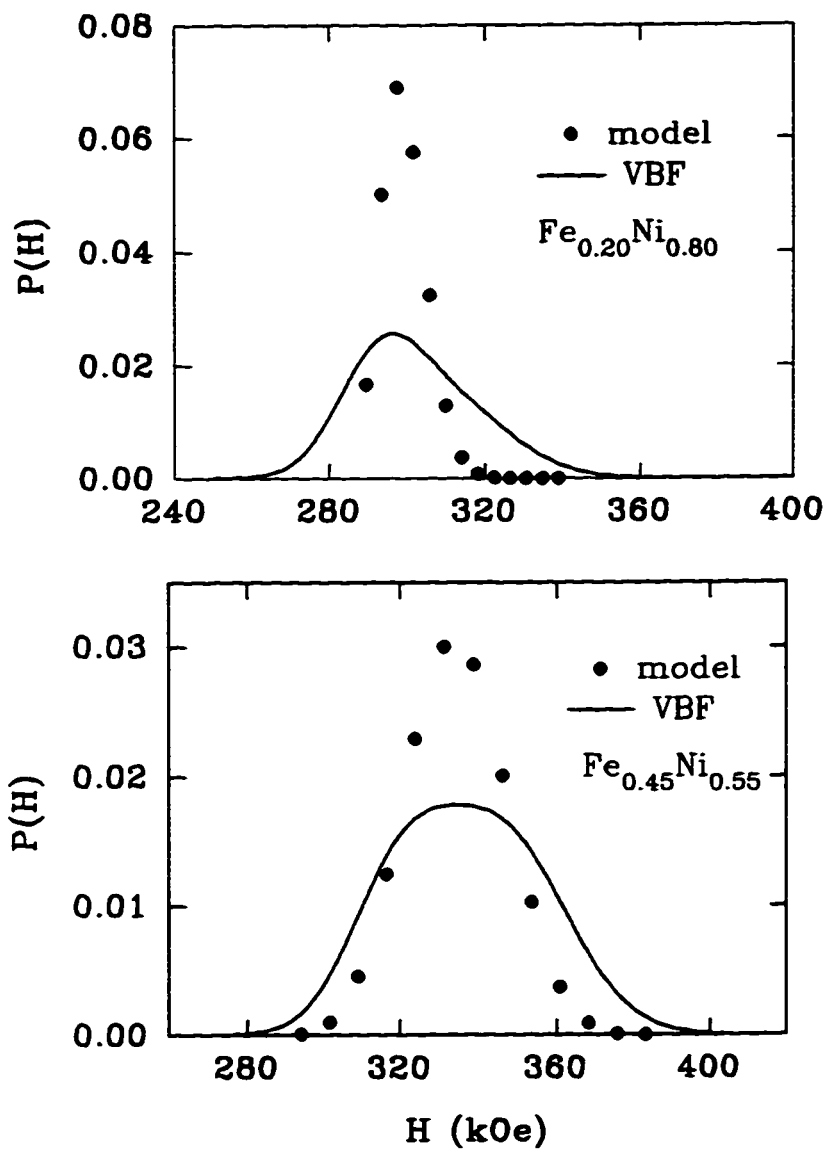

Figure 6.17 : The calculated HFDs from model-3 compared with the measured HFDs from the LHT spectra.

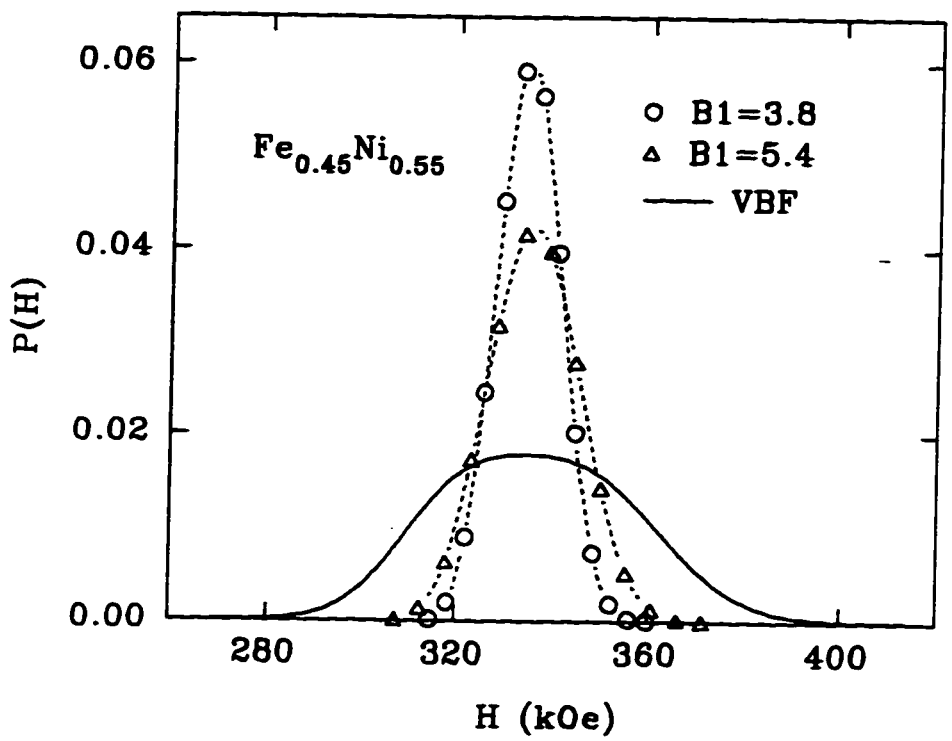

Figure 6.18 : The calculated HFDs from $A = A_0$ and $B = B_0 + B_1 y$ (model-3) with $B_1 = 3.8\frac{kOe}{\mu_B}$ and $B_1 = 5.4\frac{kOe}{\mu_B}$ compared with the HFD from VBF of the the LHT spectrum for $Fe_{0.45}Ni_{0.55}$ alloy.

in Fig.6.19. The other possible values of B_1, which turn out to be in the same range as in model-3, are also checked with the HFDs from the model. The HFDs from all these values of B_1 deviate from the experimental HFDs severely in terms of the HFD widths and the heights as shown in Fig.6.20. Therefore, this model has to be discarded because of its failure with the HFDs.

Model-5: $A = A_0 + A_1 y, B = B_0 + B_1 y$

Assuming that both the local and transferred couplings depend linearly on the concentration, we have:

$$\begin{aligned} < H > &= (A_0 + A_1 y) < \mu_{Fe} > +12(B_0 + B_1 y) < \mu_{Ni} > \\ &+ 12y(B_0 + B_1 y)(< \mu_{Fe} > - < \mu_{Ni} >) \end{aligned}$$

As known from above, three coupling parameter models (model-3 and mode-4) are able to give good fits to the average hyperfine fields. Now with one more free coupling parameter (add A_1 in model-3, or add B_0 in model-4), model-5 can always give a good fit of the average hyperfine field data, irrespective of what value of the added parameter is taken. In another words, only from fitting the average hyperfine field data, there are infinitely many solutions for the four coupling parameters. Whether all of these solutions are valid has to be examined in comparisons between the predicted and measured HFDs.

To find the best coupling parameters that can fit both the average hyperfine field data and the HFDs, we freeze A_1 at different values and each time fit the average hyperfine field data to obtain the other three coupling parameters (A_0, B_0, and B_1), then use the obtained coupling parameters to calculate the HFDs at each composition and compare with the measured HFDs from VBF method. The final coupling parameters are determined by comparison of the calculated and measured HFDs.

Fig.6.21 shows an example how HFDs change with parameter A_1 in $Fe_{0.45}Ni_{0.55}$. Comparing the calculated HFDs with the HFDs from the VBF method, we obtain the four best coupling parameters as: $A_1 = -22.0\frac{kOe}{\mu_B}$, $A_0 = 91.3\frac{kOe}{\mu_B}$, $B_0 = 3.6\frac{kOe}{\mu_B}$

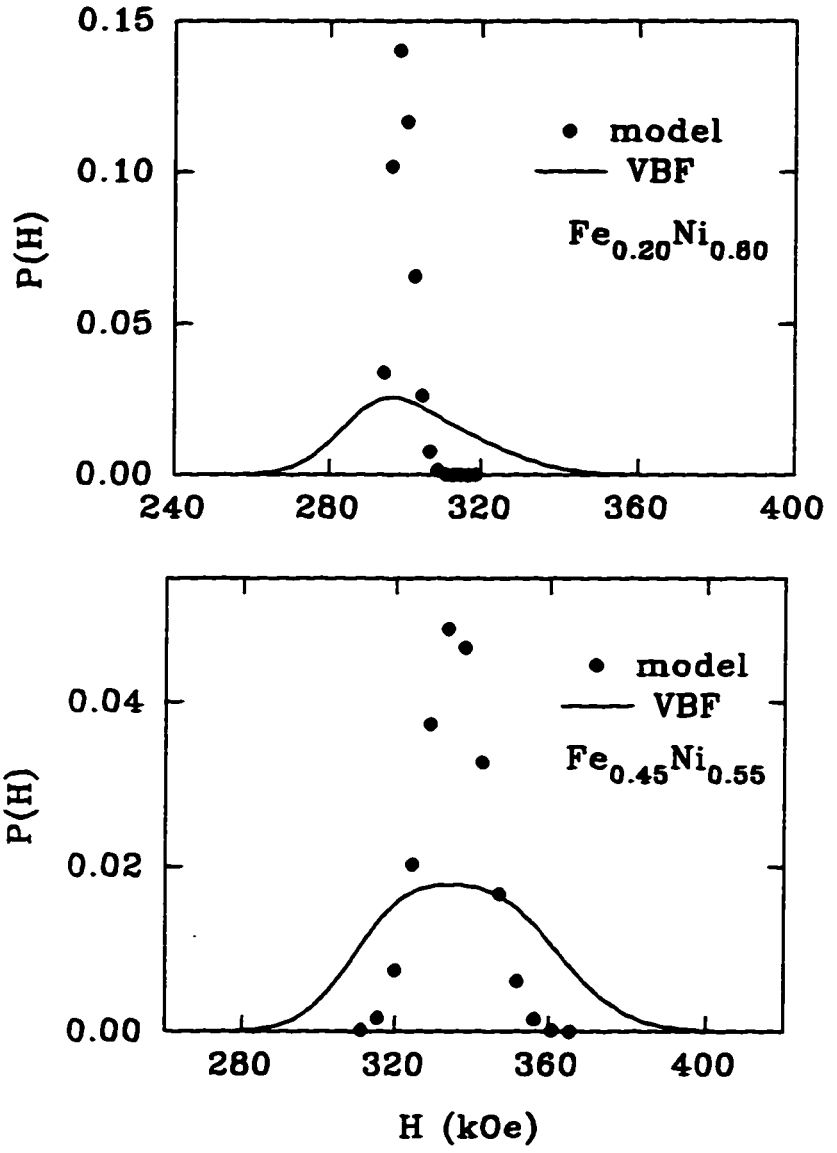

Figure 6.19 : The calculated HFDs from model-4 compared with the measured HFDs from the LHT spectra.

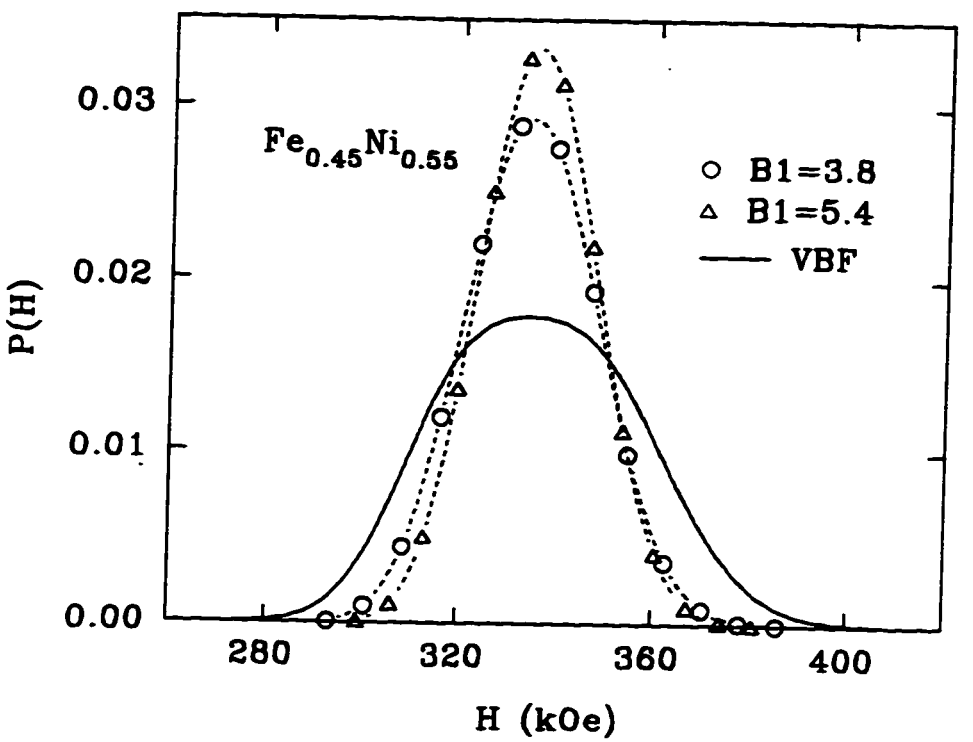

Figure 6.20 : The calculated HFDs from $A = A_0 + A_1 y$ and $B = B_1 y$ (model-4) with $B_1 = 3.8 \frac{kOe}{\mu_B}$ and $B_1 = 5.4 \frac{kOe}{\mu_B}$ compared with the HFDs from VBF of the LHT spectrum for the $Fe_{0.45}Ni_{0.55}$ alloy.

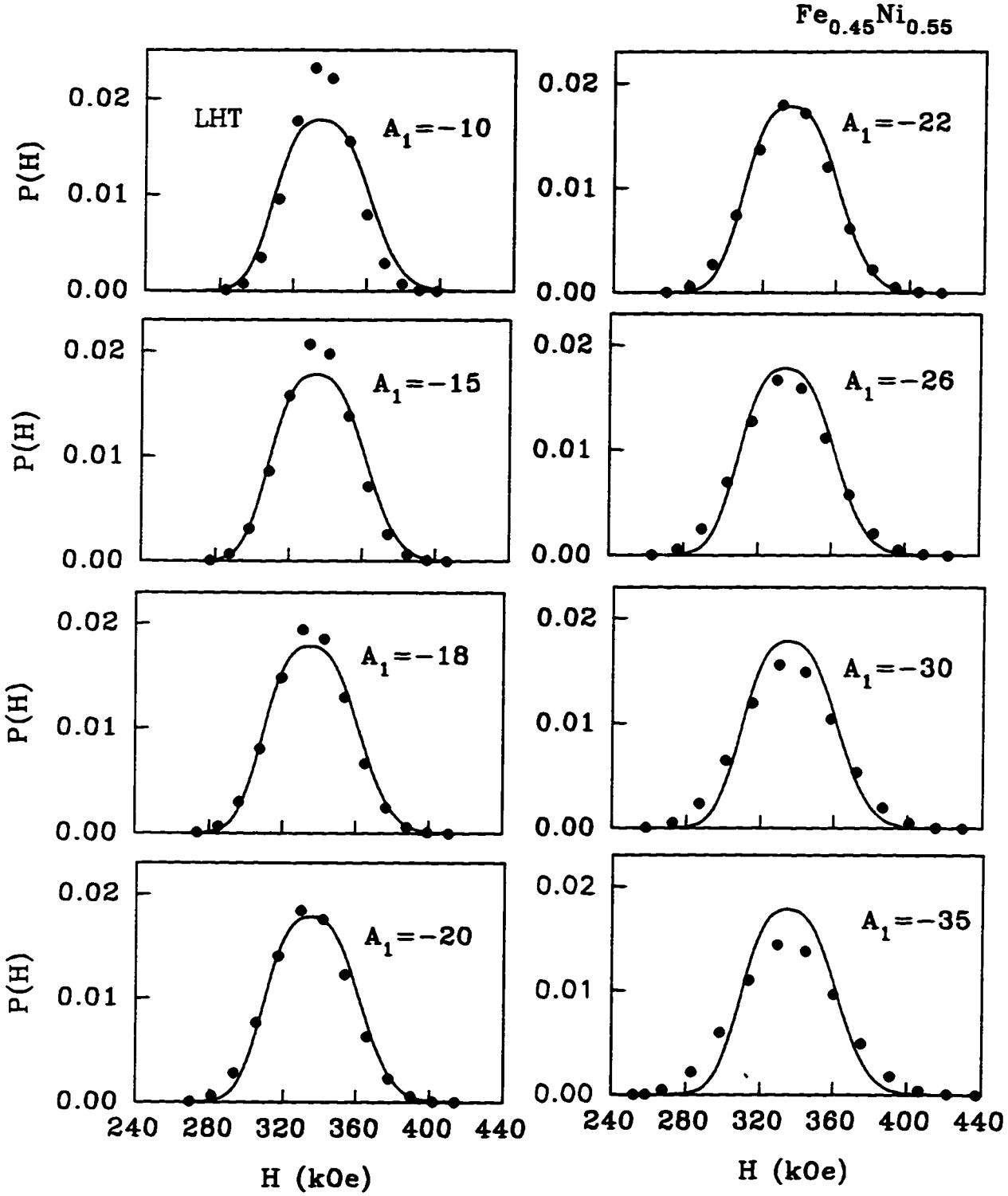

Figure 6.21 : Finding the best A_1 from the calculated HFDs.

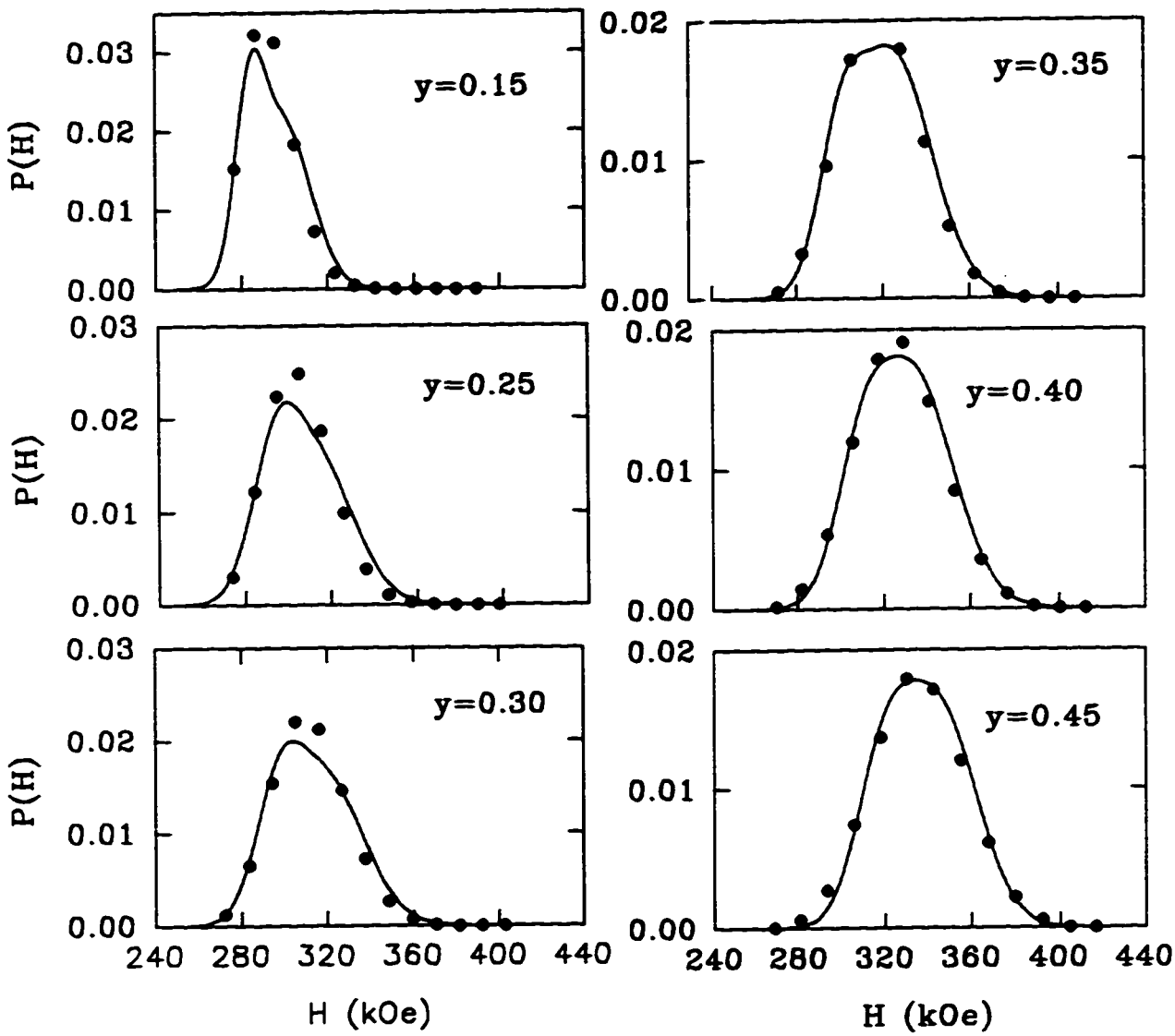

Figure 6.22 : HFDs at LHT corresponding to the best coupling parameters.

and $B_1 = 4.6\frac{kOe}{\mu_B}$. These are listed in Table 6.7. The errors on the obtained coupling parameters are estimated from the comparison of the calculated HFDs with the experimental ones. They are also listed in Table 6.7. The calculated HFDs from these four parameters at the different compositions and at LHT for the as-SQ samples are shown in Fig.6.22. Thus with four coupling parameters, the model is able to fit both the average hyperfine field data and the HFDs.

Table 6.7 summarizes all the models and the results we have tested . The fact that model-5 can make both the average hyperfine field and HFDs in good agreement with the experimental results at all concentrations of y $\leq$ 0.45 suggests that the concentration dependences of A and B are real. Possible causes of such concentration dependences are discussed in the next section.

It is the first time that a non-linearity (or curvature) is observed in the average hyperfine field versus composition in the Fe-Ni alloys. This may be due to: (1) Previous spectral analysis was not accurate enough to show such a small non-linearity. (2) Previous measurements are not as complete as ours at low iron concentration Fe-Ni alloys. (3) Previous linear phenomenological models were not rigorously tested by statistical analysis.

Our measured non-linearity is real and may well be due to an intrinsic physical mechanism that gives rise to our model-5, as we suggest here. We explore this further in the next section, in terms of the physical causes of hyperfine fields in metals. We must, however, keep in mind that the observed non-linearity may also be due to partial atomic ordering driven by the compound forming tendency at $FeNi_3$, even in these splat quenched. The latter possibility is discussed in detail in Chapter 7.

6.4 Cause of the Hyperfine Field

As mentioned in section 3.3, the hyperfine field arises from the core polarization and the conduction electron polarization. It is written as a vector sum of a local term and a transferred term. The A and B coupling parameters determine how the hyperfine field is related to the on site moment and to the near neighbor moments.

Table 6.7: Summary of the modeling results.

model	A_0 kOe/μ_B	A_1 kOe/μ_B	B_0 kOe/μ_B	B_1 kOe/μ_B	χ^2	hyperfine fields	HFDs
model-1	88.0	–	4.2	–	56	no	no
model-2	92.9	18.5	2.6	–	56	no	no
model-3	97.3 ±1.7	–	1.2 ± 0.6	4.6 ±0.8	1.5	yes	no
model-4	100.5 ±0.4	11.6 ±6.0	–	4.6 ±0.8	1.5	yes	no
model-5	91.3 ±1.1	-22.0 ±4.0	3.6 ±0.4	4.6 ±0.4	1.5	yes	yes

We know that the local coupling contains two contributions. One is the local or inner s-electrons which are polarized by the unpaired 3d-electrons - the origin of the local atomic magnetic moment. The other is the contribution from the itinerant 4s-conduction electrons which are also polarized by the local unpaired 3d-electrons. Meanwhile, these 4s-like conduction electrons are also polarized by the near neighbor moments.

When a Ni atom is replaced by an Fe atom in the near neighbor shell, this causes an increase in the hyperfine field due to that moment replacement. Meanwhile, the number of conduction electrons increases by 0.2 per replacement and there are more conduction electrons involved in the polarization. These conduction electrons are polarized by both the on site moment and the near neighbor moments. The increase in the number of conduction electrons is related to the increase in the CS of the alloys because it affects the electron spin density at the nucleus [82]. Therefore, we understand that it is not only the magnitude of the magnetic moment, but also the number of electrons involved in the polarization (which depends on composition) that determine the polarization mechanism of the hyperfine field. The magnitude of the obtained coupling parameters shows that the local coupling is dominant, for example, at y = 0.45, local coupling $A = A_0 + A_1 y = 81.4 \frac{kOe}{\mu_B}$ whereas $B = B_0 + B_1 y = 4.7 \frac{kOe}{\mu_B}$.

It is very interesting to notice that A_1 is negative whereas B_1, B_0 and A_0 are all positive. As mentioned above, A_1 and B_1 is the part related to the increment in the

conduction population. The different signs suggest that when one adds conduction electrons in the polarization, the local hyperfine field decreases but the transfered field increase for the same near neighbor environment. In other words, the conduction electron polarization changes direction when they move from probe site to their near neighbors sites. This fits in the RKKY picture for the spatial dependence of the conduction polarization in metal alloys.

Chapter 7. MÖSSBAUER RESULTS FOR RQ FCC Fe_yNi_{1-y} ALLOYS

7.1 Atomic Ordering and the Average Hyperfine Field

It is known that atomically ordered phases occur in fcc $FeNi_3$ and FeNi binary alloys and possibly in Fe_3Ni if the fcc phase could be stabilized at this concentration. Various studies show that the atomic ordering lowers the ^{57}Fe hyperfine field (e.g. [65]) and increase the magnetization and the Curie temperature T_C of the $FeNi_3$ alloy [86]. This leads to the question of whether the observed non-linearity of the hyperfine field in SQ Fe-Ni alloys (y = 0 to 0.50 in Fe_yNi_{1-y}) is related to the $FeNi_3$ atomic ordering and of how the quenching rate affects the hyperfine fields of the alloys. In order to answer these questions, three RQ samples denoted as RQ_1, RQ_2 and RQ_3 at y = 0.25 were made at different quenching rates. The quenching conditions are given in Table 7.1. With the same roller speed, the quenching rate is proportional to the spring force or pressure. These RQ samples are investigated by Mössbauer spectroscopy at RT to examine the quenching effect on the hyperfine fields.

The three spectra are fitted by the VBF method. The obtained fit parameters are given in Table 7.2. The average hyperfine field is plotted as a function of the

Table 7.1: Quenching conditions for RQ samples at y = 0.25.

sample	spring force N	roller speed rpm
RQ_1	0.	3000
RQ_2	4.	3000
RQ_3	8.	3000

Table 7.2: RT spectral fitting parameters for three RQ samples at y = 0.25.

sample	$h3_1$	$h3_2$	HF_1 (kOe)	HF_2 (kOe)	σ_1 (kOe)	σ_2 (kOe)	Γ (mm/s)
RQ_1	55040	43054	298.15	279.55	14.94	9.64	0.253
RQ_2	48245	35914	296.91	278.58	15.10	9.52	0.253
RQ_3	15977	24241	280.70	298.59	8.83	14.39	0.251

sample	δ_0 (mm/s)	δ_1	ε_0 (mm/s)	ε_1	h1/h3	h2/h3	BG	χ_{red}^2
RQ_1	0.0378	-0.003	0.323	-0.166	2.63	2.40	111168.	1.06
RQ_2	-0.0089	0.015	0.333	-0.172	2.94	2.13	2433750	4.56
RQ_3	0.0110	0.005	0.351	-0.175	2.86	2.18	1673260	1.19

In Table 7.2 $h3_i$ is the line-3 peak height for the ith Gaussian component, HF_i is the center of the ith HF Gaussian component, σ_i is the hyperfine field Gaussian component width for the component-i, where i = 1, 2.

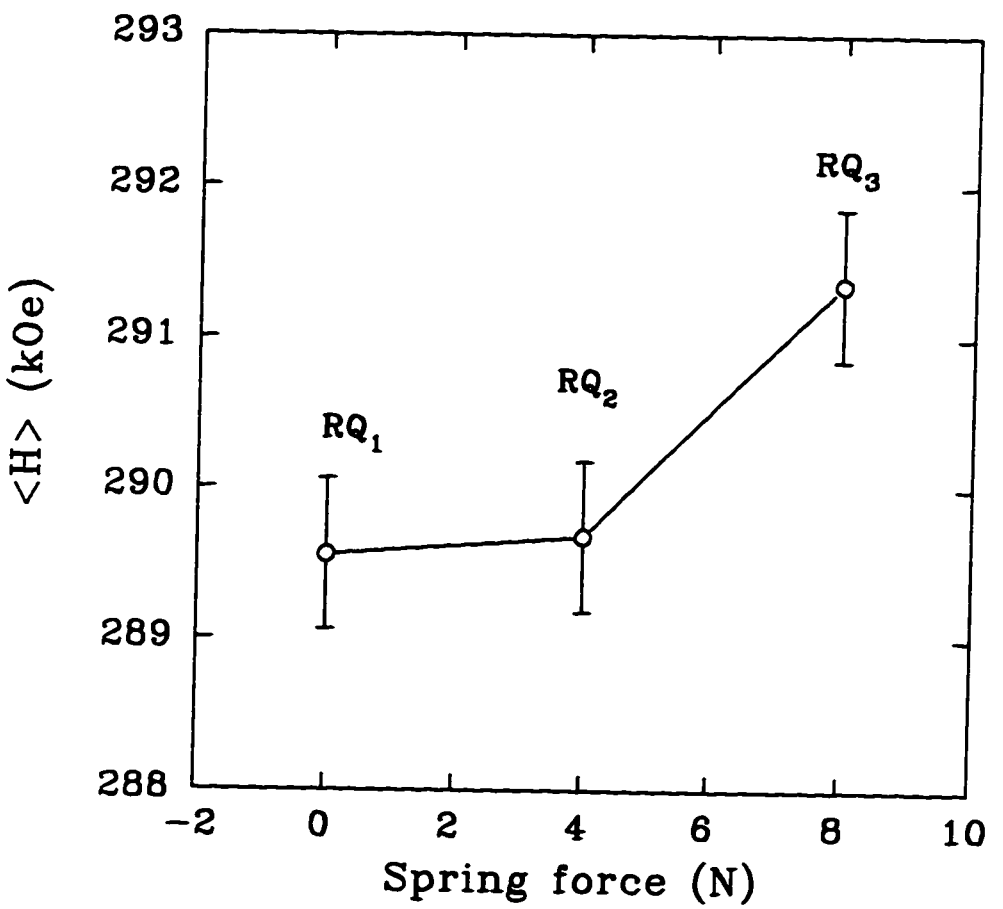

Figure 7.1: RT average hyperfine fields versus spring force in RQ samples at y = 0.25.

spring force in Fig.7.1. The quenching rate which is proportional to the spring force for the same roller speed [78] does affect the average hyperfine fields.

From the hyperfine field phenomenological model (section 3.4), we can calculate the difference of the average hyperfine field in the random and in perfectly ordered $FeNi_3$, assuming that the hyperfine field originates from the same polarization mechanism in both alloys. As given by Eq.3.10:

$$H_k = A < \mu_{Fe} > +12B < \mu_{Ni} > +Bk(< \mu_{Fe} > - < \mu_{Ni} >).$$

For perfectly ordered $FeNi_3$, there are 12 Ni atoms as the nearest neighbors of all the Fe atoms. The average hyperfine field in the ordered $FeNi_3$ $< H >_o$, is:

$$< H >_o = A < \mu_{Fe} > +12B < \mu_{Ni} >$$

whereas for perfectly random $FeNi_3$, the binomial distribution gives rise to:

$$\begin{aligned} < H > &= A < \mu_{Fe} > +12B < \mu_{Ni} > +12 \times 0.25B(< \mu_{Fe} > - < \mu_{Ni} >) \\ &= A < \mu_{Fe} > +12B < \mu_{Ni} > +3B(< \mu_{Fe} > - < \mu_{Ni} >) \end{aligned}$$

Now, we have:

$$< H > - < H >_o = 3B(< \mu_{Fe} > - < \mu_{Ni} >)$$

which equals to 6.6B at LHT. From the obtained B in SQ samples, the maximum of B is $6\frac{kOe}{\mu_B}$. We therefore estimate that the maximum difference between the average hyperfine fields of the ordered and random $FeNi_3$ is 40 kOe. Clearly, small degrees of atomic non-randomness can measurably affect the average hyperfine fields.

Since the quenching rate in RQ samples (typically 10^5 to 10^6 K/s [78])) is larger than in SQ samples (typically 10^5 K/s or less [63]), the RQ samples give the closest available estimate of truly atomic random alloys. Since faster quenching does partially remove the non-linearity in $< H >$ versus y observed in SQ samples (Chapter 6), however, we must admit that some atomic ordering effects were present in the SQ alloys and may still be present in the RQ alloys. Especially in the light of recent

theoretical calculations [87] that show equilibrium short range atomic order persisting to very high temperature, the order of the melting points. When our analysis of $< H >$ versus y in RQ samples, for simplicity, assumes perfect atomic randomness it therefore gives an upper limit to the local and transferred y-dependent hyperfine field coupling parameters.

We next investigate how the average hyperfine field varies with the alloy composition in RQ samples, and then apply the proposed model to the hyperfine field data of RQ samples.

7.2 Mössbauer Results for RQ samples

A series of RQ samples (y = 0.05, 0.15, 0.25, 0.35, 0.45, 0.50, 0.55, 0.60) which are made with the same highest quenching rate as RQ_3 are investigated by Mössbauer spectroscopy at RT and LNT. Two RQ samples at y = 0.50 and 0.60 and one SQ sample at y = 0.65 are studied at RT, LNT and LHT.

We do not expect that the quench rate has any affect on the spectra of the y = 0.65 alloy so we will report the y = 0.65 results for this SQ sample along with the results for the RQ samples. For $y \leq 0.45$ the RT spectra are shown in Fig.7.2 and the LNT spectra are shown in Fig.7.3. For y = 0.50, 0.60, and 0.65, the spectra at RT, LNT and LHT are shown in Fig.7.4, Fig.7.5 and Fig.7.6, respectively. The RT spectral fitting parameters are given in Table 7.3, the LNT spectral fitting parameters in Table 7.4, and the LHT spectral fitting parameters in Table 7.5.

From the fitting paramters, we obtain the average hyperfine fields and the HFD standard deviations using Eq.6.1 (section 6.1), as we did for SQ samples. They are sumarized in Table 7.6 for RQ samples at RT, LNT and LHT.

Since the RQ samples $y \leq 0.45$ were not measured at LHT, the required LHT average hyperfine fields are derived by the same way as we used in the SQ samples (section 6.2). Adding the corresponding difference ($\Delta H_{LHT-LNT}$; measured in the SQ samples, Fig.6.11) to the hyperfine fields at LNT, we obtain the average hyperfine fields at LHT for RQ samples at $y \leq 0.45$.

For $y \geq 0.45$, the average hyperfine field data at y = 0.50, 0.60 and 0.65 are

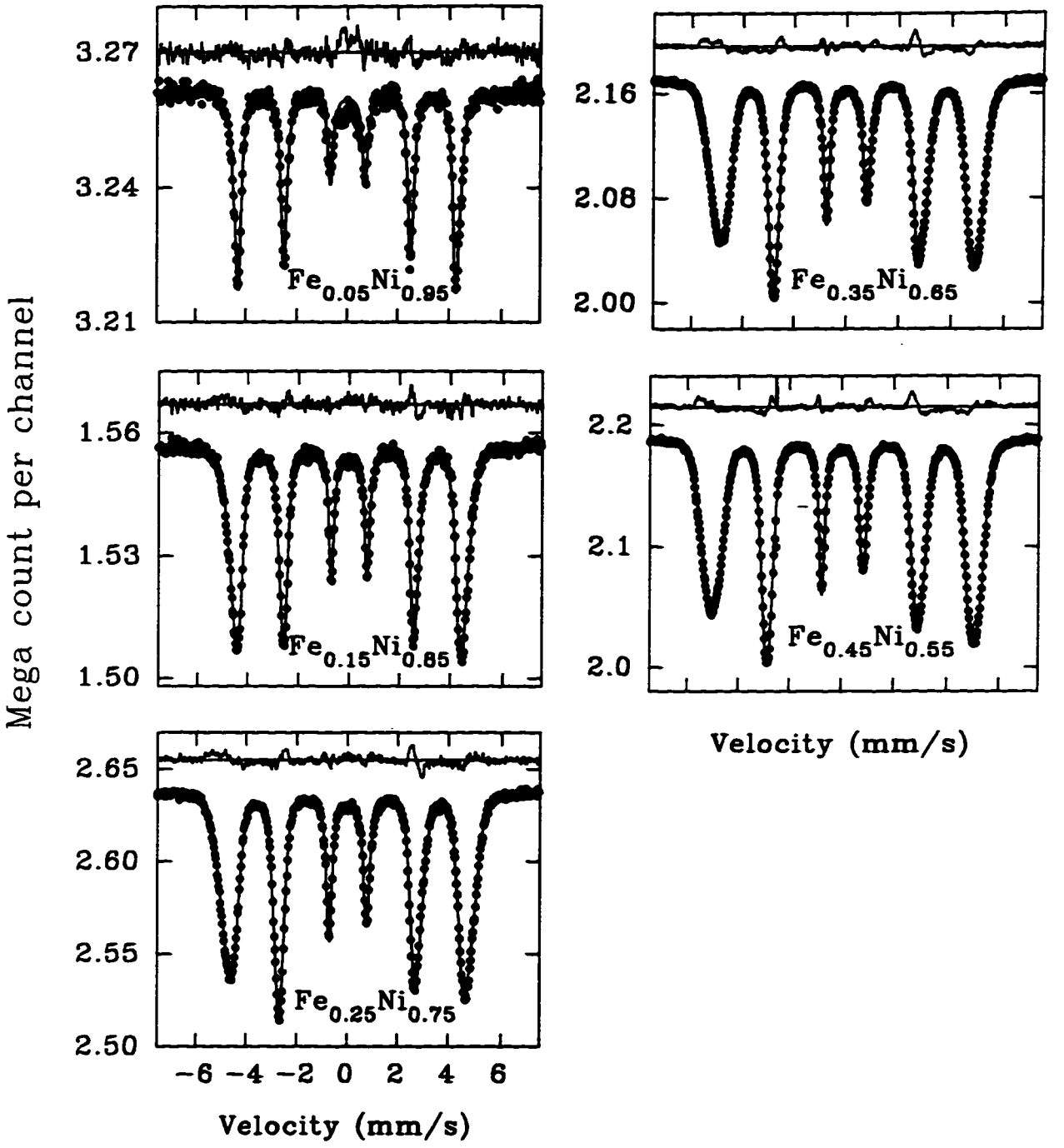

Figure 7.2: RT spectra with fitting for $y \leq 0.45$ RQ samples.

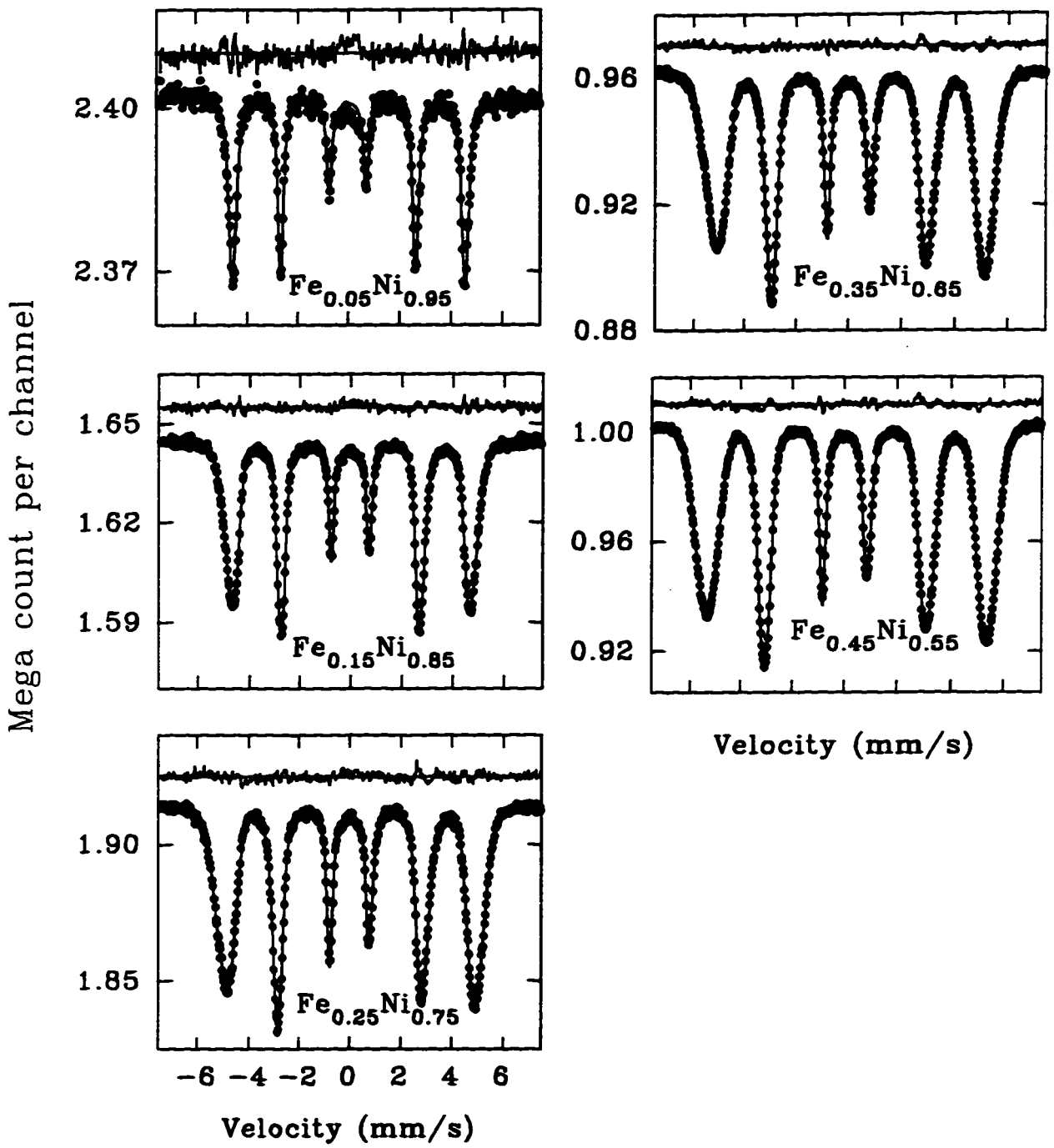

Figure 7.3: LNT spectra for $y \leq 0.45$ RQ samples.

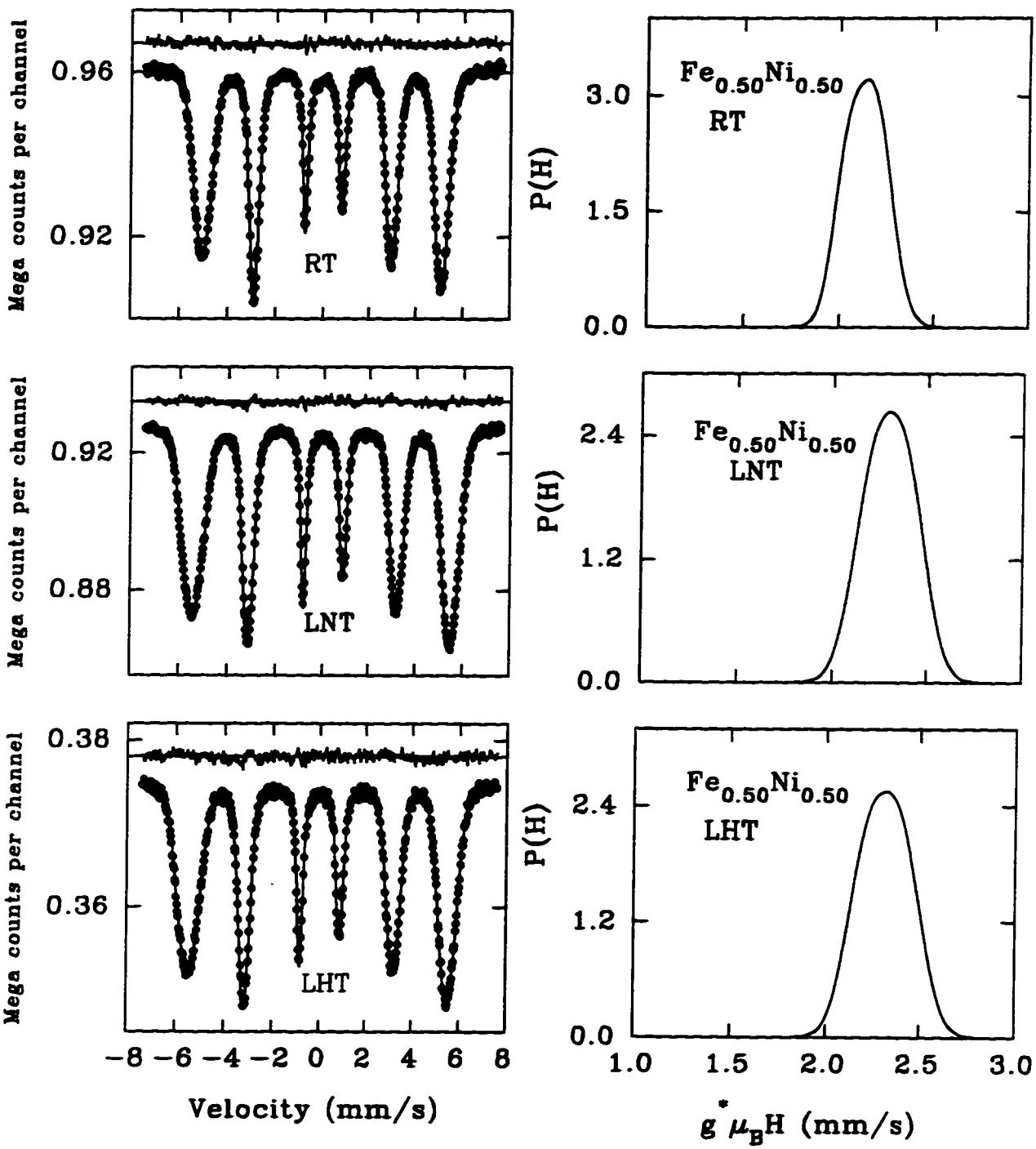

Figure 7.4: Fitted spectra for RQ $Fe_{0.50}Ni_{0.50}$ at RT, LNT and LHT.

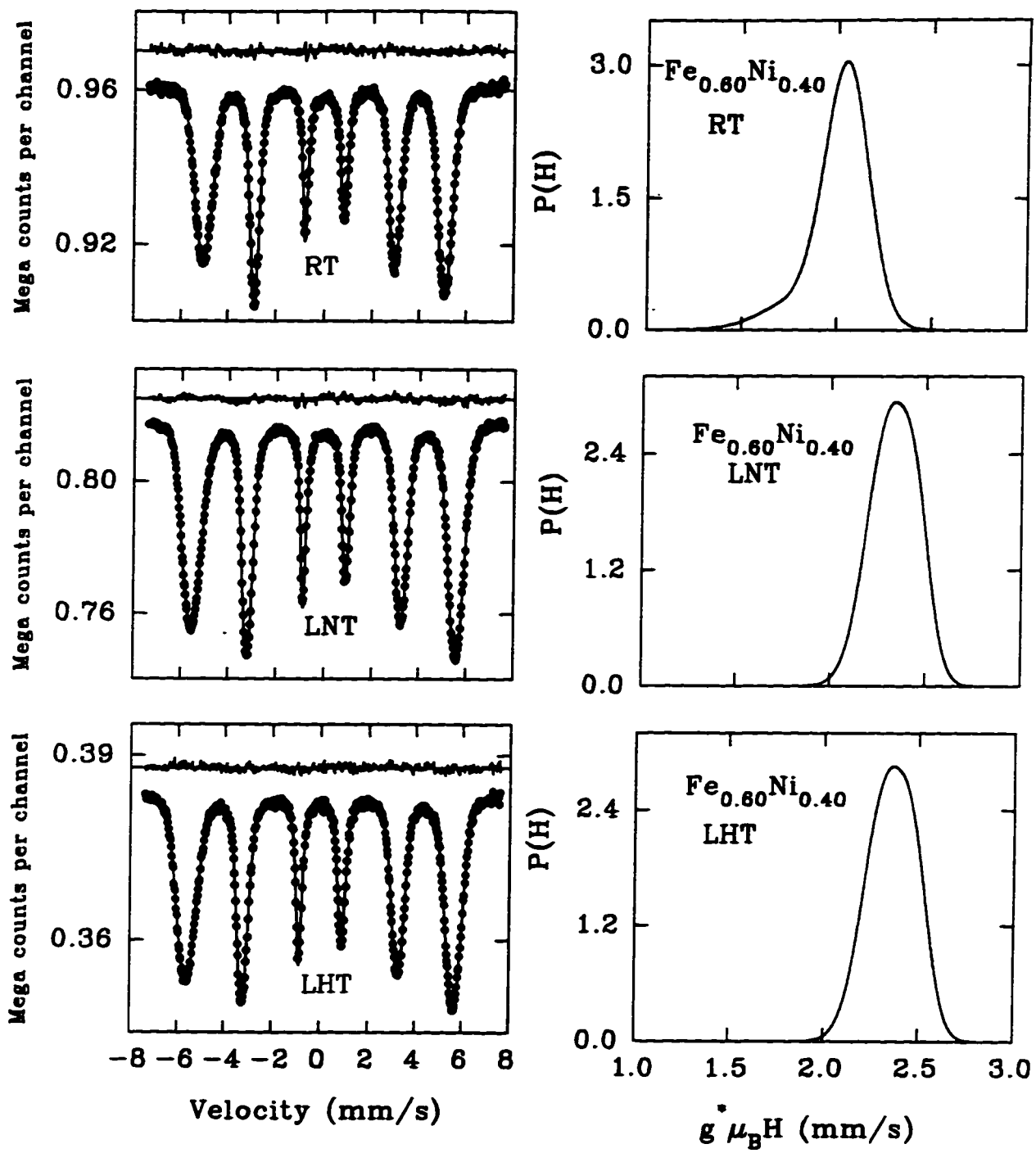

Figure 7.5: Fitted spectra for RQ $Fe_{0.60}Ni_{0.40}$ at RT, LNT and LHT.

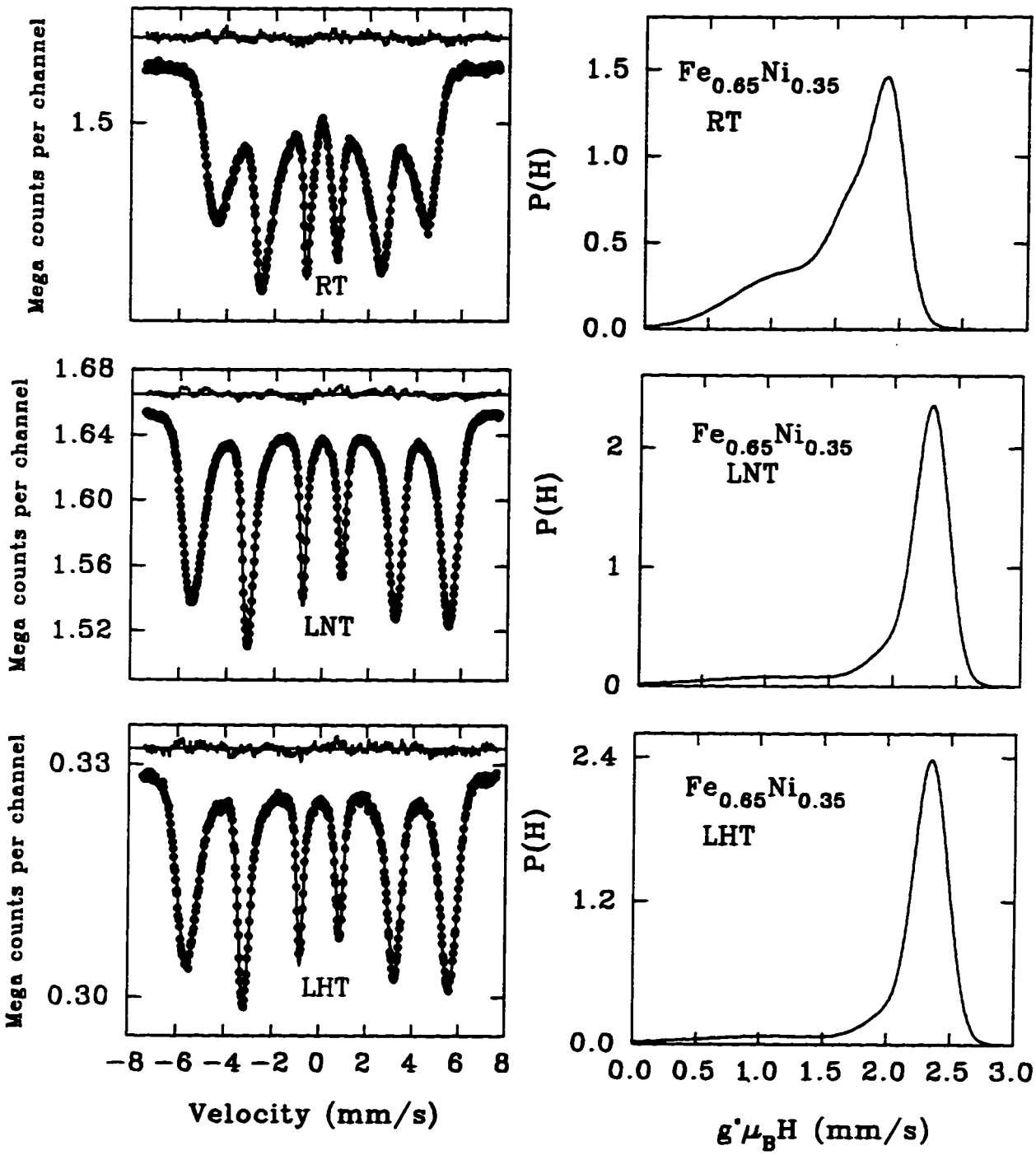

Figure 7.6: Fitted spectra for SQ $Fe_{0.65}Ni_{0.35}$ at RT, LNT and LHT.

Table 7.3: Fitting parameters for RQ samples at RT.

y	$h3_1$	$h3_2$	$h3_3$	HF_1 (kOe)	HF_2 (kOe)	HF_3 (kOe)	σ_1 (kOe)	σ_2 (kOe)	σ_3 (kOe)
0.05	15172	5252	-	265.88	276.43	-	1.34	3.43	-
0.15	9286	15629	-	270.14	283.71	-	5.15	10.44	-
0.25	15977	24241	-	280.70	298.59	-	8.83	14.39	-
0.35	75888	36346	-	310.40	288.28	-	16.43	10.31	-
0.45	51595	78405	-	297.57	321.87	-	11.70	14.18	-
0.50	13330	27205	-	300.35	322.30	-	10.93	13.83	-
0.55	24292	31174	-	300.16	320.43	-	12.38	13.02	-
0.60	7839	38847	-	267.75	302.79	-	28.82	17.01	-
0.65	32687	31039	28751	168.18	284.97	248.1	63.37	18.23	28.57

y	δ_0 (mm/s)	δ_1	ε_0 (mm/s)	ε_1	h1/h3	h2/h3	BG	Γ	χ^2_{red}
0.05	-0.031	0.016	0.150	-0.085	2.6	2.0	3261441	0.256	1.4
0.15	-0.143	0.008	-0.197	0.104	2.9	2.3	1410876	0.228	1.2
0.25	0.011	0.005	0.351	-0.174	2.9	2.2	1673260	0.251	1.2
0.35	0.055	-0.013	0.501	-0.248	2.9	2.3	2171996	0.275	7.9
0.45	0.107	-0.035	0.520	-0.252	2.9	2.2	2190836	0.282	11.5
0.50	0.102	-0.034	0.558	-0.263	2.8	2.1	961793	0.280	1.7
0.55	0.085	-0.028	0.531	-0.253	2.8	2.1	1013046	0.272	1.5
0.60	0.028	-0.001	0.384	-0.187	2.7	2.0	923633	0.288	2.1
0.65	-0.016	0.017	0.095	-0.050	2.9	2.1	1520716	0.272	2.3

In Table 7.3, $h3_i$ is the line-3 peak height for the ith Gaussian component, HF_i is the center of the ith HF Gaussian component, σ_i is the hyperfine field Gaussian component width for the component-i, where i = 1, 2, 3. All samples are RQ samples except at y = 0.65 as a SQ sample.

Table 7.4: Fitting parameters for RQ samples at LNT.

y	$h3_1$	$h3_2$	$h3_3$	HF_1 (kOe)	HF_2 (kOe)	HF_3 (kOe)	σ_1 (kOe)	σ_2 (kOe)	σ_3 (kOe)
0.05	65590	11144	-	291.15	280.97	-	5.80	1.80	-
0.15	15951	21635	-	284.22	299.29	-	7.41	12.27	-
0.25	25436	34891	-	294.84	314.41	-	11.17	16.44	-
0.35	37198	17132	-	325.66	303.38	-	18.71	12.33	-
0.45	42939	25608	-	342.55	315.90	-	17.43	13.85	-
0.50	28654	26134	-	326.60	353.18	-	15.65	15.23	-
0.55	52985	23474	-	335.68	360.18	-	16.59	12.77	-
0.60	45910	11769	-	340.21	362.47	-	17.17	11.06	-
0.65	87566	23339	16246	340.88	304.61	173.50	18.77	31.18	92.87

y	δ_0 (mm/s)	δ_1	ε_0 (mm/s)	ε_1	h1/h3	h2/h3	BG	Γ	χ^2_{red}
0.05	-0.047	0.016	0.349	-0.181	2.63	2.11	2401849	0.227	1.27
0.15	-0.017	0.008	0.141	-0.07	2.88	2.40	1644925	0.231	1.21
0.25	0.000	0.007	0.340	-0.163	2.89	2.18	1914770	0.254	2.09
0.35	0.059	-0.016	0.489	-0.226	2.88	2.20	962862	0.276	2.07
0.45	0.080	-0.025	0.474	-0.213	2.84	2.15	1004458	0.293	2.66
0.50	0.076	-0.022	0.475	-0.208	2.87	1.97	928938	0.283	2.01
0.55	0.087	-0.027	0.478	-0.207	2.84	2.05	1021624	0.288	2.39
0.60	0.061	-0.016	0.498	-0.214	2.77	1.93	819038	0.294	1.74
0.65	0.044	-0.009	0.371	-0.162	2.94	2.16	1656285	0.294	4.95

In Table 7.4, $h3_i$ is the line-3 peak height for the ith Gaussian component, HF_i is the center of the ith HF Gaussian component, σ_i is the hyperfine field Gaussian component width for the component-i, where i = 1, 2, 3. All samples are RQ except at y = 0.65 as a SQ sample.

Table 7.5: Fitting parameters at LHT.

y	$h3_1$	$h3_2$	$h3_3$	HF_1 (kOe)	HF_2 (kOe)	HF_3 (kOe)	σ_1 (kOe)	σ_2 (kOe)	σ_3 (kOe)
0.50	10562	12057	-	326.61	354.21	-	15.13	15.86	-
0.60	21723	6413	-	343.53	366.69	-	17.28	11.46	-
0.65	19417	2922	3597	346.90	166.56	305.13	19.42	96.14	31.43

y	δ_0 (mm/s)	δ_1	ε_0 (mm/s)	ε_1	h1/h3	h2/h3	BG	Γ (mm/s)	χ^2_{red}
0.50	0.075	-0.021	0.485	-0.211	2.84	1.96	375247	0.293	1.27
0.60	0.070	-0.019	0.495	-0.210	2.75	1.90	383969	0.296	1.40
0.65	0.066	-0.018	0.431	-0.184	2.96	2.15	329156	0.299	1.81

In Table 7.5 $h3_i$ is the line-3 peak height for the ith Gaussian component, HF_i is the center of the ith HF Gaussian component, σ_i is the hyperfine field Gaussian component width for the component-i, where i = 1, 2, 3. The alloys at y = 0.50 and y = 0.60 are RQ alloys while the alloy at y = 0.65 is a SQ one.

Table 7.6: Average hyperfine fields and the standard deviations of HFDs at RT, LNT and LHT from spectral fitting fir RQ samples.

y in Fe_yNi_{1-y}	$< H >_{RT}$ kOe	σ_{RT} kOe	$< H >_{LNT}$ kOe	σ_{LNT} kOe	$< H >_{LHT}$ kOe	σ_{LHT} kOe
0.05	268.6	5.2	284.7	6.3	-	-
0.15	278.7	10.8	292.9	13.0	-	-
0.25	291.5	15.3	306.2	17.4	-	-
0.35	303.2	18.0	318.6	19.8	-	-
0.45	312.2	17.7	332.6	20.8	-	-
0.50	315.1	16.6	339.3	20.4	341.3	20.8
0.55	311.6	16.3	343.2	19.2	-	-
0.60	296.9	23.5	344.8	18.5	348.8	18.8
0.65	232.2	65.2	312.8	67.5	320.8	69.7

Table 7.7: Average hyperfine fields at LHT for RQ samples from measurement(†) and the extrapolations(⋆).

y in Fe_yNi_{1-y}	$< H >_{LNT}$ kOe	$\Delta H_{LHT-LNT}$ kOe	$< H >_{LHT}$ kOe
0.05	284.7	0.92	285.7 ⋆
0.15	292.9	1.24	294.1 ⋆
0.25	306.2	1.50	307.7 ⋆
0.35	318.6	1.80	320.4 ⋆
0.45	332.6	2.18	334.8 ⋆
0.50	339.3	2.04	341.3 †
0.55	343.2	3.05	346.3 ⋆
0.60	344.8	4.06	348.8 †
0.65	312.8	7.97	320.8 †

obtained by fitting the spectra directly. For y = 0.55 we first use a linear extrapolation to get the difference $\Delta H_{LHT-LNT}$ for y = 0.55, from the results of y = 0.50 and y = 0.60 (Table 7.6), then add the difference to the average hyperfine field at LNT. This gives the average hyperfine field at LHT for y = 0.55 as $< H >_{LHT} = \Delta H_{LHT-LNT} + < H >_{LNT}$. Therefore, we have the average hyperfine fields at LHT for all the RQ alloys. They are listed in Table 7.7. The resulting average hyperfine fields at RT, LNT and LHT for RQ samples are shown in Fig.7.7.

Average hyperfine fields for RQ Fe-Ni at y$\leq$ 0.45 at RT are shown in Fig.7.8 in comparison with those of SQ samples. For most of the RQ samples, the average hyperfine fields are slightly higher (within 1 kOe) than that of the SQ samples, but at y = 0.25, the hyperfine field in RQ sample is about 3 kOe higher that of the SQ sample, which again suggests that atomic ordering may not have completely vanished in the SQ samples.

7.3 Testing the Hyperfine Field Phenomenological Model

The hyperfine field data in RQ samples are used to test model-1 to 5, having constant or composition dependent A and B coupling parameters. In the first case, with two fitting parameters A and B, the number of degrees of freedom ν is 6 - 2 = 4. A linear relationship for the average hyperfine field versus y is used to fit the hyperfine field data. For the best fit the χ^2 is 13.6 which is still greater than the $\chi^2 = x_+$ = 9.50 for a 95% confidence. Therefore, although the agreement between the data and model-1 is improved in RQ samples, the model is still beyond the acceptable probability range (or confidence level). As shown in Fig.7.9 for the best fit of the average hyperfine fields and the calculated HFD for the y = 0.45 sample, model-1 cannot fit the hyperfine field data properly, and the calculated HFDs do not have a good agreement with the experimental results either. We conclude that model-1 and other models that are equivalent to model-1 are only a first approximation. Model-2 gives a linear average hyperfine field versus y and is also rejected.

Model-3 (with $A = A_0, B = B_0 + B_1 y$) and model-4 (with $A = A_0 + A_1 y, B = B_0$) can fit the average hyperfine field versus y with $\chi^2 = 2.2$, but the HFDs from both

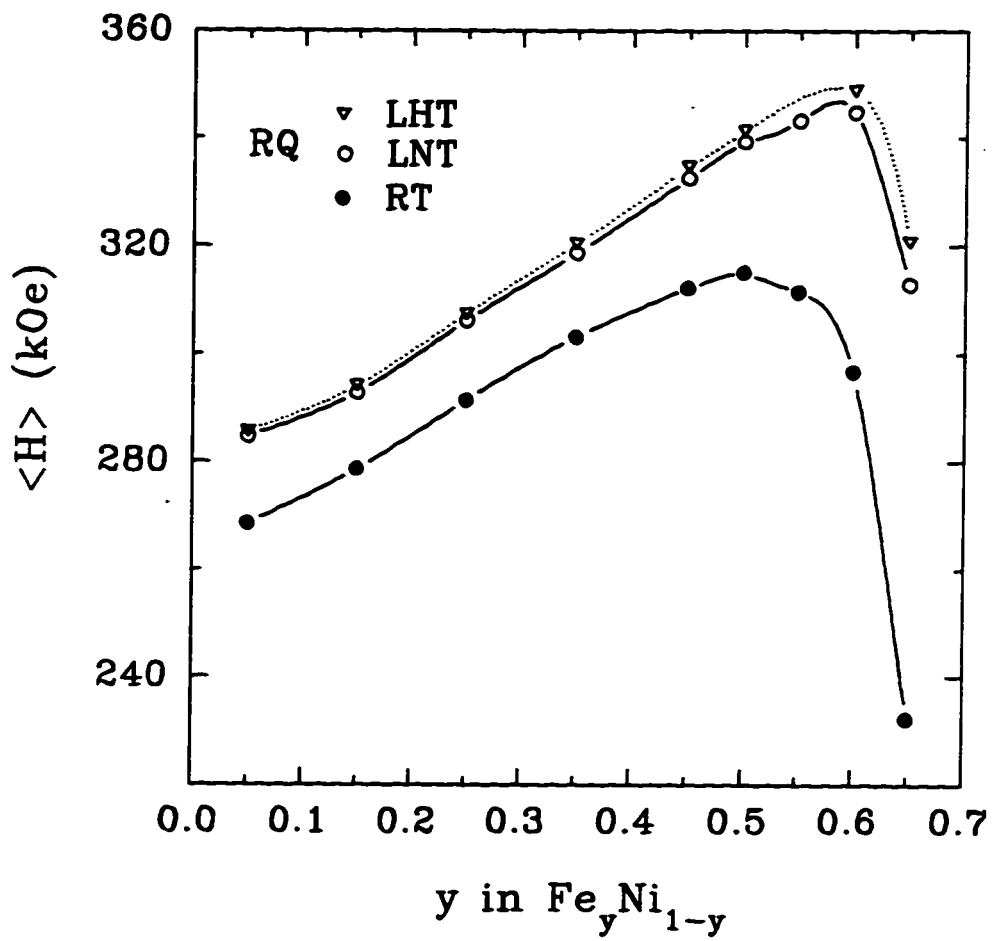

Figure 7.7: Average hyperfine field for RQ samples (except y = 0.65) at RT, LNT and LHT.

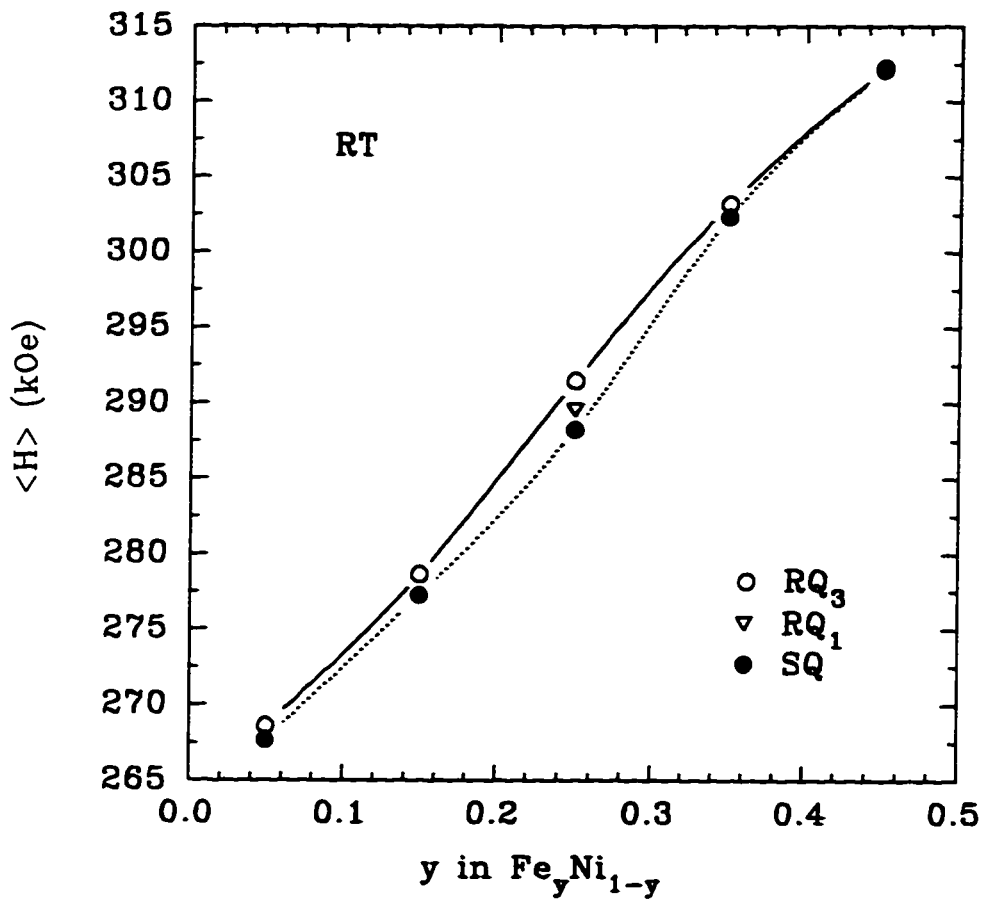

Figure 7.8: Average hyperfine fields in RQ and SQ samples at RT. Since $< H >$ for RQ_1 and RQ_2 have similar values (Fig.7.1), the hyperfine field for RQ_2 is not shown for clarity.

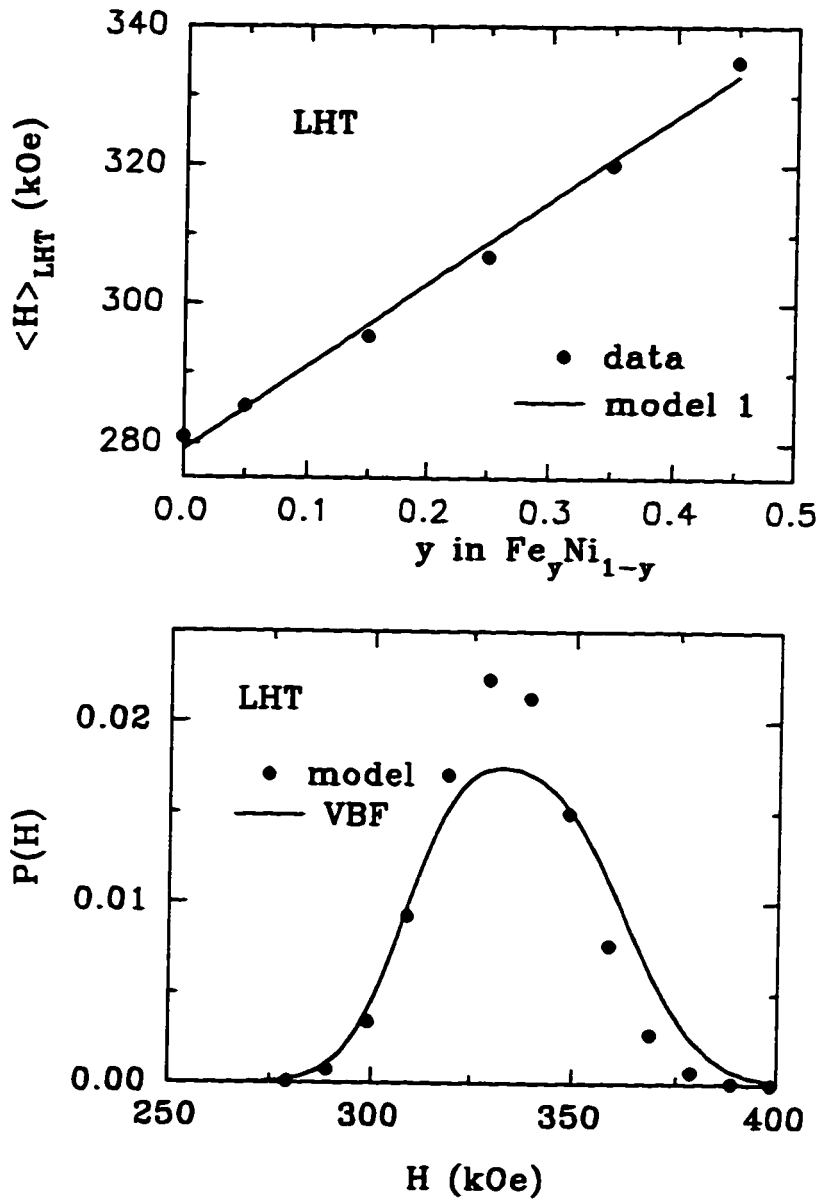

Figure 7.9: (a)Average hyperfine fields at LHT versus y for RQ samples, compared to the model-1 fit. (b)Calculated HFD at LHT for RQ $Fe_{0.45}Ni_{0.55}$ using the best model-1 parameters, compared to the measured HFD.

Table 7.8: Best coupling parameters for SQ and RQ samples.

sample	A_0 kOe/μ_B	A_1 kOe/μ_B	B_0 kOe/μ_B	B_1 kOe/μ_B
SQ	87.8	-	4.51	-
SQ	91.3±1.1	-22 ±4	3.56 ±0.42	4.60 ±0.00
RQ	88.0	-	4.53	-
RQ	89.0 ±1.4	-20 ±4	4.40 ±0.53	3.15 ±0.40

models deviate from the measured ones. Same as in SQ samples (section 6.3), HFDs from model-3 and model-4 are examined for other possible coupling parameters which can fit the average hyperfine field versus y. But they cannot produce HFDs in satisfactory agreement with the experimental results. On the other hand, model-5 can fit the hyperfine field data well. The χ^2 of the fit to the average hyperfine field versus y is 2.2. To determine the four coupling parameters, A_1 is frozen at different values. For each A_1, the other three coupling parameters are left as free parameters. The HFDs are calculated with the obtained four coupling parameters, and compared to the experimental results. Fig.7.10 shows how the couplings are determined by comparison of the calculated and measured HFDs at T = 4.2 K. The obtained best parameters and their errors are $A_0 = 89.0 \pm 1.4 \frac{kOe}{\mu_B}$, $A_1 = -20 \pm 4 \frac{kOe}{\mu_B}$, $B_0 = 4.4 \pm 0.5 \frac{kOe}{\mu_B}$, and $B_1 = 3.2 \pm 0.0 \frac{kOe}{\mu_B}$. They are listed in Table 7.8. Best coupling parameters for SQ samples are also listed in Table 7.8 for comparison. The calculated HFDs at LHT are shown in Fig.7.11. The results suggest that, as with the SQ samples, four coupling parameters are necessary for the model to fit both the average hyperfine fields and the HFDs simultaneously.

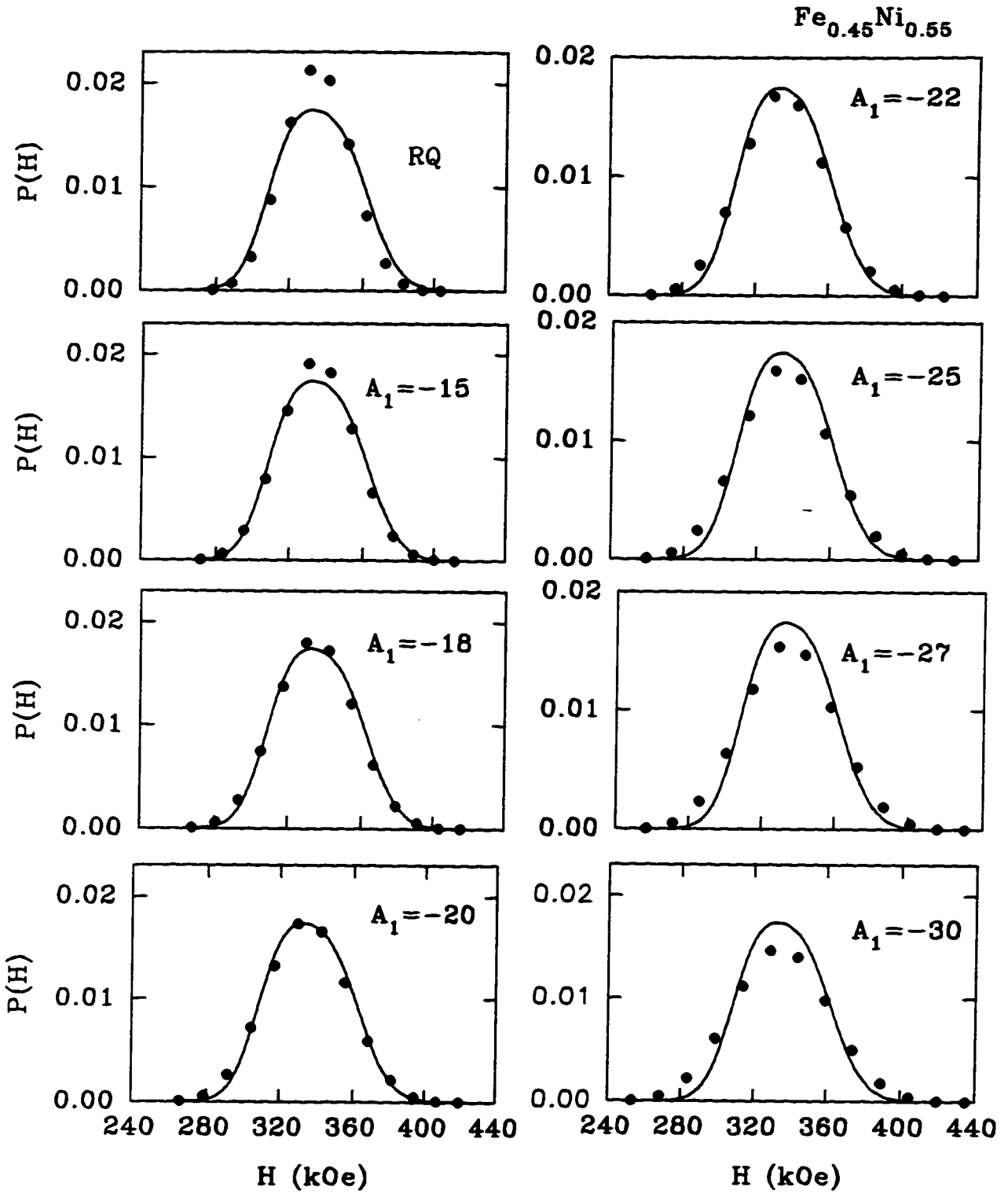

Figure 7.10: Model-5 calculated HFDs (dots) for different values of A_1 compared to the measured HFD for RQ $Fe_{0.45}Ni_{0.55}$ at T = 4.2K, used to determine the acceptable values of the model-5 parameters.

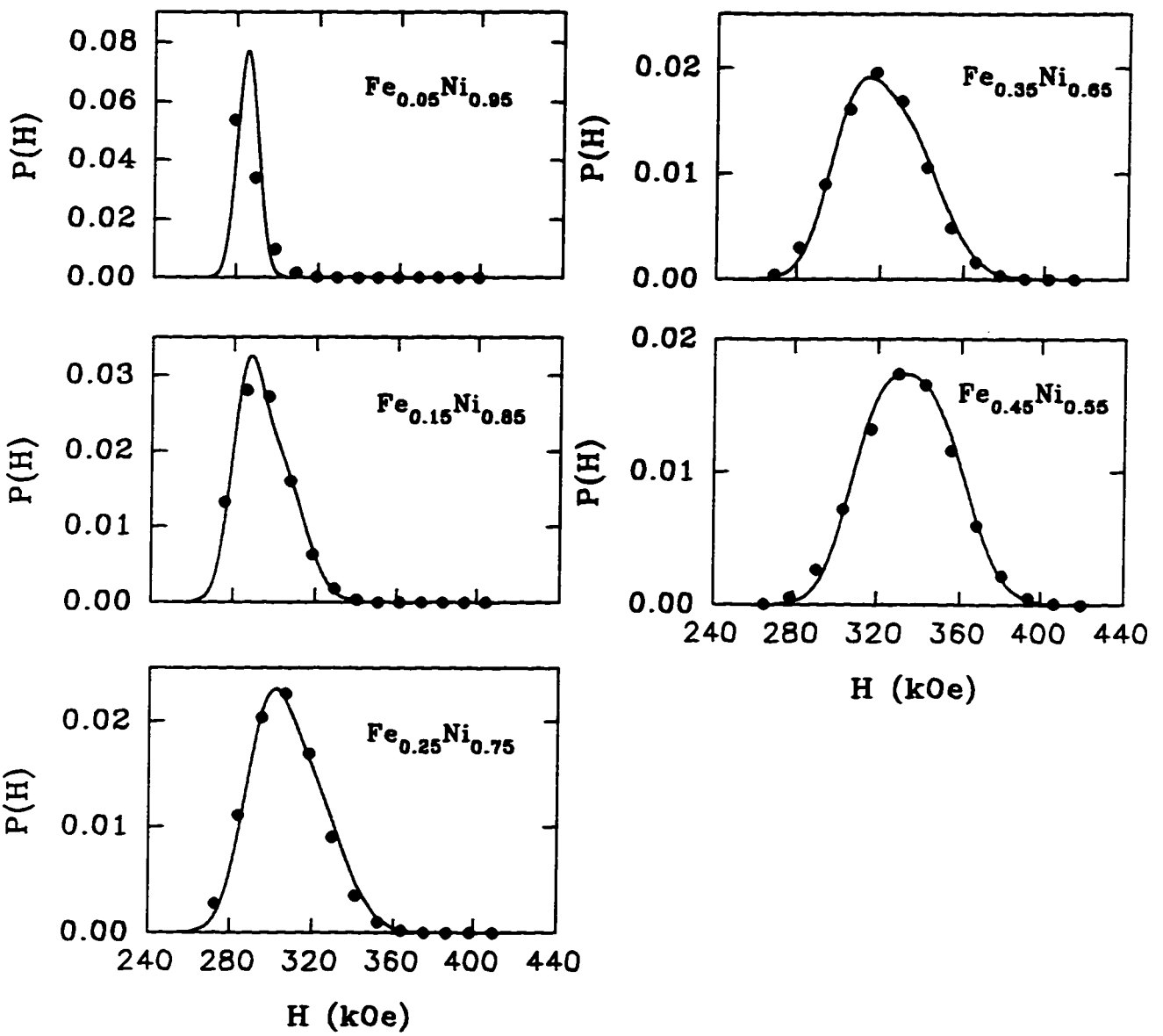

Figure 7.11: The best calculated model-5 HFDs for RQ collinear ferromagnetic Fe-Ni alloys at LHT.

7.4 Comparison of the Various Obtained Coupling Parameters

We have applied the phenomenological hyperfine field model with different coupling parameters to the experimental data for SQ (Chapter 6) and RQ (Chapter 7) samples. It was demonstrated that the model with constant A and B does not fit the average hyperfine field versus y data. If constant couplings ($A = A_0, B = B_0$) are used as others did, the best coupling parameters are $A = 87.8\frac{kOe}{\mu_B}, B = 4.51\frac{kOe}{\mu_B}$ for SQ, $A = 88.0\frac{kOe}{\mu_B}, B = 4.53\frac{kOe}{\mu_B}$ for RQ samples. The B in our model times 12 equals to the b in the model of $H = a\mu_{Fe} + b\bar{\mu}$. That gives our $a = 88\frac{kOe}{\mu_B}$, and $b = 54\frac{kOe}{\mu_B}$ in comparison with $a = 90\frac{kOe}{\mu_B}, b = 50\frac{kOe}{\mu_B}$ [70] and $a = 90\frac{kOe}{\mu_B}, b = 60\frac{kOe}{\mu_B}$ [69].

In contrast, the model with concentration dependent couplings ($A = A_0 + A_1y, B = B_0 + B_1y$) gives rise to good agreement with both the average hyperfine fields and HFDs. During the process of finding the four best coupling parameters, the parameter space of A_1 is explored to see how the other three couplings vary with the parameter A_1. This leads to the errors that are quoted in the previous section (e.g. Table 7.6). Fig.7.12 shows all the parameters which make model-5 fit the average hyperfine field versus y equally well. Only the parameters corresponding to A_1 in the range of (-20 $\pm$4)$\frac{kOe}{\mu_B}$ for RQ samples, (-22 $\pm$4)$\frac{kOe}{\mu_B}$ for SQ samples can fit the HFDs in the collinear ferromagnetic Fe-Ni alloys at LHT.

The solution domain of the four best coupling parameters for SQ and RQ samples are slightly different. Nevertheless, the trends are exactly same: the different sign of A_1 and A_0, and the very different magnitude of A and B. We can conclude that in our phenomenological model, concentration dependent couplings are necessary to make both average hyperfine field and the HFDs in good agreement with the experimental results. Such composition dependent coupling parameters can be explained in the polarization mechanism of the hyperfine field or may be an artifact due to a small degree of persistent short range atomic order or some combination of the two.

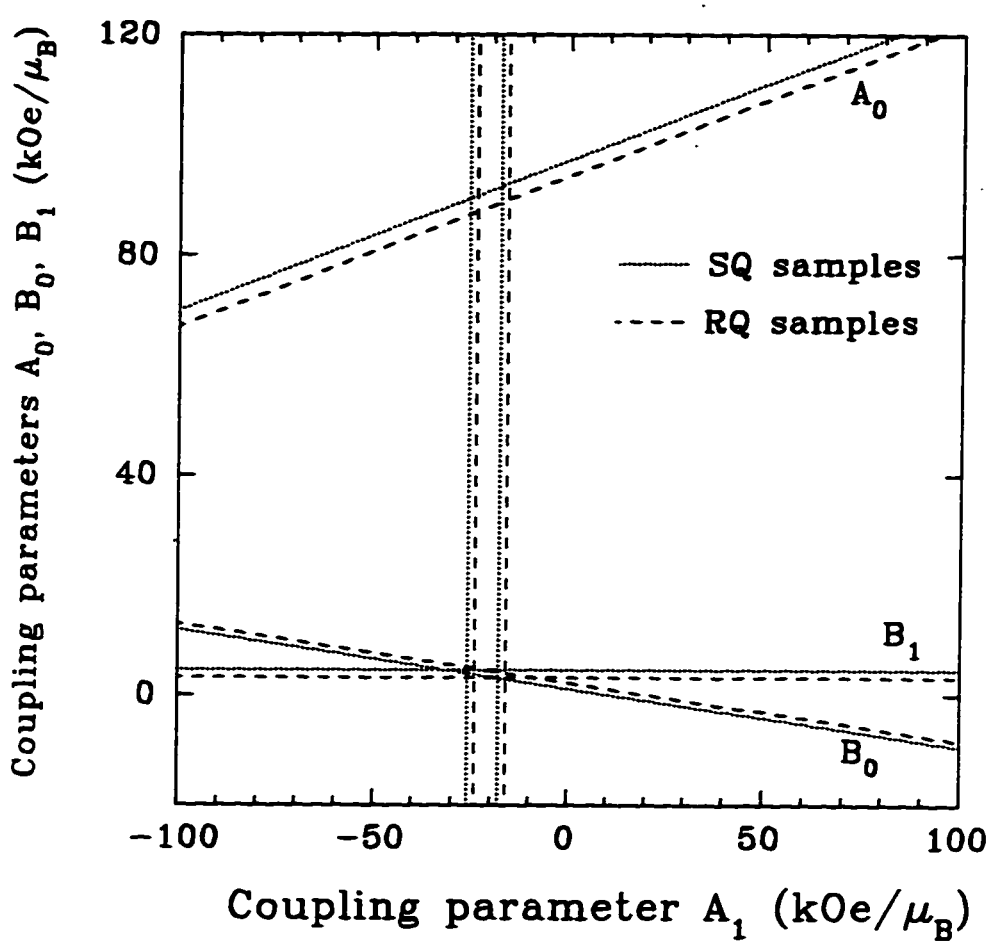

Figure 7.12: Comparison of the obtained coupling parameters for RQ and SQ samples.

7.5 Applying Model-1 for the Perfectly Random Alloys

After we have modeled the average hyperfine field versus y data in SQ and RQ samples by the concentration dependent couplings, we should also consider another possibility which attributes the curvature of the average hyperfine field versus y to the existing short range atomic order. In this case, the average hyperfine fields versus y in perfectly random collinear ferromagnetic alloys is supposed to be a straight line. This means that model-1 should be the correct model to use.

To avoid the short range order affect our modeling results, we therefore use only the average hyperfine field data at y = 0.05 and y = 0.45 to determine the constant A and B coupling parameters. Combining two equations of the average hyperfine fields with two unknown A and B, we obtain the coupling parameters $A = 88.0\ \frac{kOe}{\mu_B}$, $B = 4.62\ \frac{kOe}{\mu_B}$ for RQ samples, $A = 87.6\ \frac{kOe}{\mu_B}$ and $B = 4.73\ \frac{kOe}{\mu_B}$ for SQ samples.

This model obviously does not fit the hyperfine field data in the whole collinear ferromagnetic region (y = 0.0-0.45). However, it may be used to show the calculated HFDs in y = 0.05 and y = 0.45 RQ samples. Using these obtained A and B, HFDs are calculated. They are shown in Fig.7.13. The agreement between the calculated and the measured HFDs is not very good in these two alloys. It suggests that even in perfectly random alloys, the constant coupling model cannot fit HFDs by using binomial distribution and the phenomenological hyperfine field model. However: (1) the agreement at y = 0.05 is not bad (Fig.7.13) given the uncertainty in the measured HFD at this composition, and (2) at y = 0.45 FeNi-type atomic order may play a role. Even the disagreement at these extreme (non-$FeNi_3$) compositions (Fig.7.13) can therefore not be used to eliminate the constant coupling parameter model.

The four coupling parameter model is superior in describing both the average hyperfine fields and the HFDs of the alloys. Nevertheless, we keep in mind that there are two possible solutions for the observed curvature of the average hyperfine field versus y.

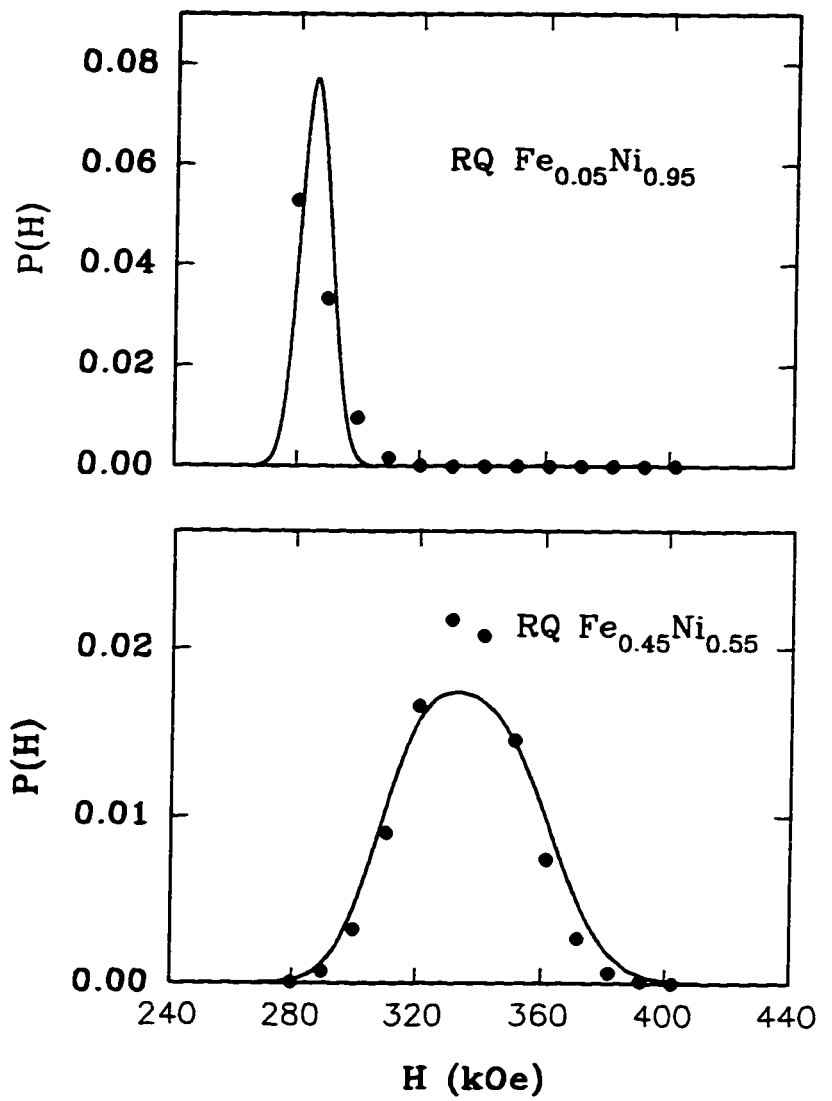

Figure 7.13 : Comparison of the calculated HFDs with the measured HFDs in the RQ samples at y = 0.05 and y = 0.45 using the obtained A and B from modeling the random alloys by the constant coupling parameter model.

Chapter 8. APPLYING THE MODELS TO LNT AND RT FOR RQ Fe_yNi_{1-y} ALLOYS AT y $\leq$ 0.45

The proposed hyperfine field phenomenological model given by Eq.3.7 is general in that it applies at any temperature. After the coupling parameters A and B are obtained from the hyperfine fields and HFDs at LHT, we extend the model to RT and LNT. By assuming that: (1) the coupling constants are independent of temperature and (2) all Fe atoms have the same thermal average moment and all Ni atoms have the same thermal atomic moment, the thermal average moments for Fe and Ni atoms ($< \mu_{Fe} >$ and $< \mu_{Ni} >$) can be obtained at any temperature by adjusting calculated hyperfine fields and HFDs to the experimental data. With the average hyperfine field and HFD given by Eqs. 3.10 and 3.11, respectively:

$$< H_k >= A < \mu_{Fe} > +12B < \mu_{Ni} > +kB(< \mu_{Fe} > - < \mu_{Ni} >)$$

$$P(H_k) = P_k(y)/(B < \mu_{Fe} > - < \mu_{Ni} >),$$

the two unknowns $< \mu_{Fe} >$ and $< \mu_{Ni} >$ are obtained by using the MINUIT package [88] to minimize the χ^2 of the HFDs.

Recall that there are two possible models for the coupling parameters A and B. One is the constant coupling model ($A = A_0, B = B_0$) from y = 0.05 and y = 0.45 alloys. The other is the four coupling parameter model ($A = A_0 + A_1 y, B = B_0 + B_1 y$) from the HFD fit. Both coupling models are considered here.

Fig.8.1 shows the calculated thermal average atomic moments of Fe and Ni species using the composition dependent couplings. The corresponding HFDs at RT are shown in Fig.8.2.

The obtained average moments $< \mu_{Fe} >$ and $< \mu_{Ni} >$ (Fig.8.1) at y < 0.45 show that (i) the obtained two average moments are very close at various compositions

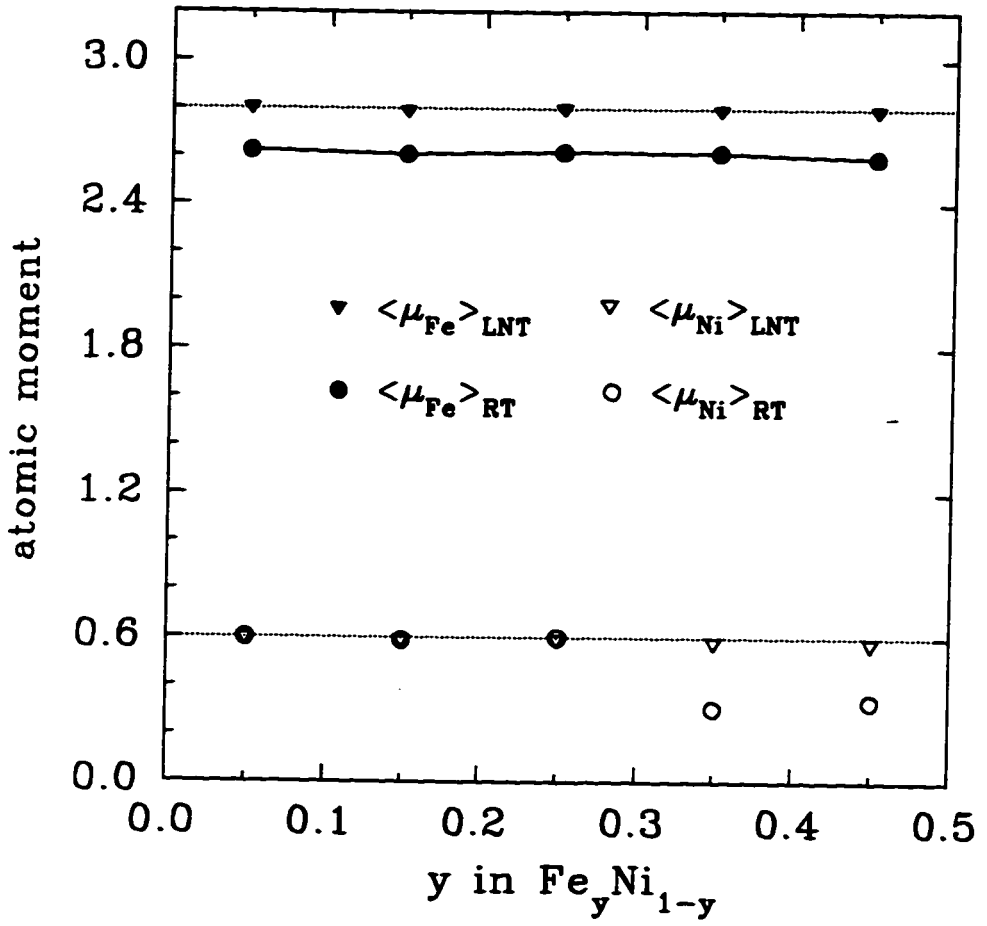

Figure 8.1: Calculated atomic moments $< \mu_{Fe} >$ and $< \mu_{Ni} >$ at RT and LNT in Fe-Ni alloys using the four coupling parameter model.

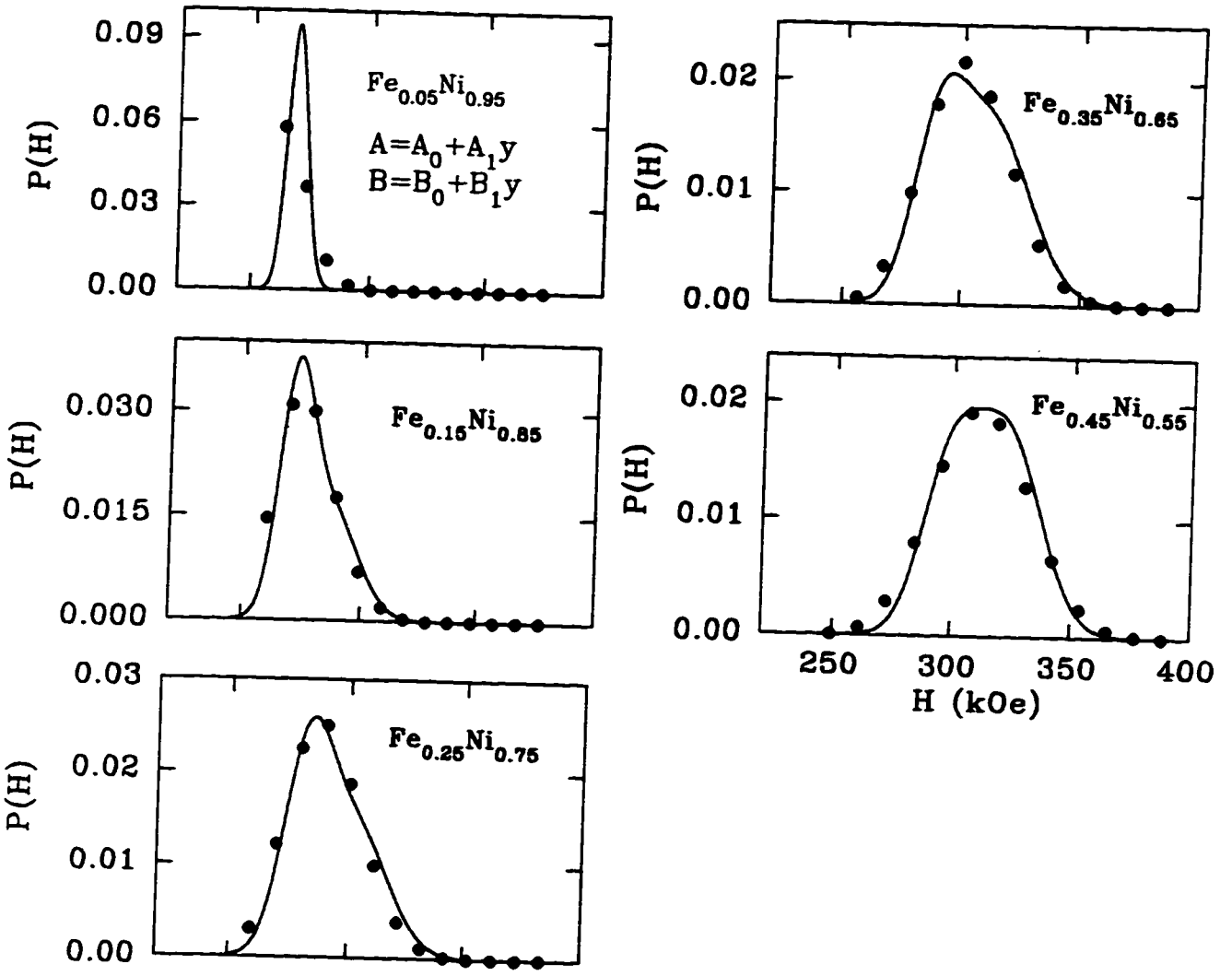

Figure 8.2: RT HFDs calculated with the four coupling parameters and the obtained $< \mu_{Fe} >$ and $< \mu_{Ni} >$ shown in Fig.8.1.

at both RT and LNT. (ii) $< \mu_{Fe} >$ and $< \mu_{Ni} >$ at LNT are both nearly at their saturation values of 2.8 μ_B and 0.6μ_B, respectively. (iii) At RT, $< \mu_{Fe} >$ drops significantly from 2.8 μ_B to about 2.6 μ_B, while $< \mu_{Ni} >$ is still at the saturation value of 0.6 μ_B. This suggests that the average Ni magnetic moment is relatively stable during the temperature change. This, later in Part III, can also be seen from the MC simulation results. Fig.8.2 shows that the calculated HFDs from the four coupling parameter model are in good agreement with the experimental data.

Similar results for the average moments $< \mu_{Fe} >$ and $< \mu_{Ni} >$ at RT and LNT can also be found for the constant coupling parameter model except that we have to freeze $< \mu_{Ni} >$ at 0.6 μ_B at y = 0.35 and y = 0.45. Otherwise, at these compositions, the fits converge to $< \mu_{Fe} > = 2.7\ \mu_B$ and $< \mu_{Ni} > = 0.3\ \mu_B$, which are very different from the moments obtained at other compositions.

In Fig.8.3 we show the calculated HFDs at RT from the constant coupling model. At y = 0.35 and y = 0.45, two calculated HFDs are shown. One is obtained with the $< \mu_{Ni} >$ free (solid dots) and the other is obtained with $< \mu_{Ni} >$ frozen (circles). We consider that the results with the Ni atomic moment as 0.6 μ_B are more physical, which can be seen later by MC simulation, the resulting HFDs in the constant coupling parameter model are not as good as those with the four coupling parameter model, especially at y = 0.35 and y = 0.45. Therefore, the model with the composition dependent couplings is in better agreement with the measured average hyperfine field and HFDs, in comparison to the results of the constant coupling parameter model. Late, these two models will be examined again by the MC simulation results in both the collinear (y $\leq$ 0.45) and iron rich (y > 0.45) region in Part III.

From the obtained atomic moments $< \mu_{Fe} >$ and $< \mu_{Ni} >$, we can also explain the observed HFD width change from LNT to RT (section 6.1). Given the probability density function $P(H_k) = P_k(y)/(B(< \mu_{Fe} > - < \mu_{Ni} >))$, when temperature changes from LNT to RT, the moment difference $(< \mu_{Fe} > - < \mu_{Ni} >)$ varies from 2.8 - 0.6 = 2.2 μ_B to about 2.6 - 0.6 = 2.0 μ_B, therefore the probability $P(H_k)$ becomes larger such that the width of the normalized distribution must decrease.

In summary, with the binomial distribution and the phenomenological model,

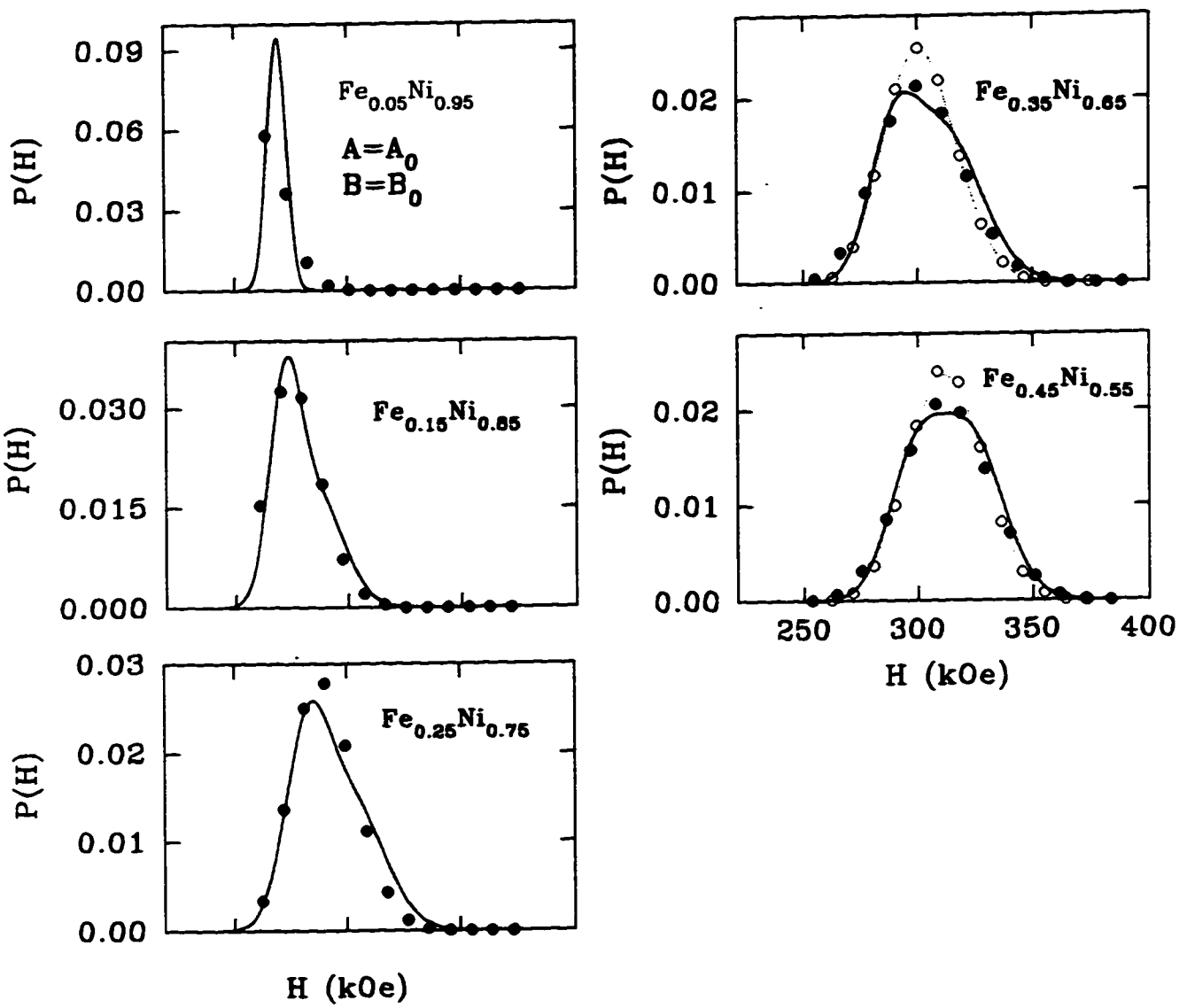

Figure 8.3: RT HFDs calculated with the best constant coupling parameters and the obtained $< \mu_{Fe} >$ and $< \mu_{Ni} >$. At y = 0.35 and y = 0.45, there are two results given. One (circles) is obtained with the $< \mu_{Ni} >$ frozen at 0.6 μ_B, the other (filled dots) is the results obtained from the fitting without any constraint which leads to $< \mu_{Ni} > = 0.3\ \mu_B$.

we can obtain the average iron and nickel moments in collinear ferromagnetic Fe-Ni alloys at any temperature, as long as we have the experimental HFDs from the spectral analysis. This provides a powerful approach for measuring the average atomic moments of different atomic species in an alloy.

Chapter 9. CONCLUSION OF PART I

A detailed Mössbauer study for SQ and RQ fcc Fe-Ni alloys was carried out at RT, LNT and LHT. A non-linear average hyperfine field versus y in the collinear ferromagnetic region ($y \leq 0.45$) is observed. With a new proposed microscopic vector hyperfine field model, the cause of the hyperfine fields and HFDs are characterized quantitatively.

Applying the hyperfine field model and the binomial distribution to hyperfine field data at LHT for $y \leq 0.45$, where the local atomic moments of Fe and Ni are known from the Slater-Pauling curve, the coupling parameters in the hyperfine field model can be obtained. Two possible causes are proposed to explain the curvature of the average hyperfine field versus y. The first one explains the curvature as an artifact of residual short range atomic order, so the average hyperfine field versus y in truly random binary alloys would be a straight line. Here, two constant coupling parameters are extracted from the hyperfine fields at $y = 0.05$ and $y = 0.45$. The other attributes the curvature to a conduction electron density dependence of the intrinsic polarization mechanism of the hyperfine field. It requires two composition dependent coupling parameters ($A = A_0 + A_1 y, B = B_0 + B_1 y$) to fit both the average hyperfine field and the HFDs. The four coupling parameters are determined by fitting the calculated HFDs to the experimental ones.

With the obtained coupling parameters, A and B, the model is applied to RT and LNT. The average atomic moments of Fe and Ni atoms are obtained by fitting the calculated HFDs to the experimental HFDs. This provides a new approach to obtain the magnetic moments by the Mössbauer spectroscopy.

Our phenomenological hyperfine field model can also be used in non-collinear ferromagnetic Fe-Ni alloys ($y > 0.45$). If the spin configuration is known at any composition, the hyperfine field for Fe atoms in a given local environment can be obtained by the vector sum of a local term and a transferred term. In Part III, we

will combine the MC simulation method and the phenomenological hyperfine field model to calculate the HFDs at all compositions of fcc Fe-Ni alloys. The proposed two models of the coupling parameters (constant and composition dependent) will be tested further in the iron rich alloys ($y>0.45$) where the difference resulting from the two coupling models is become significant. But we first use MC simulations to calculate the magnetic properties of Fe-Ni alloys in Part II, that gives an idea of how the simple local moment model works and how far we can go with the simple model. The effect of atomic order on the magnetism will be investigated and illustrated from MC simulations of simultaneous magnetic and atomic interactions in $FeNi_3$, FeNi and Fe_3Ni alloys in Part IV.

Part II

MONTE CARLO SIMULATION OF THE LOCAL MOMENT MAGNETISM IN FCC RANDOM FE-NI ALLOYS

Chapter 10. INTRODUCTION

MC simulation is a computer simulation or computer "experimental" method which has widespread applications in science [90]. It can yield information on "model systems" with specific assumptions. The purpose of it is two fold: comparing the simulation results with data from experiments on a real system where one checks the extent to which the model system approximates the real system; comparing the results with other theoretical results that start with the same model where one checks the validity of the various approximations. By MC simulation, the microscopic information on the system, both in space and in time, can be obtained. This information can be much more detailed than what is available from experiments on real systems and hence it gives insight into some problems which cannot be solved otherwise.

The MC simulation method has been applied to study magnetic properties of metallic alloy system. For example: magnetic ordering study with antiferromagnetic Ising spin interactions in an fcc system [92] and in a body centered cubic (bcc) system [93], a critical temperature study on a two-dimensional ferromagnetic binary Ising system [91], ferromagnetism in small clusters [94], and a structural phase diagram calculation of magnetic alloys [95, 96].

In this part, we apply MC simulations to study the magnetic properties of the Fe-Ni alloys. With Ising approximation of the latent antiferromagnetic local moment ($J_{FeFe} < 0$, and $J_{FeNi} > 0$ and $J_{NiNi} > 0$), the magnetic properties are calculated by the MC simulation method. By comparing the simulated results with the experimental measurements, we investigate the extent to which the simple local moment model is applicable.

Chapter 11. MC Simulation Method

11.1 Metropolis Algorithm

The algorithm we used is the Metropolis algorithm [97]. It can be used, in principle, to sample any multivariable probability density function (PDF) $f(\vec{x})$ no matter how large the dimension of $\vec{x} = (x_1, x_2, ...x_d)$. The idea is to introduce a set of one-step transition probabilities $W(\vec{x} \mid \vec{y})$ to find the system in state $\vec{x}$ at time τ, given that the system is in the state $\vec{y}$ at time $\tau - 1$. It is an important sampling method.

We restrict ourselves to kinetic processes determined only by the one step transition probabilities. Such processes are called Markov processes (chains). If $f_\tau(\vec{x})$ denotes the PDF of $\vec{x}$ at time τ, the PDF $f_{\tau+1}(\vec{x})$ at time $\tau + 1$ is given by the following Master equation:

$$f_{\tau+1}(\vec{x}) = \int d\vec{y} W(\vec{x} \mid \vec{y}) f(\vec{y}) \tag{11.1}$$

In order to find the value of each $W(\vec{x} \mid \vec{y})$ such that starting from any $f_0(\vec{x})$ we will end up into a $f_\tau(\vec{x})$ which will be a good approximation of our desired PDF $f_\tau(\vec{x}) = f(\vec{x})$. Therefore we must first ensure the desired $f(\vec{x})$ is a stationary solution. This requires the detailed balance condition:

$$W(\vec{x} \mid \vec{y}) f(\vec{y}) = W(\vec{y} \mid \vec{x}) f(\vec{x}) \tag{11.2}$$

In practice, one also needs to find experimentally the value of τ_{max} for which $f_{\tau_{max}}(\vec{x})$ approximates sufficiently $f(\vec{x})$.

Many solutions (of detailed balance) exists for $W(\vec{x} \mid \vec{y})$. To find them, $W(\vec{x} \mid \vec{y})$ is split into a trial transition probability $T(\vec{x} \mid \vec{y})$, from which a trial value will be sampled, and an acceptance probability $A(\vec{x} \mid \vec{y})$ from which we will decide if the trial value will be accepted or rejected:

$$W(\vec{x} \mid \vec{y}) = A(\vec{x} \mid \vec{y}) T(\vec{x} \mid \vec{y}) \tag{11.3}$$

Now the problem is that given the desired PDF $f(\vec{x})$, how to choose $A(\vec{x} \mid \vec{y})$, and $T(\vec{x} \mid \vec{y})$, the answer is: we just need to satisfy detailed balance. Two well defined solutions are well known. One is the Metropolis function:

$$A(\vec{x} \mid \vec{y}) = min\{1, q(\vec{x} \mid \vec{y})\} \tag{11.4}$$

The other is given by:

$$A(\vec{x} \mid \vec{y}) = \frac{q(\vec{y} \mid \vec{x})}{1 + q(\vec{x} \mid \vec{y})} \tag{11.5}$$

where $q(\vec{x} \mid \vec{y})$ is defined as:

$$q(\vec{x} \mid \vec{y}) \equiv \frac{T(\vec{y} \mid \vec{x}) f(\vec{x})}{T(\vec{x} \mid \vec{y}) f(\vec{y})} = \frac{1}{q(\vec{y} \mid \vec{x})} \tag{11.6}$$

It can be proved that the two solutions for $A(\vec{x} \mid \vec{y})$ satisfy detailed balance for any choice of $T(\vec{x} \mid \vec{y})$. In the case of our MC simulation for a for canonical ensemble, we use the one defined by Eq.11.5: and

$$q(\vec{x} \mid \vec{y}) = \frac{T(\vec{y} \mid \vec{x})}{T(\vec{x} \mid \vec{y})} e^{-(H(\vec{x}) - H(\vec{y}))} \tag{11.7}$$

$T(\vec{y} \mid \vec{x})$ is chosen as a normalized uniform distribution for simplicity. Hence, the Metropolis algorithm for sampling according to $f(\vec{x})$ can be written as:

(a) Initialization: choose $T(\vec{y} \mid \vec{x}), A(\vec{y} \mid \vec{x}), \tau_{max} \cdots\}$

(b) Repeat τ_{max} times:

(i)sample ξ according to $T(\vec{x} \mid \vec{x}_\tau)$

(ii) If $\xi \leq A(\vec{x} \mid \vec{x}_\tau)$ then set $\vec{x}_{\tau+1} = \vec{x}$

(iii)Else set $\vec{x}_{\tau+1} = \vec{x}_\tau$

(iv)set $\tau = \tau + 1$ }

(c) Return $\vec{x}_{\tau_{max}}$

11.2 Modeling System

To simulate the fcc Fe-Ni alloys with the latent antiferromagnetism model, we first set up a fcc lattice with periodic boundary conditions. For simplification, we disregard both the lattice vibrations and elastic strains and also do not allow vacancies,

interstitials or other lattice defects. Fe and Ni atoms are placed randomly on the sites of the lattice. The lattice size for Fe-Ni alloys is chosen as 10×10×10 conventional fcc unit cells, which corresponds to 4000 atoms. Each atom possesses a constant magnitude of magnetic moment or spin number: S(Fe) = 1.4 and S(Ni) = 0.3 according to the saturation moment from the Slater-Pauling curve. All the spin moments are only allowed orientations in two directions (up and down), by the Ising approximation, and only the nearest neighbour (NN) interactions are taken into account. The Hamiltonian of the system is written as:

$$\mathcal{H} = -\sum J_{ij}\vec{S}_i \bullet \vec{S}_j \tag{11.8}$$

where the sum is over all NN pairs of the whole lattice. J_{ij} is the magnetic exchange parameter between atom i and atom j. There are three such exchange parameters in the Fe-Ni alloy system: J_{FeFe}, J_{NiNi}, and J_{FeNi}. These are the only parameters we adjust to make the simulated properties agree with the measurements. Mean field theory (MFT) calculation [98] for the same properties of the alloys provides three best J_{ij} parameters, called best MFT J values, which are J_{FeFe} = -20 K, J_{NiNi}= 405 K and J_{FeNi} = 280K. They are selected as our starting parameters.

11.3 Algorithm of the Simulation Program and Accuracy Consideration

The MC simulation algorithm is given as:

(1) Set up lattices. Initial spin directions for Ni atoms are all up. The direction for Fe atoms are randomly put in either up or down orientations

(2) Repeat τ_{max} times:

(i) Select one lattice site i at which the spin S_i is considered for flipping ($S_i \rightarrow -S_i$).

(ii) Compute the energy change ΔE associated with that flip.

(iii) Calculate the transition probability $T = \frac{e^{-\Delta E/k_BT}}{1+e^{-\Delta E/k_BT}}$ for that flip.

(iv) Draw a random number ξ uniformly distributed between zero and one.

(v) If $\xi \leq T$, flip the spin, otherwise do not.

(vi) Return

(3) Analyze the resulting configuration as desired and store its properties to calculate the necessary averages.

In implementing this algorithm, some details need to be considered. (i) Before calculating the physical properties, one must make sure that the system is in an equilibrium state. Therefore, τ_{max} MC steps were accomplished before analyzing the physical properties of the system. (ii) Since the subsequent states differ only by a single flip, their physical properties are correlated. Step-3 is only carried out after a time interval τ to get rid of the correlation of two subsequent states. Both the τ_{max} and the correlation time τ are determined by trial and error.

In order to assure the system reaches the equilibrium state, the simulated properties are first calculated as a function of the number of MC steps, from which τ_{max} is obtained. Here, one MC step means that every atom on average is visited once. In our calculation, $\tau_{max} = 1000$ MC steps are used for the simulated magnetic properties.

The correlation time τ is obtained by estimating the auto-correlation function:

$$C_g(\tau) \equiv < g(\vec{s_{\tau+i}})g(\vec{s_i}) > - < g >^2 \tag{11.9}$$

where $g(\vec{s})$ is a simulated property like the magnetization or energy. $C_g(\tau)$ is run as a function of the number of MC steps, and τ is chosen such that $C_g(\tau) = 0$. $\tau =$ 30 to 50 is chosen in our calculations.

Once τ_{max} and τ are obtained, we start sampling each uncorrelated $\vec{S_\tau}$, and compute the properties $\bar{g}$ by:

$$\bar{g_n} = \frac{1}{n}\sum_1^n g(\vec{S_{i\tau}}) \tag{11.10}$$

For most properties, we use a total 10^4 to 10^5 MC steps in our simulation. The uncertainty for the computed properties, estimated by $\sigma = < g^2 > - < g >^2$, are about 1% to 2 %.

Two programs are used in this part. "CARLO8.FOR" is the program to calculate the magnetization as a function of temperature, with no external magnetic field

applied on the system. It reads in three NN magnetic exchange constants J_{ij} and output the magnetization as a function of temperature. "MONT4.FOR" is the program used to calculate the magnetization at T = 0 K as a function of the applied field. Both are given in Appendix B as B-1 and B-2.

Chapter 12. Results and Discussion

12.1 Finite Size Effects

Different lattice sizes have been tested for finite size effects. In simulation of the spontaneous moment of the alloys at different temperatures, N = 5, 8, 10, 15, 20 (corresponding to 500, 2048, 4000, 13500, 32000 atoms, respectively) are selected. The results are shown in Fig. 12.1. It is found that the lattice size for N>8 does not change the calculated properties very much. Here, only the smallest size (N = 5) gives a significantly different result on the moment where finite size effects are present in the form of lingering tails on the high temperature side of the Curie point.

In our MC simulations, we choose N = 10 for all of the simulations. In such case, the finite size effects are not significant in the MC results.

12.2 Temperature-composition Magnetic Phase Diagram

The Curie points T_C are obtained from spontaneous magnetization versus temperature. Fig.12.2 shows comparisons between the measured T_C versus composition and those obtained from MC simulations for three sets of the J parameters: (1) best MFT J's: J_{NiNi} = 405 K, J_{FeNi} = 280 K, J_{FeFe} = -20 K. (2) the same J values except that the value of J_{NiNi} is increased in order to give the correct T_C for pure nickel: J_{NiNi} = 700 K, J_{FeNi} = 280 K, J_{FeFe} = -20 K. (3) the J values that gives the best agreement with the measured Curie points at lower Fe concentrations: J_{NiNi} = 700K, J_{FeNi} = 355 K, J_{FeFe} = -25 K. The latter J values are hereafter referred to as "the best MC J values" and are used below to calculate the other magnetic properties.

One first notes that, as expected, MFT overestimates the values of T_C for given

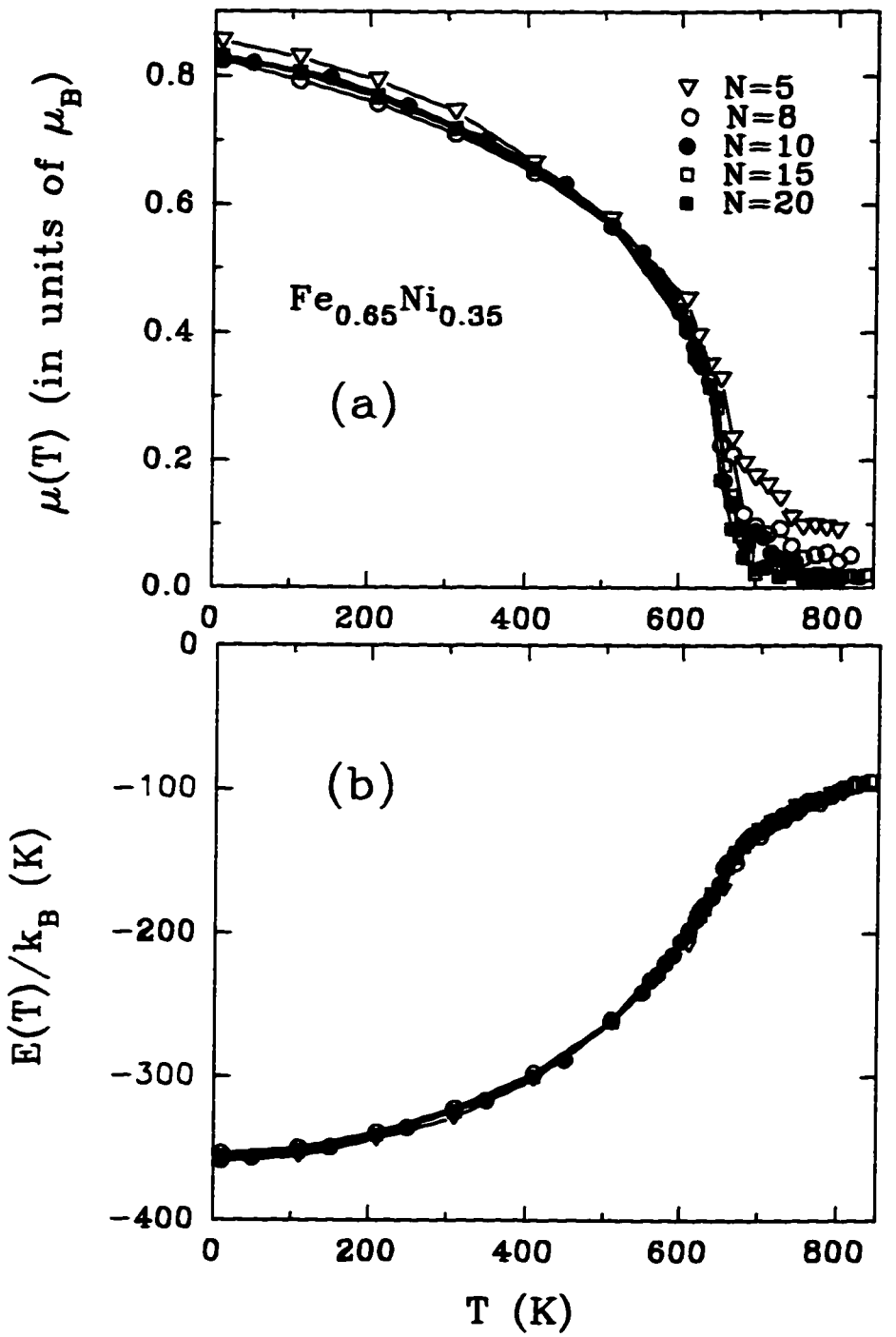

Figure 12.1 : Example of lattice size effects. Spontaneous (zero field) moment per atom versus temperature for $Fe_{0.65}Ni_{0.35}$ alloy simulated using different lattice sizes (N×N×N), as indicated, and with periodic boundary conditions.

J values. Equivalently, the best MFT J values obtained by comparison with experiment are underestimates. On the other hand, similar to the MFT results, it is noticed that the experimentally observed sharp drop in T_C that occurs at high Fe concentrations as Fe content is increased is not reproduced by using the same J parameters at all the compositions, although the overall agreement is better than in the MFT calculation. The remaining disagreement may be due to such factors as: the Ising approximation, longer range exchange interactions, chemical clustering in Fe-rich alloys, and composition dependent J values, inaccurately measured T_Cs due to atomic ordering effects, magnetovolume coupling, etc. [98].

Finally, we note that at the lower Fe concentrations the T_Cs obtained from MC are related to the MC magnetic energy per atom at T = 0 K as: $T_C \simeq$ -1.65 E_0/k_B, where k_B is Boltzmann's constant. This is shown in Fig.12.3 where the measured and calculated T_Cs and -1.65 E_0/k_B are shown together versus composition for the case J_{NiNi} = 700K, J_{FeNi} = 355 K, J_{FeFe} = -25 K. The simple relationship breaks down as Fe content increases and as the number of unsatisfied (frustrated) exchange bonds also increases. By comparison, MFT of a single component ferromagnet with near neighbor Heisenberg exchange and ionic spin S gives:

$$T_C/E_0 = -Z(S+1)/(3k_B N_a S) \tag{12.1}$$

where z is the number of near neighbors and N_a is the number of exchange bonds per atom. N_a = 6 and z = 12 in fcc structure such that, for pure Ni, $k_B T_C/E_0$ = -2.89.

12.3 Spontaneous Saturation Moments Versus Composition (Slater-Pauling curve)

The spontaneous saturation moment, μ_0, is the average moment per atom at T = 0 K and H = 0. As we know in the local moment model, the fact that the average moment deviates from the Slater-Pauling curve in the iron rich region is interpreted as resulting from spin flip due to the antiferromagnetic Fe-Fe exchange interaction. This can be tested by MC simulations. Fig.12.4(a) shows the measured

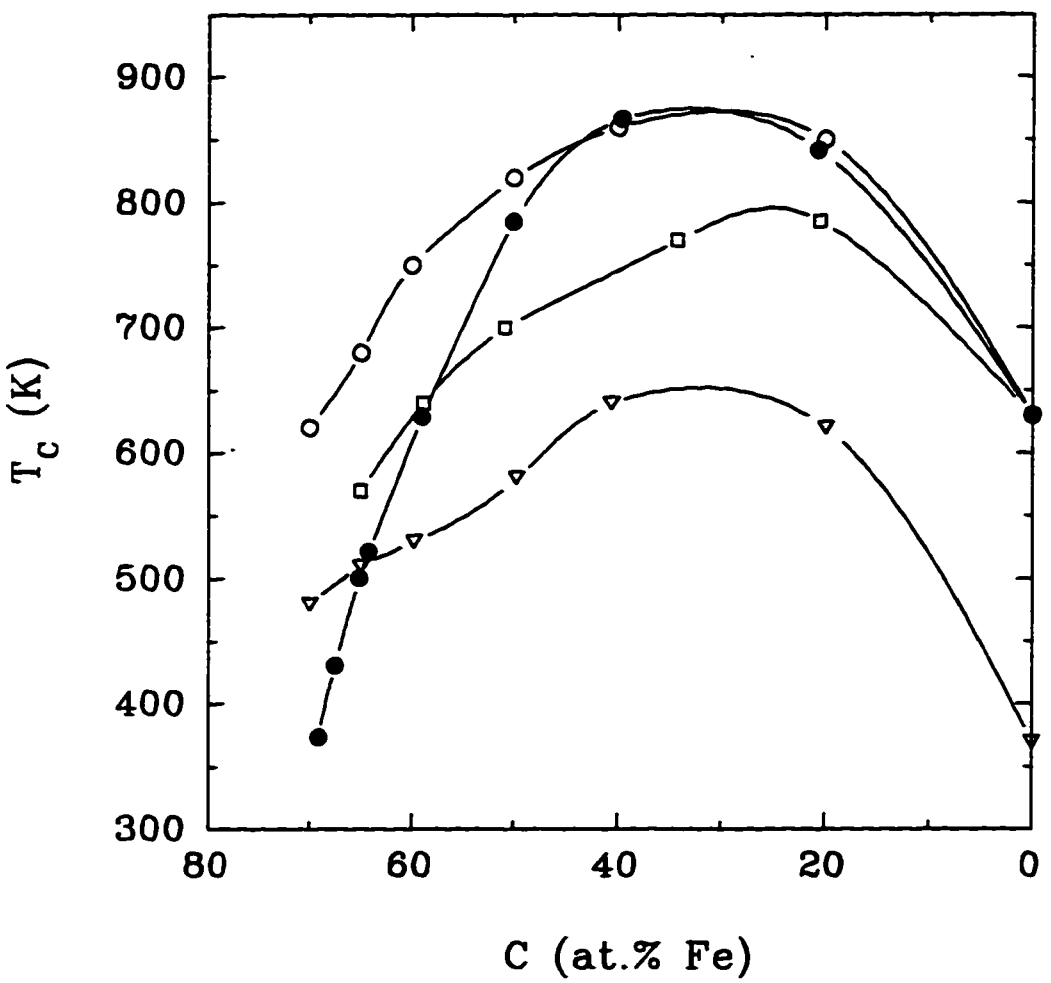

Figure 12.2 : Calculated Curie points versus composition for three sets of J values (open symbols) compared to the measured Curie points from [7] (filled circles). J_{NiNi} = 405 K, J_{FeNi} = 280 K, J_{FeFe} = -20 K, open triangles; J_{NiNi} = 700 K, J_{FeNi} = 280 K, J_{FeFe} = -20 K, open squares; J_{NiNi} = 700 K, J_{FeNi} = 355 K, J_{FeFe} = - 25 K, open circles.

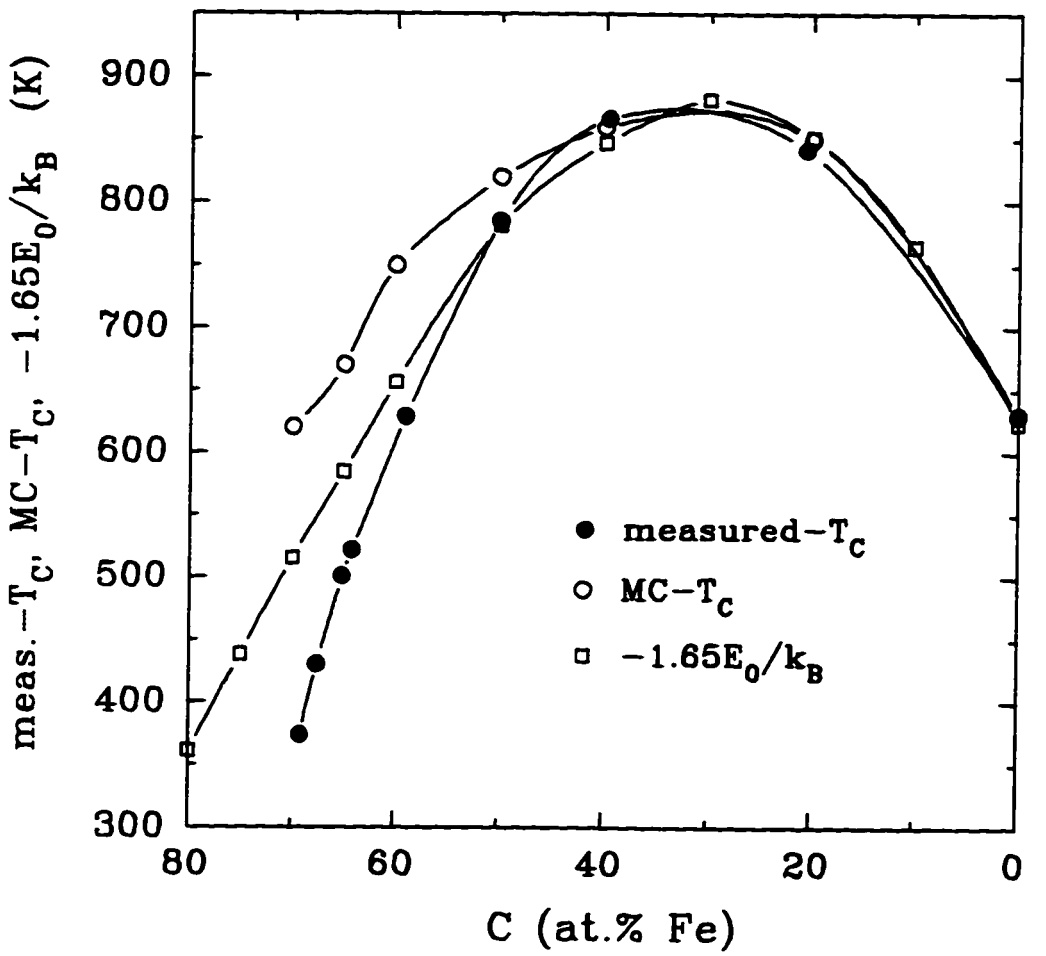

Figure 12.3 : Rescaled MC zero field magnetic energy per atom at T = 0 K, - $1.65E_0/k_B$, versus composition compared to the MC T_C for the best MC J values (J_{NiNI} = 700 K, J_{FeNi} = 355 K, J_{FeFe} = - 25 K) and the measured T_C [7].

μ_0 at various compositions compared to the MC μ_0s for the best MC J values and two other values of J_{FeFe}. Fig.12.4(b) shows the same data, but expressed as deviations from the Slater-Pauling curve. It is seen that with the local moment model and antiferromagnetic Fe-Fe exchange, we indeed observe the moment deviation from the Slater-Pauling curve. The magnitude of the deviation depends on the magnitude of the antiferromagnetic bond strength. The general features of the MC results agree with the experimental results, but quantitatively, it is not good in the iron rich region. This, as described above, may be due to the fact that we use the same J values over all the compositions.

A problem is posed when comparing with measurements made in non-zero applied fields and extrapolated to zero applied field if frustrated spins are present. Frustrated spins are those with orientations ($\pm$) that do not affect the zero-zero field magnetic energy: They have no energetic preference to point up or down. At T = 0 K, any non-zero applied field (always applied along the Ising axis in the MC simulations) will align all the frustrated spins. However, at zero applied field, the frustrated spins have random up and down orientations. It is therefore important that, when the MC μ_0 is to be compared with the measured μ_0, it be simulated with a small field that is large enough to align all the frustrated moments but not large enough to affect any of the other moments.

In the real alloys, true frustration probably does not occur because of magnetovolume coupling that causes local lattice distortions that stabilize particular spin configurations in the neighborhood of otherwise frustrated moments. Assuming that such magnetovolume distortions cause frustrated spins to point down gives an upper bound on the deviation from the Slater-Pauling curve whereas assuming that the otherwise frustrated spins point up is equivalent to the above small applied field calculation and gives lower bound on the deviation. In this way, the MC simulations give two bounds on μ_0:

$$\mu_0 = \mu_{sat} - 2f_d(2.8\mu_B) \tag{12.2}$$

and

$$\mu_0 = \mu_{sat} - 2(f_d + f_f)(2.8\mu_B) \tag{12.3}$$

where μ_{sat} is given by the Slater-Pauling curve, f_d is the fraction of the total moments that are down spins (at H = 0, and not counting frustrated spins that are accidentally down), and f_f is a fraction of the total moments that are frustrated spins (at H = 0 and with no magnetovolume coupling). Eq.12.2 corresponds to the case with the frustrated moments taken to point up whereas Eq.12.3 assumes that they point down. Within the context of simple local moment models that do not consider magnetovolume coupling, the relevant prediction for μ_0 is half way between the above upper and lower bounds:

$$\mu_0 = \mu_{sat} - (2f_d + f_f)(2.8\mu_B) \tag{12.4}$$

because the frustrated spins have zero averages.

Fig.12.5 shows the f_d and f_f as a function of composition for both the best MC J values and the best MFT J values. This enables one to ascertain the number of spins involved in causing the deviations from Slater-Pauling behaviour and to ascertain the importance of frustration in Fe-Ni alloys. Note that a significant number of frustrated moments occur with the best MFT J values (J_{NiNi} = 405 K, J_{FeNi} = 280 K, and J_{FeFe} = -20 K). For other selected J values, only Fe moments with 12 Fe near neighbors of which 6 are down and 6 are up are frustrated. The corresponding f_f are so small that the upper and lower bounds on μ_0 are indistinguishable.

12.4 Spontaneous Magnetization Versus Temperature

As mentioned previously, one of the Invar anomalies is the flattened spontaneous magnetization. With the same MC best J values, we simulate spontaneous magnetization at different temperatures for essentially the same compositions as in the measurements [7], using program CARLO8.FOR. The results are shown in Fig.12.6. Curie points can be extracted from such curves with an error of ± 5 K (or 1 %) of typical Curie points. Here the frustrated spins are simply treated by MC averaging

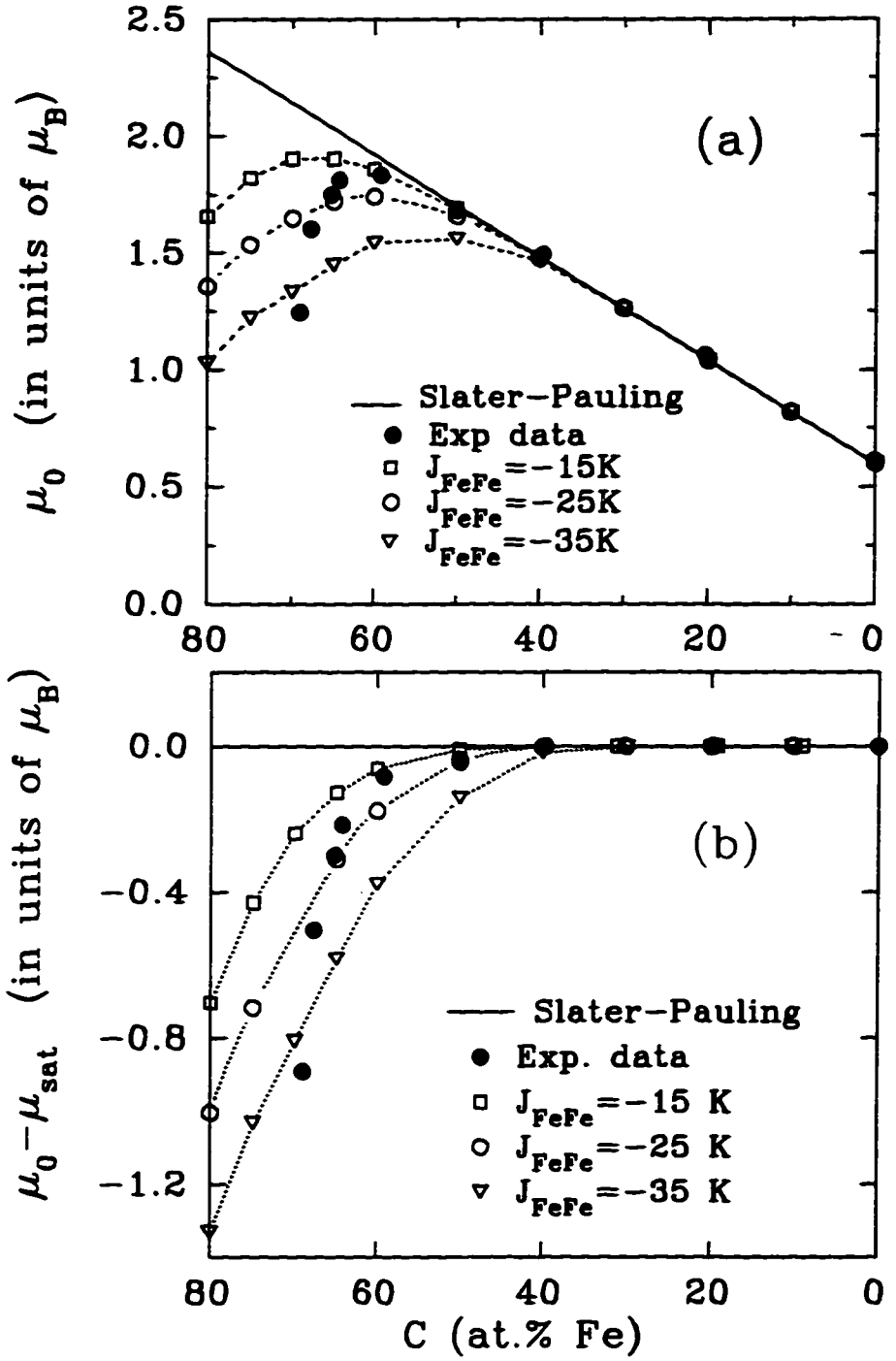

Figure 12.4 : (a)Calculated spontaneous saturation moments per atom (T = 0 K, H = 0) versus composition for J_{NiNi} = 700 K, J_{FeNi} = 355 K, and three different values of J_{FeFe}, as indicated, compared to the measured values [7] and the Slater-Pauling line. (b) The same calculated and measured saturation moments as in (a) expressed as deviations from the Slater-Pauling line.

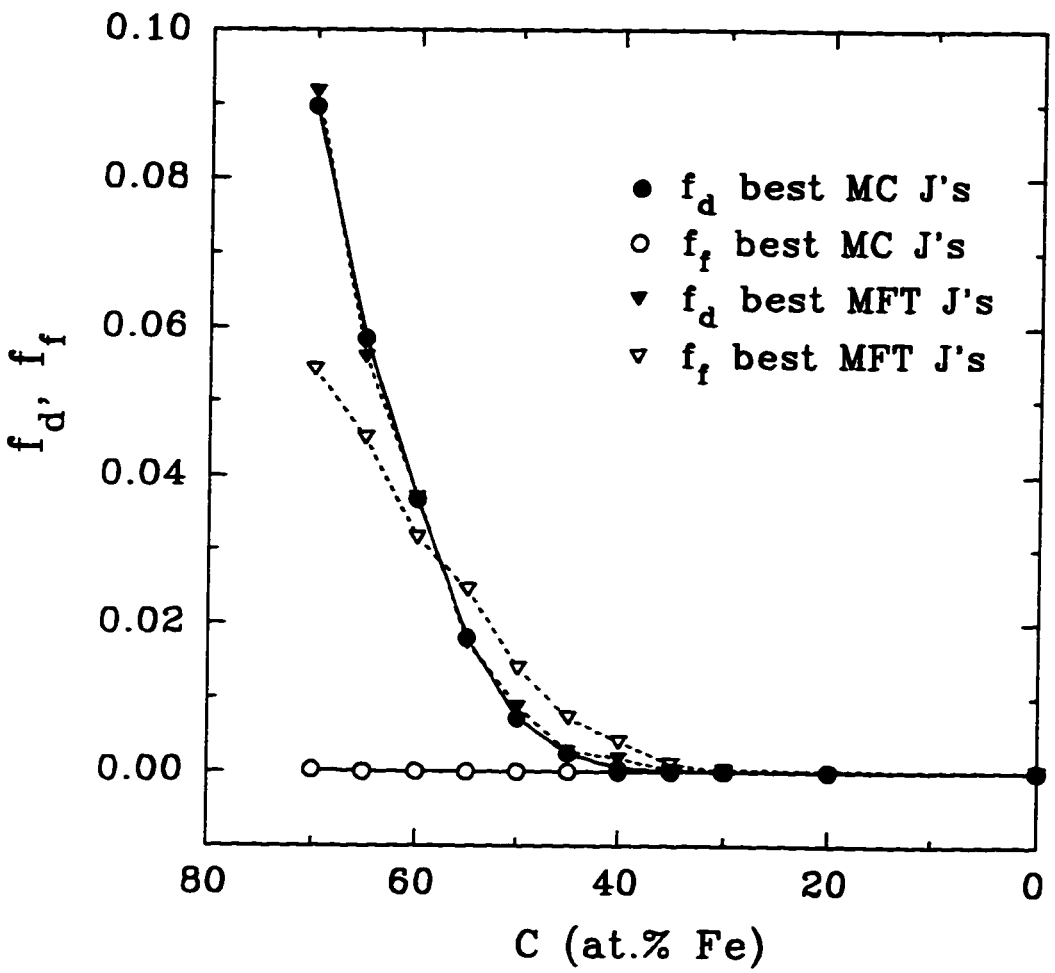

Figure 12.5 : Fraction, f_d, of the total number of moments that are down spins (at H = 0 and not counting frustrated spins that are accidentally down) and fraction, f_f, of the total number of moments that are frustrated spins (at H = 0 and with no magneto-volume coupling) as functions of composition and for two sets of J values: best MC Js and best MFT Js.

like all the other spins, and the spins that are frustrated at T = 0 K, in general, are not frustrated at higher temperatures.

The corresponding curves of magnetic energy per atom versus temperature, $E(T)/k_B$, are shown in Fig.12.7 where the fact that T_C and E_0 are correlated is illustrated again. These curves can be used to obtain the magnetic specific heat, $c_m(T)$, since $c_m(T) = \frac{\partial E(T)}{\partial T}$. The maximum in $c_m(T)$ give the same Curie points as those obtained from the magnetization versus temperature curves. Fig.12.7 shows that significant (i.e., beyond finite size effects) magnetic short range order persists above T_C, unlike in the MFT calculation where such short range order is not admitted and artificially large T_Cs are obtained instead.

Fig.12.8 shows the MC normalized spontaneous sample magnetization, $\mu(T)/\mu_0$ versus T/T_C for the best J values at various compositions. To compare with the measurement, spontaneous magnetization data from Crangle and Hallam [7] are presented in Fig.12.9. On the other hand, MFT results for the same property using the best MFT J values are shown in Fig.12.10 [98]. It is noticed that the agreement between the MC results and the data are much better than that using MFT. The curves are flattened at iron rich compositions, as they should be, but much less than in the MFT case. MFT probably exaggerates the flattening by giving overly large Curie points [98]. That is, MFT is known to overestimate T_C whereas it gives reasonable low temperature behavior. These facts are consistent with overly flattened $\mu(T)/\mu_0$ versus T/T_c curves. The artificially large Curie points of MFT in disordered alloys that have regions of strong exchange coupling are a direct consequence of neglecting fluctuations, just as are predicted non-zero ordering temperatures in low-dimensional magnets.

12.5 High-field Susceptibility at T = 0 K

When the magnetization of Fe-rich fcc Fe-Ni alloys is measured at low temperatures in varying high magnetic fields, one finds that beyond technical saturation (with all non-aligned domains driven out) there is a monotonic increase with increasing applied field, to the highest fields used [38, 99]. To first order, this increase is

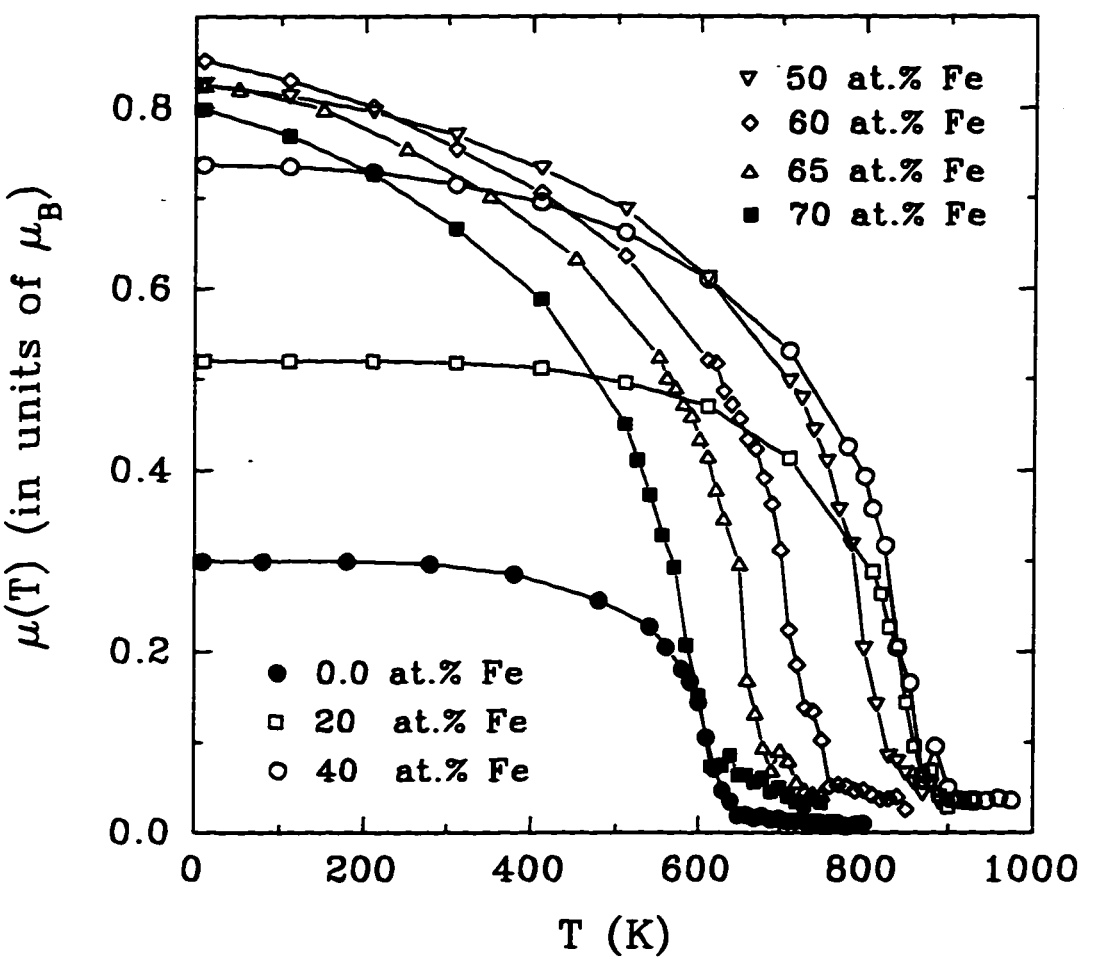

Figure 12.6 : MC spontaneous sample magnetization per atom in units of μ_B versus temperature for various compositions, as indicated, using the best MC J values.

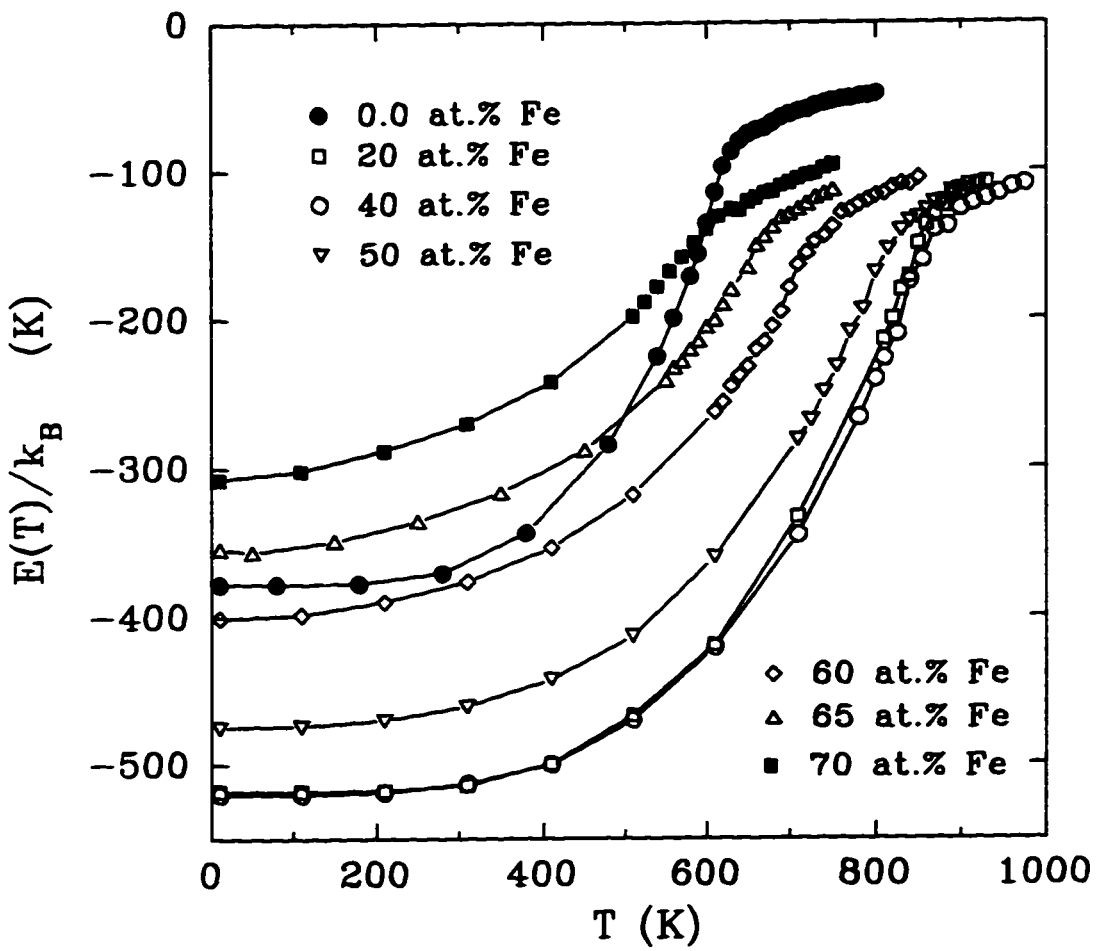

Figure 12.7 : MC zero field magnetic energy per atom versus temperature for various compositions, as indicated, using the best MC J values.

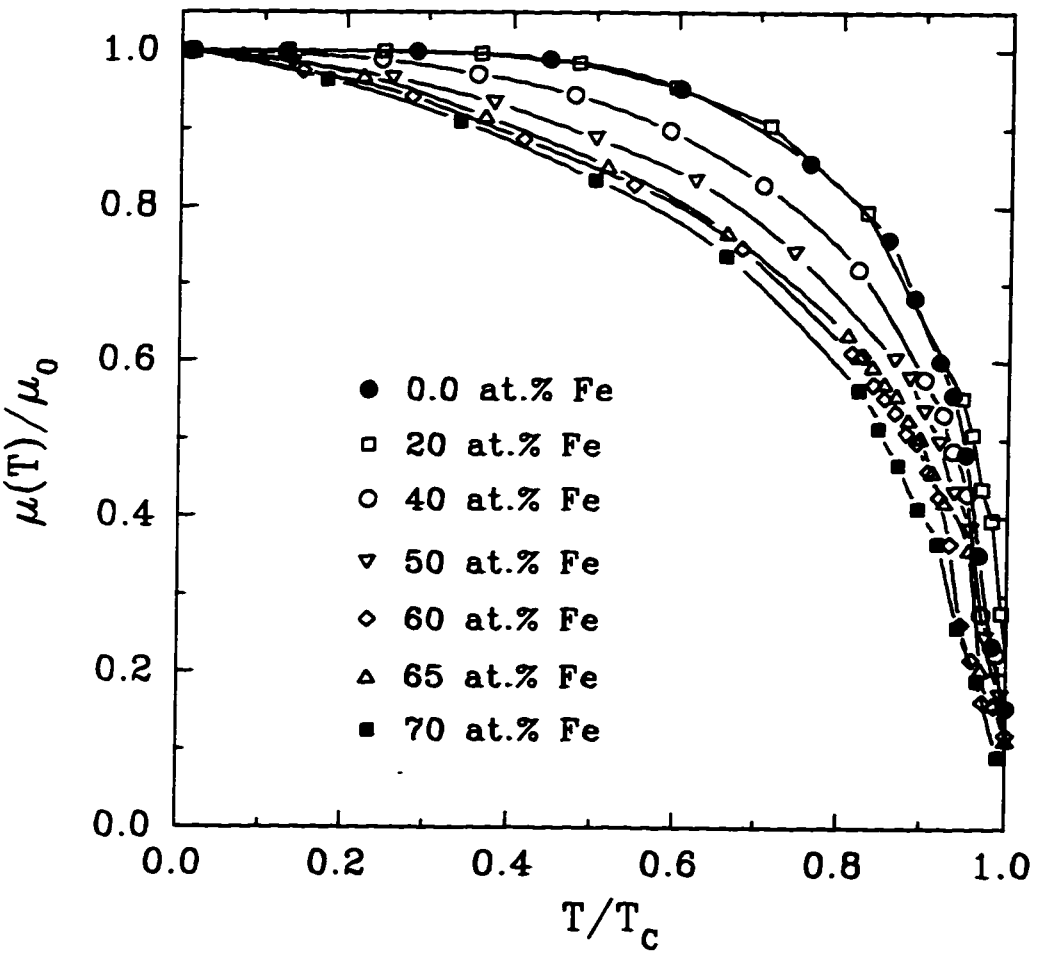

Figure 12.8 : MC normalized spontaneous sample magnetization, $\mu(T)/\mu_0$, versus T/T_C using the best MC J values, and for various compositions, as indicated

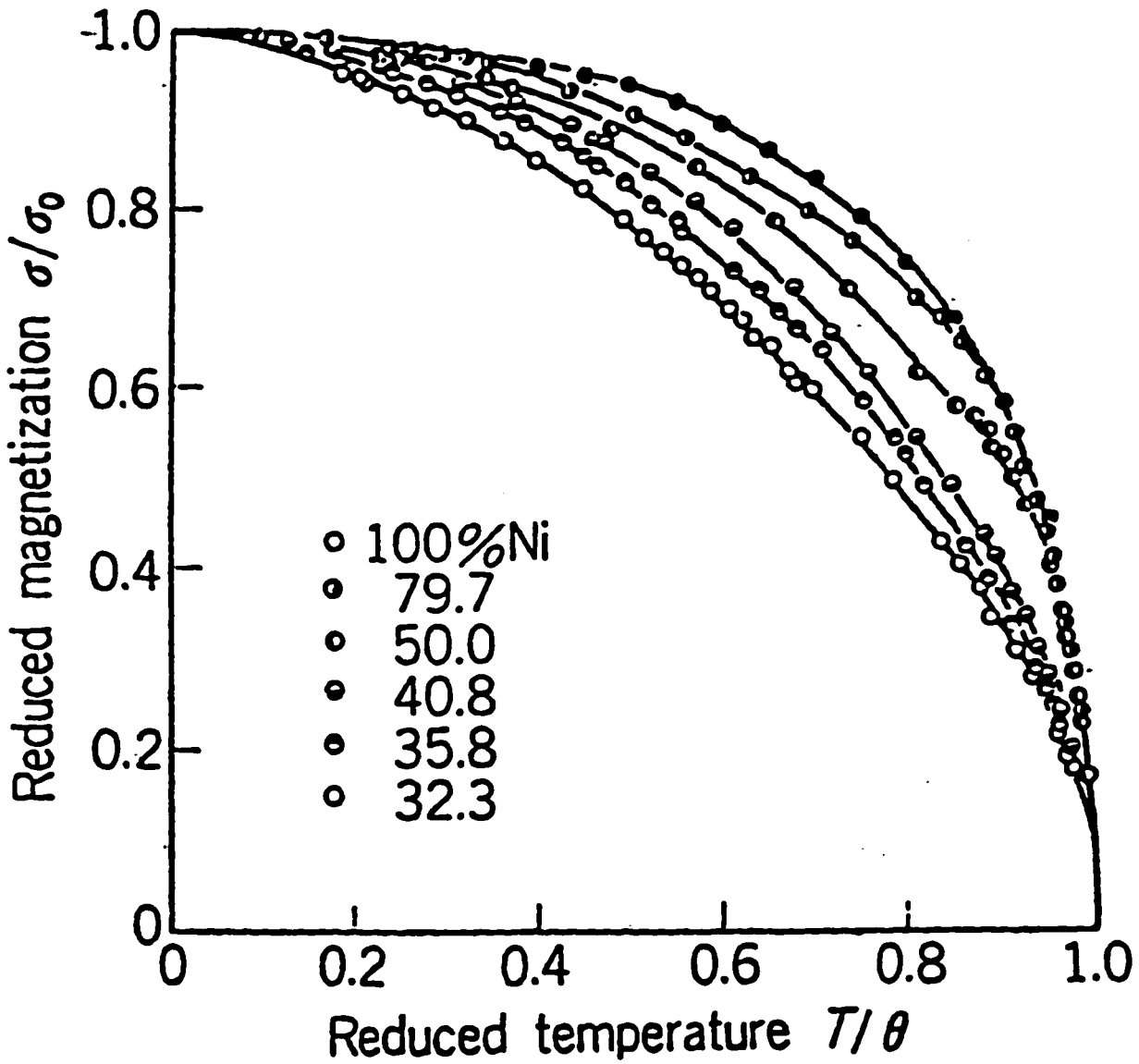

Figure 12.9 : Experimental results of $\mu(T)/\mu_0$ versus T/T_C at various compositions from the measurements [7].

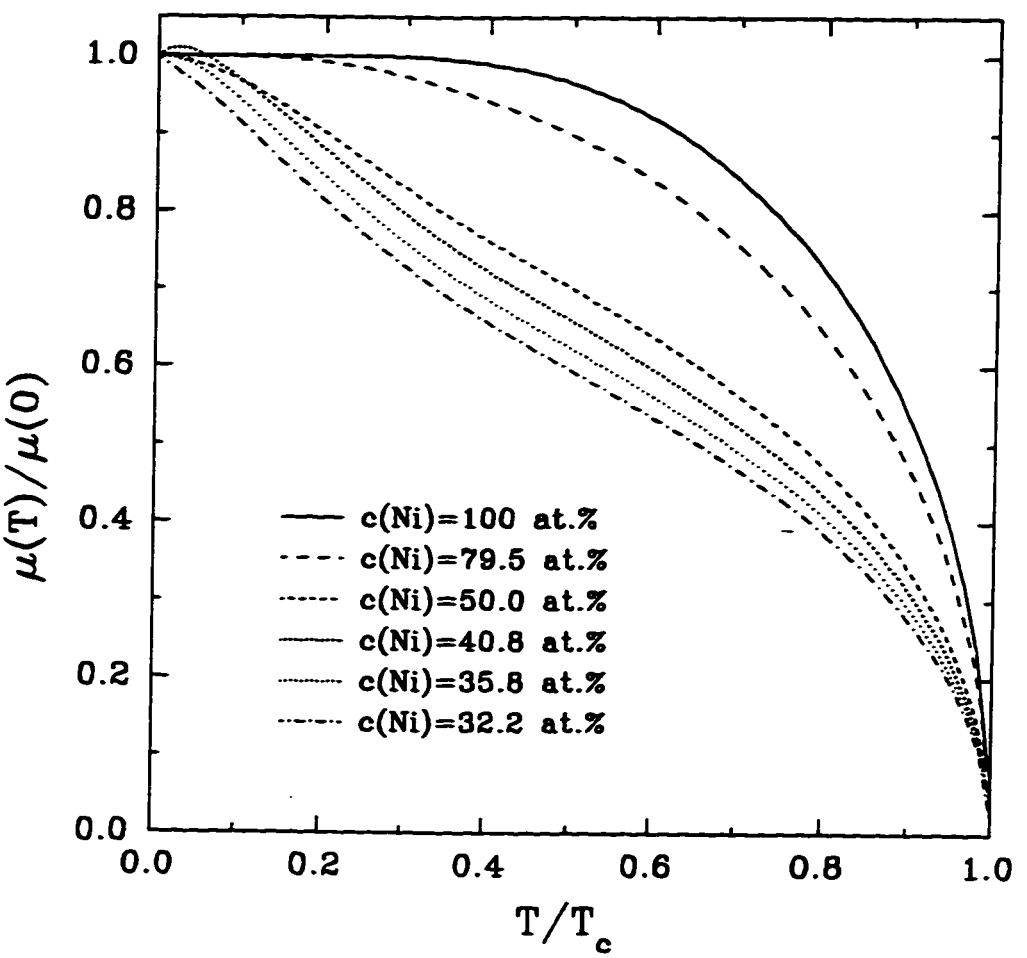

Figure 12.10 : MFT normalized spontaneous sample magnetization, $\mu(T)/\mu_0$, versus T/T_C using best MFT J values [89] and for various compositions, as indicated.

linear. It has become practice to define the high-field susceptibility (above technical saturation) as the slope $\Delta M/\Delta H$ and to refer to it as the paraprocess susceptibility, χ_p. Values of χ_p extrapolated to T = 0 K (or measured at T = 4.2 K) are found to be near zero at high Ni contents (as with all ordinary ferromagnets), to start increasing at $\sim$ 40 at.% Fe, and to reach a value as high as $\sim$ 0.004 μ_B/atom-Tesla at y = 0.70 which is the stability limit for the fcc structure.

For comparison, we calculate the sample and thermal average moment at T = 0 K as a function of applied field, $\mu_0(H)$, from MC simulation using "MONT4.FOR" given in Appendix A: A-2. It is normalized using the true saturation value defined as $\mu_{sat} = g\mu_B S_{sat} = g\mu_B[(1-y)S_{Ni} + yS_{Fe}]$ where y is the concentration of Fe, which is the moment value given by the Slater-Pauling curve. The saturation field, H_{sat}, is defined as the field at which true saturation is first obtained with increasing field.

Fig.12.11 shows the average moment at T = 0 K as a function of applied field, $\mu_0(H)$, normalized by the true saturation moment, μ_{sat}, for the best J values at various compositions. Here $\mu_0(0) = \mu_0$ as given by Eq.12.4, is in equilibrium and in the limit of large sample size. As seen in Fig.12.11, each abrupt step in a given $\mu_0(H)$ curve is due to a population of Fe moments that have ϵ Fe near neighbors of which η point down on the low field side of the step and up on the high field side. With the spins of 1.4 and 0.3 for Fe and Ni, respectively, the spin flop field for a given such population is a simple function of ϵ and η:

$$H_{sf}(\epsilon,\eta) = [0.7(2\eta - \epsilon)J_{FeFe} - 0.15(12-\epsilon)J_{NiFe}]/\mu_B \qquad (12.5)$$

where $J_{FeFe} < 0$. The magnitude of each spin flop step depends on the particular population, $f(\epsilon,\eta)$, expressed as a fraction of the total number of moments:

$$\Delta\mu_0(H_{sf}) = \mu_0(H_{sf}+h) - \mu_0(H_{sf}-h) = 2(2.8\mu_B)f(\epsilon,\eta) \qquad (12.6)$$

Table 12.1 gives all the values of $H_{sf}(\epsilon,\eta)$, associated $f(\epsilon,\eta)$ and $\Delta\mu_0(H_{sf})/\mu_{sat}$ values for $Fe_{0.65}Ni_{0.35}$ alloy with the best MC J values. Therefore, the features in the corresponding curve in Fig.12.11 can be understood in detail. The saturation

Table 12.1: $H_{sf}(\epsilon,\eta), f(\epsilon,\eta)$ and $\Delta\mu_0(H_{sf})/\mu_{sat}$ at 65 at.% Fe

ϵ	η	$H(\epsilon,\eta)$(Tesla)	$f(\epsilon,\eta)$	$\Delta\mu_0(H_{sf})/\mu_{sat}$)
10	0	101.97	0.01275	0.0352
10	1	49.87	0.01950	0.0538
11	0	207.30	0.00225	0.0062
11	1	155.20	0.00650	0.0179
11	2	103.09	0.00650	0.0179
11	3	50.98	0.00350	0.0097
12	0	312.60	0.00025	0.0007
12	1	260.52	0.00025	0.0007
12	2	208.41	0.00100	0.0028
12	3	156.30	0.00125	0.0034
12	4	104.20	0.00025	0.0007
12	5	52.10	0.00050	0.0014
12	6	0.00	0.00000	0.0000

field, H_{sat}, is simply the highest spin flop field, occuring when $\epsilon = 12$ and $\eta = 0$. As in [98], the calculated average paraprocess susceptibility can be defined as:

$$\chi_p = [\mu_0(H_{sat}) - \mu_0(0)]/H_{sat} \tag{12.7}$$

However, $\mu_0(0) \equiv \mu_0$ has three calculated values: the value straight from the zero-field MC simulation (Eq.12.4) and upper and lower bounds (Eq.12.2 and Eq.12.3) that arise from considering how the frustrated moments would behave if magnetocrystalline coupling was included in the model. This leads to the simple MC value and upper and lower bounds for the predicted average paraprocess susceptibility. These are compared to the measured χ_p for the best MC Js and best MFT Js in Fig.12.12, for the best MC J values where the upper and lower bounds (not shown) are essentially equal to the mean value and for the best MFT values where the upper and lower bounds are significantly different because of the large fractions of frustrated spins.

Nevertheless, our calculated χ_p begins to deviate from near zero values at about

the correct composition, and is of the correct sign and order of magnitude.

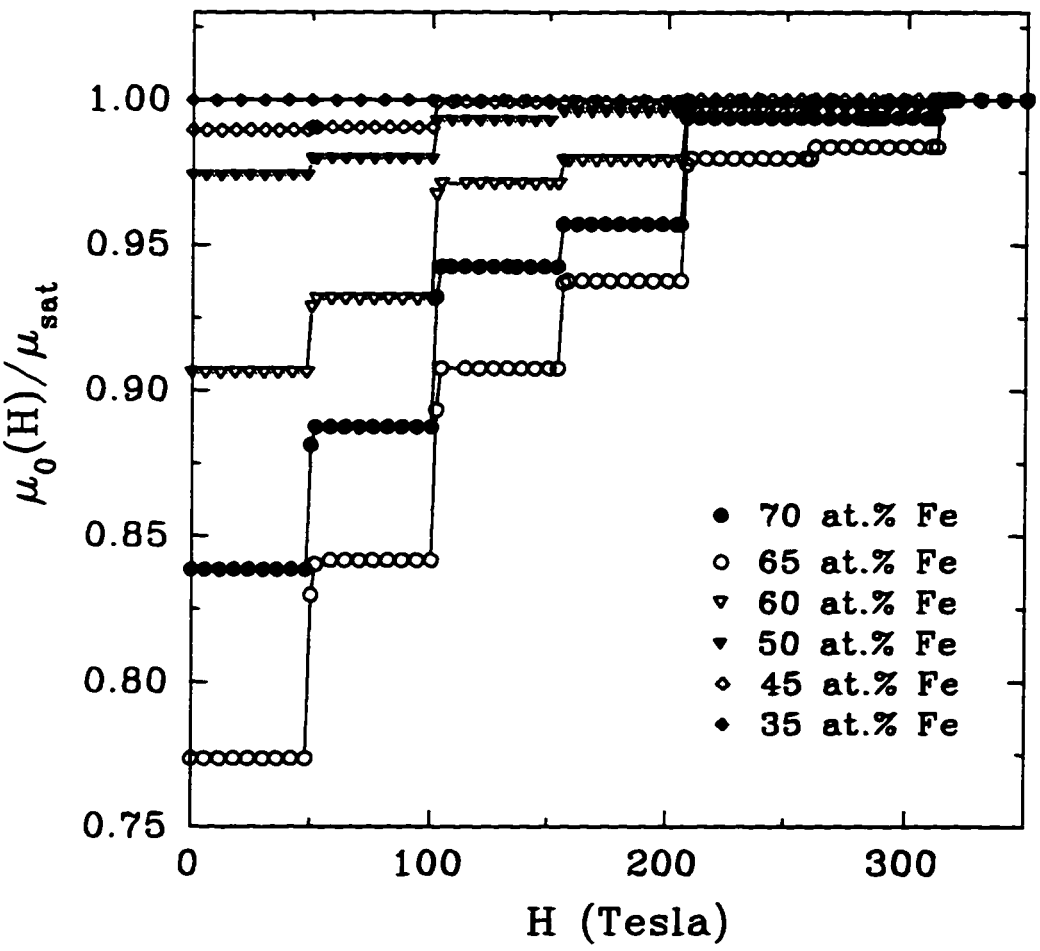

Figure 12.11 : Normalized MC average moment per atom at T = 0 K versus applied field for various compositions, as indicated, using best MC J values. The solid line are only guide to the eye.

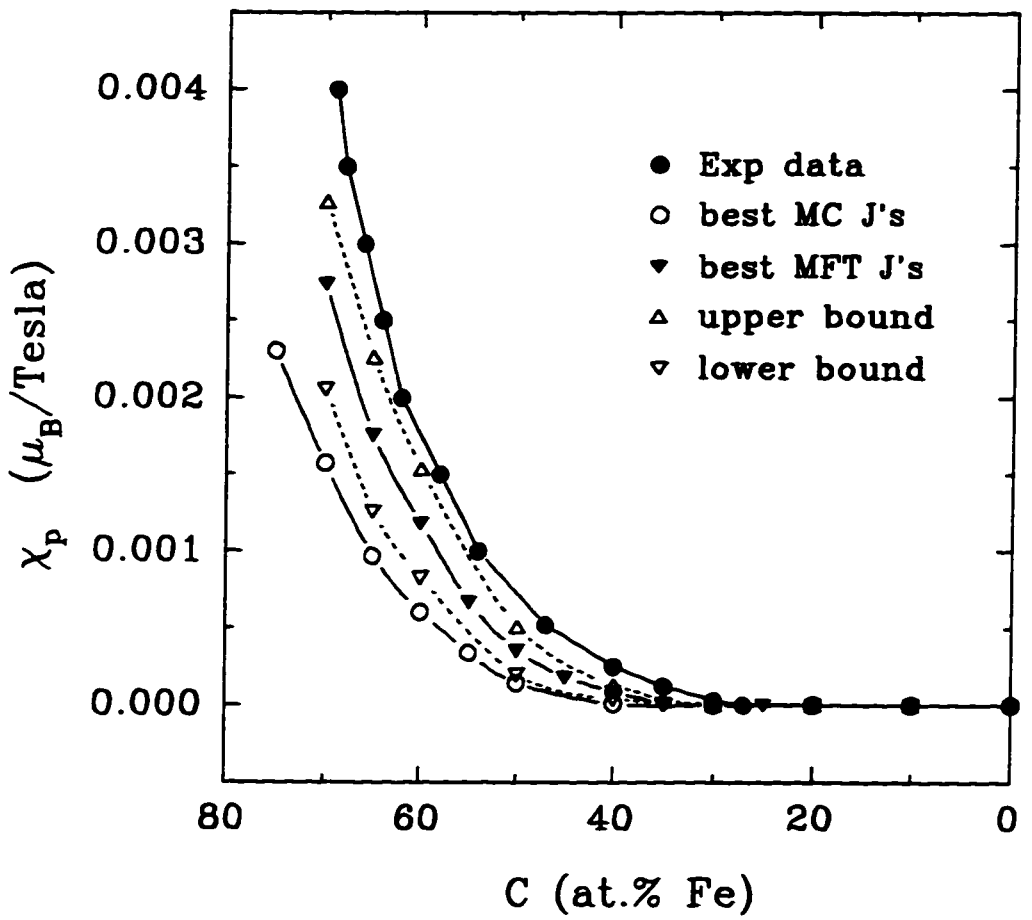

Figure 12.12 : MC average high field susceptibility at T = 0 K versus composition for two sets of J values compared to the experimental data. For best MC J values (J_{NiNi} = 700 K, J_{FeNi} = 355 K, J_{FeFe} = -25 K) only the middle value (see text) is shown because the upper and lower bounds coincide with it whereas for the best MFT J values (J_{NiNi} = 405 K, J_{FeNi} = 280 K, J_{FeFe} = -25 K) the middle value and the upper and lower bounds are shown, as indicated.

Chapter 13. Conclusion

Using a purely local moment model with only three adjustable parameters (the three pair-specific NN exchange constants: J_{NiNi}, J_{FeNi}, and J_{FeFe}, we can reproduce the main features of the magnetic properties in fcc Fe-Ni alloys. Qualitative agreement (i.e. the correct signs, magnitudes, and compositional dependencies of all the magnetic properties) between the model predictions and all the measured magnetic properties is obtained. This is the first time that a local moment model is used to simulate the magnetic properties such as the Curie temperature versus composition, the spontaneous saturation moment versus composition, the spontaneous magnetization versus temperature, the average magnetic moment versus the applied magnetic field and the high field paraprocess susceptibility at T = 0 K. The results show that simple local moment models should be considered strong contenders to explain Invar behavior. It also suggests that the fcc Fe-Ni alloys are strong local moment systems with non-integer but stable moments that persists far above T_C.

The model works better at low iron concentrations and has worse agreement at high Fe concentrations from y = 0.60 to 0.70 in Fe_yNi_{1-y}. The latter difficulties may be due to several causes within the context of strong local moment magnetism since cluster MFT calculations [98] show the same difficulties on the same magnetic properties.

One way to get quantitative agreement at all compositions would have been to allow J_{FeFe} (or all three Js) to vary with composition. In fact, the Js much vary with compositions because magneto-volume coupling is required to explain the Invar properties and the lattice parameter varies with composition. The electronic densities also vary with composition. It is not clear whether the needed change in J values would be those required to give quantitative agreement with magnetic properties at all compositions. A model with the composition dependent coupling J_{FeFe} would will tested later in Part III.

There is also much experimental evidence suggesting that chemical clustering on a length scale of $\sim$ 15 Åoccurs at high Fe concentrations (e.g. [42]). This would invalidate our assumption of ideal randomness at the Fe-rich end and could significantly affect the behavior. Including long-range (e.g. next-near-neighbour) exchange interactions, depending on their signs and magnitudes, might also produce better agreement at all compositions.

The limited but real success of the present simple model shows that more realistic effects should be included and studied systematically within local moment models in order to ascertain their relative importance and impact on both the magnetic and Invar properties.

Part III

MC SIMULATIONS OF HFDs IN FCC FE-NI ALLOYS

Chapter 14. INTRODUCTION TO PART III

We have seen in Part II that a simple local moment model with three composition independent pair-wise NN magnetic exchange parameters (J_{FeFe}, J_{FeNi} and J_{NiNi}) reproduces the main features of the all macroscopic magnetic properties of fcc Fe-Ni alloys [111]. In this part, we calculate the microscopic magnetic properties of Fe-Ni alloys. That is, the spin structures and corresponding HFDs by using the same local moment model and MC simulation.

With a combination of our hyperfine field phenomenological model (Chapter 3 and Chapter 6) and the MC simulations of the spin structures, the HFDs of the alloys at different temperatures and compositions are calculated. The distributions of the atomic site-specific thermal average moments are also obtained.

Detailed comparisons are made between the simulated HFDs and the average hyperfine fields and the experimental results, by which the proposed hyperfine field vector model, coupling models for the hyperfine field model, local moment model and the latent antiferromagnetism model for Invar are tested. It is significant that this method can be applied not only to study the alloys in the collinear region ($y \leq 0.45$) but more importantly to study the alloys in iron rich region ($y > 0.45$) where the binomial distribution cannot be used in the spin structure calculation.

By this new approach, the microscopic relationships between spin structure, thermal effects, latent antiferromagnetism and corresponding HFD shapes are elucidated.

Chapter 15. METHOD OF HFD SIMULATION

15.1 Four Steps of the HFD Calculation

The key part of the HFD calculation is obtaining the site-specific average atomic moments of the lattice, which is different from the spatial average thermal average atomic moment that is also obtained from the MC simulation method. At a given temperature, the orientations and magnitudes of site-specific thermal average moments of the lattice is referred to as "the spin structure". Then the hyperfine field phenomenological model can be applied to calculate the hyperfine field for each iron site. The HFDs are obtained from binning the hyperfine field values.

To give a complete view about the HFD calculation, we describe it in four parts. (1) The site-specific thermal average spin moments are calculated using MC simulation method, giving the equilibrium spin structure at a given composition and temperature. (2) The phenomenological vector hyperfine field model with the coupling parameters known from modeling the average hyperfine fields and HFDs at LHT in the collinear ferromagnetic region is applied to calculate the site-specific hyperfine fields for all the iron sites. (3) The HFDs are constructed by binning the site-specific hyperfine field data in a sequence of their magnitudes by counting the occurrence of each value in the lattice. (4) Simulated Mössbauer spectra are generated from the calculated HFDs using sextets of Lorentzian lines with zero CS and QS. The four corresponding programs are given in Appendix C as C-1, C-2, C-3 and C-4.

15.2 Finite Size Effects on the Calculated HFDs

Similar to the local moment magnetism simulation, finite size effects on the HFD simulation are examined with different sizes N = 5, 10, 15 and 20 at T = 0 K. Fig.15.1 shows the simulated HFDs from the different sizes with the best MC Js from Part II. It shows that the HFDs do not show a finite size effect at T = 0 K when $N \geq 10$. At T close to T_C ($T/T_C = 0.96$), the HFDs for the same four sizes are calculated to examine the finite size effects again. The results are shown in Fig.15.2. Clearly, the finite size effect becomes important on the HFDs at T close to T_C. One has to be aware of this in using the MC method to calculate the properties near T_C. In the HFD simulations in this thesis, we use N = 10 (4000 atoms), which is sufficient except very near T_C.

15.3 Average Time Effect on the Calculated HFDs

As we mentioned in section 15.1, calculating the site-specific thermal average moments is the first step for the HFD calculation. We use the time average of a local moment to get its site-specific thermal average moment. A parameter n is used to describe how long such an average is taken or how many MC steps are used in getting the average. Recall that (section 11.3), τ_{max} is the number of MC steps acomplished before the equilibrium state is reached and τ is the MC steps between the two consecutive data sampling. If N_{tot} is the total number of MC steps used in the simulation, then we have:

$$n = (N_{tot} - \tau_{max})/\tau. \tag{15.1}$$

During the HFD simulation, we found that the parameter n can affect the results dramatically. To get the average moments that truly represent the thermal average moments in the equilibrium state for all sites, we need a large n. To demonstrate this effect, a hypothetical fcc ferromagnetic pure iron is used in order to avoid spin frustration. Fig.15.3 shows how the simulated HFDs and the corresponding spectra are affected by n, giving different N_{tot}, τ_{max} = 3000 MC steps and τ = 20 MC steps.

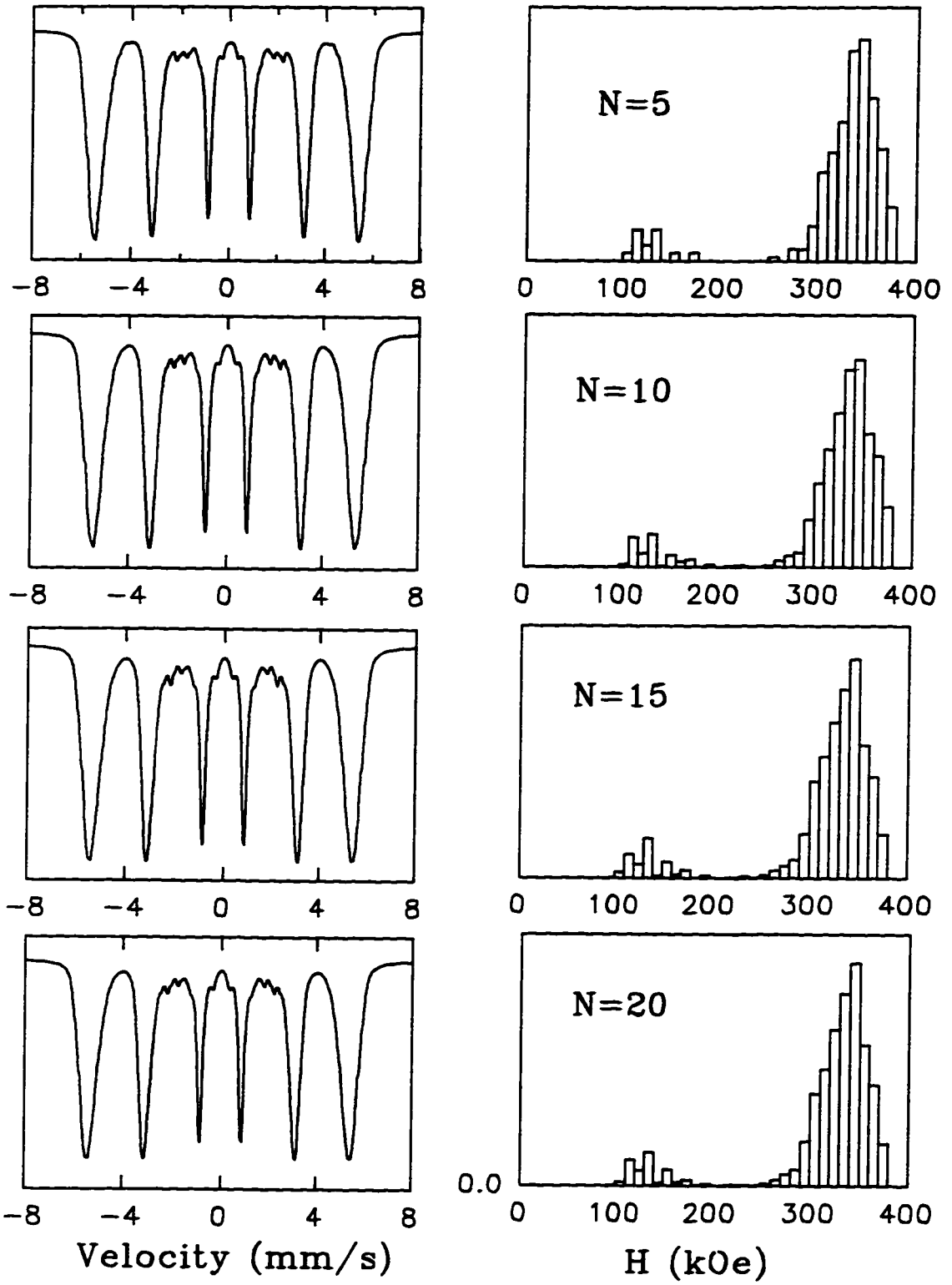

Figure 15.1 : Simulated spectra and HFDs at N = 5, 10, 15, 20 for y = 0.65 in Fe_yNi_{1-y} at T = 0 K to examine the finite size effects.

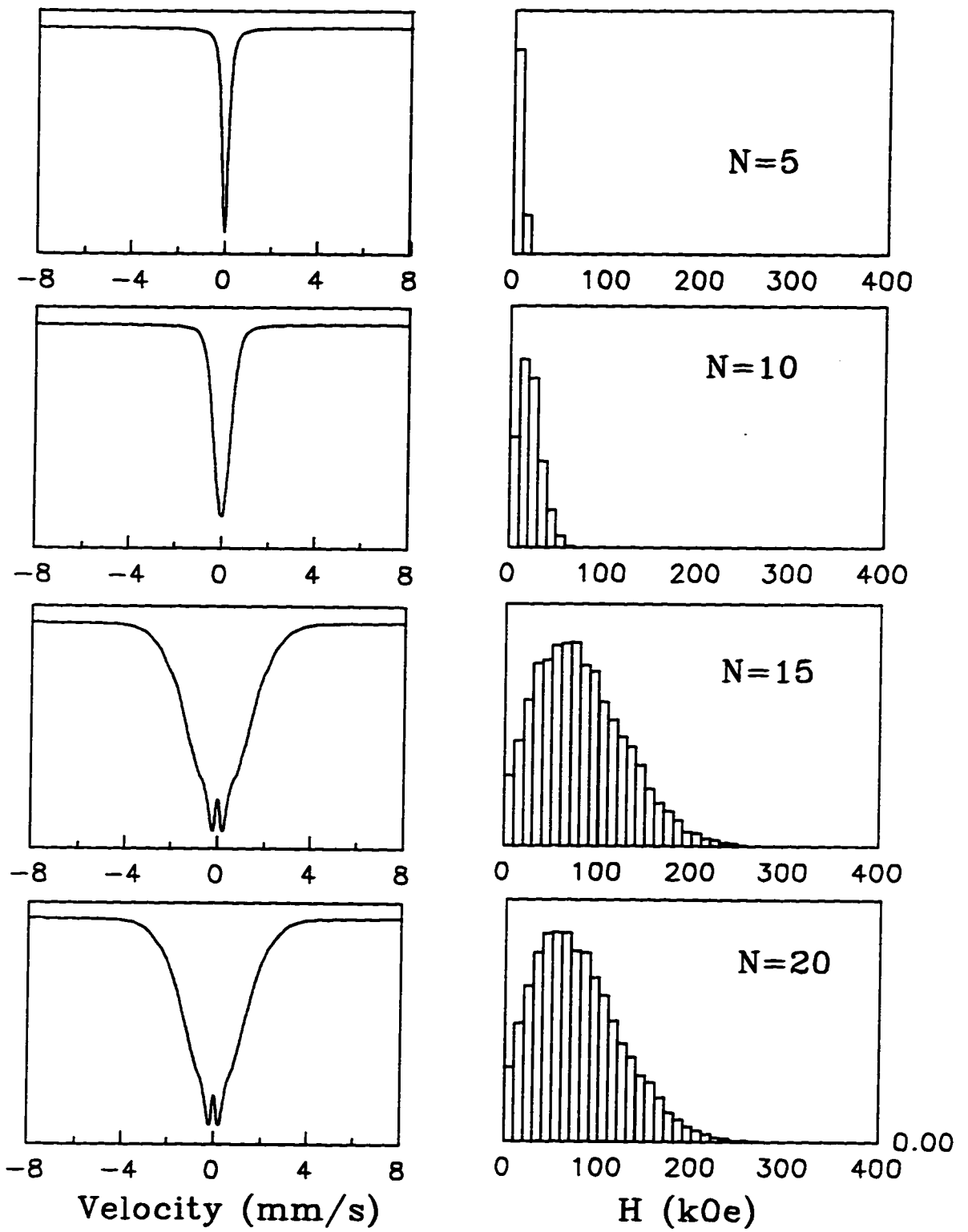

Figure 15.2 : Simulated spectra and HFDs at N = 5, 10, 15, 20 for y = 0.65 at $T/T_C = 0.96$.

For fcc Fe-Ni alloys, some arbitrarily selected site-specific moments are checked as a function of the averaging time at $T/T_C = 0.96$, which gives a confidence about the total number of MC steps used for the average. An example of this is given in Fig.15.4.

We use $N_{tot} = 10^5$ in all calculations except the one at $T/T_C = 0.96$ for $Fe_{0.50}Ni_{0.50}$ alloy where we use $N_{tot} = 10^6$. Thus in all but one of the calculations , n = (10^5 - 3000)/20 = 4965.

15.4 Bin Width Determination

When we bin the site-specific average hyperfine field values for the HFD, it is necessary to choose the proper bin width. If the bin width is too small, the HFD data will be discrete like the probability, which does not represent the true HFDs in the alloys. But if the bin width is too large, the features of the HFDs will be lost.

Fig.15.5 shows how HFDs shapes changes with different bin widths in y = 0.70 and 0.65 in Fe_yNi_{1-y} at T = 0 K. A bin width at 10 kOe is used in our HFD presentations.

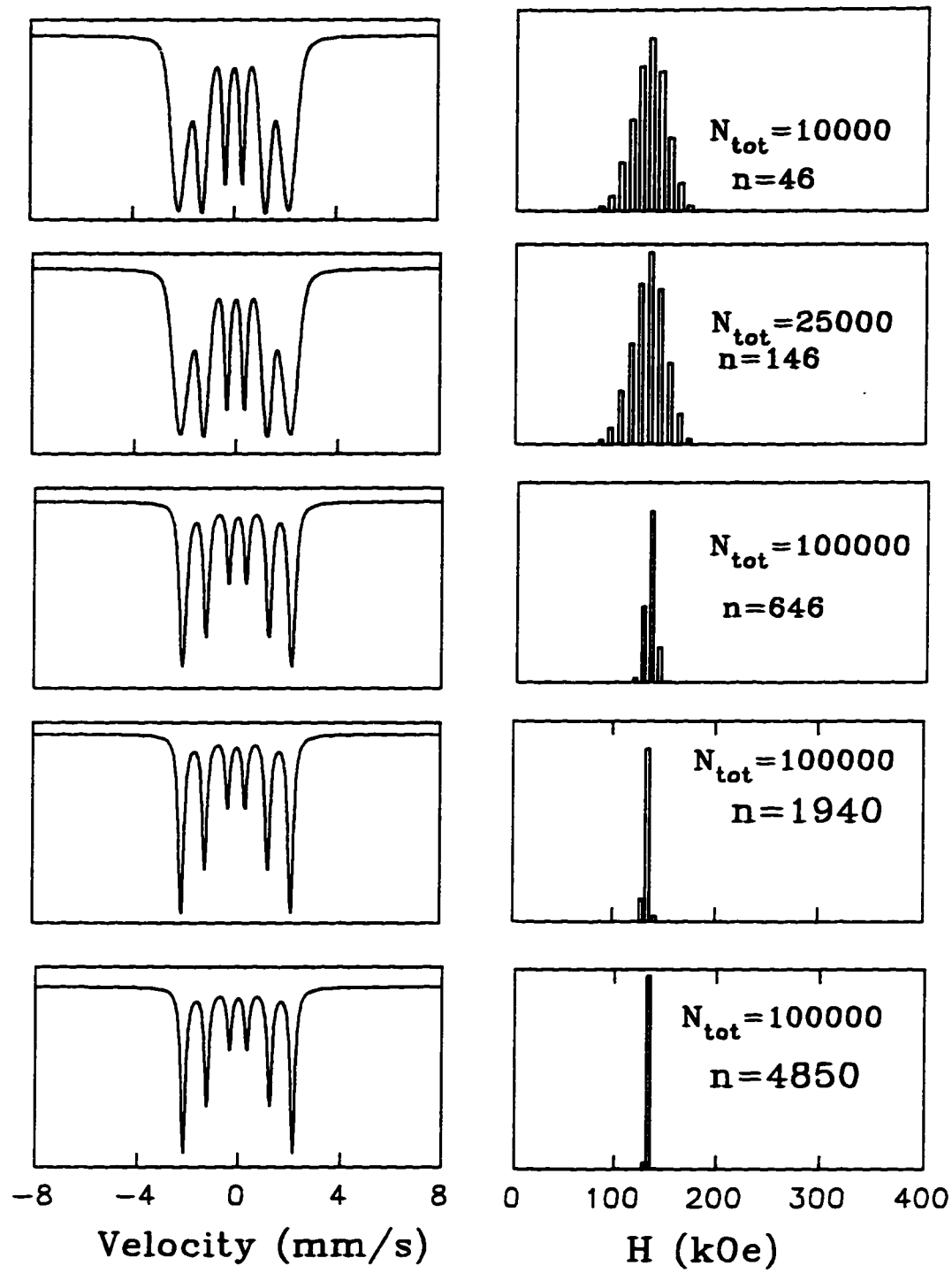

Figure 15.3 : Simulated HFDs and the corresponding spectra at different n (Eq.15.1) in fcc pure iron at $T/T_C = 0.96$.

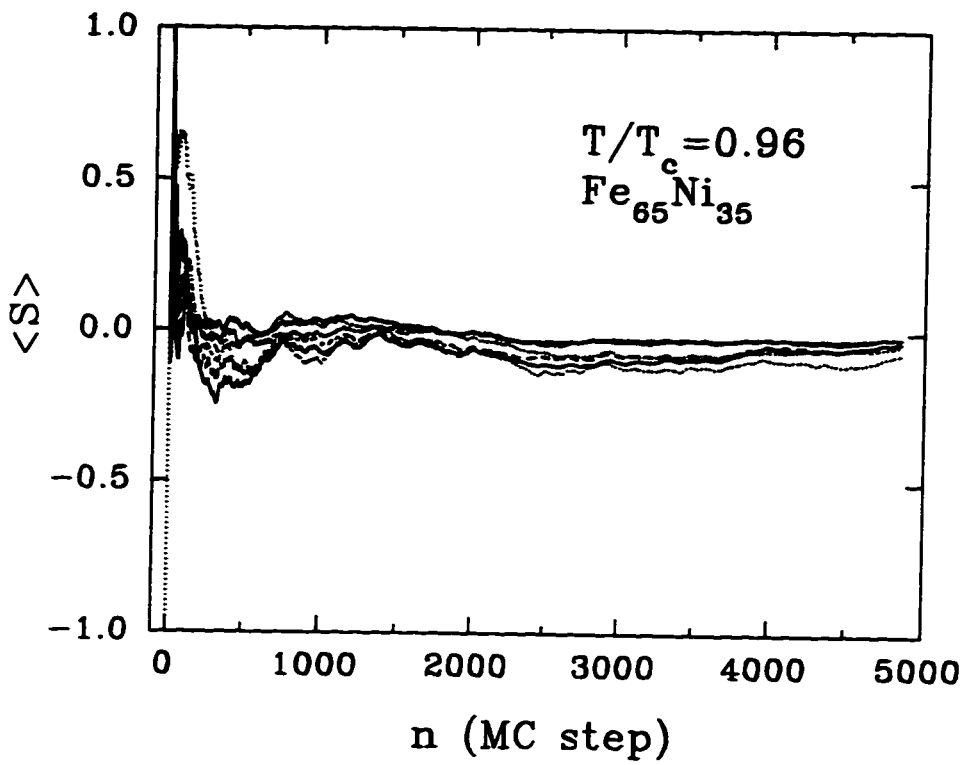

Figure 15.4 : Some arbitrarily selected site-specific moments versus n (Eq.15.1) at y = 0.65 and T/T_C = 0.96 K.

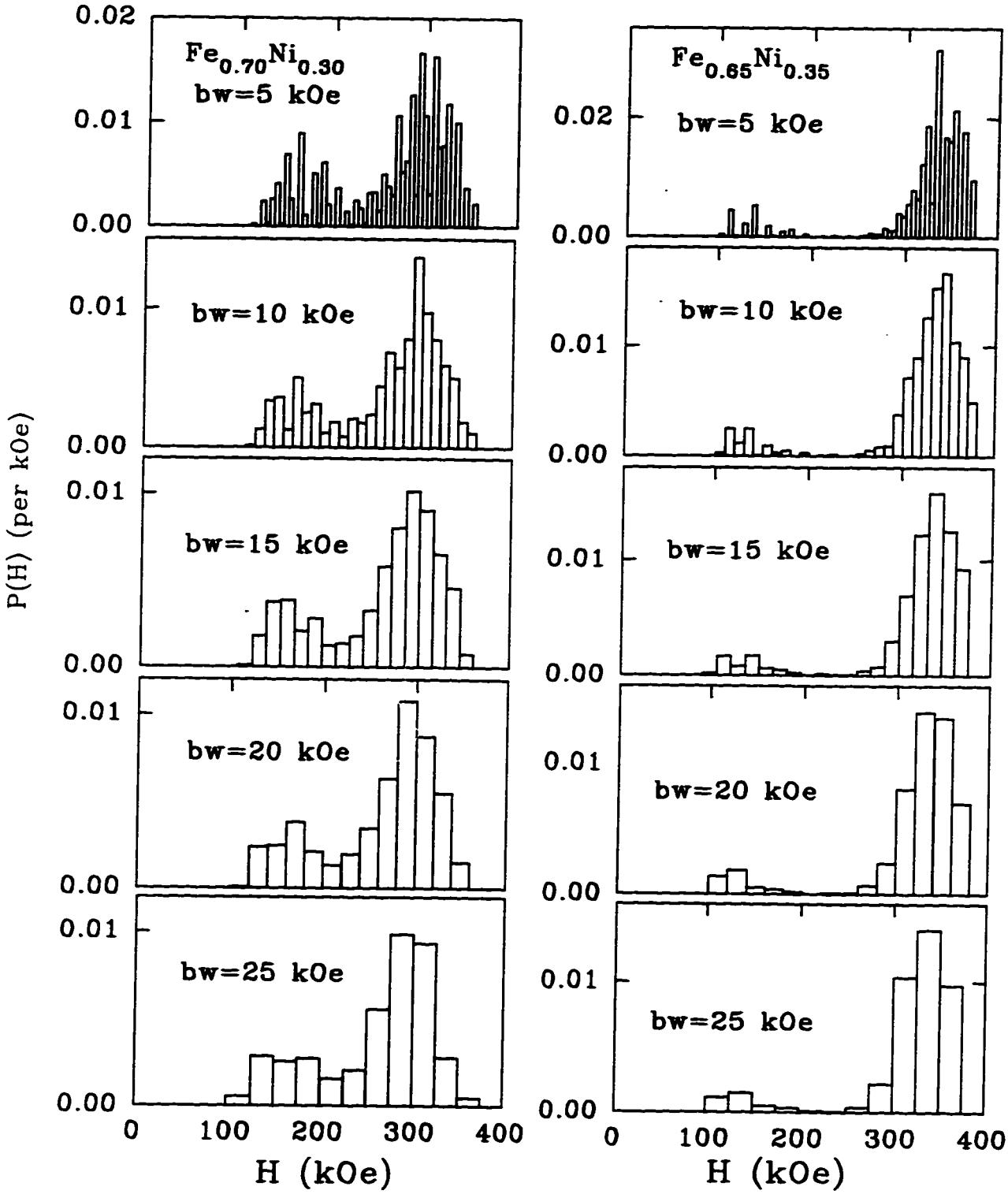

Figure 15.5 : The simulated HFDs at different bin widths at T = 0 K in y = 0.70 and 0.65 in Fe_yNi_{1-y}.

Chapter 16. GROUND STATE SPIN STRUCTURES AND CORRESPONDING SIMULATED HFDs

16.1 Simulated Ground State Spin Structures and Corresponding HFDs Using Composition-independent Js

First, the three composition-independent best MC Js (J_{NiNi} = 700 K, J_{FeNi} = 355 K, and J_{FeFe} = -25 K) are used for the HFD calculations. Ground state spin structures are obtained with the MC simulation using Ising approximation for the local moment model [111]. The corresponding HFDs are calculated using our phenomenological hyperfine field model (Part I):

$$\vec{H}_k = A < \vec{\mu}_k > + B \sum_j < \vec{\mu}_j >$$

and the two constant coupling parameters A = A_0 = 89 kOe/μ_B and B = B_0 = 3.6 kOe/μ_B. The calculated HFDs and their corresponding simulated spectra are shown in Fig.16.1 for Fe-rich alloys (y > 0.45) and in Fig.16.2 for Ni-rich alloys (y $\leq$ 0.45) in comparison with the measured HFDs from the VBF method [41].

The simulated HFDs show that in the collinear ferromagnets (y $\leq$ 0.45), the shape of the HFDs are close to binomial. It has one peak centered at high field (above 300 kOe), which corresponds to the spin structures having all the atomic moments aligned ferromagnetically.

In y>0.45 alloys, however, a low hyperfine field field bump appears at about 120 kOe. This low field component becomes more significant as Fe-content increases up to the fcc stability limit (y = 0.70 to 0.75). This feature, as we know from the calculated spin structure, arises from the down spin moments. The number of down

spin moments increases with the number of Fe-Fe NN pairs when the iron content increases.

The standard deviations σ_H of the simulated HFDs are shown in Fig.16.3 with their experimental counterparts. A good agreement is observed in the collinear ferromagnets (y <0.45). At y = 0.45 the simulated HFD standard deviation σ_H starts deviating from the experimental data. A significant deviation is observed at y = 0.50, 0.55 and 0.60. But at y = 0.65 and 0.70 the deviations are smaller.

The calculated average hyperfine fields from the same ground state spin structures are shown in Fig.16.4 in comparison with the experiment. The agreement at low iron concentration is good if we ignore the problem of the short range atomic ordering. This is the assumption when we use two constant coupling parameters in the hyperfine field model, see section 7.5. Again significant deviation is seen in the Fe-rich region (y > 0.45).

Actually, the disagreement seen in the HFD width and the average hyperfine fields is within our expectations because we have seen such disagreement in our local moment magnetism simulations of Part II where all simulated properties show discrepancies in the Fe-rich region. These discrepancies are born from the simple local moment model. It may be due to factors such as the Ising approximation, longer range exchange interactions, chemical clustering in Fe-rich alloys, composition-independent J values, inaccurately measured T_Cs due to atomic ordering effects [87], magneto-volume coupling, etc. Next we will improve the simple local moment model by allowing J_{FeFe} to change with the alloy composition.

16.2 Improving the Local Moment Model With a Composition-dependent J_{FeFe}

To improve the agreement between the simulated results and the measurements at all the compositions, we consider Js that vary with composition, which is based on the fact that the magneto-volume effect is required to explain the Invar behavior (e.g. [2, 27, 103]).

We only allow J_{FeFe} to be composition-dependent. The required amount of

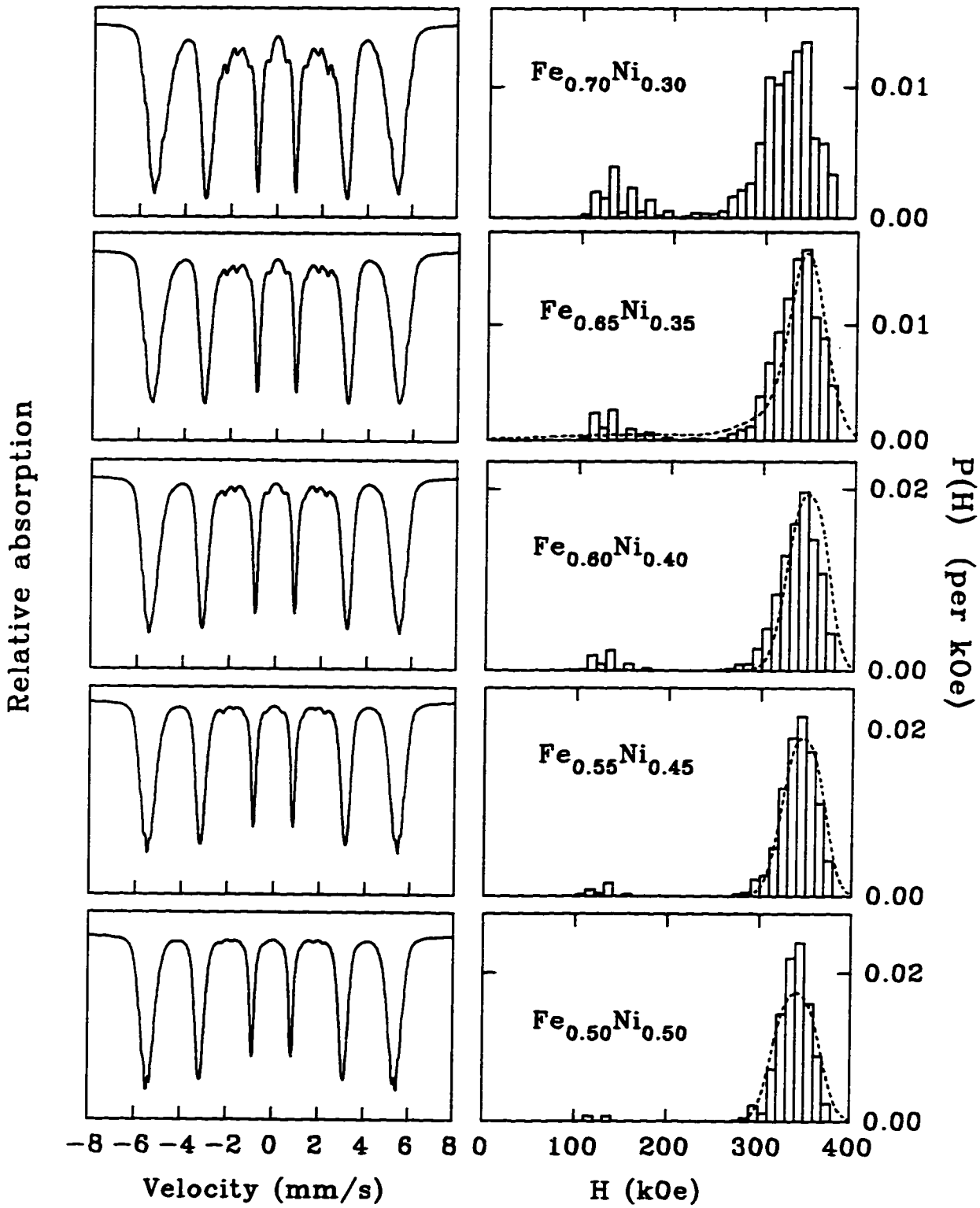

Figure 16.1 : The simulated ground state HFDs in the Fe-rich fcc Fe-Ni alloys (y > 0.45) at T = 0 K using J_{NiNi} = 700 K, J_{FeNi} = 355 K and J_{FeFe} = -25 K and compared with the experimental VBF HFDs.

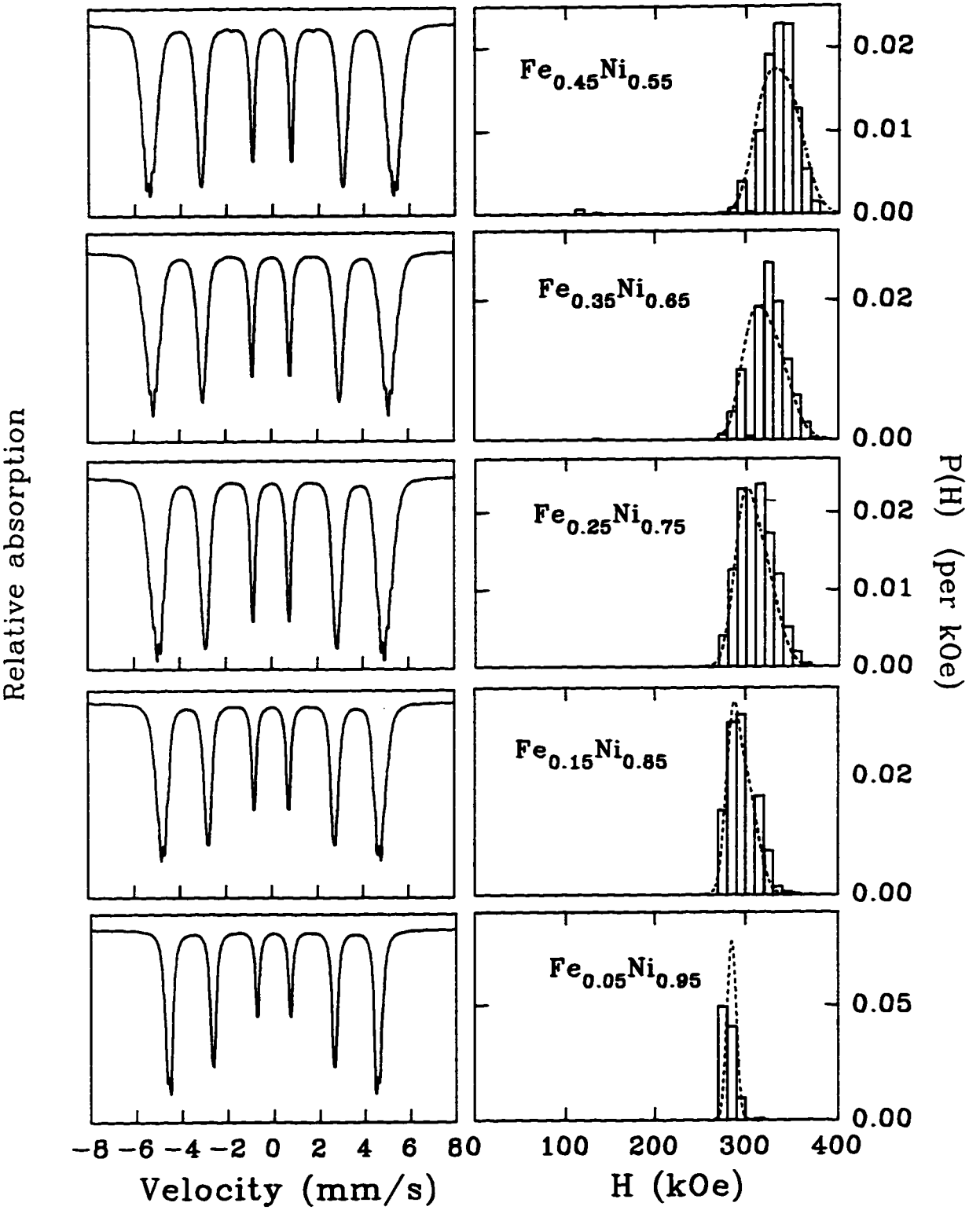

Figure 16.2 : The simulated ground state HFDs in the collinear ferromagnetic fcc Fe-Ni alloys ($y \leq 0.45$) at T = 0 K using J_{NiNi} = 700 K, J_{FeNi} = 355 K and J_{FeFe} = -25 K and compared with the experimental VBF HFDs.

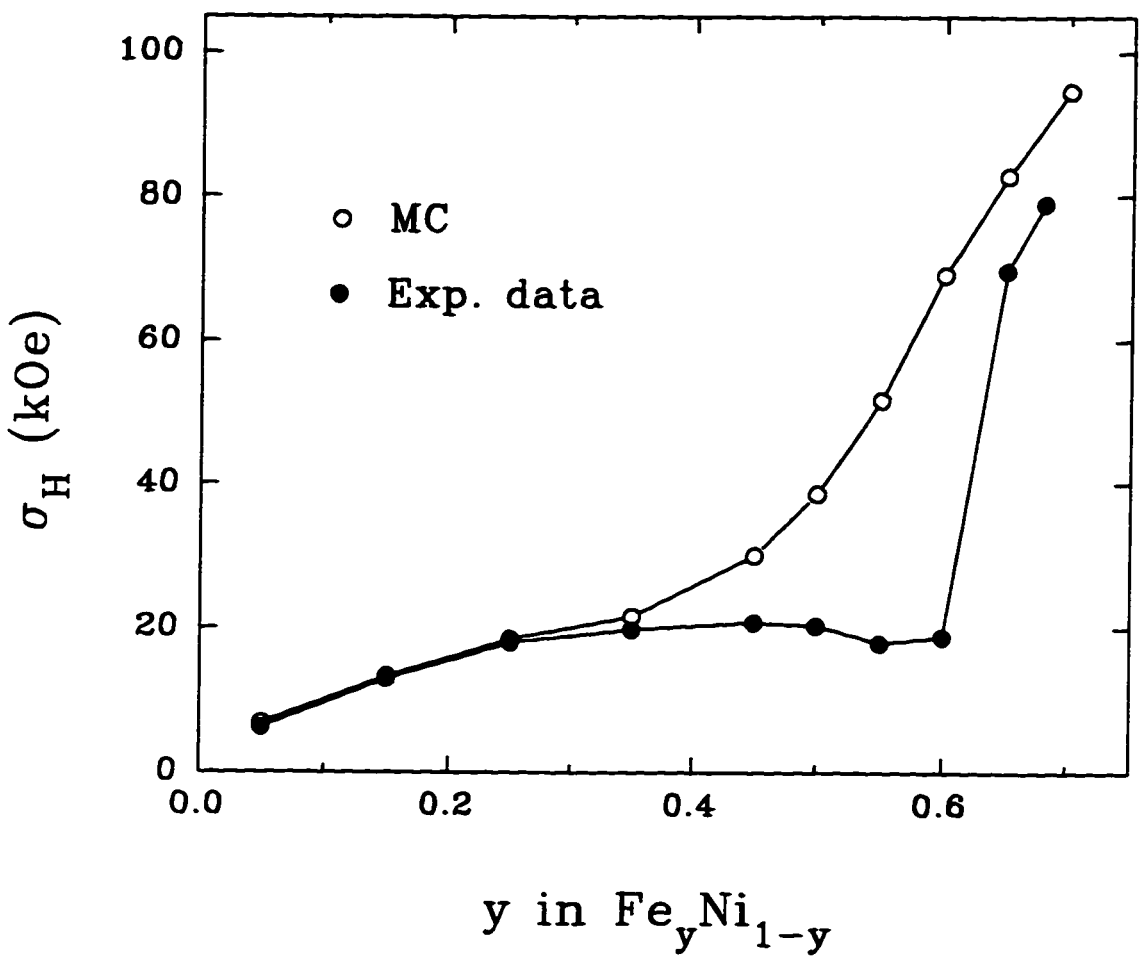

Figure 16.3 : The standard deviations of the simulated HFDs at T = 0 K using J_{NiNi} = 700 K, J_{FeNi} = 355 K and J_{FeFe} = -25 K and compared to the measurements.

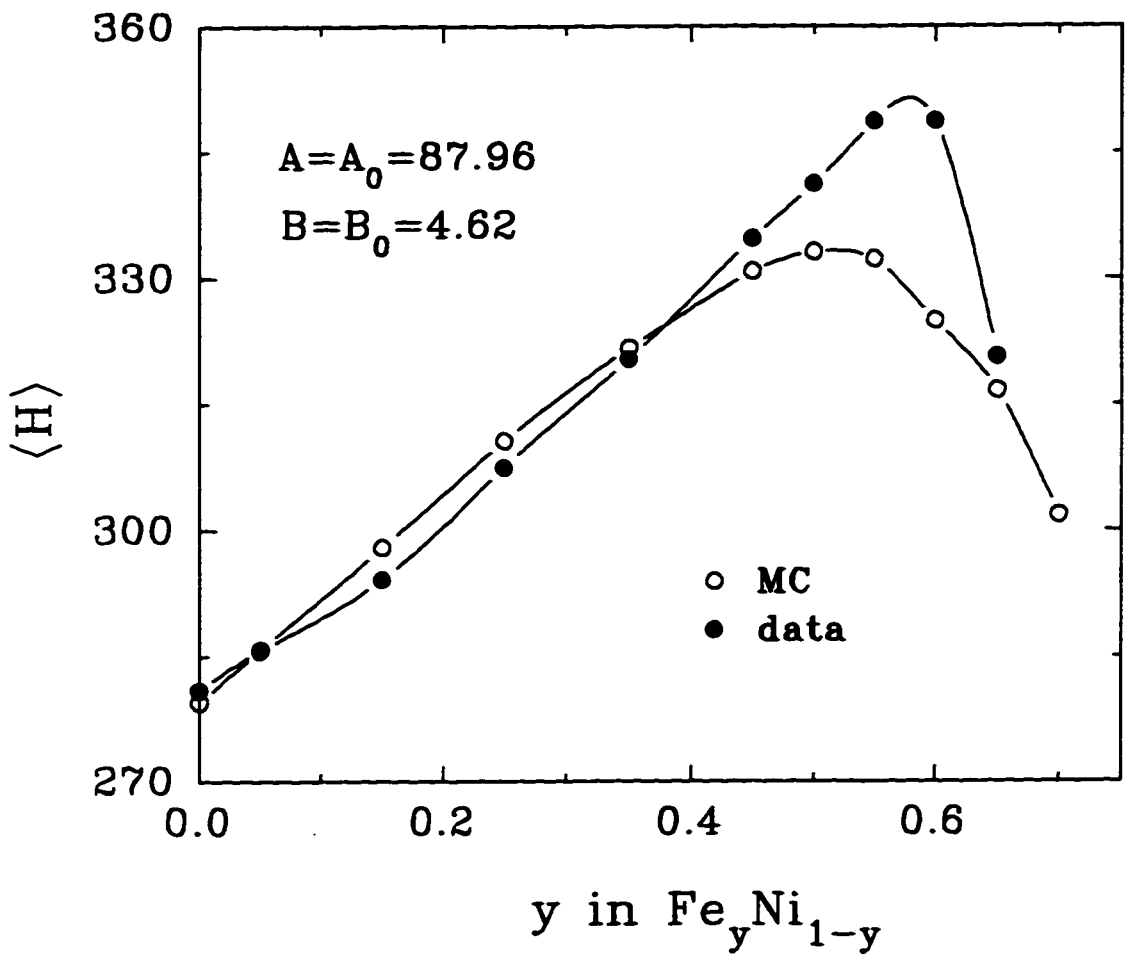

Figure 16.4 : The calculated average hyperfine fields at T = 0 K using J_{NiNi} = 700 K, J_{FeNi} = 355 K and J_{FeFe} = -25 K, compared to the experimental average hyperfine fields at LHT.

Table 16.1: The obtained J_{FeFe}s in fcc Fe-Ni alloys at T = 0 K.

y in Fe_yNi_{1-y}	J_{FeFe}
0.05	>-200
0.15	>-60
0.25	>-50
0.35	>-25
0.45	>-15
0.50	-15
0.55	-15
0.60	-15
0.65	-20
0.70	-40

the change in J_{FeFe} is to make the simulated saturation moments agree with the measured ones from Slater-Pauling curve at all compositions.

Fig.16.5 shows how to find the correct J_{FeFe} values at the compositions y = 0.70, 0.65, 0.60, 0.55 and 0.50 and 0.45. The best J_{FeFe}s are obtained by changing J_{FeFe} until the correct saturation moment is found (see Fig.16.5 where $< S > = < \mu > /2$ is used). In finding the best J_{FeFe}, the spin structures change with the variations of J_{FeFe}. For example, the fraction of down spin moments f_{amf} and the fraction, f_{usb}, of the bonds that are unsatisfied both depend on J_{FeFe}. By unsatisfied bond we mean a pair of ferromagnetically aligned Fe-Fe NN moments, or an antiferromagnetic alignment of Fe-Ni or Ni-Ni NNs. These ground state properties will be discussed in detail later in this section. The obtained J_{FeFe}s for all the compositions are given in Table 16.1. Notice that the obtained J_{FeFe} is not a single value in the low Fe content alloys. Any J_{FeFe} in the given region gives rise to the same saturation moment per atom. The magnetic properties in these alloys are not sensitive to the J_{FeFe} values. The calculated saturation moments with the composition dependent J_{FeFe} are shown in Fig.16.6 in comparison with the measurements. It shows that with composition dependent J_{FeFe}s we can get the correct macroscopic properties from the simulated ground state spin structure.

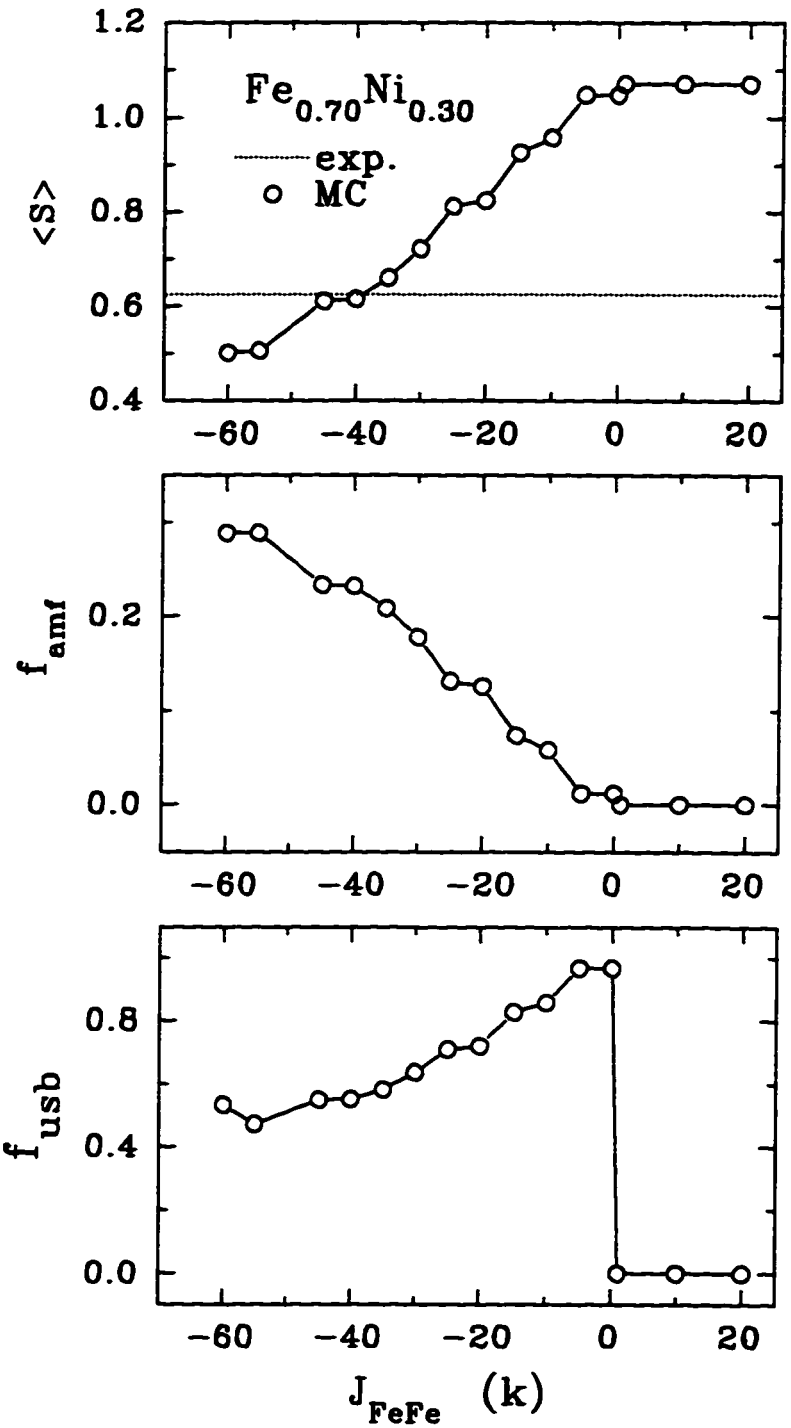

Figure 16.5 : Finding the best J_{FeFe}s in y = 0.70, 0.65, 0.60, 0.55, 0.50 and 0.45. The dotted horizontal line in $< S >$, is the measured values of the saturation moment [7]. f_{amf} is the fraction of down spin moments and f_{usb} is the ratio of unsatisfied bonds over the total number of NN bonds.

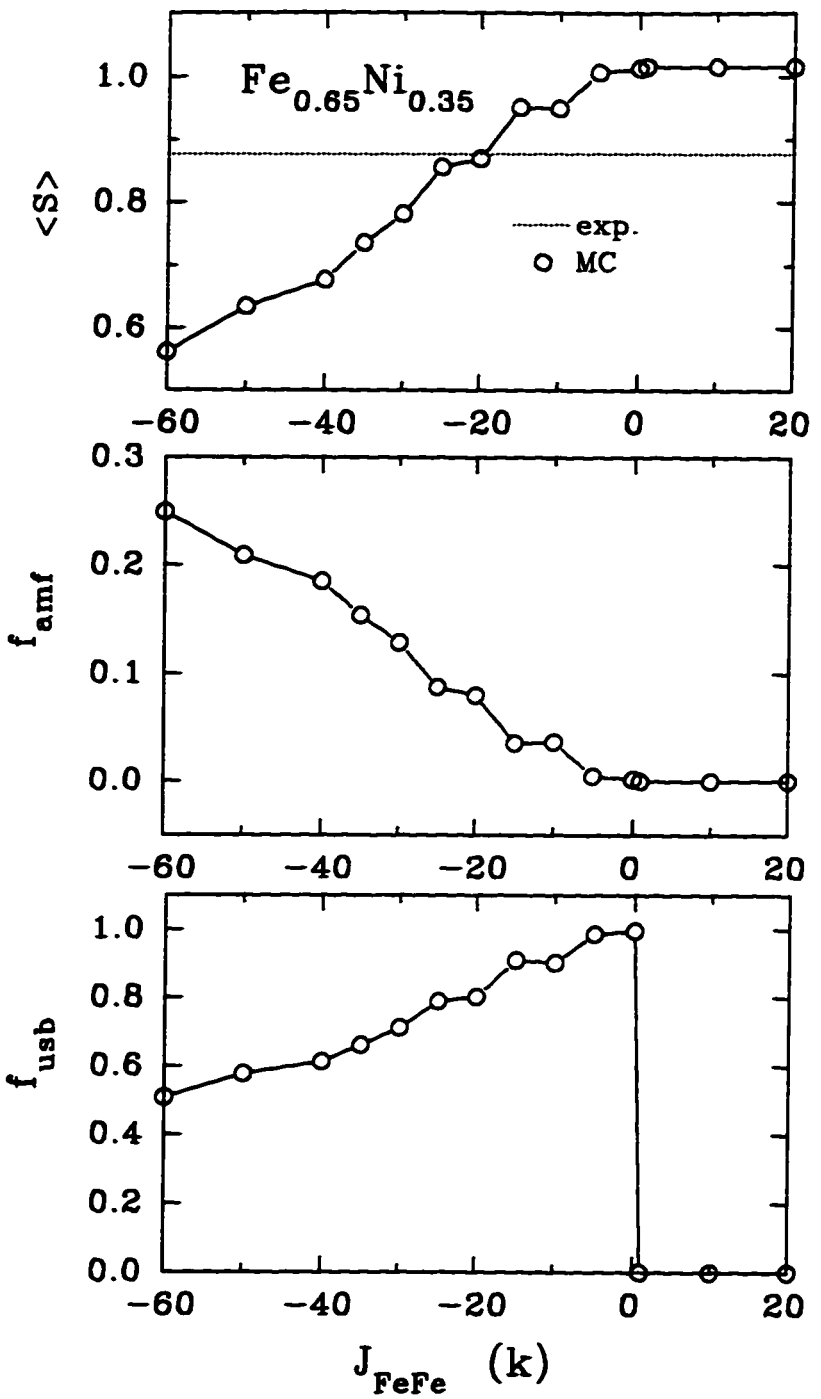

Fig.16.5 continued...

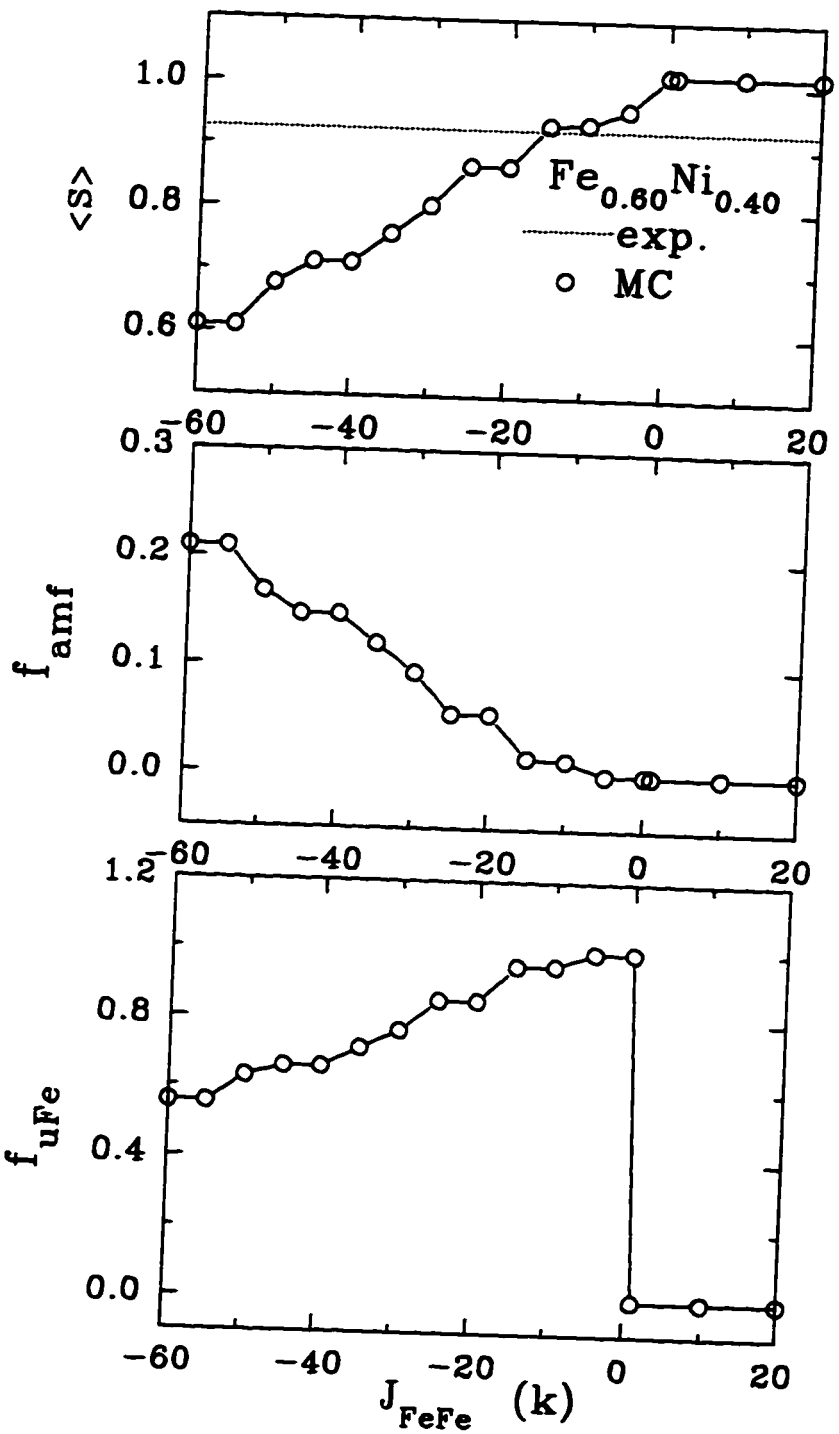

Fig.16.5 continued...

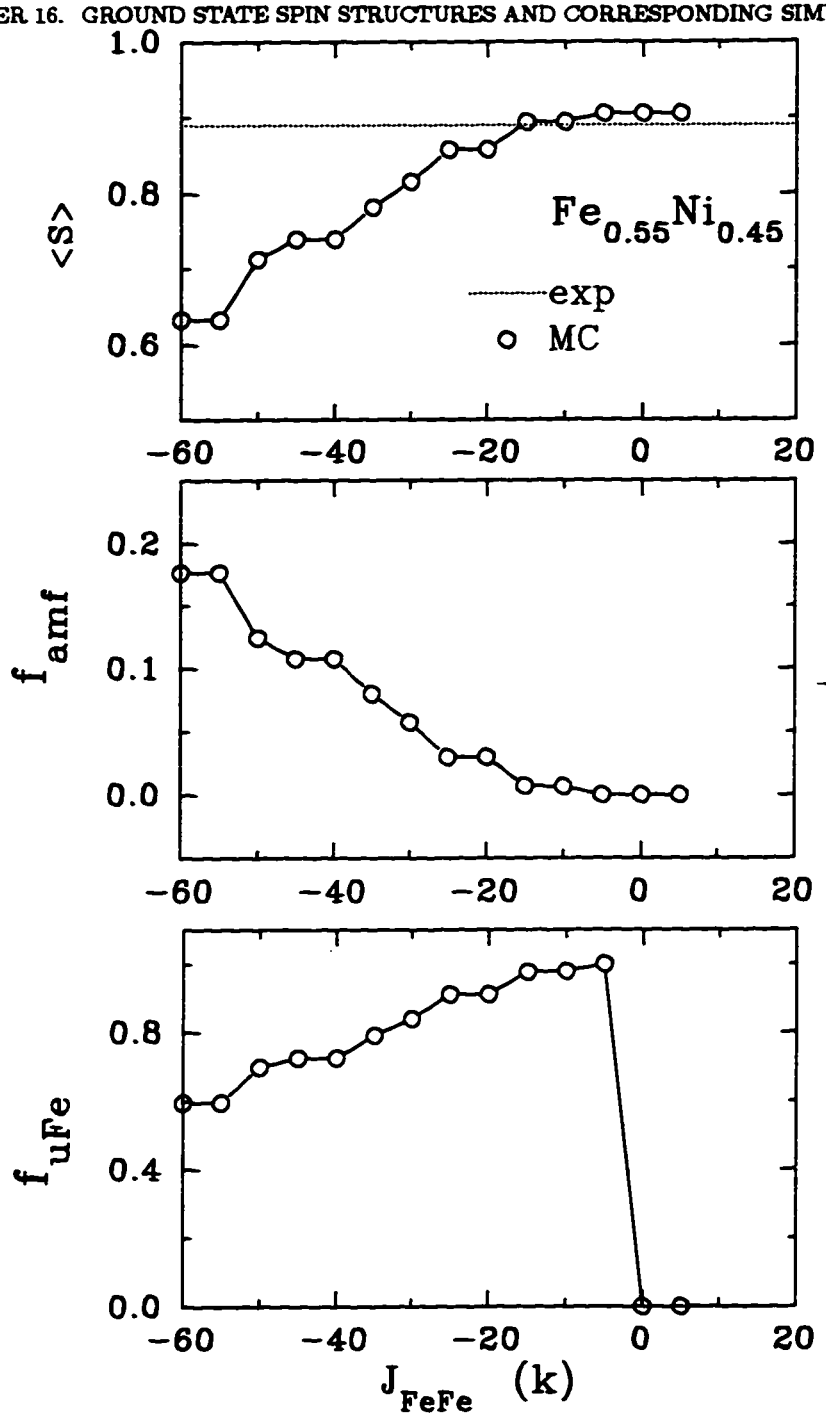

Fig.16.5 continued...

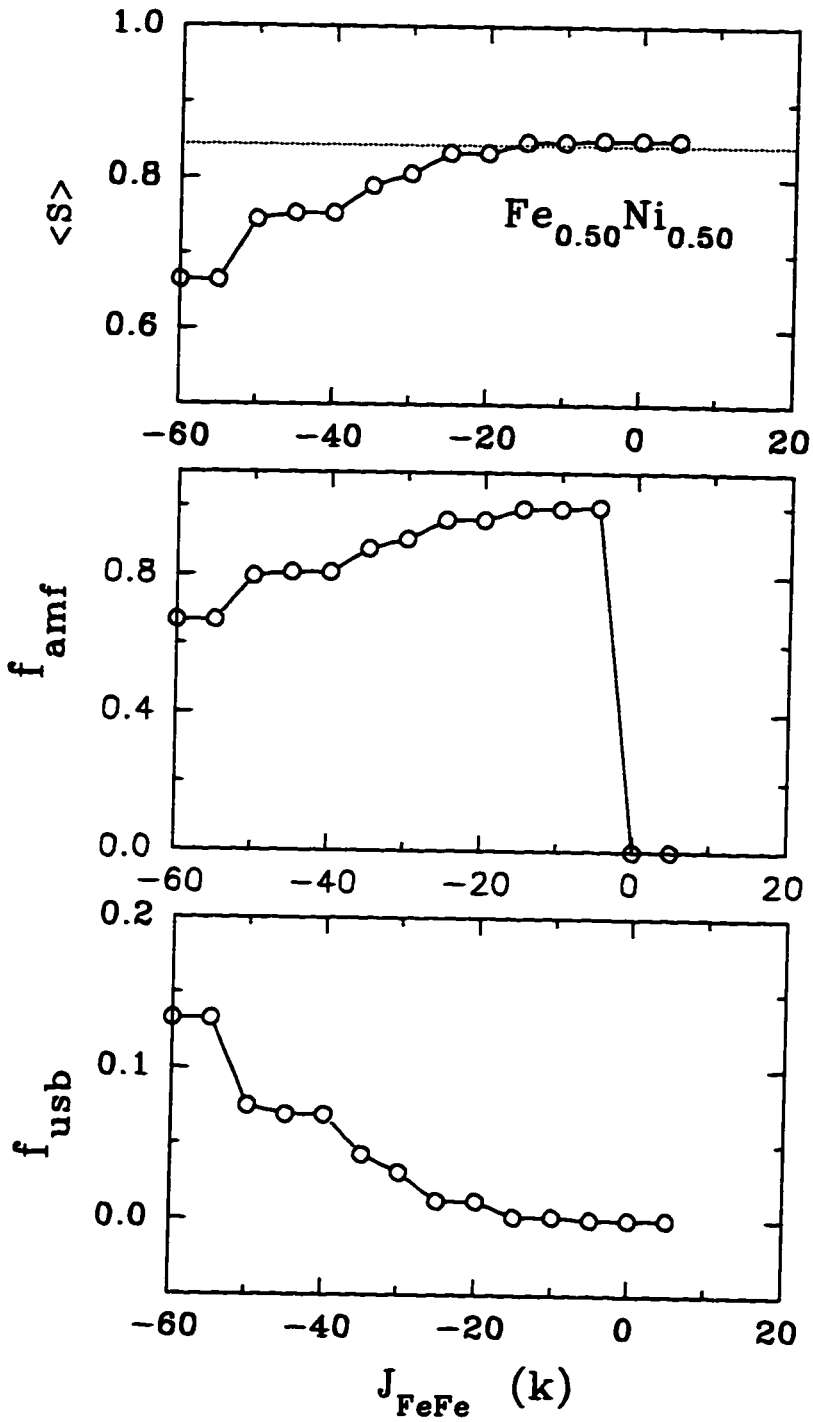

Fig.16.5 continued...

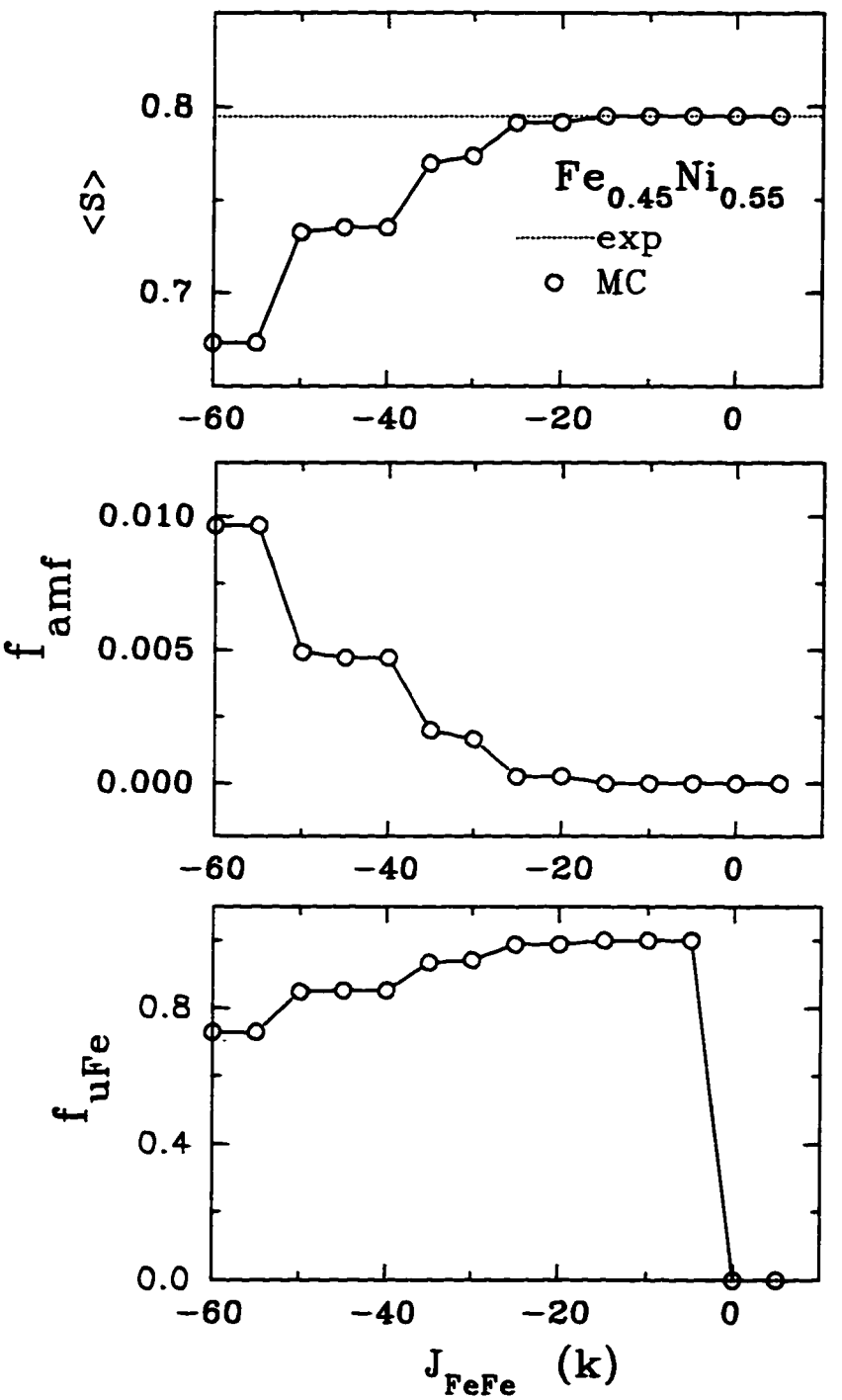

Fig.16.5 continued...

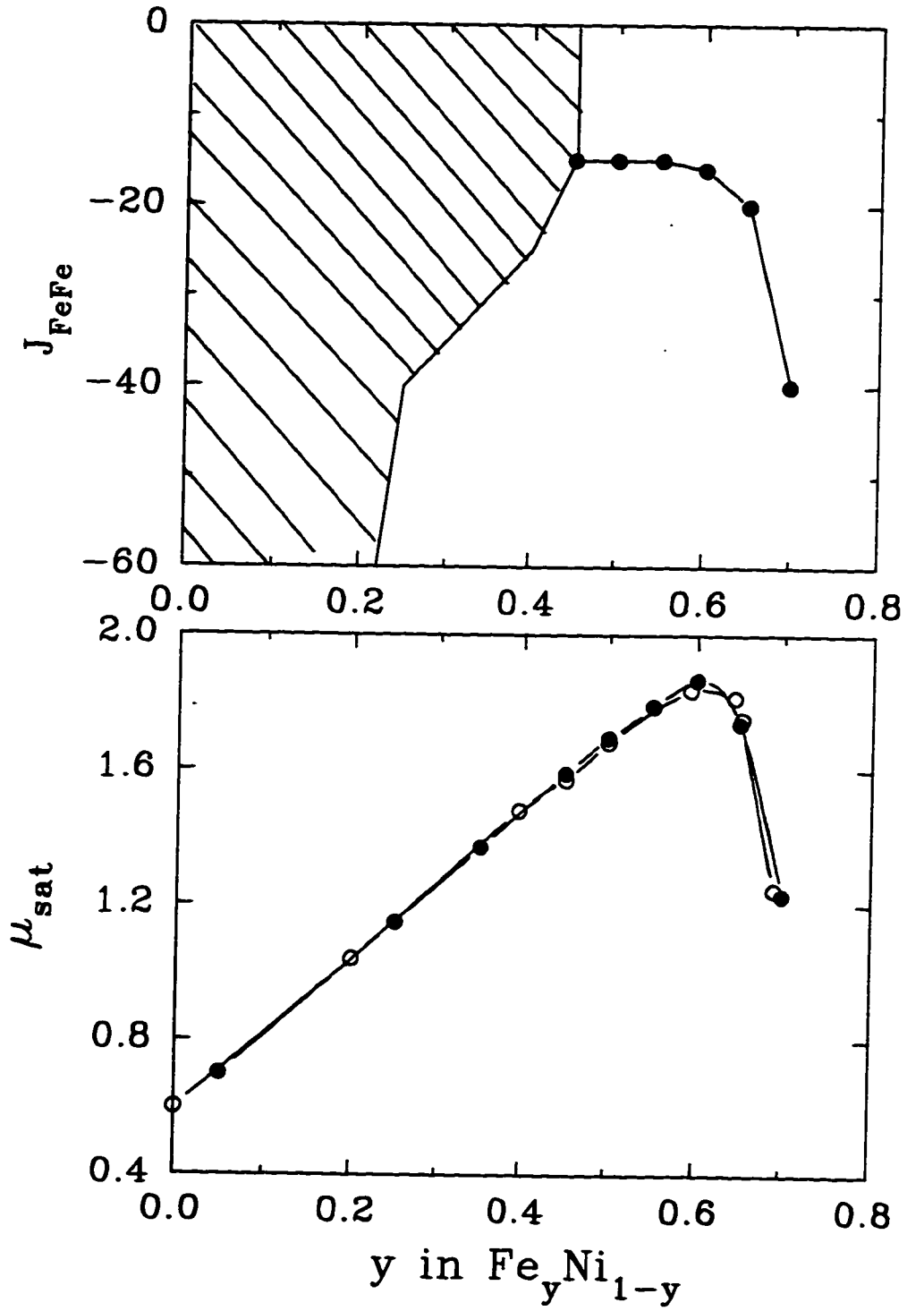

Figure 16.6 : The obtained best J_{FeFe}s and the corresponding calculated saturation moments with the experimental data using composition dependent J_{FeFe}s and J_{NiNi} = 700 K J_{FeNi} = 355 K.

Fig.16.7 shows some ground state properties using the new composition dependent J_{FeFe}s and the constant J_{FeNi} (355 K) and J_{NiNi} (700 K), as a function of the alloy composition. The first property is the fraction of down spin moments f_{amf}. The second, f_{usb}, is the fraction of unsatisfied bonds over the total number of NN bonds. The last one, f_{uFe}, is the ratio of unsatisfied bonds to the total number of Fe-Fe bonds. When iron concentration increases, the number of down moments increases, and unsatisfied bonds appear. It is important to notice that f_{uFe} does not show a monotonous increase with the iron concentration. It reaches a maximum at $y = 0.65$, i.e. the Invar concentration, then drops as the iron content increases. On the other hand, f_{uFe} drops from 1 to 0.50 as one goes from the Ni-rich to the Fe-rich alloys. These unsatisfied or frustrated Fe-Fe bonds may give a clue to explain the Invar effect. Rancourt and Dang [103] have for the first time pointed out this connection and calculated the magneto-volume properties quantitatively using a simple local moment model.

The simulated HFDs, from the composition dependent J_{FeFe}s and $J_{NiNi} = 700$ K and $J_{FeNi} = 355$ K, are shown in Fig.16.8 for Fe-rich alloys and in Fig.16.9 for Ni-rich alloys. Fig.16.10 and Fig.16.11 show the corresponding HFD standard deviations (σ_H) and the average hyperfine fields. It is observed that with the new J values, the calculated average hyperfine fields agree very well with the measurements in Fe-Ni alloys. In particular, the standard deviations σ_H of the simulated HFDs are improved significantly.

The results show that the composition dependent Js with only J_{FeFe} being composition dependent can improve our simple local moment model greatly in calculating the ground state HFDs, average hyperfine fields, HFD widths and other properties. It is necessary to allow a composition dependent J_{FeFe} just as it was to obtain quantitative agreement with the macroscopic properties.

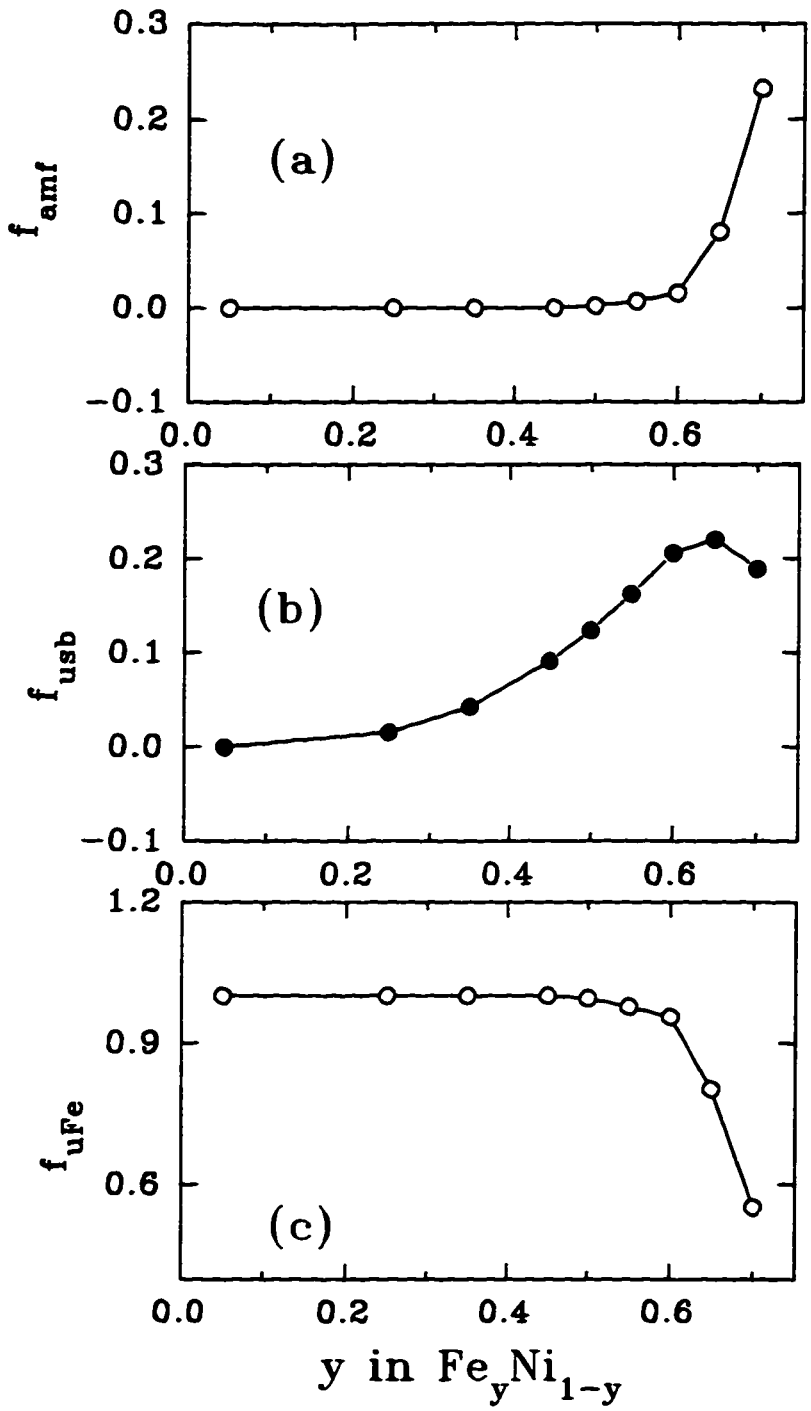

Figure 16.7 : Ground state spin structure using composition dependent J_{FeFe} where f_{amf} is the fraction of down spin moments, f_{usb} is the fraction of the unsatisfied bonds over total number of bonds, and f_{uFe} is the fraction of the unsatisfied bonds over number of Fe-Fe bonds.

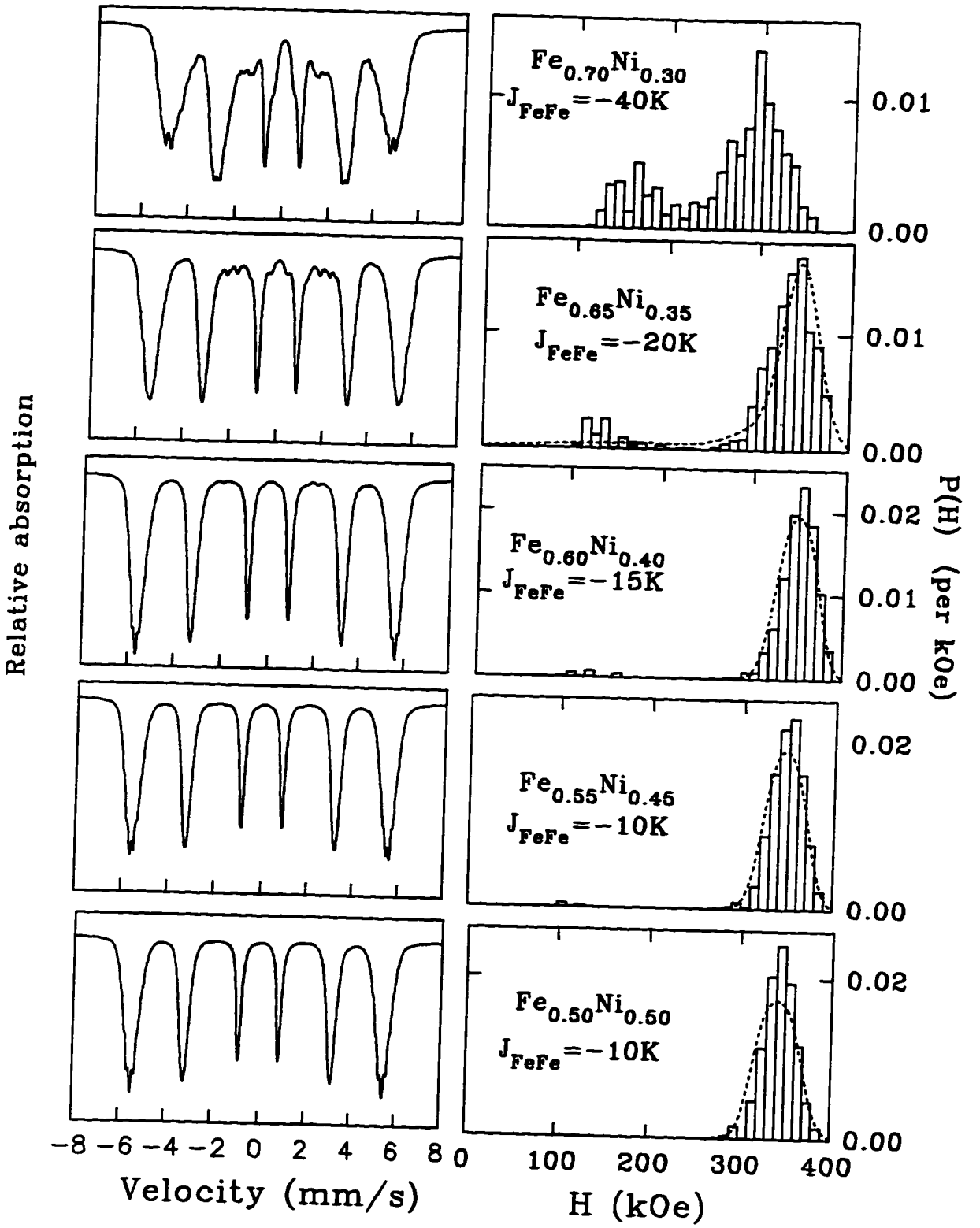

Figure 16.8 : The simulated ground state HFDs in Fe-rich (y > 0.45) fcc Fe-Ni alloys using the composition dependent J_{FeFe} values and J_{FeNi} = 355 K and J_{NiNi} = 700 K, compared to the measured HFDs.

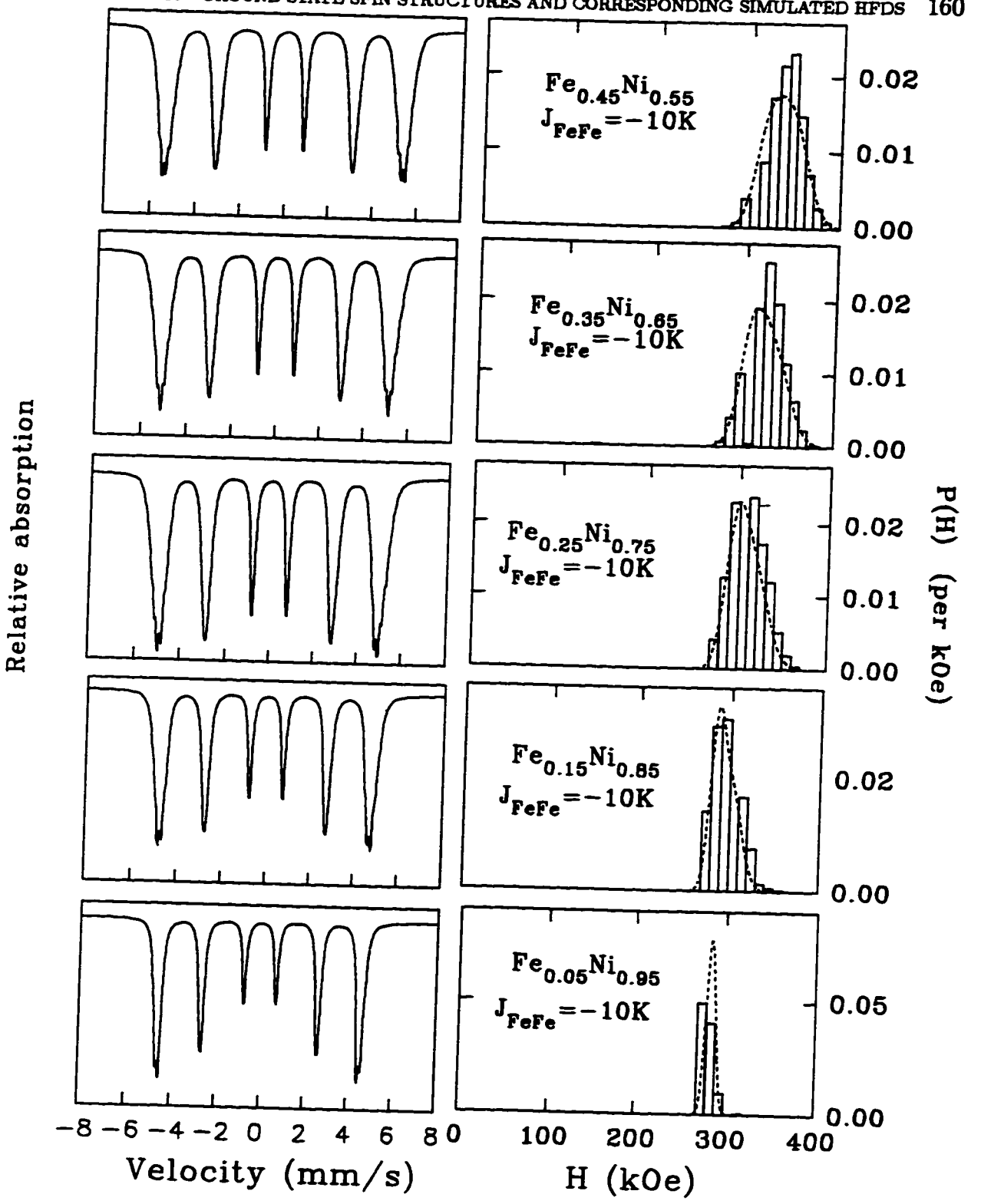

Figure 16.9 : The simulated ground state HFDs in Ni-rich ($y \leq 0.45$) fcc Fe-Ni alloys using composition dependent J_{FeFe} values and J_{FeNi} = 355 K and J_{NiNi} = 700 K, compared to the measured HFDs.

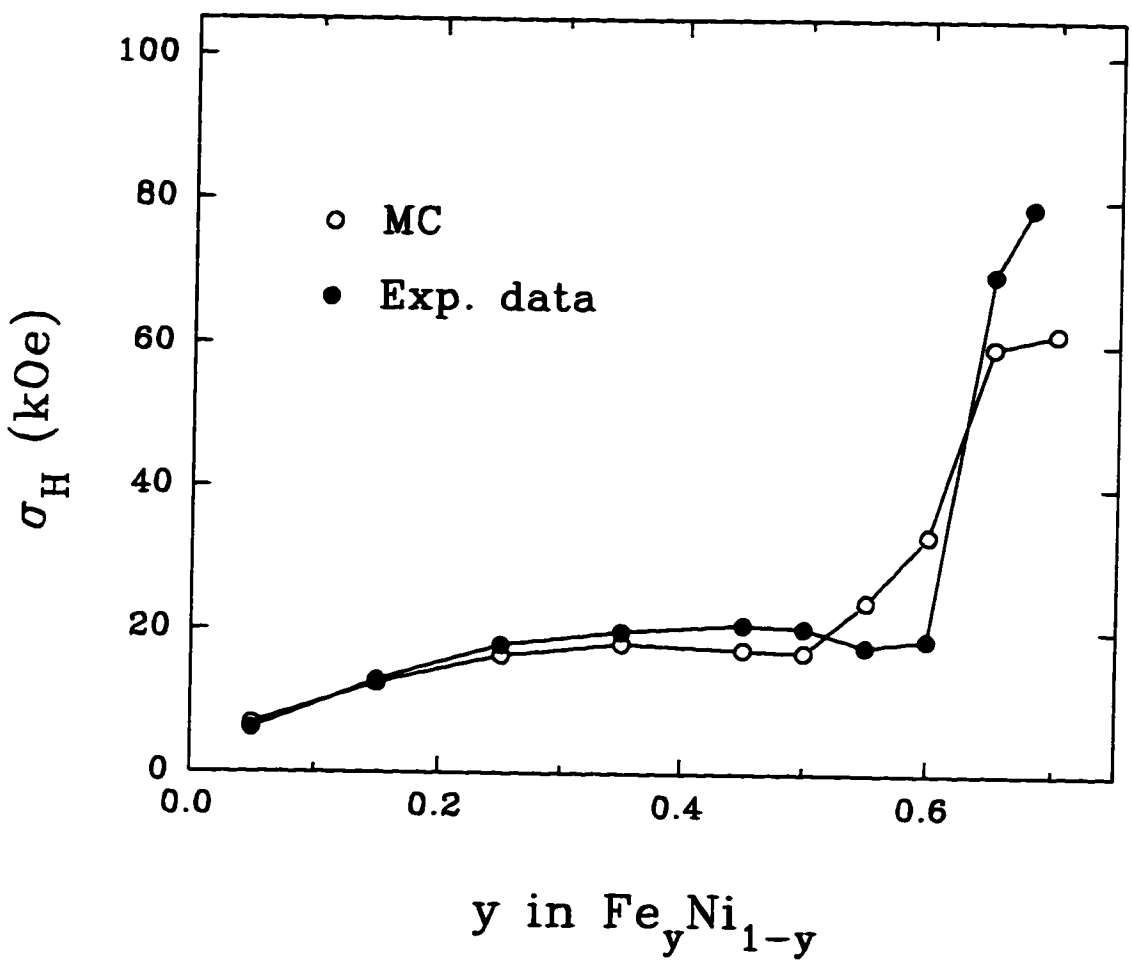

Figure 16.10: The standard deviation of the simulated HFDs compared to the measurements at T = 0 K with the composition dependent J_{FeFe} values.

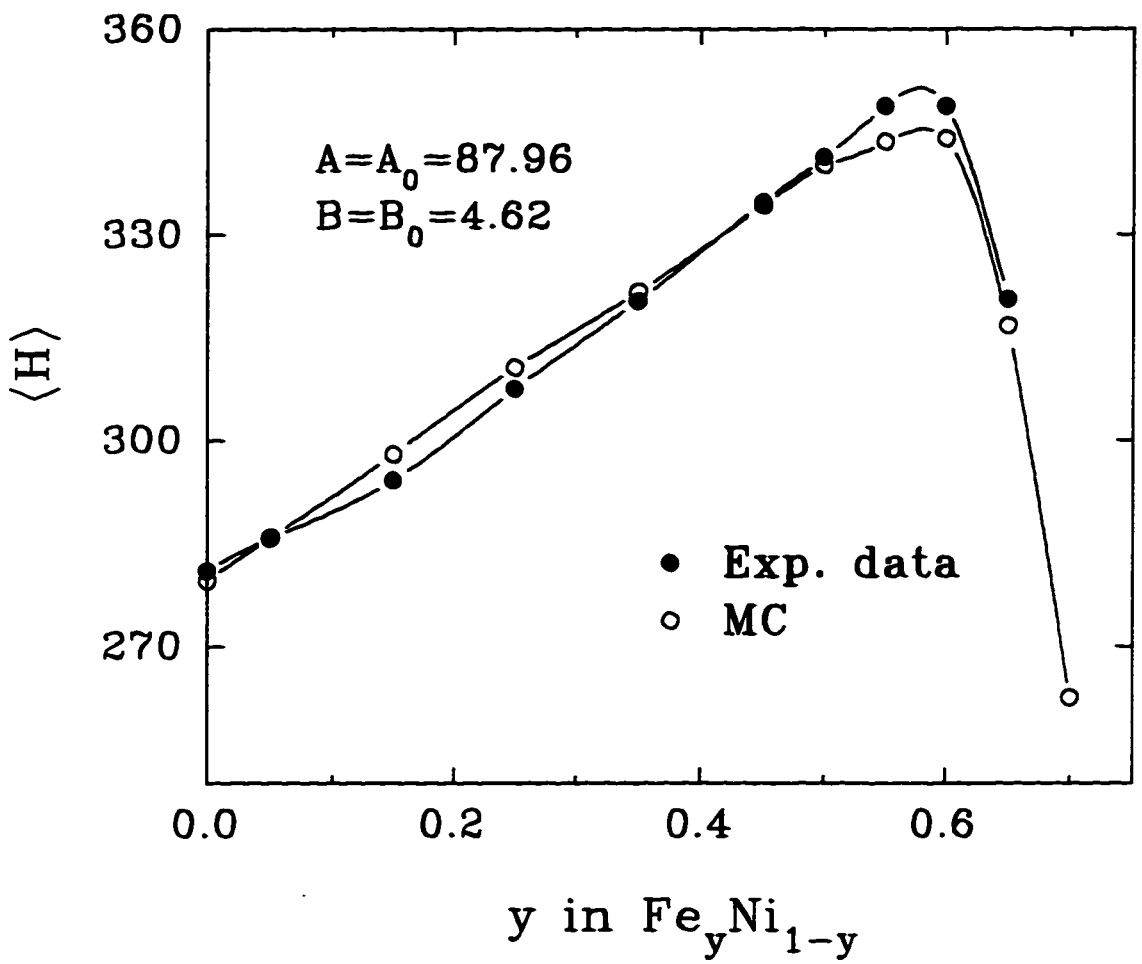

Figure 16.11 : The corresponding average hyperfine fields at T = 0 K compared with the experimental data using the composition dependent J_{FeFe} values.

16.3 Hyperfine Field Model Testing: Constant Coupling Versus Composition Dependent Coupling

Hyperfine field models with different couplings have been proposed and tested to interpret the measured average hyperfine fields and HFDs in the collinear ferromagnetic region (y $\leq$0.45; chapter 6 and chapter 7). Among them, two are accepted as plausible models. The first uses constant coupling parameters, the other uses composition dependent coupling parameters. Now we are able to test these models, using MC results, in all fcc Fe-Ni alloys up to the very Fe-rich alloys (y = 0.70). The differences resulted from the different models will become more apparent in this region.

The first model, CP-model-1 uses two constant coupling parameters, A_0 and B_0, assuming that the nonlinear average hyperfine field versus y at y $\leq$ 0.45 is due to residual short range atomic ordering. Model CP-model-2 uses composition-dependent coupling parameters, $A = A_0 + A_1 y$ and $B = B_0 + B_1 y$. It relates the observed curvature in the average hyperfine field versus y to the conduction electron density dependence of the s-electron polarization that causes the hyperfine field.

Similar to CP-model-2, another model (CP-model-3) is also proposed that uses composition dependent coupling parameters up to y = 0.45 but in the Fe-rich alloys at y > 0.45, y = 0.45 is used in the coupling coefficients A and B. This is based on the isomer shift measurements where the electron density stays at a plateau after y > 0.45 [82].

We use the new J values for the model testing: J_{NiNi} = 700 K, J_{FeNi} = 355 K and J_{FeFe} as given in Table 16.1. Fig.16.12 shows the average hyperfine fields from the three coupling models. It is seen that both CP-model-2 and CP-model-3 give very good agreement in all fcc Fe-Ni alloys whereas CP-model-1, in addition to its apparent disagreement in the collinear ferromagnetic region, shows a deviation in the Fe-rich region, especially at y = 0.55 and y = 0.60. The resulting HFD standard deviations from the three models are given in Fig.16.13. To compare these three coupling models in detail, Fig.16.14 shows the difference between the experimental average hyperfine fields (a) and HFD widths (b) and the calculated results. We can

see that CP-model-3 gives better agreement in the average hyperfine fields and the HFD width in all fcc Fe-Ni alloys ($0< y \leq 0.70$).

The simulated HFDs in the collinear ferromagnetic region ($y \leq 0.45$) are very similar to what we obtained in the previous section. In Fig.16.15, we show the simulated HFDs in Fe-rich alloys ($y = 0.50, 0.55, 0.60, 0.65$) from the different coupling parameter models in comparison with the experimental HFDs at $T = 4.2$ K obtained from the VBF method [41].

Considering the comparisons of the average hyperfine fields and HFDs in $y = 0.50, 0.55, 0.60$ and 0.65 from the three coupling parameter models, we conclude that CP-model-3 is the one resulting in an overall better agreement with the experiments.

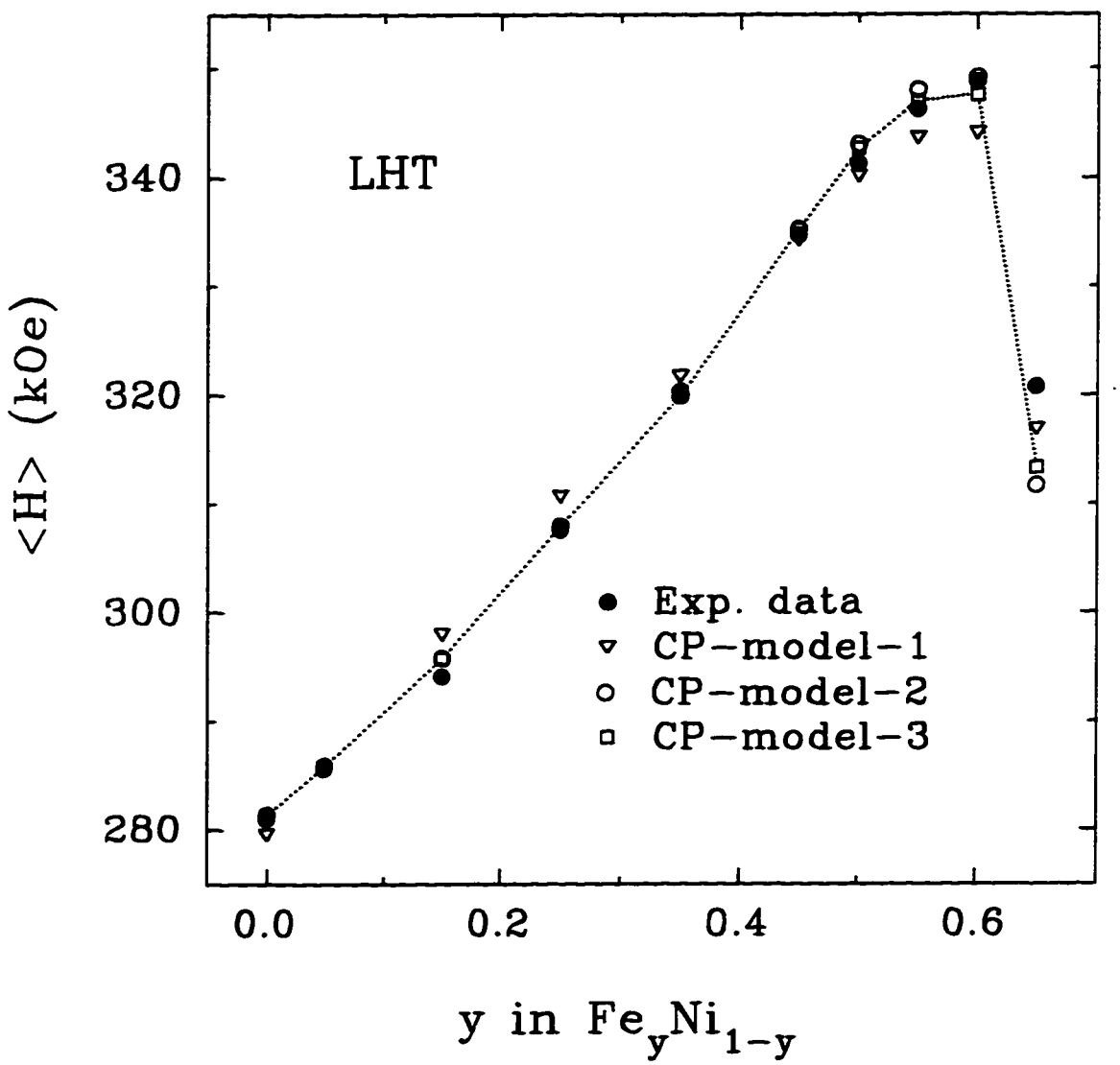

Figure 16.12 : The corresponding average hyperfine fields at T = 0 K from the three coupling parameter models, as indicated, and compared with the experimental data.

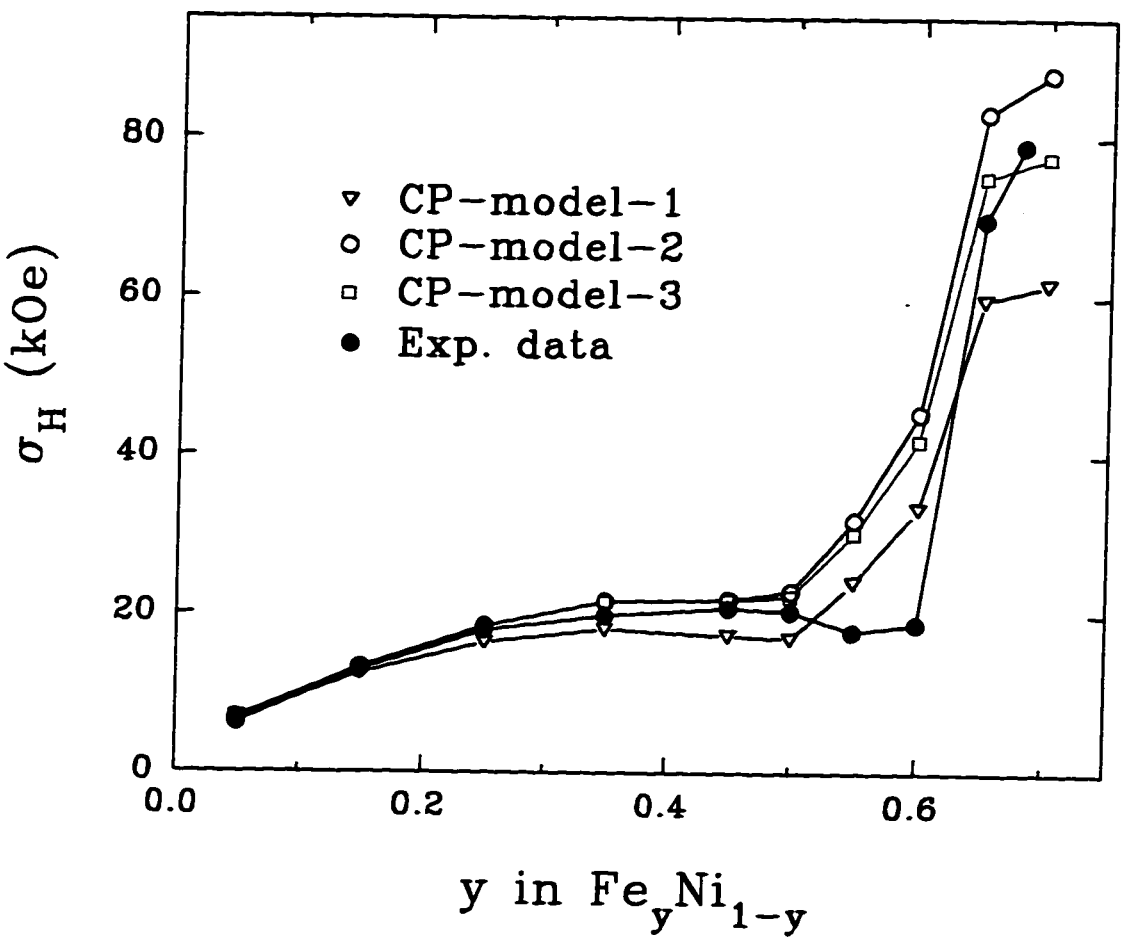

Figure 16.13 : Comparison of the HFD widths from the three coupling parameter models with the experimental data.

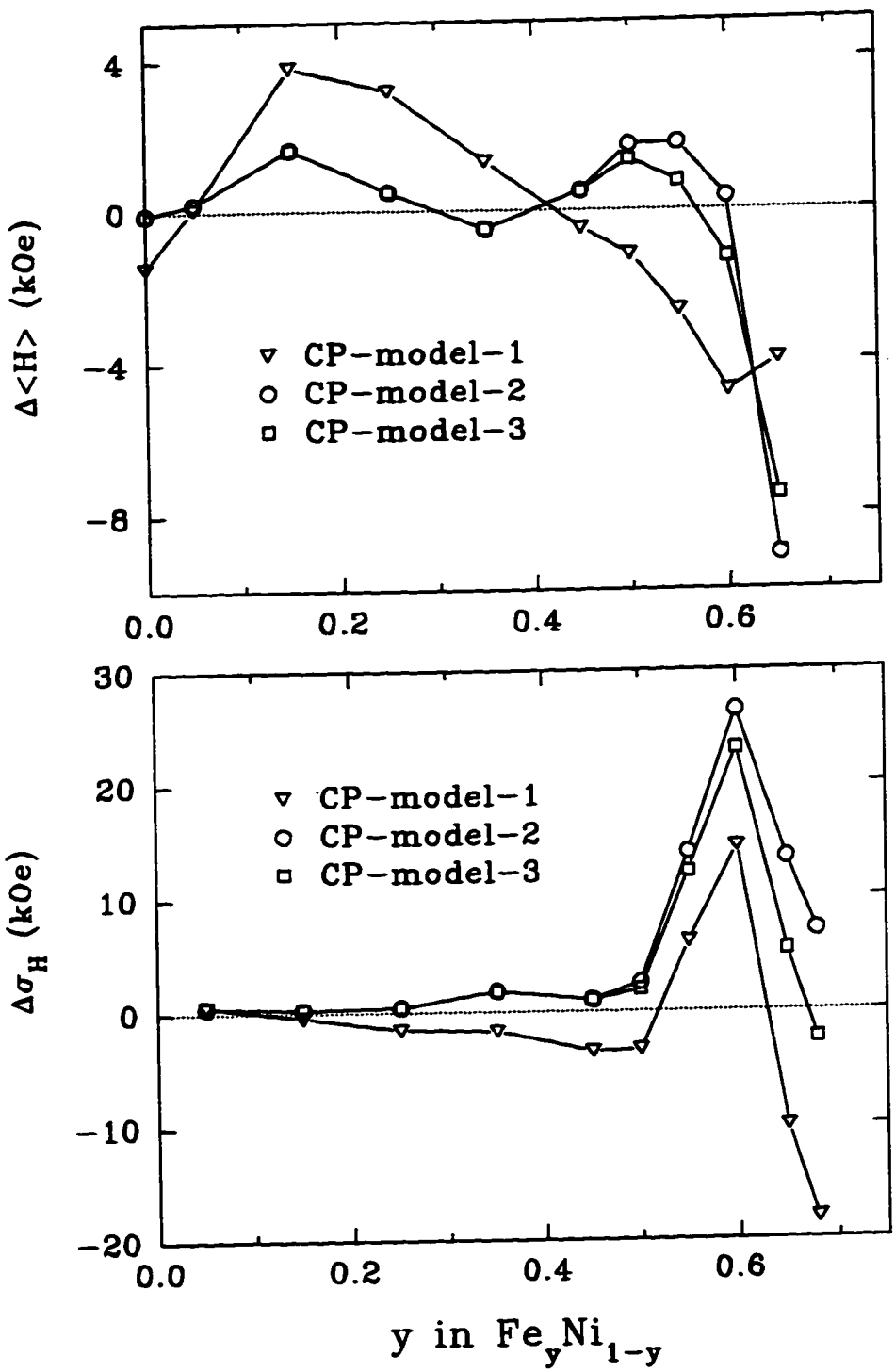

Figure 16.14 : Difference between the experimental average hyperfine fields $< H >$ and HFD standard deviations σ_H and the calculated results from the three coupling parameter models, as indicated.

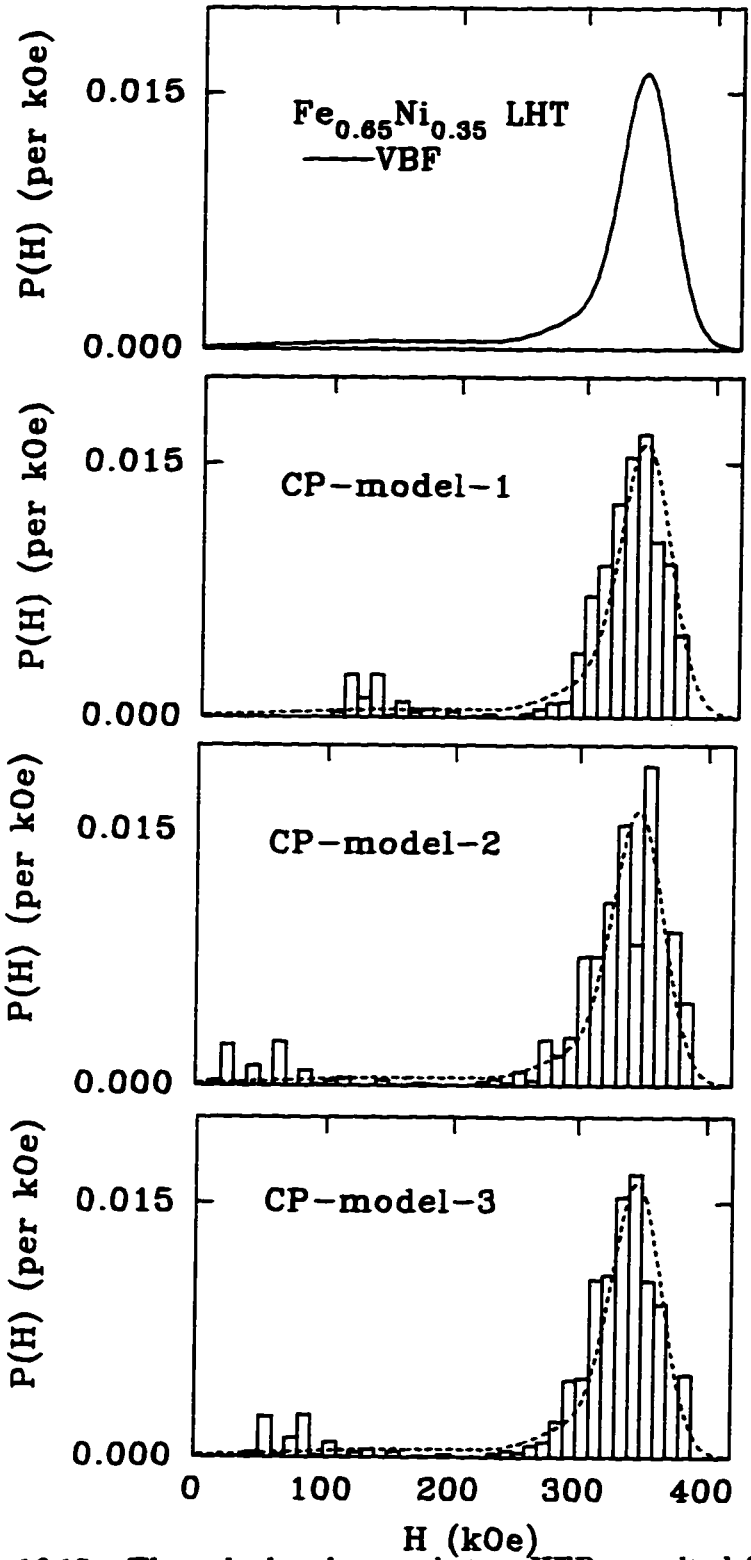

Figure 16.15 : The calculated ground state HFDs resulted from different hyperfine field models in comparison with the experimental HFDs for the Fe-rich alloys (y = 0.65, 0.60, 0.55 and 0.50) at LHT.

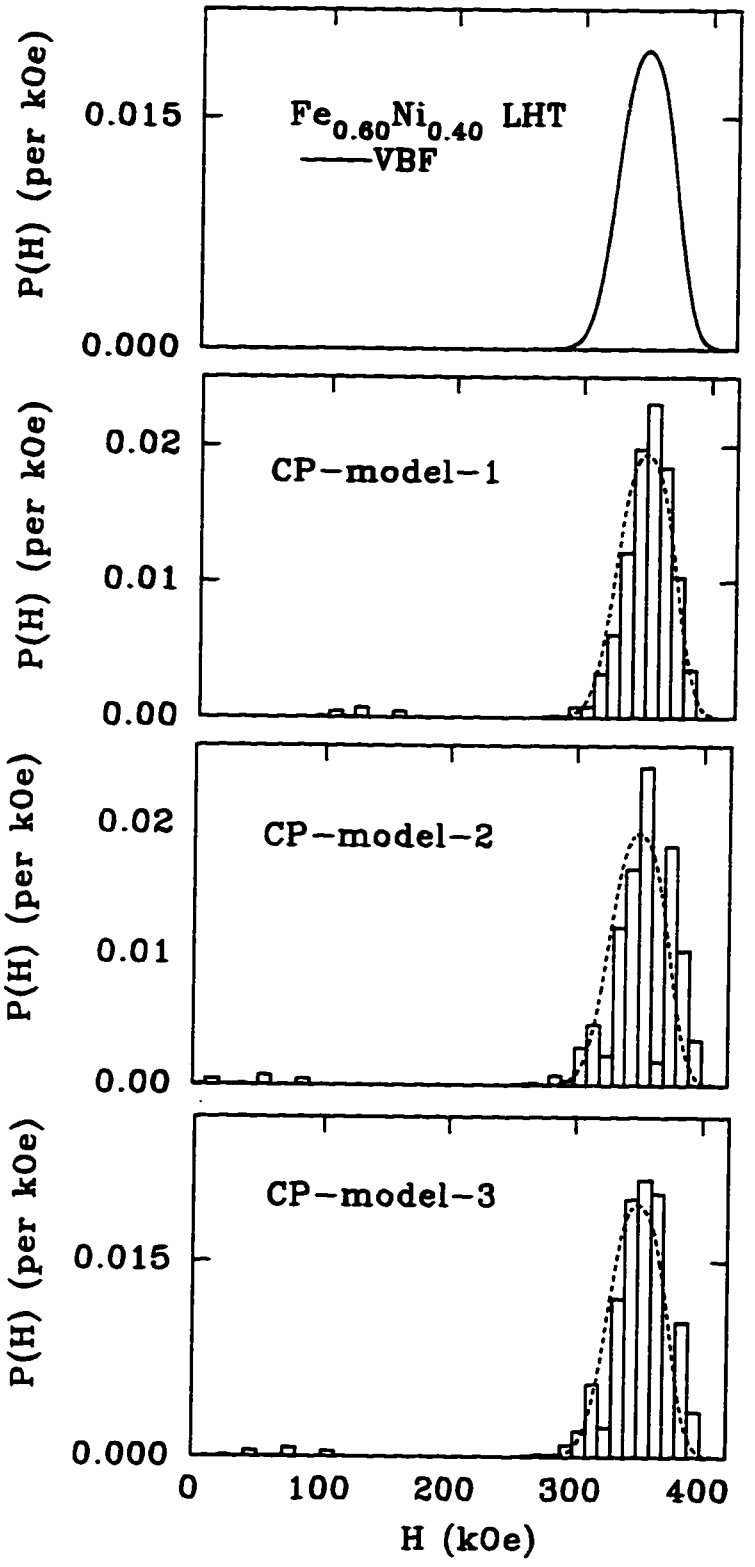

Fig.16.15 continued...

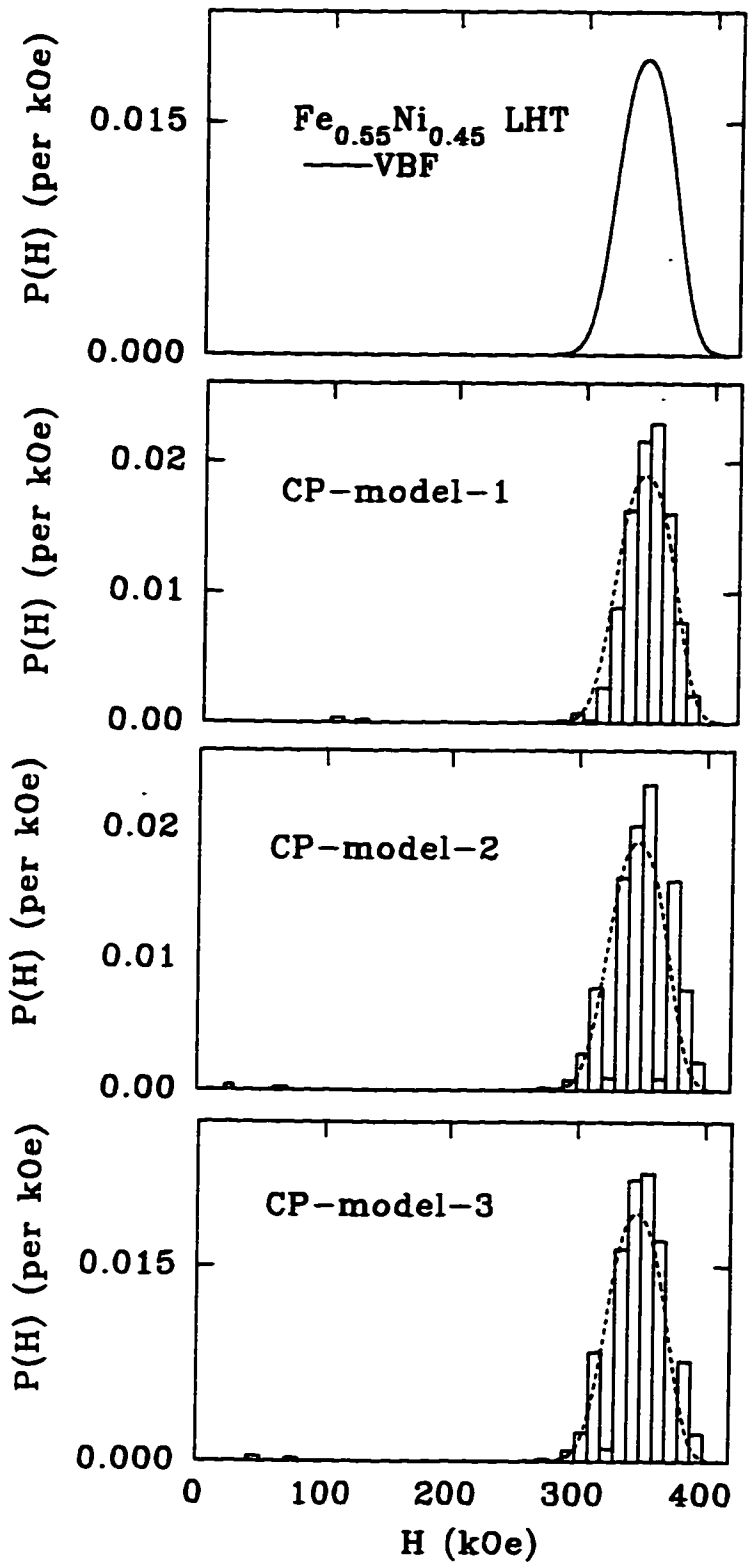

Fig.16.15 continued...

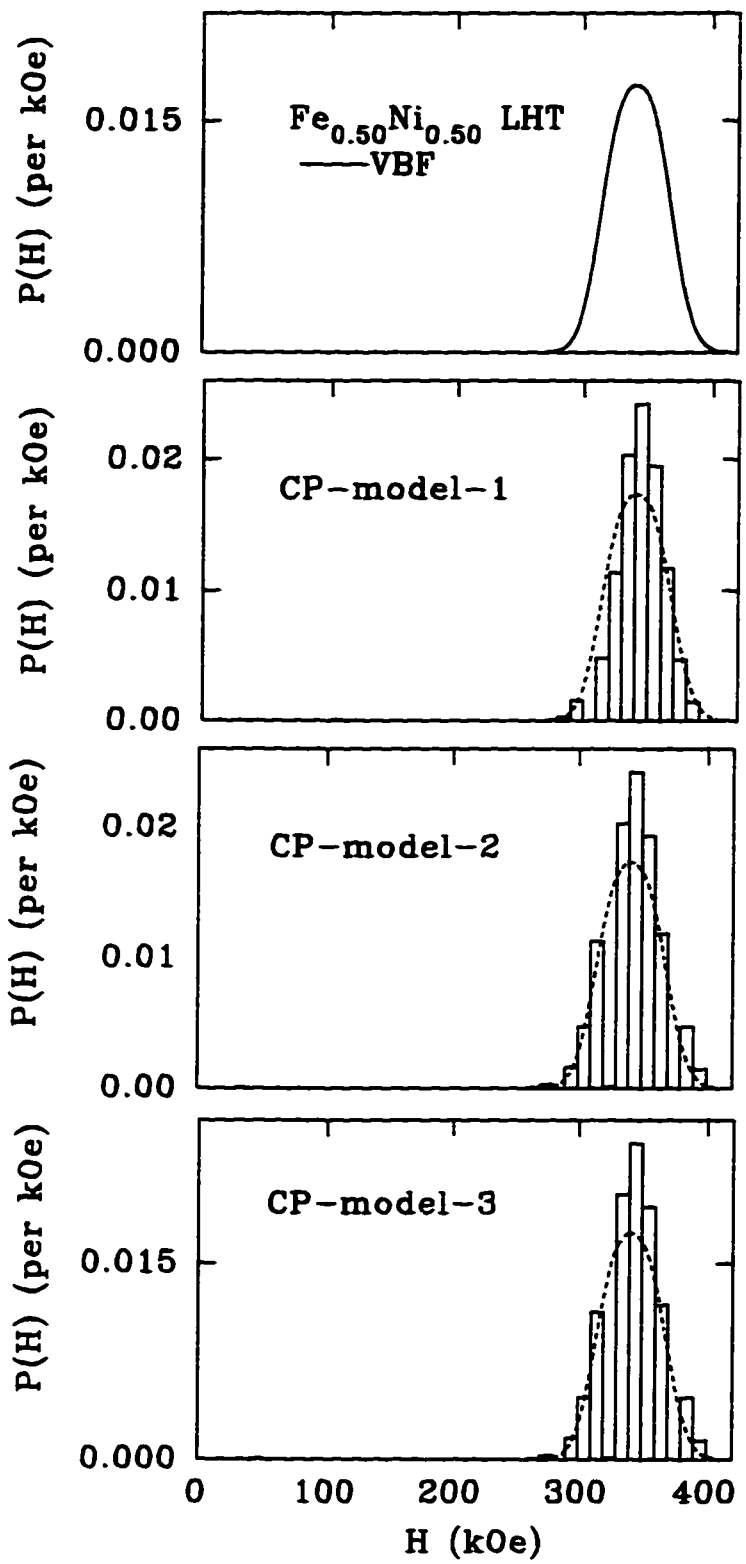

Fig.16.15 continued...

Chapter 17. SIMULATED HFDs AT HIGHER TEMPERATURES

17.1 Thermal Average Effect on HFDs

To study HFDs at non-zero temperatures using the MC simulation method, we chose Fe_yNi_{1-y} alloys with y = 0.50, 0.65 and 0.75 and a hypothetical fcc pure iron (high-spin γ-Fe) to show how HFDs change with temperature and composition. This is to demonstrate how the thermal average effect and latent antiferromagnetism simultaneously affect the HFDs of fcc Fe-Ni alloys.

Fig.17.1 shows the calculated HFDs and the corresponding simulated spectra at different T/T_C, using the four calculation steps described in section 15.1.

Like the HFD calculated at T = 0 K, the HFDs in different alloys at the same T/T_C are different, depending on their iron contents. This is from the effect of the latent antiferromagnetism (i.e. from composition-dependent non-collinear thermal average spin structures). On going from low temperature to higher temperature (from $T/T_C = 0$, to $T/T_C = 0.78$), the HFDs in each of the alloys (y = 0.50, 0.65 and 0.75) get broader and the centers of the distributions shift to lower field values. The HFDs are broader as the iron content increases. At $T/T_C = 0.96$, however, the HFDs become narrower and centered at very low field values, close to zero field. At y = 0.50 the average hyperfine field at $T/T_C = 0.96$ is not as low as that at y = 0.75 and 0.65. This agrees with the results in Part II, that the curve of $\mu(T)/\mu_{sat}(0)$ versus T is less flat than these curves for the other Fe-Ni alloys with higher iron contents.

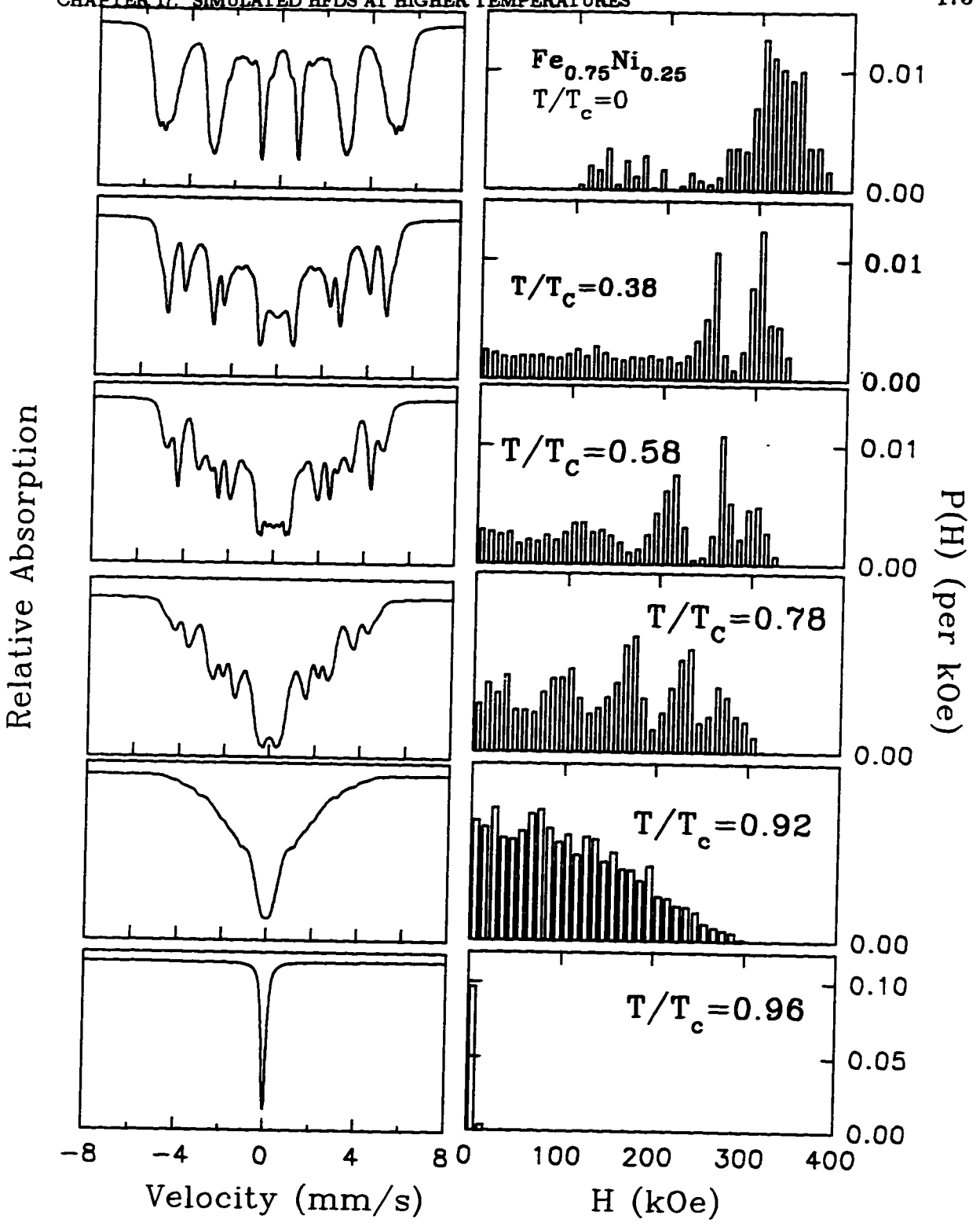

Figure 17.1 : The simulated HFDs at different T/T_C for Fe-rich alloys (y = 0.75, 0.65 and 0.50) and a fcc pure iron using J_{NiNi} = 700 K, J_{FeNi} = 355 K and J_{FeFe} = -25 K and the CP-model-1 coupling parameter model.

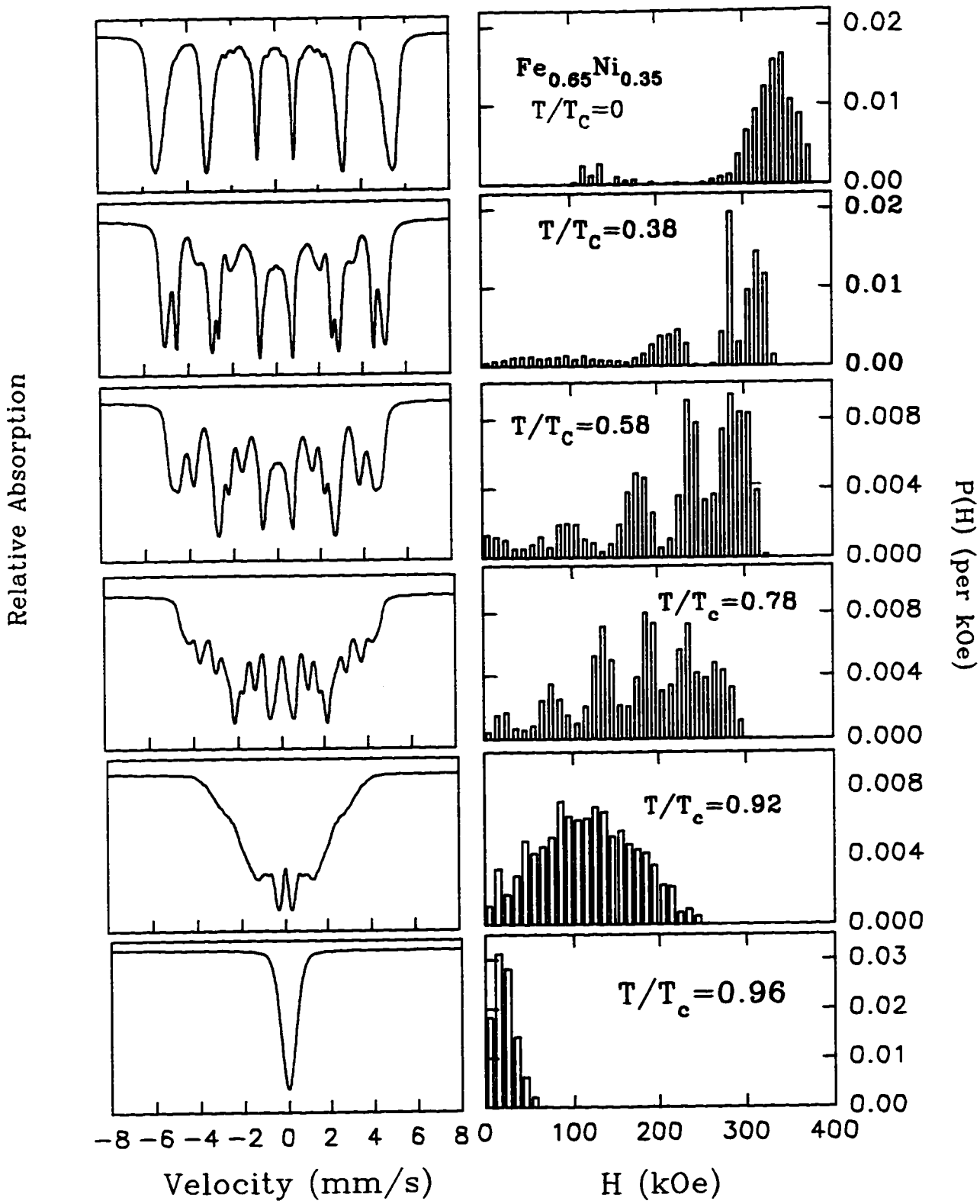

Fig.17.1 continued...

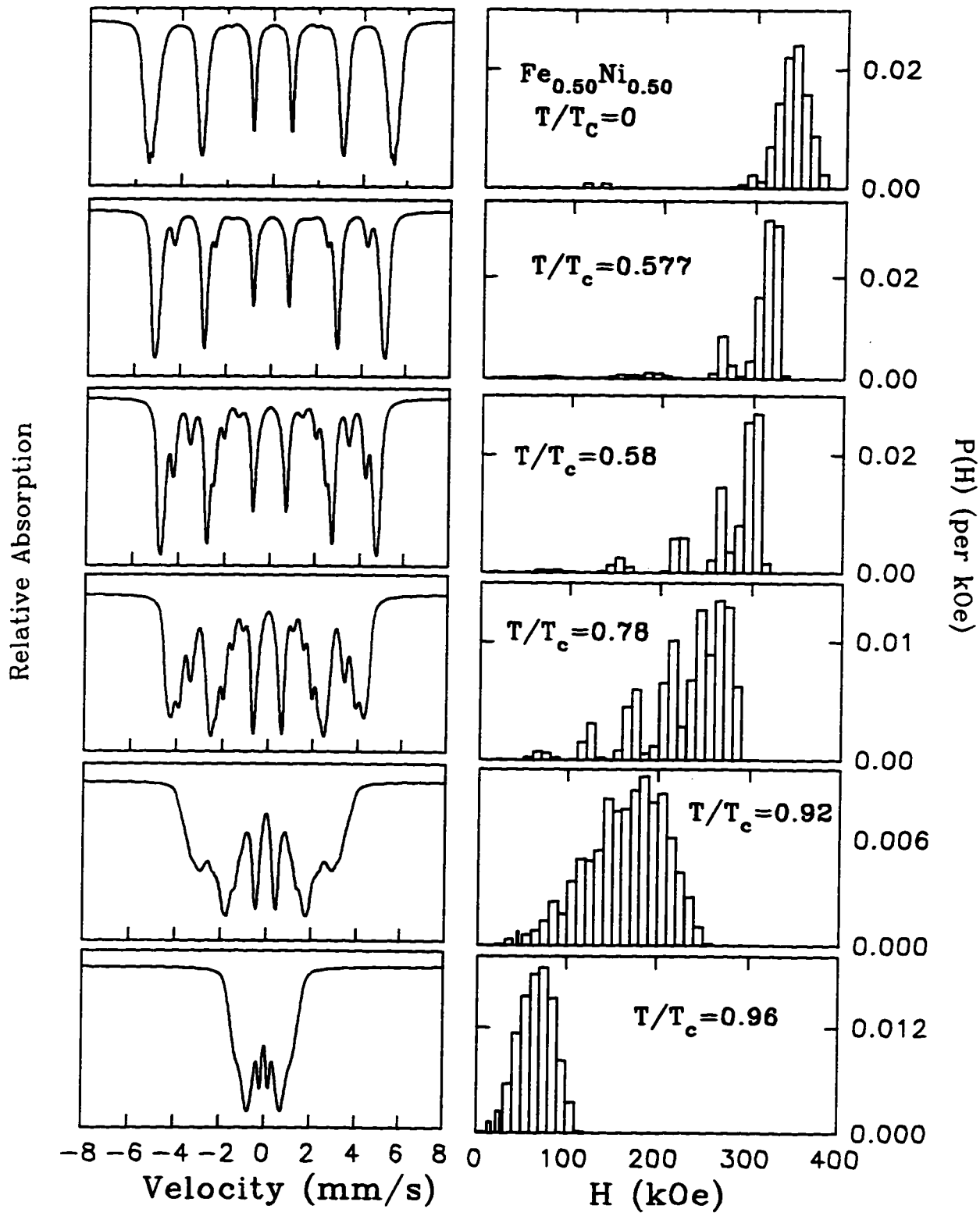

Fig.17.1 continued...

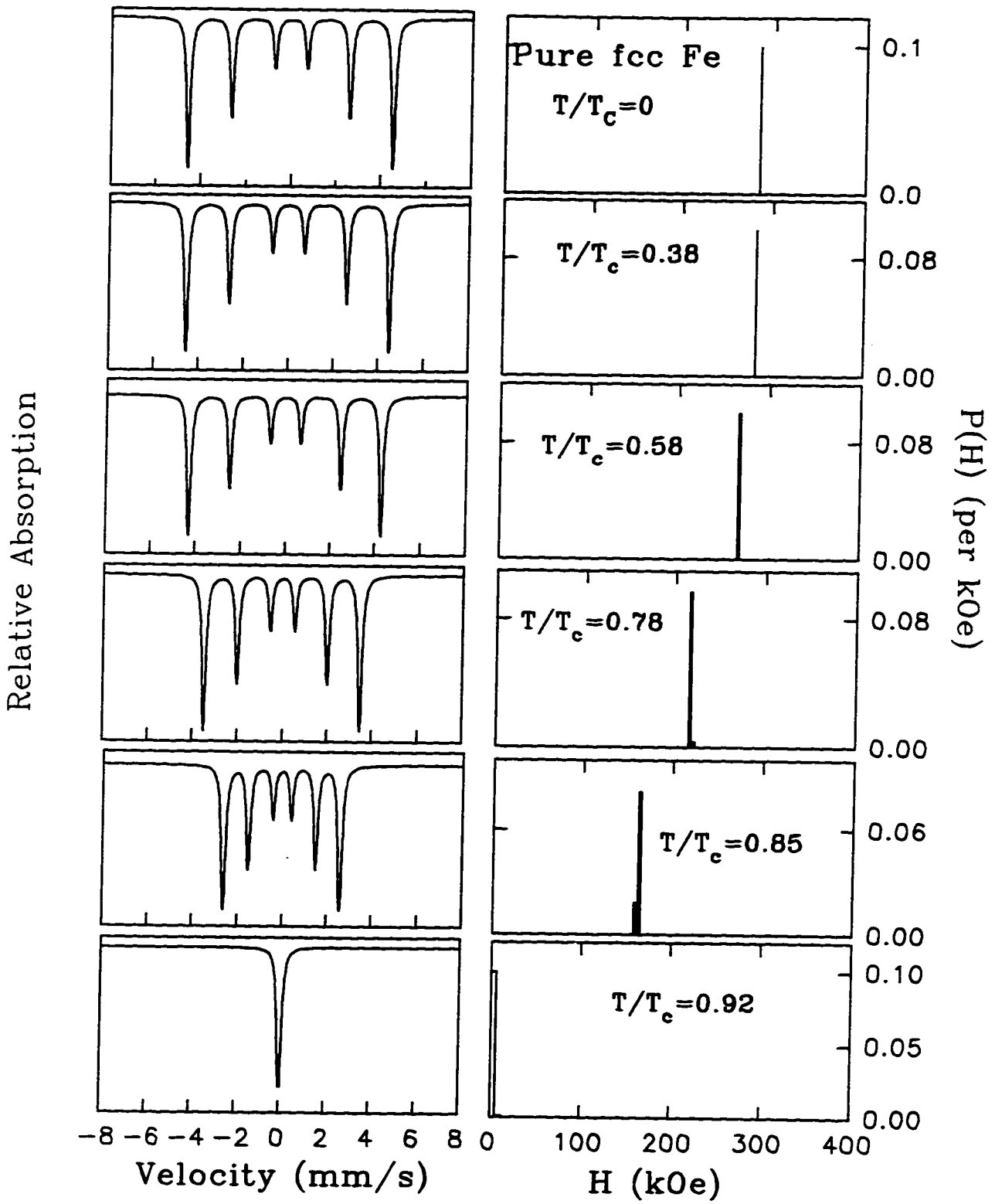

Fig.17.1 continued...

The HFDs in pure fcc iron are by symmetry always δ-functions, irrespective of the temperature. Comparing the HFD in fcc pure iron and in the alloys, we note that the HFDs in the alloys, in terms of shape and width, are very temperature and composition dependent and significantly different from that of the pure iron. In the alloys, the atomic moments and their local environments are affected by temperature and composition. In next section we will look into the distributions of average spin moments in the alloys.

The HFDs of the alloys in the intermediate temperature range (T/T_C = 0.38, 0.57 and 0.77) show discontinuities that lead to artificial structures in the corresponding simulated spectra, compared to the measurements [70]. That may be due to one or more of the approximations (i.e. assumptions) of our simple local moment model: the Ising approximation, NN interactions only, J_{ij} being temperature independent, finite cell size, etc. This needs to be explored further to improve higher temperature magnetic behavior simulations.

17.2 Thermal Effect on the Distributions of Average Atomic Moments in fcc Fe-Ni Alloys

To reveal the dependence of the HFDs on the surrounding magnetic moments which cause the local hyperfine fields, we calculate the atomic magnetic moment distributions for Fe atoms and for Ni atoms at y = 0.50, 0.65, 0.75 in Fe_yNi_{1-y} and in the pure fcc iron. Fig.17.2 shows the distribution of Fe atomic moments at different T/T_C at y = 0.75 and 0.65 in Fe_yNi_{1-y}. Fig.17.3 shows the moment distribution for Fe atoms at different T/T_C for y = 0.50 and for our hypothetical fcc pure iron. Fig.17.4 shows the nickel atomic moment distributions for y = 0.75 and 0.65. Fig.17.5 shows the moment distribution for nickel atoms at different T/T_C for y = 0.50.

Our calculations show that the atomic moment distributions for both iron and nickel species are δ-functions at T = 0 K, irrespective of the alloy composition. At y = 0.75 and 0.70, the Fe atomic moments take two values only, $\pm$ 2.8 μ_B, whereas for nickel atomic moments only one single value, 0.6 μ_B, is obtained.

As temperature rises, thermal effects cause the average atomic moment magnitudes to be distributed. The site-specific thermal average moments are no longer the same at each site. The values are spread from low (about zero) to high (about the saturation value) values depending on the local surroundings. This causes the non-zero temperature HFDs via Eq.3.10 of our phenomenological model (Chapter 3). That is why the HFDs at temperatures higher than T = 0 K present much broader distributions. As temperature increases the atomic moment distributions for both iron and nickel atoms get broader in a way that depends on the iron content because of the different signs and magnitudes of J_{FeFe}, J_{FeNi} and J_{NiNi}. When T is close to T_C, all the moments are close to zero values.

Comparing the HFDs and the atomic moment distributions we see that the two distributions are, in general, significantly different in character. They are not simply proportional to each other because a HFD is a probability distribution of hyperfine field magnitudes, where these magnitudes depend on both the magnitudes and orientations ($\pm$ in our Ising calculations) of the neighbouring thermal average atomic local moments. Each of these site-specific thermal average atomic moments in turn depends on its local environment, specified by the magnitudes and orientations of its neighbouring thermal average atomic moments.

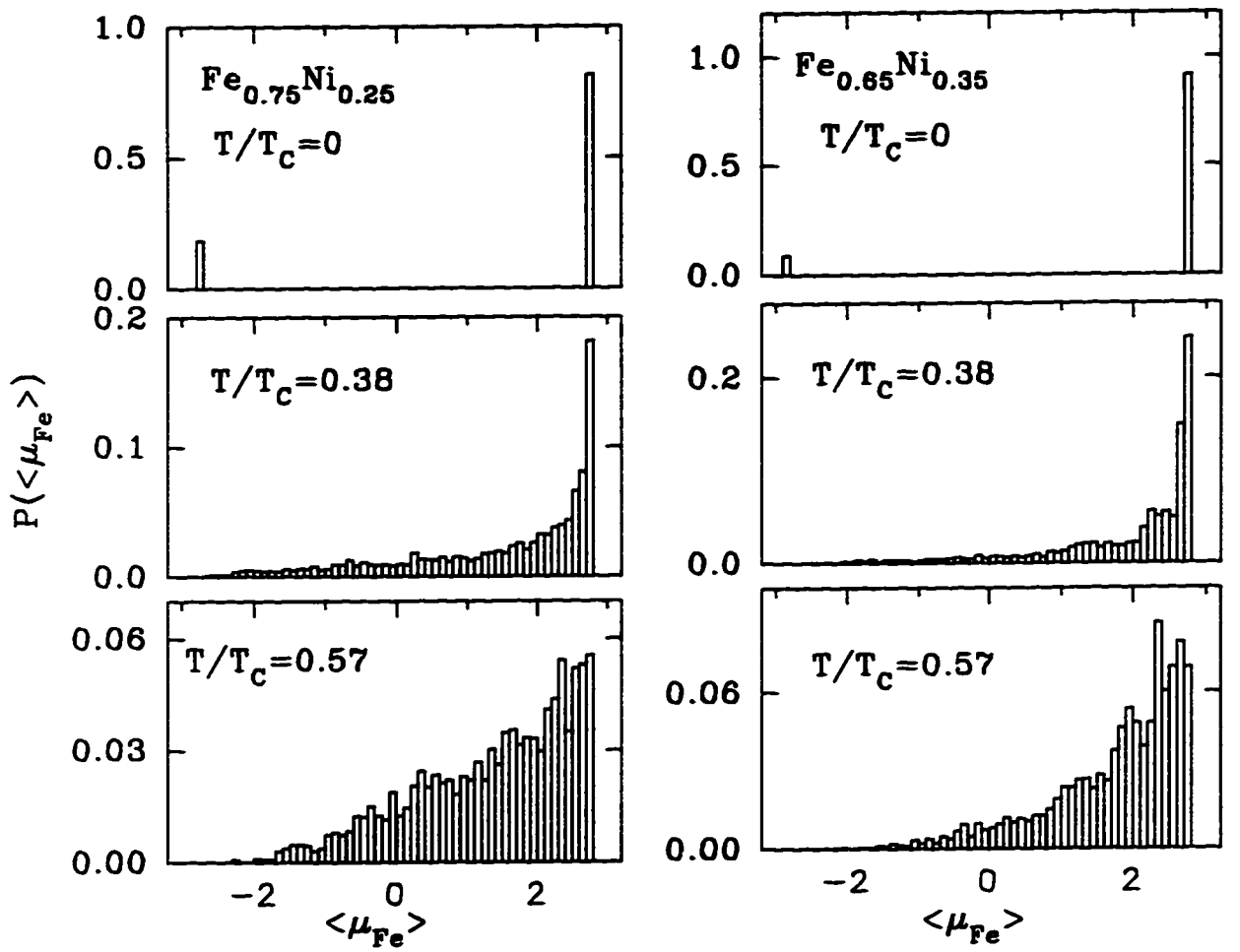

Figure 17.2 : The simulated Fe atomic moment distribution at different T/T_C for y = 0.75 and 0.65 in Fe_yNi_{1-y}.

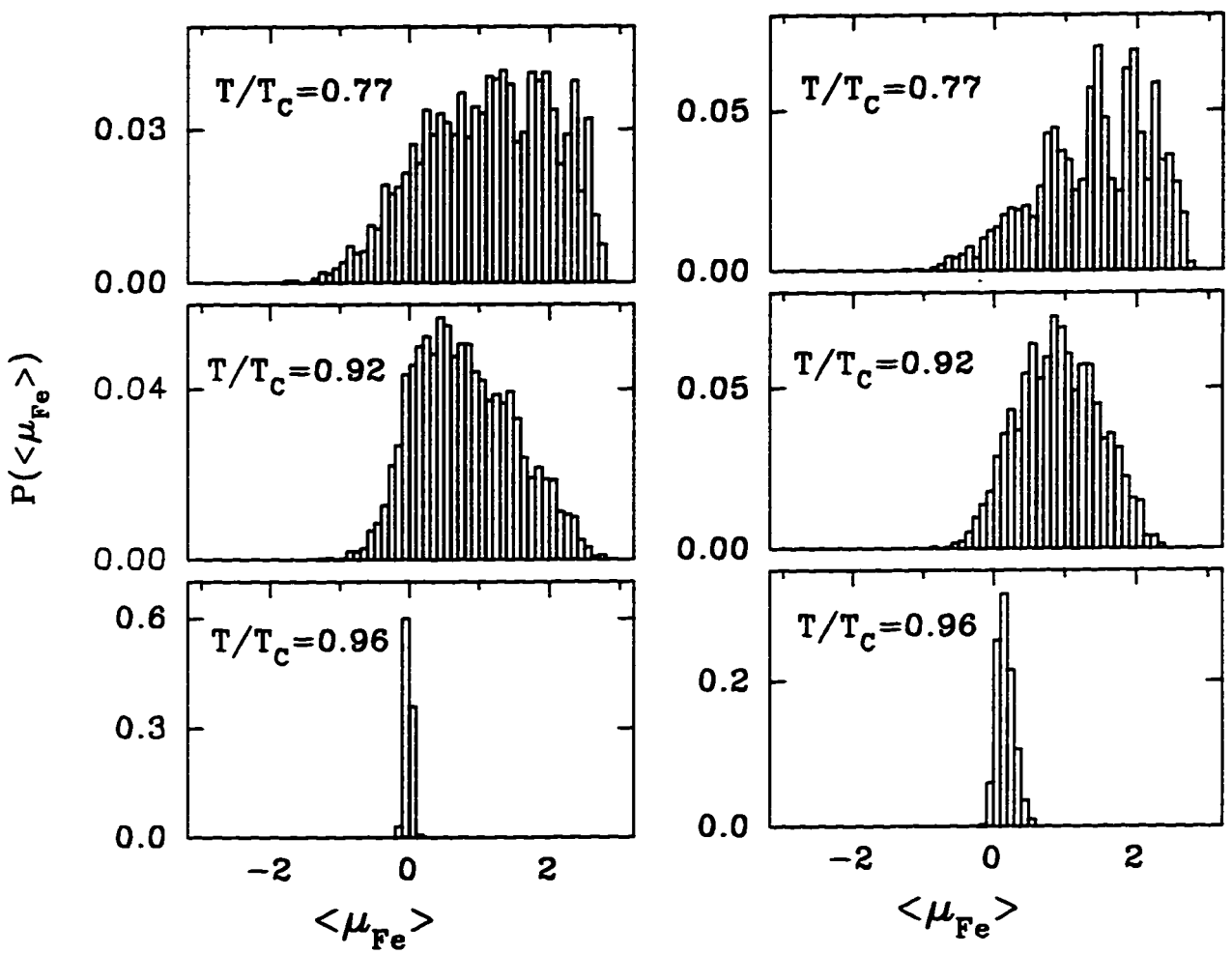

Fig.17.2 continued...

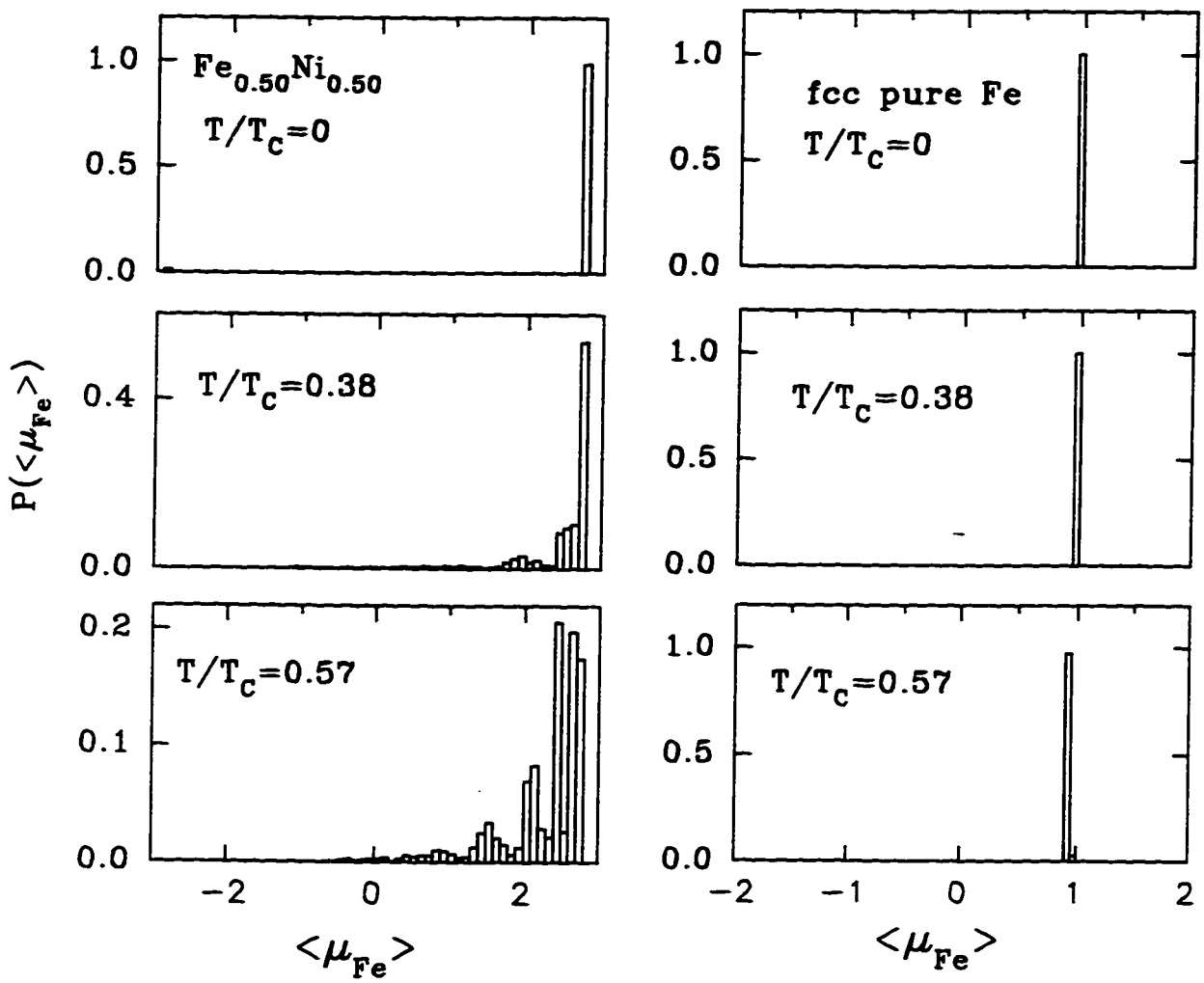

Figure 17.3 : The simulated Fe atomic moment distributions at different T/T_C for y = 0.50 and for fcc pure iron.

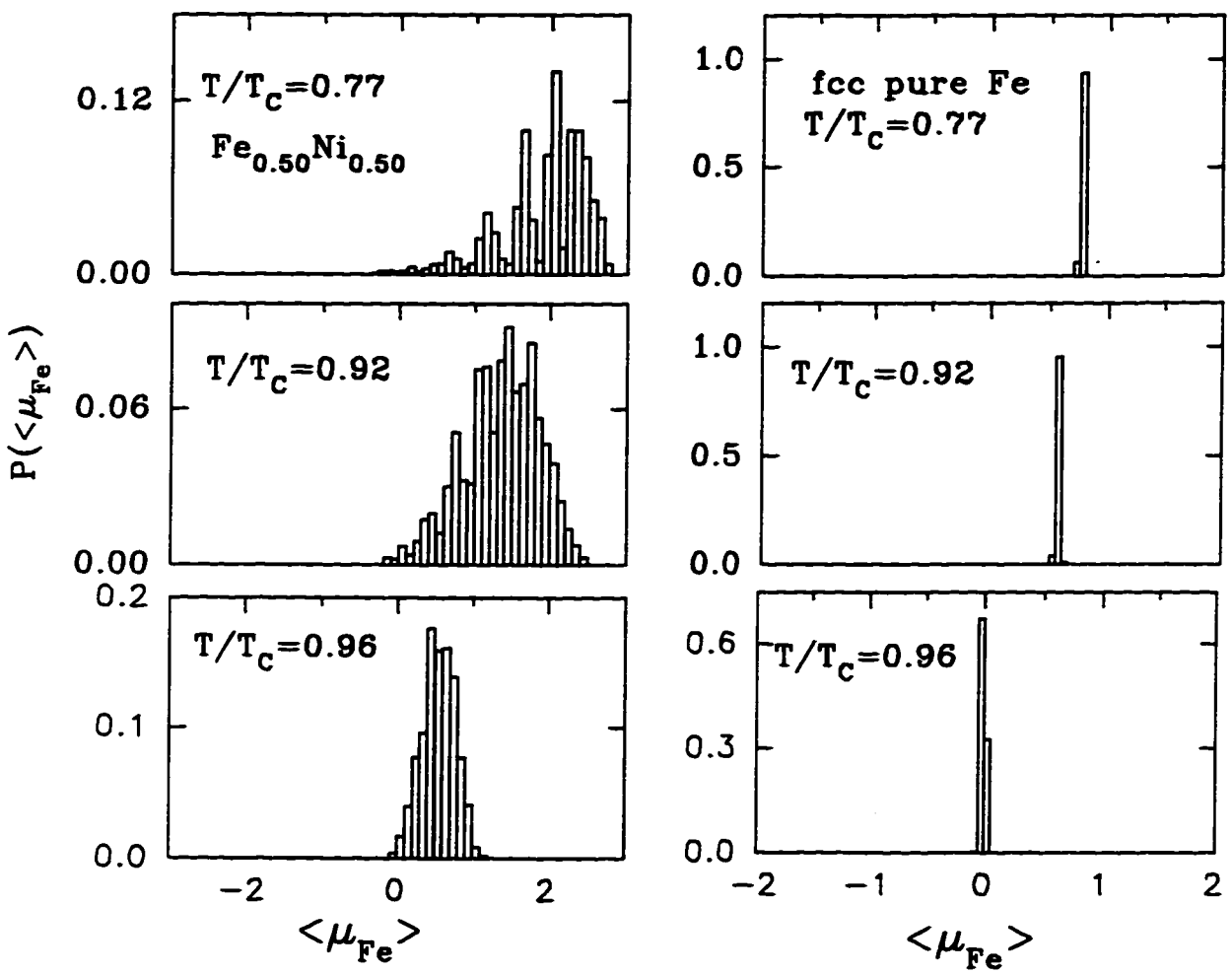

Fig.17.3 continued...

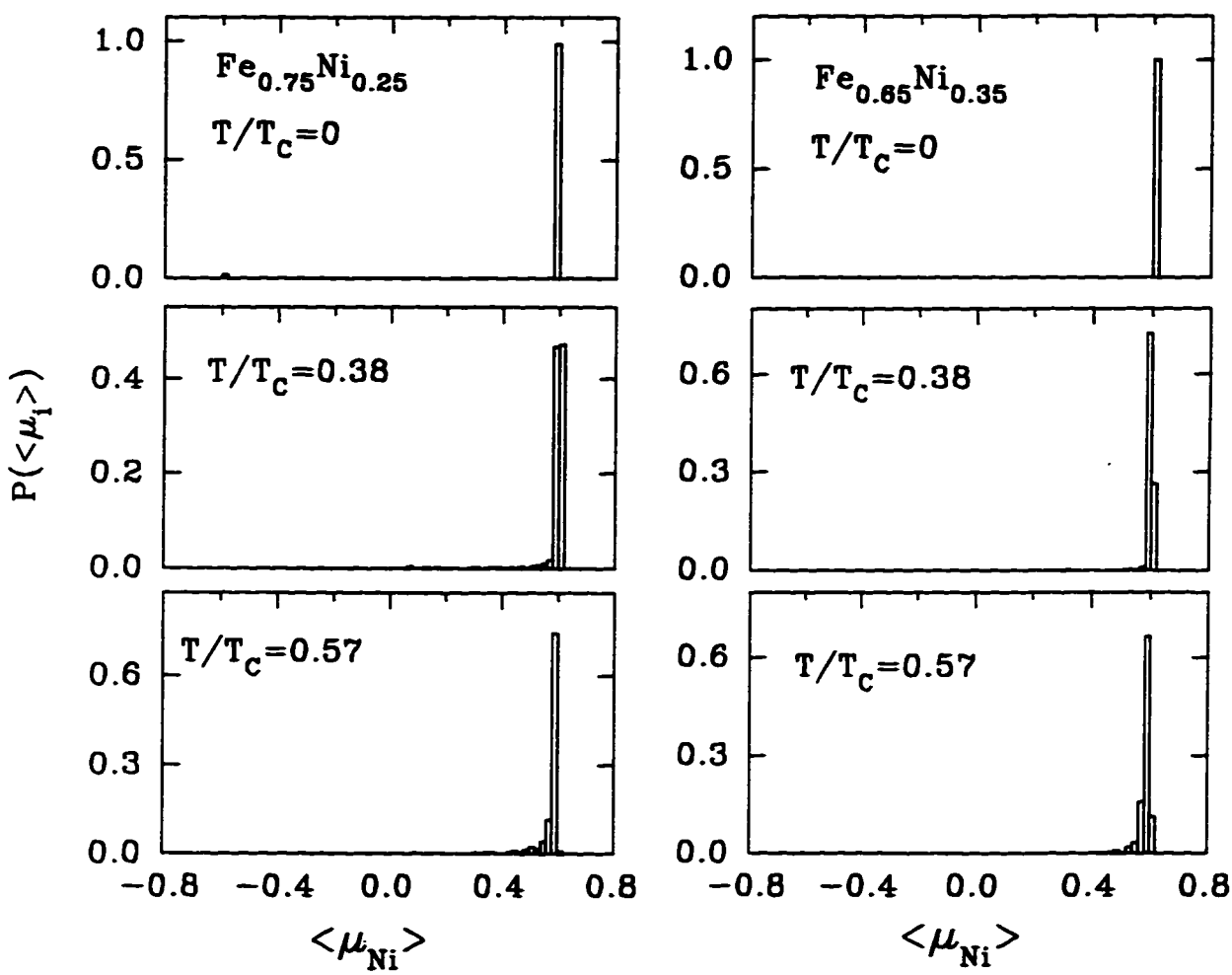

Figure 17.4 : The simulated Ni atomic moment distributions at different T/T_C in y = 0.75, 0.65.

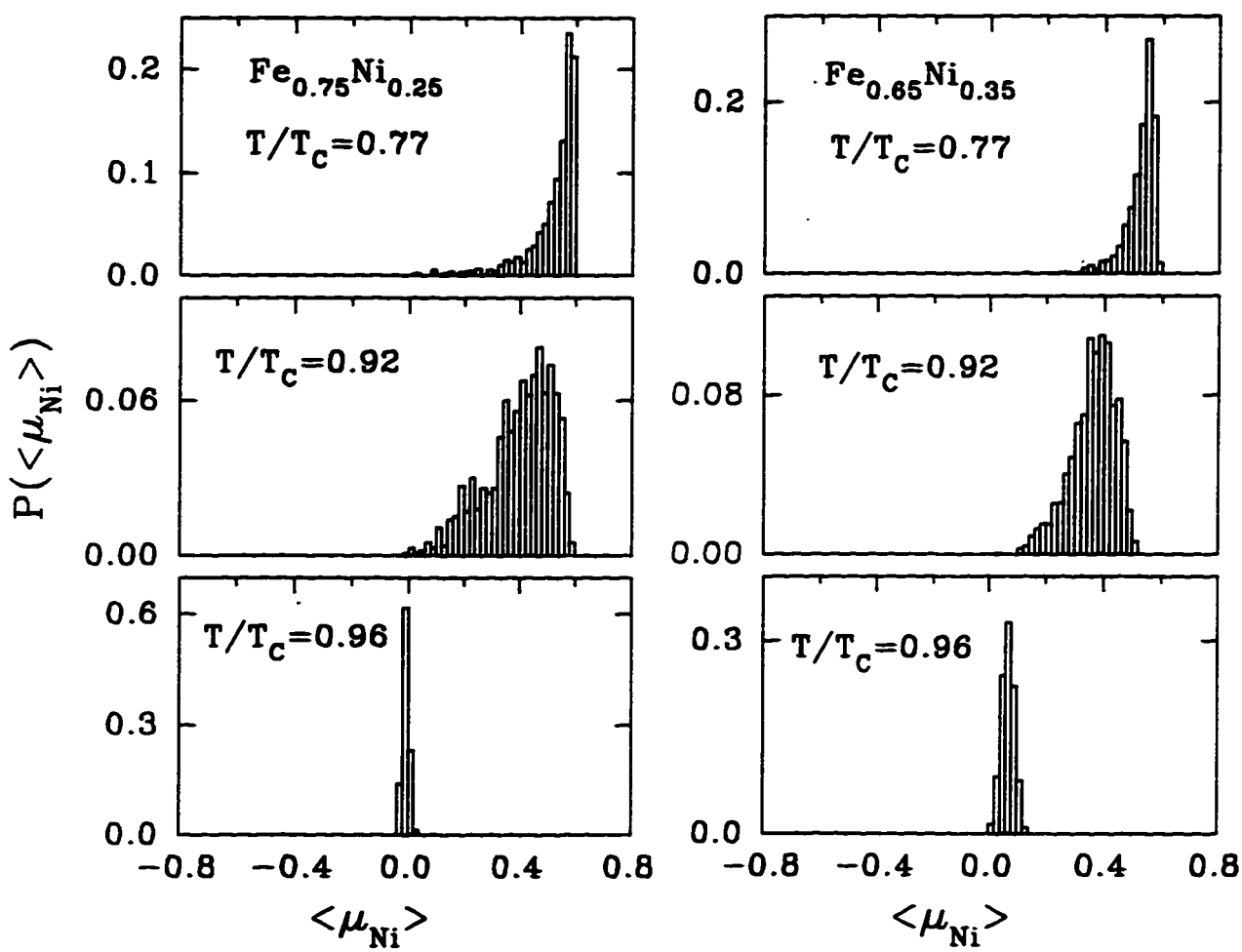

Fig.17.4 continued...

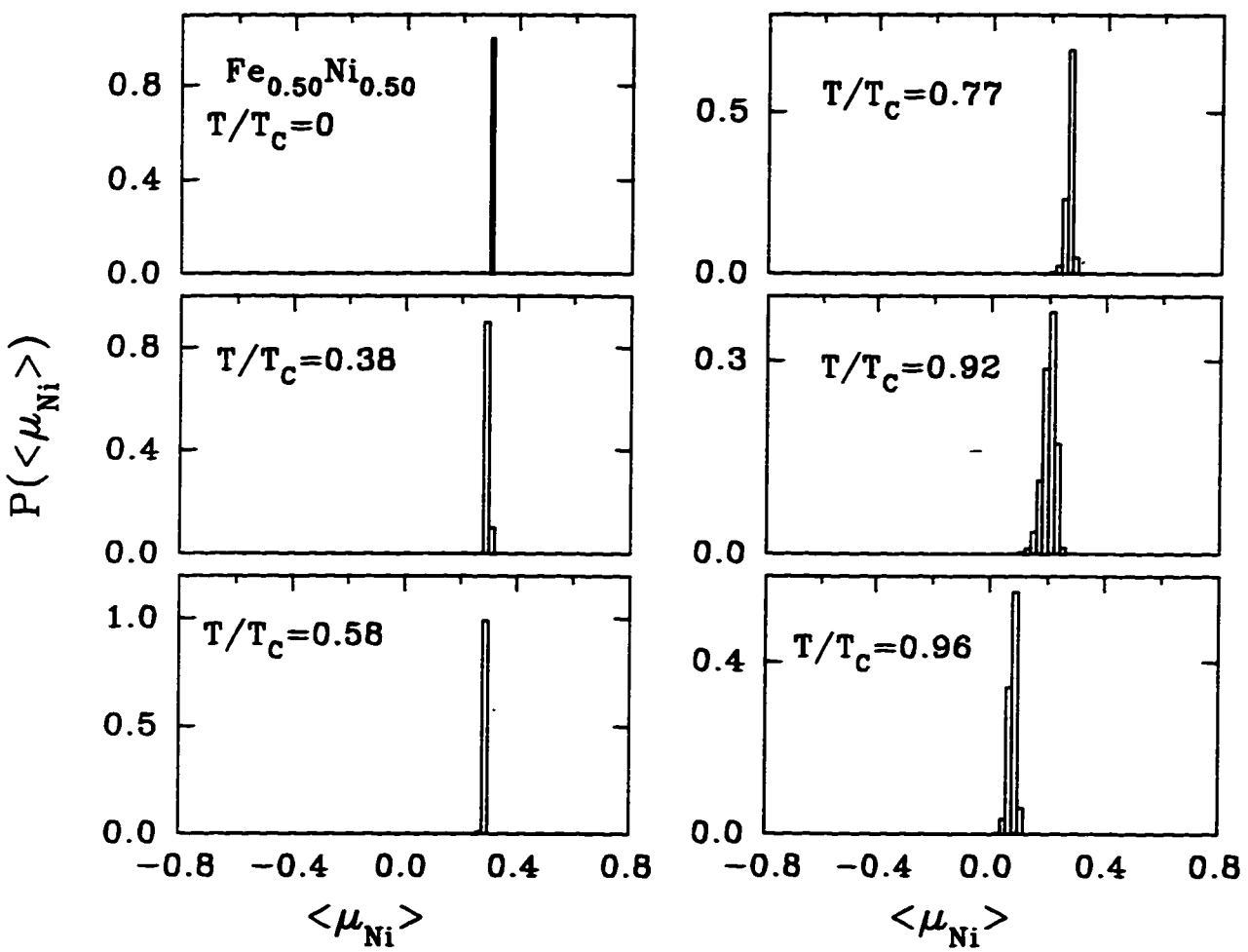

Figure 17.5 : The simulated Ni atomic moment distributions at different T/T_C in y = 0.50.

Chapter 18. CONCLUSION of Part III

With MC simulations and our phenomenological hyperfine field vector model (Part I) we obtain the ground state and non-zero temperature spin structures and their resulting HFDs as functions of composition in fcc Fe-Ni alloys. We show how the HFDs and the atomic moment distributions change with temperature and composition. The simultaneous thermal effect and the latent antiferromagnetism effect on the HFDs are illustrated. The atomic moment distributions of both iron and Ni atoms are also shown as functions of temperature, which elucidates the cause of the corresponding HFDs and their changes. The HFD calculation results lead us to a better understanding of the microscopic relationships between atomic moments, local chemical environments, spin structures, thermal effects and corresponding HFDs.

This is the first such calculation of HFDs in any magnetic alloy system. Comparing the calculated magnetic properties to the measurements for fcc Fe-Ni alloys, we see the success of the simple local moment model that makes quantitative calculations, of this complicated system, simple and gives good agreement between the calculated and measured magnetic properties. Meanwhile, we also see the model's limits due to its intrinsic simplifications: the Ising approximation, NN interactions only, finite size effects, composition and temperature independent J_{ij} values, etc.

Part IV

Simultaneous magnetic and chemical order-disorder phenomena in Fe_3Ni, FeNi, and $FeNi_3$

Chapter 19. INTRODUCTION

The importance of treating the magnetic and chemical (i.e. binding and atomic position exchange) degrees of freedom on an equal footing in magnetic alloys has often been recognized but such calculations usually only involve ground state properties or use approximations such as cluster-variation method and MFT [100, 101, 102]. Our calculations are among the first to treat this problem exactly, by MC simulations, that we apply to Fe-Ni alloys that are known or suspected to exhibit atomic order.

The Fe-Ni alloy system has complicated temperature-composition structural phase diagram at ambient-pressure [105, 106]. It includes: an Fe-rich body centered cubic (bcc) phase (α-phase), an fcc phase (γ-phase) that can be quenched over a broad composition range (0 - 70 at.% Fe at room temperature; Invar and Elinvar are two such alloys), a low-spin fcc phase (γ_{LS}-phase), and chemically ordered fcc phases centered at $\sim$ 50 and $\sim$ 25 at.% Fe (FeNi and $FeNi_3$ phases, respectively). A chemically ordered Fe_3Ni fcc phase also has often been proposed but its existence has never been substantiated by firm experimental evidence. In addition, high pressures stabilize a non-magnetic hexagonal close packed (hcp) phase (ϵ-phase) [107, 108, 109] that is closely related to the γ_{LS}-phase [106].

It was shown in Part II that a simple local moment model with three composition-independent pair-specific NN magnetic exchange parameters (J_{NiNi}, J_{FeNi}, and J_{FeFe}) reproduces all of the main purely magnetic properties of the quenched γ-phase alloys: the Curie point versus composition, the spontaneous saturation moment versus composition, the spontaneous magnetization versus temperature at each composition, and the high field (paraprocess) susceptibility at T = 0 K versus composition.

With the improvement of the local moment model by allowing J_{FeFe} to be dependent on the composition (Part III), we achieve a very good agreement between

the calculated ground state magnetic properties such as the saturation moment, average hyperfine field and HFDs and the measurements for all fcc Fe-Ni alloys. This shows again that the simple local moment model is useful to explain the magnetism of fcc Fe-Ni alloys including the Invar alloy.

In this Part IV, we assume that the same simple model of the magnetism holds for the chemically ordered γ-phase counterparts (Fe_3Ni, FeNi, and $FeNi_3$) and include the chemical order-disorder process using NN-only chemical bonds in MC simulations. The three constant NN J values used are: $J_{NiNi} = 700$ K, $J_{FeNi} = 355$ K and $J_{FeFe} = -25$ K.

In FeNi and $FeNi_3$ the degree of chemical order is known to have a significant effect on the measured magnetic properties and a previous MFT calculation [113] showed that magnetism measurably perturbs the $FeNi_3$ phase boundaries in the structural phase diagram. We now ask: how in detail does magnetism affect the chemical ordering processes? One might think that the effects should be very small because the chemical bond energies are much larger than the magnetic exchange bond energies. This however is incorrect: What matters is that the magnetic and chemical contributions to the change in energy on ordering are comparable. Indeed, we find large effects where the chemical and magnetic ordering processes are not simply mutually perturbed.

To our knowledge, only three previous MC studies [95, 114, 115] have simultaneously included magnetic and chemical order-disorder processes in alloys. These studies were concerned with bcc Fe-Al alloys in which only one species is magnetic and all magnetic bonds are ferromagnetic ($J_{FeFe} > 0$).

Ours is the first such study in which there are two magnetic species and the possibility of frustration. However, we do not go beyond NN-only chemical interactions nor do we treat entire regions in composition of the phase diagram as in previous studies. Instead, we mainly aim to illustrate both the necessity for taking magnetic and chemical interactions into account simultaneously and the most interesting features that arise. With Fe-Ni, except in limited regions of the phase diagram, one must allow coexisting bcc and fcc phases which greatly complicates true phase diagram calculations at arbitrary compositions.

We study the magnetic and chemical order-disorder transitions in fcc $FeNi_3$, FeNi, and Fe_3Ni, by MC simulations using the Ising approximation. The calculations are done: (1) with magnetic interactions only, assuming fixed preset degrees of chemical order, (2) with chemical interactions only, and (3) with both magnetic and chemical interactions acting simultaneously. As expected and known from measurements, the degree of chemical order is found to have a large influence on the magnetic transitions. On the other hand, although one might expect the effects of magnetism on the chemical ordering processes to be small (because the chemical bond energies are much larger than the magnetic exchange bond energies), one finds that the latter effects are also large.

Several new features arise that are not predicted by MFT or MC simulations with chemical interactions only. For example: (1) chemical order can be induced where using chemical interactions only leads to the prediction of no chemical order, (2) chemical segregation can be induced where using chemical interactions only leads to the prediction of no chemical segregation, (3) $FeNi_3$ and Fe_3Ni are found to have significantly different chemical ordering temperatures where chemical interactions only lead to equal ordering temperatures, (4) chemical ordering temperatures are significantly shifted from their chemical interactions only values, even when the chemical ordering temperature is larger than the magnetic ordering temperature (or Curie point), (5) abrupt steps can occur in the spontaneous magnetization at the chemical ordering temperature, when the latter is smaller than the magnetic ordering temperature, and (6) non-linear relations arise between the chemical ordering temperature and the usual differential bonding parameter $U \equiv 2U_{FeNi} - U_{FeFe} - U_{NiNi}$, where the U_{ij}s are the near neighbour pair-wise chemical bonds.

Chapter 20. MC METHODS

As is always the case in such calculations [96], we disallow the phonon degrees of freedom and ignore thermal expansion and elastic strain effects, etc. We also disallow all types of lattice defects such as vacancies, interstitials, inter-grain boundaries, magnetic domain walls, etc. We take only the chemical and magnetic (i.e. atomic and spin configuration) disorders into account and conveniently model both using Ising model statistics by usual MC methods.

We have used lattice sizes, in units of the fcc conventional unit cell edge length, of 10×10×10, 15×15×15, and 20×20×20 (corresponding to 4000, 13500, and 32000 atoms, respectively), with periodic boundary conditions. We find that the lattice size does not affect the reported calculated properties for these sizes.

Three types of simulations were performed for each alloy: 1) magnetic-only excitations allowed with a set predetermined chemical order, 2) chemical-only processes considered with magnetic interactions ignored, and 3) chemical and magnetic excitations allowed simultaneously.

For case-1, the usual metropolis single flip algorithm was applied (Part II). Here, the Hamiltonian is:

$$H = -\sum_{ij} J_{ij}(\mu_i\mu_j/4\mu_B^2)\sigma_i\sigma_j, \tag{20.1}$$

where the sum is over all NN pairs, μ_i is the atomic moment at site-i, μ_B is the Bohr magneton, J_{ij} is either J_{NiNi}, or J_{FeNi} or J_{FeFe} depending on i and j, and σ_i is the usual Ising variable (or spin) equal to ± 1.

For case-2, rather than work in the usual grand-canonical ensemble where the composition is controlled by a chemical potential [96], we work directly in the canonical ensemble with fixed composition and use the following algorithm rather than map onto the equivalent spin system: two sites are selected at random and the atoms at these site are interchanged if they are of different species and the MC condition

is satisfied. The same final configurations were found if the two sites were imposed to be NN sites however equilibration times were much longer. As in the magnetic calculation, we avoid the problem of domain walls by starting with a perfectly ordered state at T $\simeq$ 0 K and moving up in temperature with small enough steps, using the previous equilibrium state as the new initial state.

For case-3, the same strategy for avoiding domain walls is used except that the system is spin-equilibrated at the new temperature before the MC algorithm that combines both chemical and magnetic equilibration is applied. The latter algorithm consists in picking two atoms of different species at random. One also chooses one of the following three options at random: (i) the spins of the two atoms are not changed, (ii) the spin of one atom is flipped, (iii) both spins are flipped. One then exchanges the two atoms (preserving their new spin orientations) if the MC condition with the chosen spin option is satisfied. This algorithm again allows us to work at a constant chosen composition.

Three programs corresponding to the above three cases are given in Appendix A and C. "CARLO8.FOR", the same program used in Part II, is given in Appendix A. It calculates the atomic moment averaged over the whole lattice at a given temperature and a composition. It presets the atoms either in perfectly ordered or in random positions. It reads in the three Js, and outputs the average atomic moment as a function of temperature. "CARLO4D.FOR" is given in Appendix D as D-1. It calculates the degree of atomic order of the alloy as a function of temperature, using chemical interation alone. It reads in three chemical bond parameters only and outputs the the atomic order parameter as a function of temperature. "MCM-CRT.FOR" is the program to calculate the both the magnetic order and chemical order paprameters simutaneously as a function of temperature. It is given in Appendix D as D-2.

Chapter 21. RESULTS AND DISCUSSION

Each alloy of interest has a single true equilibrium magnetic ordering temperature (or Curie point), T_C(equil), and a single true equilibrium chemical (or atomic) ordering temperature, T_a(equil). At and above T_C(equil), the alloy can have long range chemical order (if T_C(equil) < T_a(equil)) or short range chemical order only (if T_C(equil) > T_a(equil)). Similarly, at and above T_a(equil), the alloy can have long or short range magnetic order. In addition, magnetic ordering temperatures of non-equilibrium (metastable) states can be measured. For example, the alloy can be quenched from the melt into an almost perfectly random chemical state and then its magnetic transition, T_C(random), is measured in a time too short to allow significant chemical ordering. Similarly, when T_C(equil) << T_a(equil), the magnetic ordering temperature of the perfectly chemically ordered state, T_C(ordered), is approximately given by T_C(equil).

21.1 Magnetic Interactions Only

In this section, we simulate the magnetic properties of Fe_3Ni, FeNi, and $FeNi_3$ alloys that are either in a perfectly ordered chemical state or in a perfectly random chemical state. This shows conclusively the large effect that the degree of chemical order is predicted to have on the magnetic properties. The NN magnetic exchange constants (J_{ij}s in Eq.20.1) that we use are those obtained from a detailed comparison between simulations and experiments on quenched chemically random state alloys in the entire accessible composition range: J_{NiNi} = 700 K, J_{FeNi} = 355 K, and J_{FeFe} = -25 K. These correspond to magnetic bond energies ($| J_{ij}\mu_i\mu_j/4\mu_B^2 |$) of 65, 150, and 50 K, respectively.

The crystal structure of the chemically ordered state of $FeNi_3$ is the $L1_2$ structure which is shown in Fig.21.1. The results for $FeNi_3$ are illustrated in Fig.21.2 where

the spontaneous average moment per atom, μ, and the zero field average magnetic energy per atom, E_{magn}, are shown as functions of temperature for the chemically ordered and random states. Here μ(T) shows the usual finite size effects just above T_C, however, E_{magn}(T) does not have noticeable finite size effects and its tails above T_C are due to true magnetic short range order. The magnetic ordering temperatures are equally well estimated from the μ(T) curves or from the inflection points in the E_{magn}(T) curves. These estimates give sufficiently small errors of approximately 5-10 K ($\sim$ 1-2 %) such that it was not necessary to use the cumulant intersection method to locate T_C.

The simulation values for T_C(ordered) and T_C(random) in $FeNi_3$ are 1180 and 870 K, respectively. This compares favourably with the best experimental values of 940 [116] and 850 K [7], respectively. The experimental value for T_C(ordered) is an underestimate related to the fact that the measured T_a in $FeNi_3$ is 770 K [118], significantly below T_C(ordered) at temperatures where diffusion is relatively fast for the magnetization measurements used. Our simulation therefore predicts the true value of T_C(ordered), to be compared with an eventual value from a sufficiently fast measurement. Even an instantaneous measurement of T_C by heating would also represent an underestimate, however, because the perfectly chemically ordered initial state cannot be prepared and is ultimately limited by the required annealing times at low temperatures.

Finally, note that the simulated saturation moments per atom of both chemically ordered and random $FeNi_3$ are exactly the same and equal to the measured value of 1.15 μ_B. This value corresponds to all Fe and Ni moments being ferromagnetically aligned (i.e. $0.25\times2.8\mu_B + 0.75\times0.6\mu_B$). The difference in ground state magnetic energy per atom of the chemically ordered and random alloys is E_{magn}(ordered;T=0) - E_{magn}(random;T=0) = -107 K.

The crystal structure of the chemically ordered state of FeNi is the $L1_0$ structure which is shown in Fig.21.3. The results for FeNi are illustrated in Fig.21.4. Here, the simulation values for T_C(ordered) and T_C(random) are 1020 and 820 K, respectively. The latter compares well with the measured value of 785 K [7]. Because of the low chemical ordering temperature of only 593 K [120] for this alloy, the measured

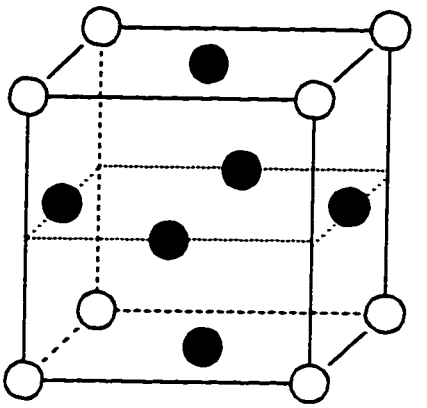

Figure 21.1 : Conventional unit cell of chemically ordered $FeNi_3$(or Fe_3Ni) with filled circles representing Ni (or Fe) atoms and open circles representing Fe (or Ni) atoms.

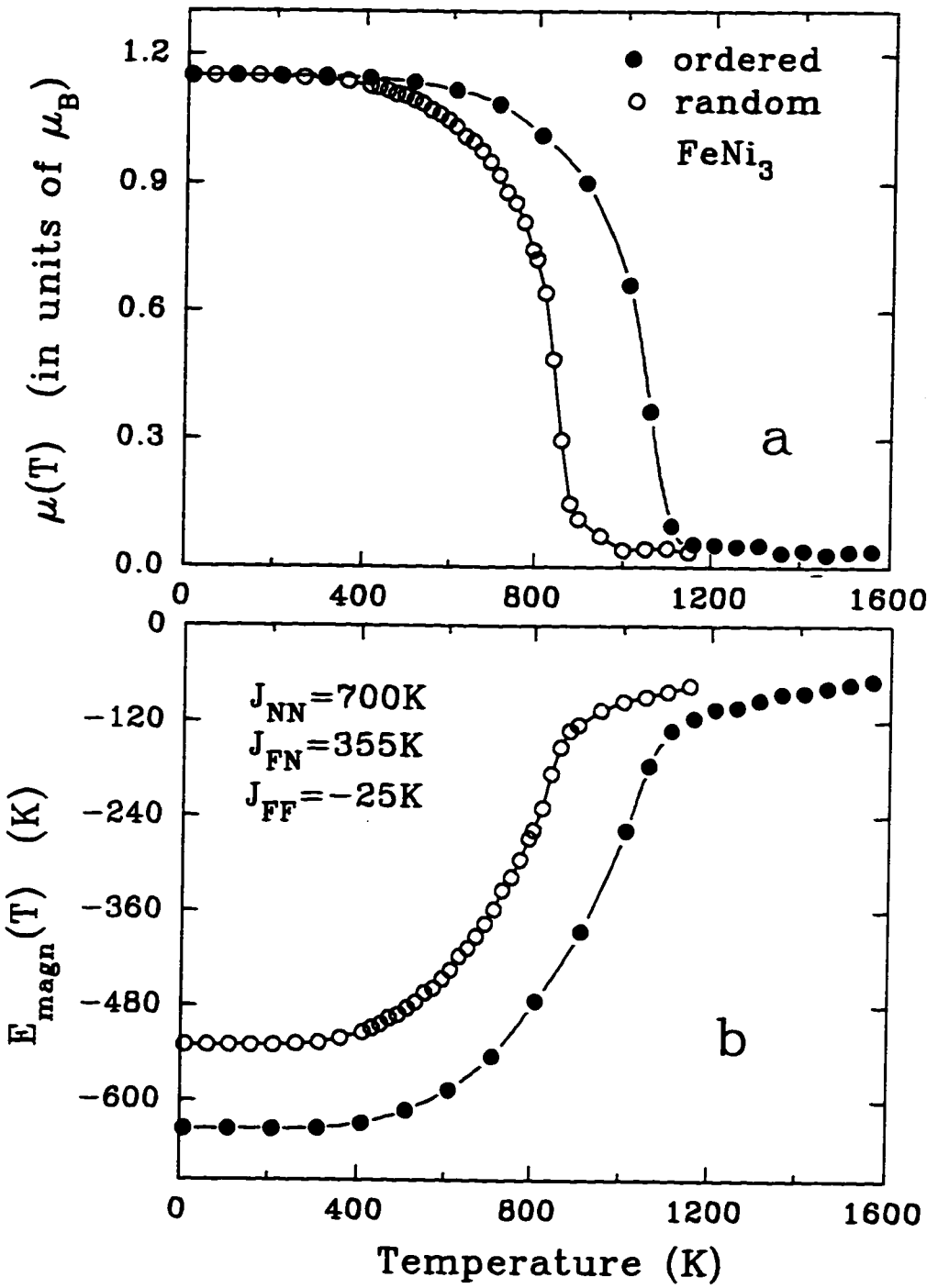

Figure 21.2 : MC simulated magnetic properties of $FeNi_3$ allowing only the magnetic degrees of freedom and assuming either perfect chemical randomness (open circles) or perfect chemical order (filled circles): (a) spontaneous average moment per atom versus temperature, (b) average magnetic energy per atom versus temperature.

T_C(ordered) for FeNi should be considered an underestimate and is 840 K [121]. Indeed, an FeNi sample with significant chemical order has, to our knowledge, never been synthetically produced by simple annealing. Particle irradiation is required in the laboratory and most of what is known about chemically ordered FeNi comes from iron meteorite studies where it is called tetrataenite [106].

For FeNi, the chemically ordered state again has a higher T_C but the spontaneous magnetic moment curves for the ordered and random phases now have two notable differences that were not exhibited in $FeNi_3$. First, the saturation moments per atom are significantly different. That of the chemically ordered phase is 1.70 μ_B corresponding as expected to complete ferromagnetic alignment ($0.5\times2.8\mu_B$ + $0.5\times0.6\mu_B$) whereas that of the chemically random phase is 1.68 μ_B corresponding to 0.71 % of the Fe moments being in local environments such that they are antiferromagnetically aligned with the sample magnetization. Secondly, the μ(T) curve for the chemically random phase is flattened in comparison with that of the chemically ordered phase. This is a common effect of disorder in magnetic systems and arises from the fact that there are many local environments in which the moments can be thermally excited even at the lower temperatures compared to T_C.

The crystal structure of the chemically ordered state of Fe_3Ni is taken to be the same as that of $FeNi_3$ (Fig.21.1) with Fe and Ni atoms interchanged. Chemically ordered Fe_3Ni has never been synthesized or conclusively observed in nature. At this composition, synthetic alloys are usually bcc since the bcc/fcc instability occurs at $\sim$ 70 at.% Fe at RT. Nonetheless, there have been suggestions [106] that the occurrence of chemically ordered Fe_3Ni could resolve various difficulties related to the metallurgy of both particle irradiated synthetic Fe-Ni alloys and meteoritic Fe-Ni alloys. It therefore seems worthwhile to extend our simulations to Fe_3Ni and to consider our results as predictions that cannot yet be compared with sufficiently complete experimental data.

Note that, at this composition, a low-spin fcc state may be more thermodynamically stable than the high-spin fcc state [106, 122] that we model for the sake of describing its characteristics. Also, recently, bulk amounts of high-spin fcc phase have been produced by mechanical alloying, to Fe contents as high as 80 at.% Fe

[123].

The results for Fe_3Ni are illustrated in Fig.21.5. Here again, the chemically ordered state has a higher T_C than the chemically random state, 580 K versus 520 K, respectively. The μ(T) curves themselves, however, for the chemically ordered and random states are much more different for Fe_3Ni than they are for $FeNi_3$ or FeNi. The saturation moment per atom for chemically ordered Fe_3Ni is 2.25 μ_B, corresponding to all Fe and Ni moments being ferromagnetically aligned, whereas, for disordered Fe_3Ni it is only 1.41 μ_B, corresponding to 20.0 % of the Fe moments being antiferromagnetically aligned to the bulk magnetization. Fig.21.5 also shows that the μ(T) curve for chemically ordered Fe_3Ni has some structure in the T_C= 100 - 400 K range. This arises from the very different magnetic coupling strengths of Fe and Ni in this structure.

21.2 Chemical Interactions Only

21.2.1 MFT results

We first study atomic ordering in $FeNi_3$, FeNi and Fe_3Ni with the chemical interactions only by MFT. The chemical binding forces are modeled by NN-only bonds, U_{NiNi}, U_{FeNi}, and U_{FeFe}, that depend only on the identities of the interacting NN atoms. In describing the degree of chemical order and the chemical order-disorder transition, we define the long range order parameter (LROP), p. It has the value 1 in the perfectly ordered state and the value 0 in the perfectly random state. The lattices of the ordered binary alloys are divided into sublattices A and B; the two sublattices that receive Fe and Ni atoms, respectively, in the perfectly ordered states.

In the FeNi system, p is defined by:

$$N_{Fe,A} = N(1+p)/2 \tag{21.1}$$

where $N_{Fe,A}$ is the number of Fe atoms on sublattice A and N is the total number of Fe atoms. Similarly, in the $FeNi_3$ system, the LROP, p, is defined by:

$$N_{Fe,A} = N(1+3p)/4 \tag{21.2}$$

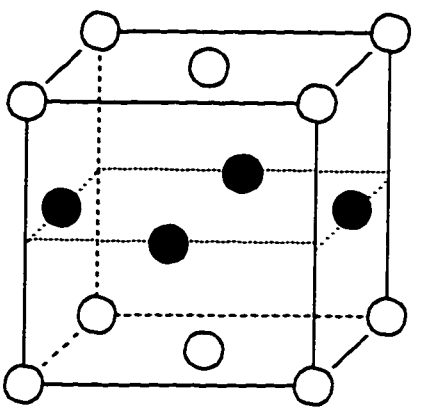

Figure 21.3 : Conventional unit cell of chemically ordered FeNi with filled circles representing Ni (or Fe) atoms and open circles representing Fe (or Ni) atoms.

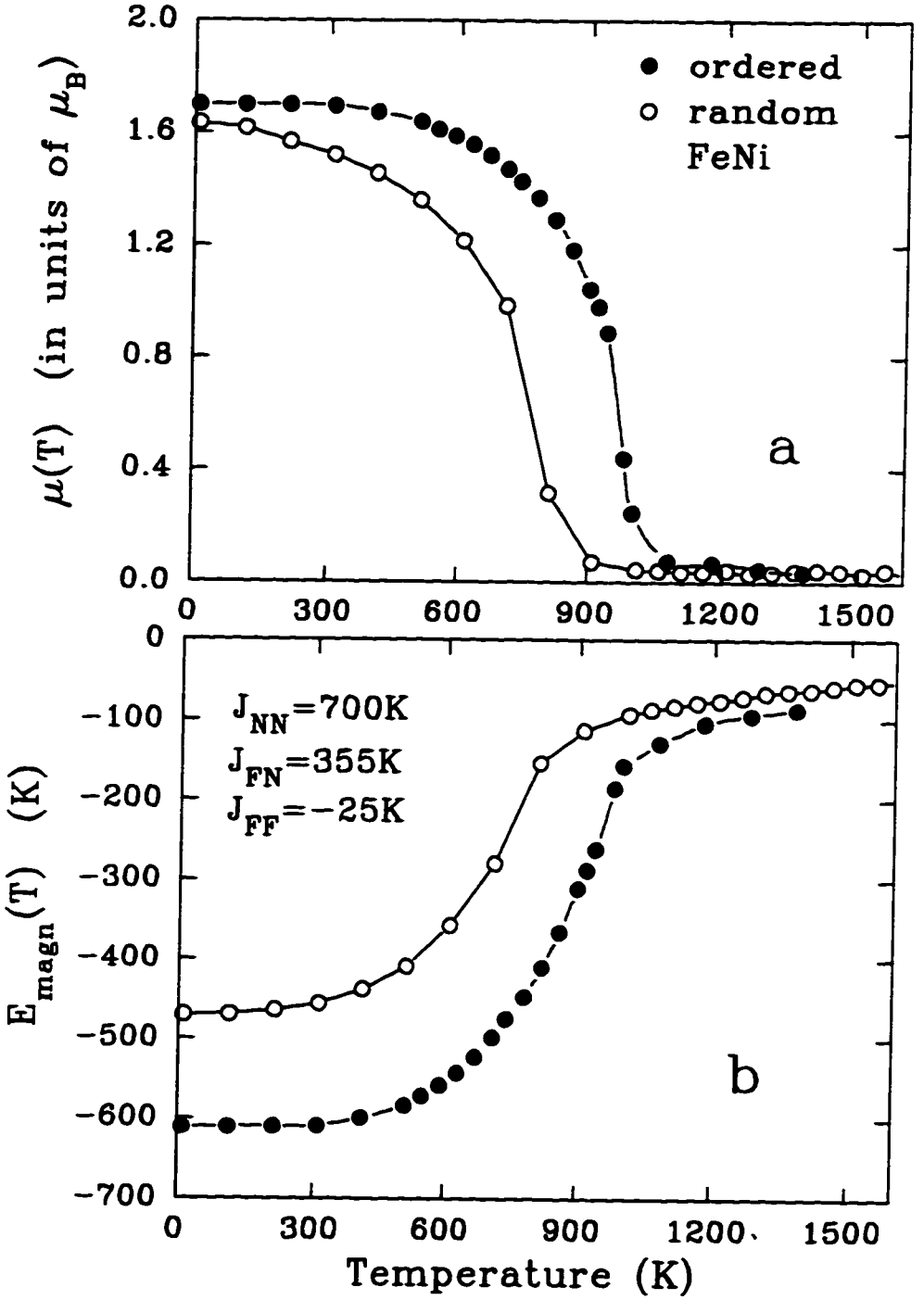

Figure 21.4 : MC simulated magnetic properties of FeNi allowing only the magnetic degrees of freedom and assuming either perfect chemical randomness (open circles) or perfect chemical order (filled circles): (a) spontaneous average moment per atom versus temperature, (b) average magnetic energy per atom versus temperature.

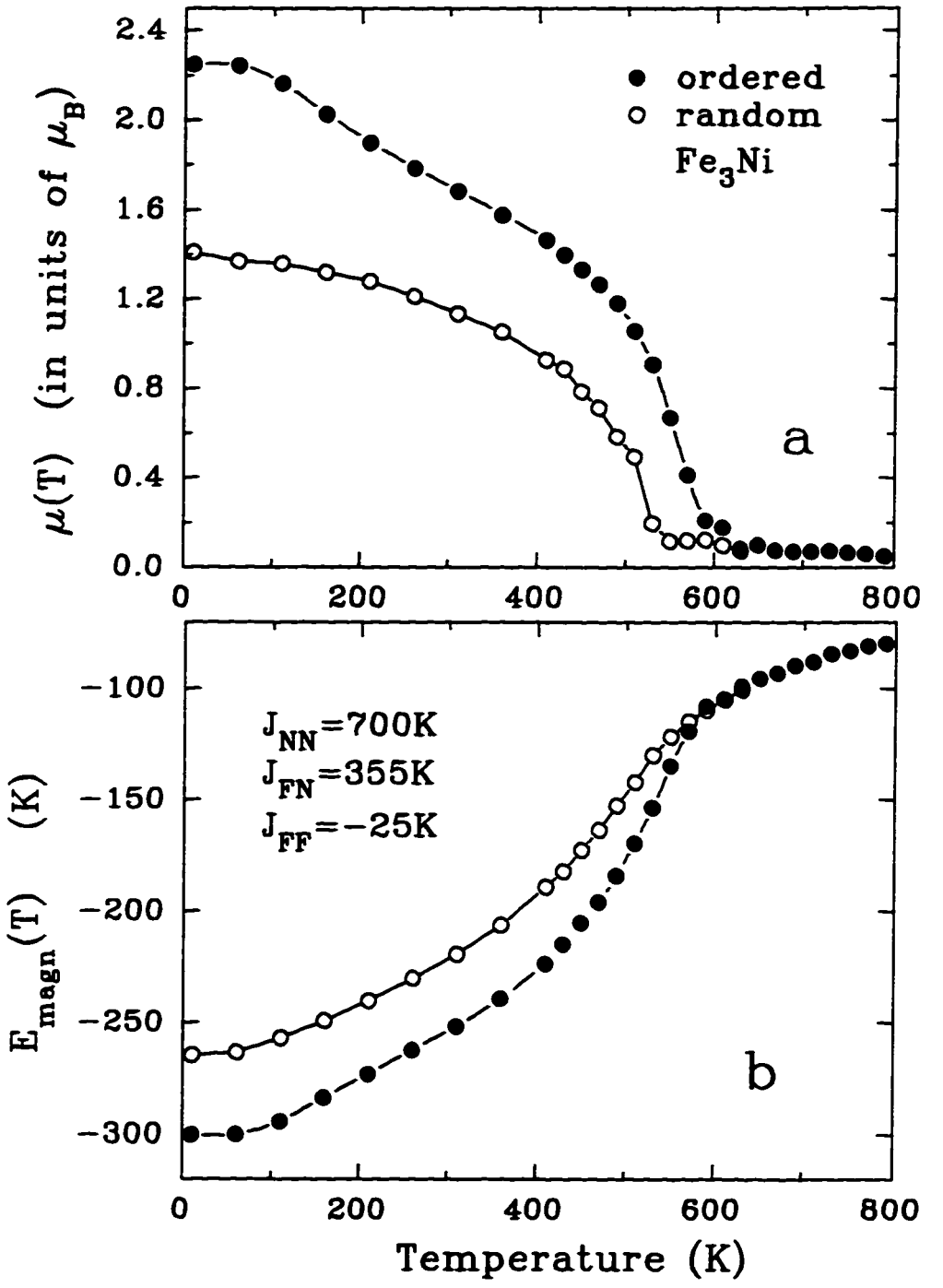

Figure 21.5 : MC simulated magnetic properties of Fe_3Ni allowing only the magnetic degrees of freedom and assuming either perfect chemical randomness (open circles) or perfect chemical order (filled circles): (a) spontaneous average moment per atom versus temperature, (b) average magnetic energy per atom versus temperature.

The same holds for Fe_3Ni, with Fe and Ni interchanged.

The system with 2N atoms in the FeNi alloy has the total energy E:

$$E = N_{FeFe}U_{FeFe} + N_{NiNi}U_{NiNi} + N_{FeNi}U_{FeNi} \tag{21.3}$$

where N_{ij} is the total number of NN i-j bonds in the alloy, with i, j = Fe or Ni. We have:

$$\begin{aligned} N_{FeFe} &= N_{NiNi} \\ &= \frac{N}{2}(1+p)[4(1+p)/2 + 8(1-p)/2] \\ &+ \frac{N}{2}(1-p)[8(1+p)/2 + 4(1-p)/2] \\ &= N(3-p^2) \end{aligned}$$

and

$$\begin{aligned} N_{FeNi} &= \frac{N}{2}(1+p)[8(1+p)/2 + 4(1-p)/2] \\ &+ \frac{N}{2}(1-p)[4(1+p)/2 + 8(1-p)/2] \\ &= 2N(3+p^2). \end{aligned}$$

The total energy therefore, is:

$$\begin{aligned} E &= N(3-p^2)U_{FeFe} + N(3-p^2)U_{NiNi} + 2N(3+p^2)U_{FeNi} \\ &= 3N(U_{FeFe} + U_{NiNi} + 2U_{FeNi}) + Np^2U \end{aligned}$$

where $U \equiv 2U_{FeNi} - U_{FeFe} - U_{NiNi}$. The number of arrangments G of these atoms is given by:

$$G = [\frac{N!}{(\frac{N}{2}(1+p))!(\frac{N}{2}(1-p))!}]^2. \tag{21.4}$$

Knowing $S = k_B \ln G$, where S is the entropy of the system, k_B is the Boltzmann constant, we minimize the free energy F = E - TS and obtain:

$$T = -\frac{2Up/k_B}{ln(\frac{1+p}{1-p})}. \tag{21.5}$$

At T $\sim$ T_a, which is the atomic order-disorder transition temperature, $T_a = -\frac{U}{k_B}$ for FeNi alloy.

Similarly, the total energy for $FeNi_3$ is givens by:

$$E = \frac{3N}{2}(1-p^2)U_{FeFe} + \frac{3N}{2}(9-p^2)U_{NiNi} + (9+3p^2)U_{FeNi}$$

and the number of arrangements G for Fe_3Ni and $FeNi_3$ are given by:

$$G = \frac{N!}{(N(1+3p)/4)!(3N(1-p)/4)!}\frac{(3N)!}{(3N(3+p)/4)!(3N(1-p)/4)!} \qquad (21.6)$$

By minimization of F = E - TS, we obtain the equilibrium state condition:

$$2Up + \frac{k_BT}{4}[(3ln(1+3p) - 3ln(3-3p) + 3ln(3+p) - 3ln(1-p)] = 0 \qquad (21.7)$$

and, when T $\sim$ T_a, we have T_a = -3U/4k_B.

Therefore the MFT results about the LROP p and the chemical interation parameter U are given in Eq.21.5 for FeNi and in Eq.21.7 for $FeNi_3$. Both the LROP p and the corresponding energy E_{chem} are shown in Fig.21.6 for FeNi as functions of temperature, with U_{NiNi} = -8567 K, U_{FeNi} = -12560 K and U_{FeFe} = -15211 K. Fig.21.7 shows the same results for for $FeNi_3$. Fe_3Ni has the same results as Fig.21.7 except that its E_{chem} per atom has different magnitudes. The atomic order-disorder transition shown in Fig.21.6 for FeNi alloy is of a typical second order transition. However, the transitions for Fe_3Ni and $FeNi_3$ are of first order (Fig.21.7).

21.2.2 MC results

We model the chemical ordering phenomena by NN-only bonds, U_{NiNi}, U_{FeNi}, and U_{FeFe} using MC simulations. The Ni-Ni bond is taken to be U_{NiNi} = -8590 K, which corresponds to the measured cohesive energy of fcc nickel [125], assuming that the chemical bond energy is the dominant contribution. The Fe-Fe bond is taken to correspond to the cohesive energy of high-spin fcc iron, obtained by extrapolation from the measured cohesive energies of fcc copper, fcc nickel, and hcp cobalt: U_{FeFe} = -8400 K. This leaves U_{FeNi} which is taken to give the best agreement between

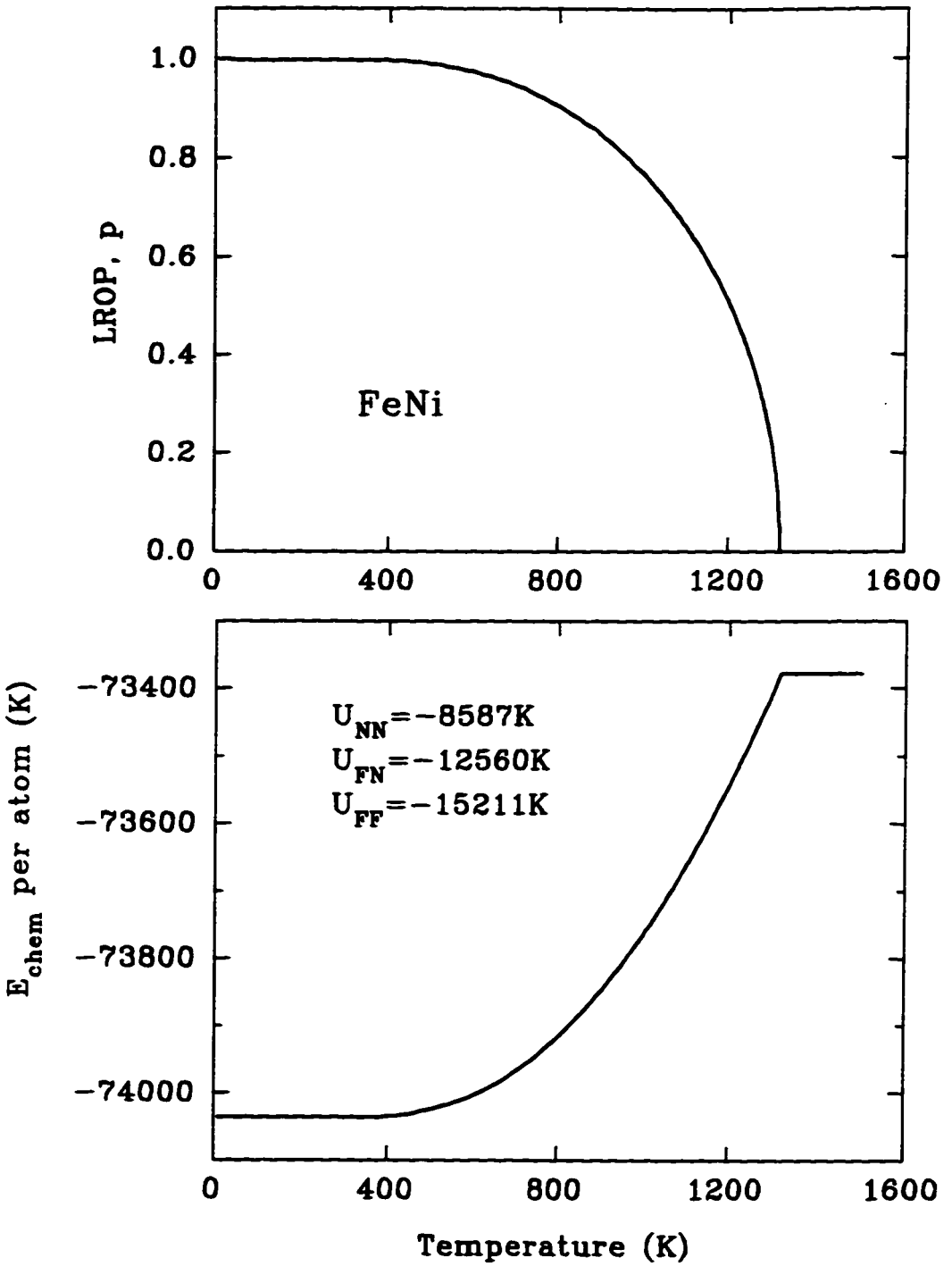

Figure 21.6 : The calculated MFT results of the atomic LROP p (top) and the chemical interaction energy E_{chem} (bottom) as functions of temperature in FeNi alloy with U_{NiNi} = -8567 K, U_{FeNi} = -12560 K and U_{FeFe} = -15211 K.

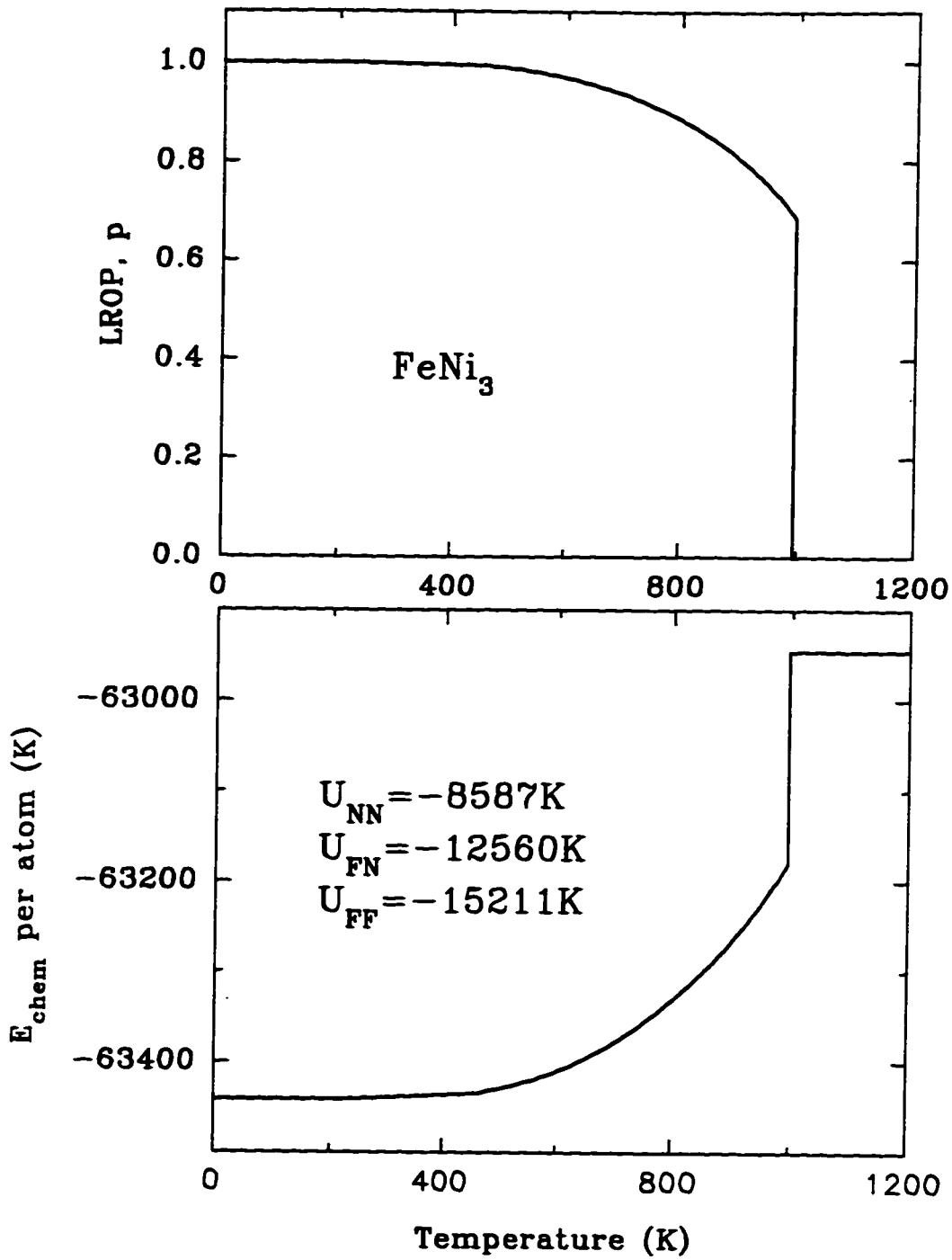

Figure 21.7 : The calculated MFT results of the atomic LROP p (top) and the chemical interaction energy E_{chem} (bottom) as functions of temperature in $FeNi_3$, with U_{NiNi} = -8567 K, U_{FeNi} = -12560 K and U_{FeFe} = -15211 K. Fe_3Ni has the same results (i.e. same type of transition and same order-disorder transition temperature) except that its E_{chem} has different magnitudes.

the measured T_a(equil) values for FeNi and $FeNi_3$ and the MC values, T_a(chem), including only chemical interactions (see below): U_{FeNi} = -9200 K.

Many other values of the bond energies were also used in order to evaluate how they determine the value of T_a(chem), allowing chemical interactions only. Typical results are shown in Fig.21.8 where it is seen that, just as in MFT, T_a(chem) is proportional to the particular combination $U \equiv 2U_{FeNi}$-U_{FeFe}-U_{NiNi}, irrespective of the individual values used. Also, just as in MFT, the T_a(chem) for Fe_3Ni is the same, for a given value of U, as that for $FeNi_3$. The proportionality constants, however, are different for MFT and MC simulations: As usual, MFT overestimates the ordering temperatures because it disallows fluctuations.

Another interesting difference between the MFT and MC predictions seen in Fig.21.8 is that MFT has the T_a(chem) of FeNi being larger than that of $FeNi_3$ whereas MC has the T_a(chem) of FeNi being smaller than that of $FeNi_3$, in better agreement with the measured T_a(equil) values. Also, MFT predicts a second order transition for FeNi and first order transitions for Fe_3Ni and $FeNi_3$. The transitions obtained by MC appear similar in character for all three alloys (see below) and are probably first order, which agrees with Landau theory [130].

In describing the degree of atomic order and the atomic order-disorder transition, in addition to the LROP, p, we often use another quantity which is the short range order parameter (SROP), r. In the FeNi system, the SROP is defined by:

$$r = q - 3 \tag{21.8}$$

where q is the average number of NN Fe-Ni bonds per atom. Here, q = 4 for perfectly ordered FeNi and q = 3 for perfectly random FeNi (Fig.21.3). In other words, r measures the preference for Fe-Ni bonds that drives the ordering process. It can be non-zero above T_a where the LROP is zero.

The SROP in the $FeNi_3$ system is defined by:

$$r = (4q - 9)/3 \tag{21.9}$$

where q = 3 for perfectly ordered $FeNi_3$ and q = 9/4 for perfectly random $FeNi_3$. The same holds for Fe_3Ni, with Fe and Ni interchanged.

Fig.21.9 shows the LROP, the SROP, and the chemical bond energy per atom, E_{chem}, as functions of temperature for $FeNi_3$. Fig.21.10 and Fig.21.11 show the same properties for FeNi and Fe_3Ni, respectively. In all three cases both the SROP and E_{chem} show significant short range order far above T_a. This, with the results of the previous section, shows that chemical order can significantly affect the magnetic properties even when T_C is much larger than T_a. It also suggests, contrary to what is often assumed, that rapid quenching from the melt to a perfectly random state is impossible.

Finally, Fig.21.8 shows that it is impossible to match the measured T_a(equil) values for FeNi and $FeNi_3$ (593 and 770 K, respectively) with the MC T_a(chem) values using a single value of U. Fair agreement occurs at U = -1410 K and this was used to evaluate U_{FeNi} but it is not good agreement (Fig.21.8). This is not surprising given the simplicity of the model: NN-only two-body interactions, etc. Nonetheless, it is interesting to explore the extent to which such matching is possible simply by simultaneously allowing the chemical and magnetic degrees of freedom. It is equally interesting to see the extent to which each of the isolated behaviours is changed by the coexistence. Note that, with NN-only interactions, the low temperature equilibrium states of the alloy are at the exact boundaries between $D0_{22}$ and $L1_2$ ($FeNi_3$), or $L1_0$ and A_2B_2 (FeNi) [131].

21.3 Simultaneous Magnetic and Chemical Interactions

In section 21.1, we calculated T_C(ordered) and T_C(random) by allowing only the magnetic interactions and by assuming either perfect chemical order or perfect chemical randomness, respectively. As mentioned above, it is possible to perform non-equilibrium measurements of T_C(ordered) and T_C(random) because the magnetic equilibration time is much shorter than the chemical equilibration time. Of course, with a sufficiently slow measurement, what is measured is T_C(equil). In section 21.2.2, we calculated T_a(chem) by allowing only the chemical interactions. What is measured, however, is always T_a(equil). In this section, we calculate T_a(equil) and T_C(equil) by assuming that the chemical and magnetic interactions are the

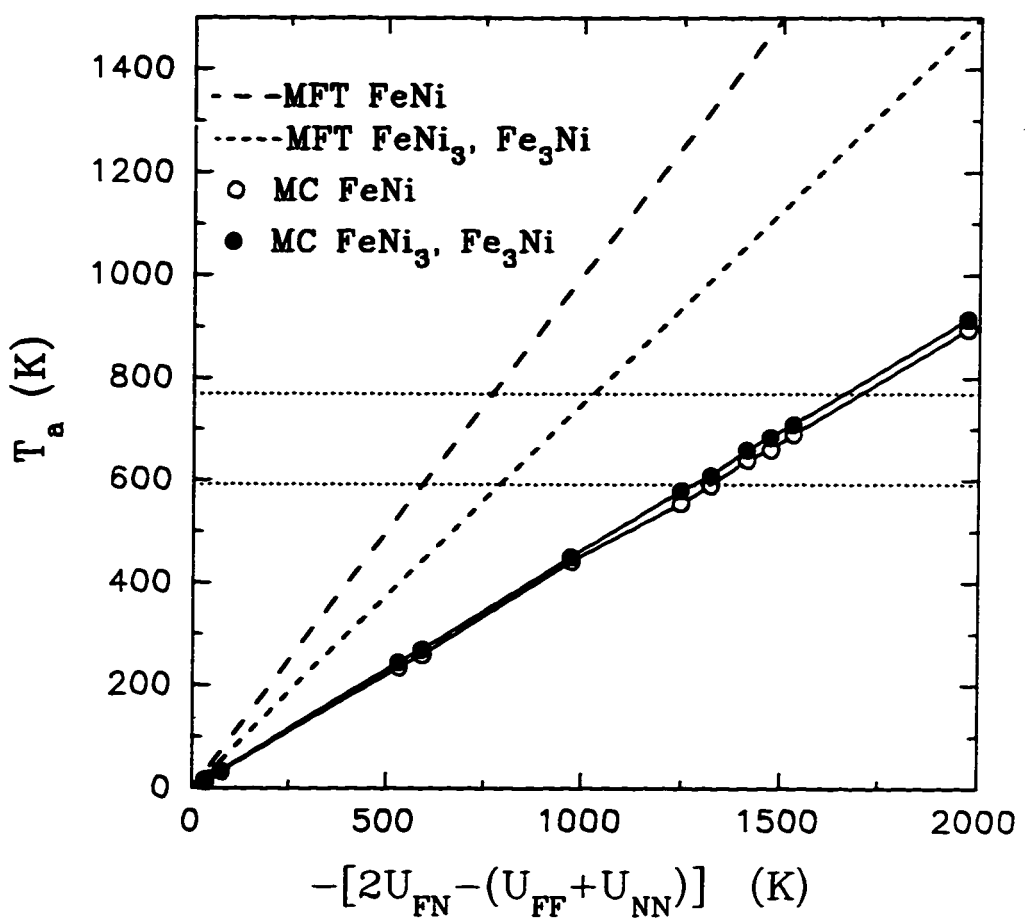

Figure 21.8 : Chemical (or atomic) order-disorder transition temperature, T_a, versus minus the bond energy parameter $U \equiv 2U_{FeNi} - U_{FeFe} - U_{NiNi}$ calculated: by MFT for FeNi(dashed line), by MFT for $FeNi_3$and Fe_3Ni (dotted line), by MC for FeNi (open circles), by MC for $FeNi_3$ and Fe_3Ni (closed circles). The horizontal lines show the measured T_a values for FeNi (593 K) and $FeNi_3$ (770 K).

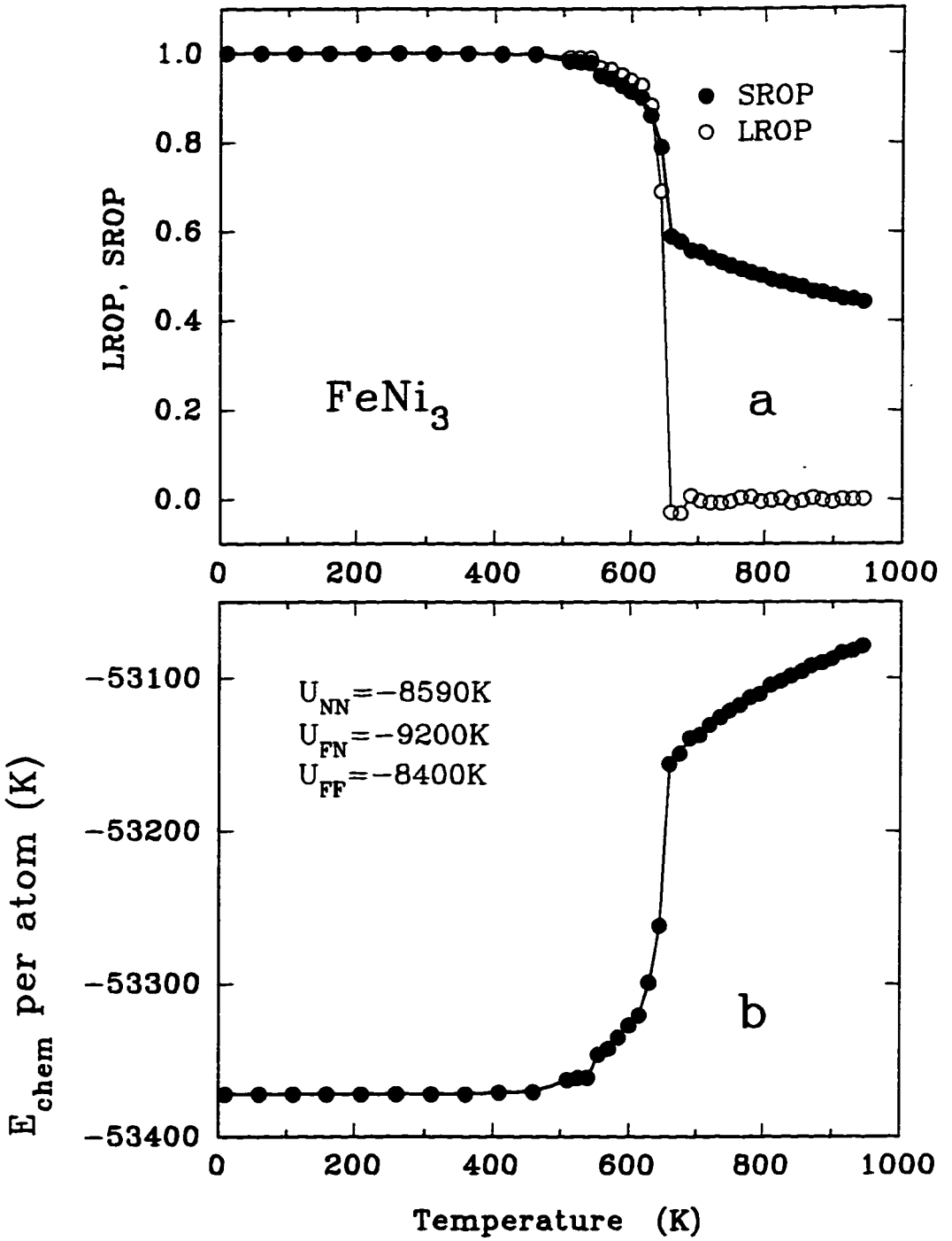

Figure 21.9 : MC simulated crystal chemical properties of $FeNi_3$ allowing only the chemical (i.e. atomic position exchange) degree of freedom and neglecting the magnetic interactions: (a) the LROP, p, (open circles) and SROP, r, (filled circles) versus temperature, (b) the average chemical bond energy per atom versus temperature.

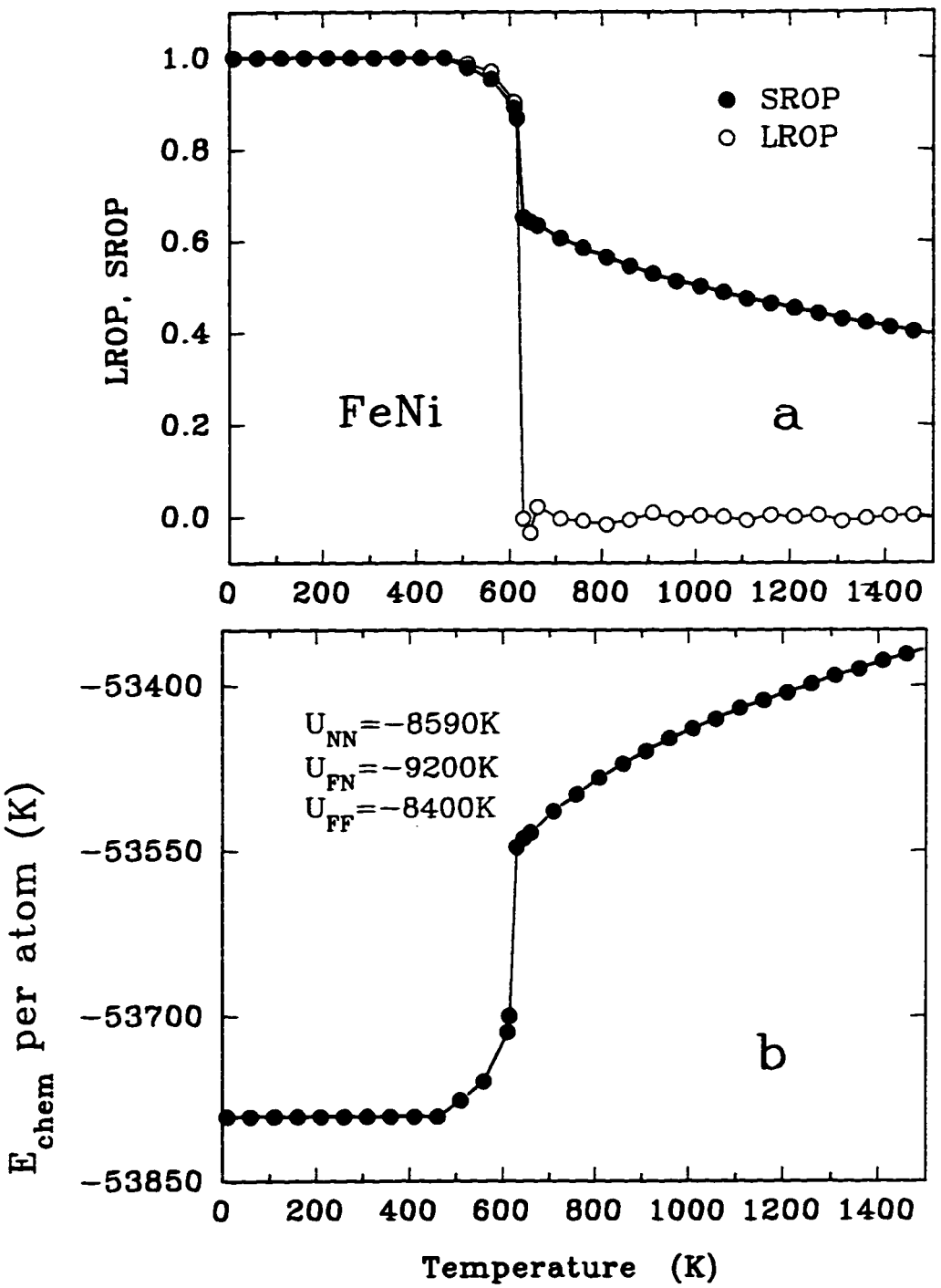

Figure 21.10 : MC simulated crystal chemical properties of FeNi allowing only the chemical (i.e. atomic position exchange) degree of freedom and neglecting the magnetic interactions: (a) the LROP, p, (open circles) and SROP, r, (filled circles) versus temperature, (b) the average chemical bond energy per atom versus temperature.

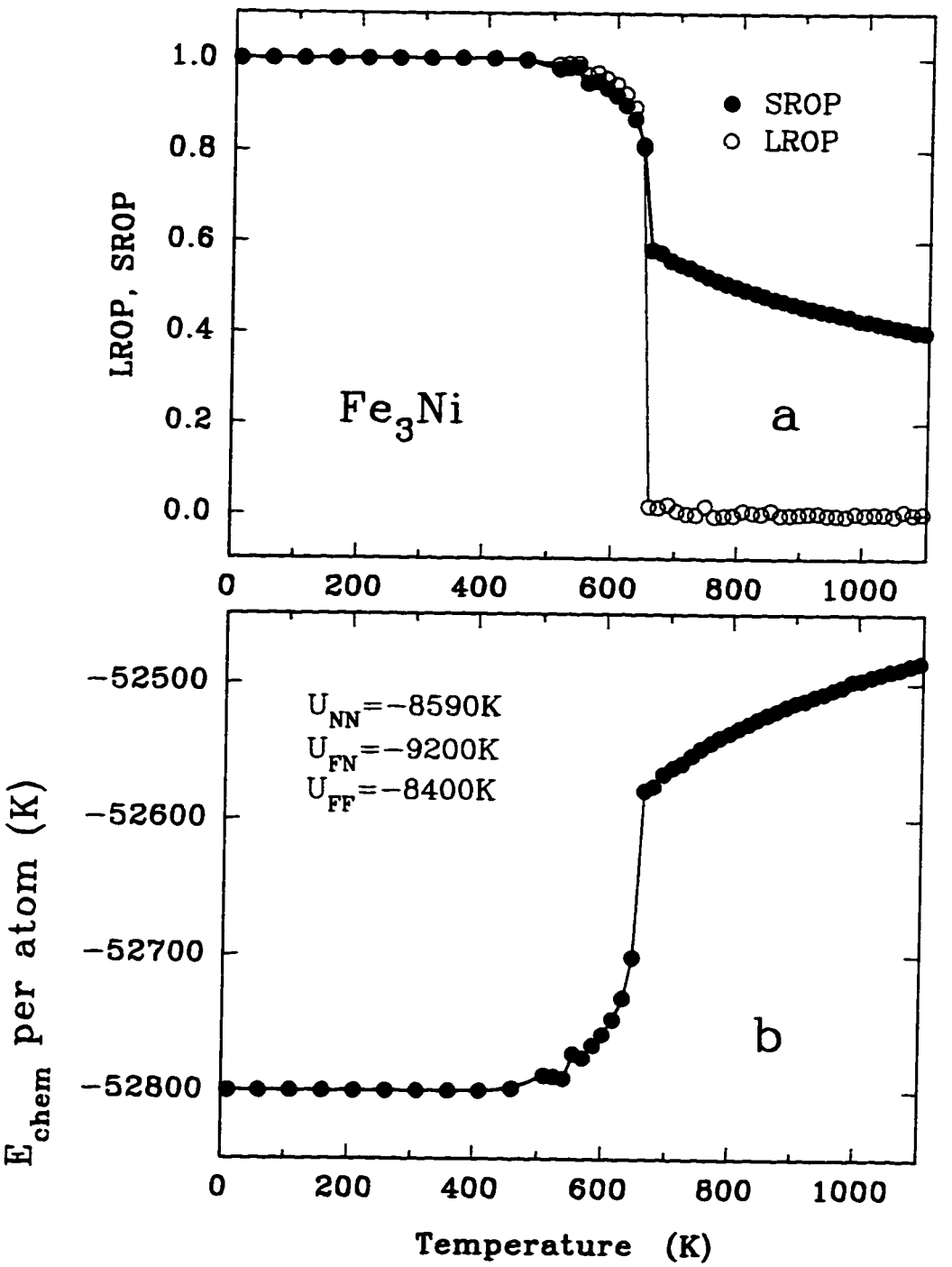

Figure 21.11 : MC simulated crystal chemical properties of Fe_3Ni allowing only the chemical (i.e. atomic position exchange) degree of freedom and neglecting the magnetic interactions: (a) the LROP, p, (open circles) and SROP, r, (filled circles) versus temperature, (b) the average chemical bond energy per atom versus temperature.

dominant interactions.

Clearly, T_C(equil) will be between T_C(random) and T_C(ordered), depending on the degree of chemical long or short range order at T_C(equil). In addition, one of the main results of the present paper, is that T_a(equil) is significantly different from T_a(chem), even if T_a(equil)> T_C(equil), and is only equal to T_a(chem) if T_a(equil) >> T_C(equil) such that magnetic short range order is negligible at T_a(equil).

The results for $FeNi_3$, taking the same magnetic and chemical interaction parameters as before, are shown in Fig.21.12. Here, the average spin per atom, $< S >$, is shown instead of the average moment per atom ($< S > = \mu(T)/2\mu_B$), on the same scale as the chemical long range and short range order parameters. The chemical and magnetic contributions to the total average energy per atom and the latter total energy are also shown. In comparing Fig.21.12 to Figs. 21.2 21.9, for $FeNi_3$, we note that T_C(equil) is larger than T_C(random) and smaller than T_C(ordered) because of the chemical short range order. We also note that T_a(equil) is larger than T_a(chem) because of the presence of magnetic order, and that an abrupt step of magnitude 0.04 μ_B per atom occurs in the equilibrium spontaneous magnetization at T_a(equil).

Similar results for FeNi are shown in Fig.21.13. An abrupt step of magnitude 0.1 μ_B per atom occurs in the equilibrium spontaneous magnetization at the presumably first order chemical ordering transition. The chemical and magnetic ordering temperatures are affected by the combined magnetic and chemical interactions in a qualitatively similar way as in $FeNi_3$.

The results for Fe_3Ni are shown in Fig.21.14. Contrary to $FeNi_3$ and FeNi, Fe_3Ni has T_C(equil) < T_a(equil). In comparing Fig.21.14 to Fig.21.5, one notes that the spontaneous average moment per atom for the case of combined interactions is the same within error as for the case of magnetic only interactions with fixed perfect chemical order. This is because, even for temperatures up to T_C(equil) in the case of combined interactions, the chemical LROP is not significantly lower than 1. In particular, the same structure at T_C= 100-400 K in $< S >$ versus T (or μ(T)) is present and T_C(equil) = T_C(ordered), within error. The chemical ordering temperature in the case with combined interactions (Fig.21.14) is also the same within error as in the case of chemical only interactions (Fig.21.11). However, we

Table 21.1: MC and measured chemical ordering temperatures, in K.

	MC	MC	Measured
Alloys	T_a(chem.)	T_a(equil)	T_a(equil)
$FeNi_3$	660	760	770
FeNi	620	720	593
Fe_3Ni	660	660	-

have found that with different choices of the NN chemical bond parameters that give comparable values of T_a(equil) it is usual for T_a(equil) to be larger than T_a(chem), by typically 30 K or so. This occurs despite the fact that T_C(equil) < T_a(equil) because of magnetic short range order above T_C(equil). Most interestingly, whereas with chemical only interactions $FeNi_3$ and Fe_3Ni had the same chemical ordering temperatures (Fig.21.8), with combined chemical and magnetic interactions they have significantly different T_a(equil) values.

The above results concerning the various ordering temperatures are given more quantitatively in Tables 21.1 and 21.2. We see that (Table 21.1), in the cases of $FeNi_3$ and FeNi where T_C(equil)>T_a(equil), the chemical ordering temperatures are increased by 100 K, relative to chemical only interactions. Regarding the magnetic ordering temperatures (Table 21.2), recall (section 21.1) that the measured values are estimates, given the kinetics involved and the non-zero and finite measurement times. For all three alloys, T_C(random) $\leq$ T_C(equil) $\leq$ T_C(ordered), as expected. All three alloys have T_C(random) < T_C(ordered) and the difference between T_C(random) and T_C(ordered) decreases as Fe content increases. The relationship between the latter difference and Fe content is expected to be complicated because the degree of magnetic frustration in the disordered alloys increases with Fe content.

It is also of interest to examine how long and short range magnetic order affect chemical short range order above T_a(equil). This is shown in Fig.21.15 and Fig.21.16 where the chemical SROPs are plotted versus T/T_a for chemical only and combined chemical and magnetic interactions, for $FeNi_3$ and FeNi, respectively. For both

Table 21.2: MC and measured magnetic ordering temperatures, in K.

	MC	MC	MC	Measured	Measured
Alloys	T_C(random)	T_C(ordered)	T_C(equil)	T_C(random)	T_C(ordered)
$FeNi_3$	870	1180	970	850	940
FeNi	820	1020	910	785	840
Fe_3Ni	520	580	580	-	-

alloys, the value of T_C(equil)/T_a(equil) on the T/T_a axis is shown by a vertical dashed line. The corresponding chemical SROPs as functions of T/T_a for Fe_3Ni, which has T_C(equil) < T_a(equil), are equal within error (± 0.003) at all $T/T_a > 1$.

Fig.21.15 and Fig.21.16 show that, in cases where T_C(equil) > T_a(equil), the magnetically induced contributions to the chemical short range order are largest at temperatures below T_C(equil) and decrease monotonically as T/T_a goes to T_C(equil)/T_a(equil) but remain significant far above T_C(equil)/T_a(equil), as they continue to decrease as temperature is increased. Below T_C(equil) the magnetically induced increase in chemical short range order is about 10 % whereas just above T_C(equil) it is about 1-2 %. Therefore, both magnetic long range order and magnetic short range order affect chemical short range order above T_a.

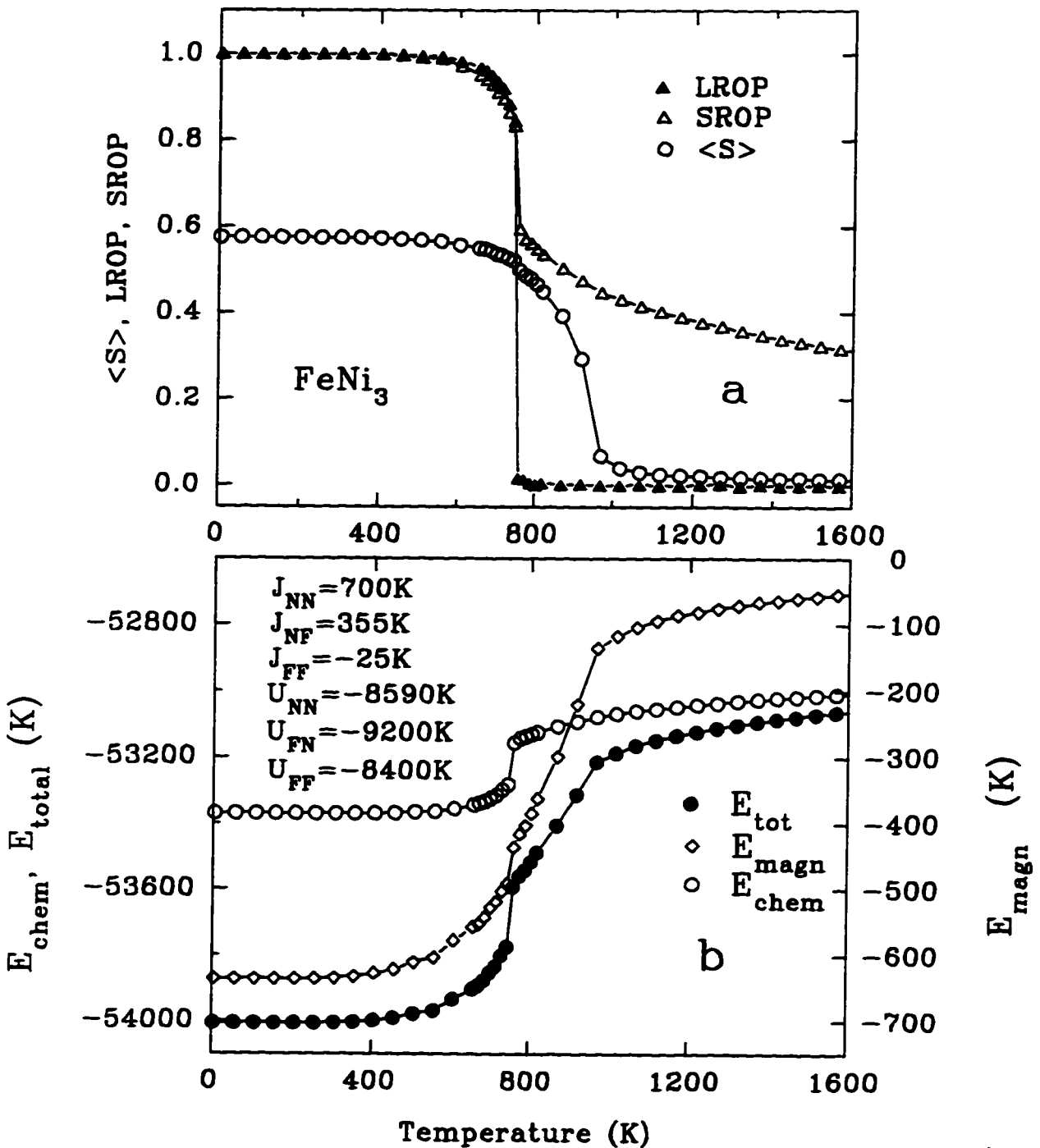

Figure 21.12 : MC simulated crystal chemical and magnetic equilibrium properties of $FeNi_3$ allowing both chemical and magnetic degrees of freedom simultaneously: (a) chemical LROP (filled triangles), chemical SROP (open triangles), and average spin per atom $< S >$ (open circles), as functions of temperature; (b) chemical energy per atom (open circles, left scale), magnetic energy per atom (open diamonds, right scale), and total energy per atom (filled circles, left scale), as functions of temperature.

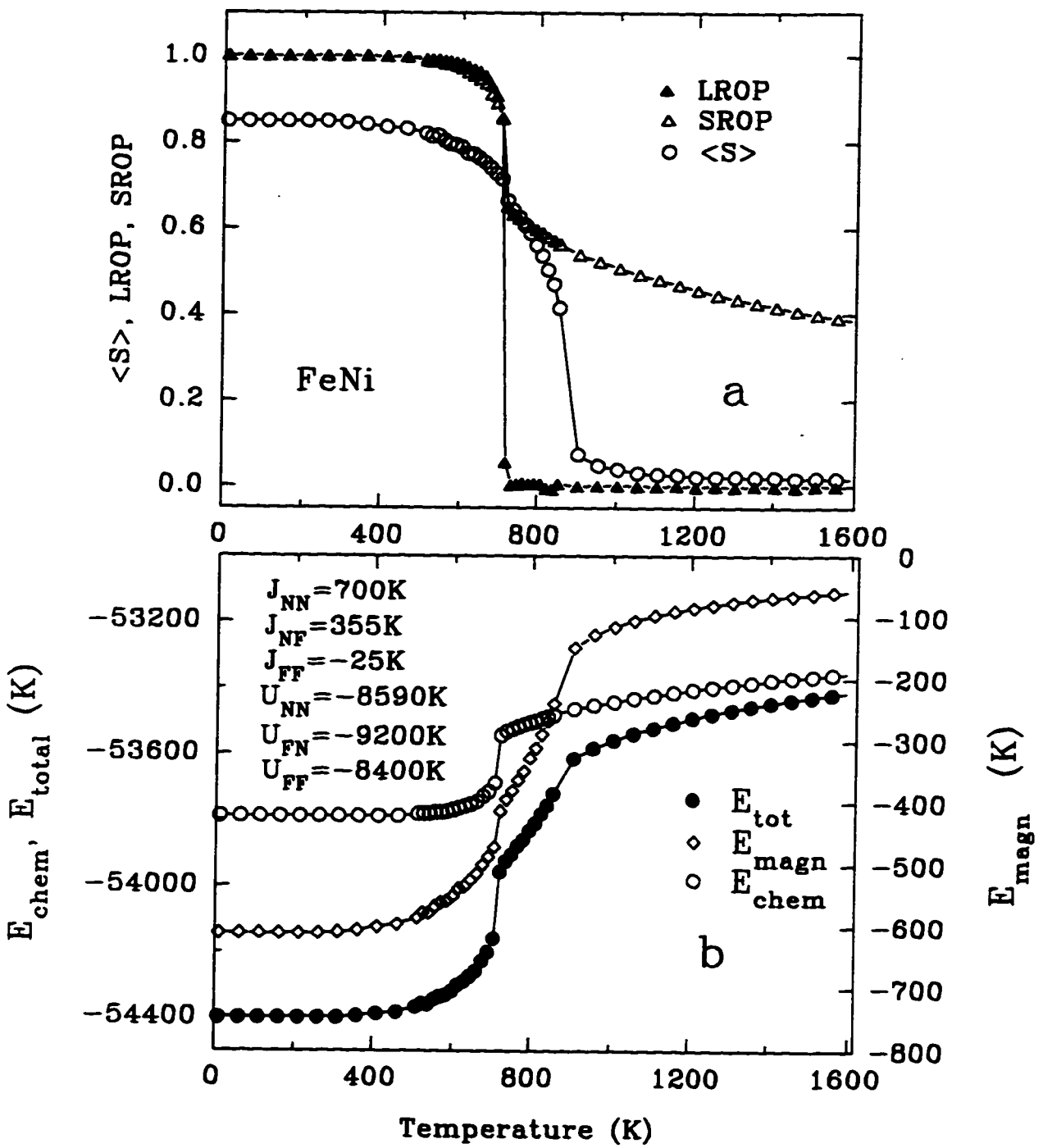

Figure 21.13 : MC simulated crystal chemical and magnetic equilibrium properties of FeNi allowing both chemical and magnetic degrees of freedom simultaneously. The symbols have the same meanings as in Fig.21.12.

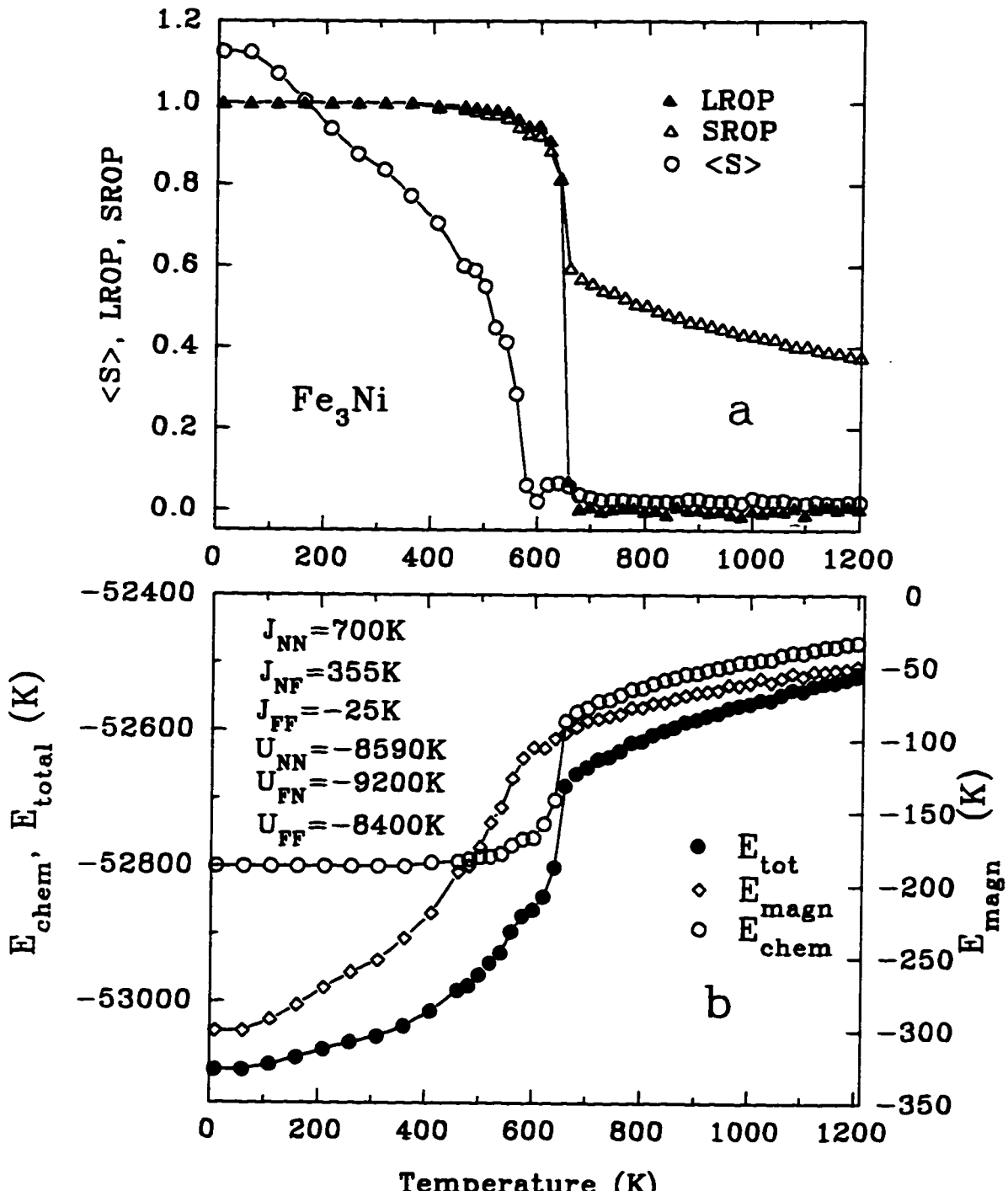

Figure 21.14 : MC simulated crystal chemical and magnetic equilibrium properties of Fe_3Ni allowing both chemical and magnetic degrees of freedom simultaneously. The symbols have the same meanings as in Fig.21.12.

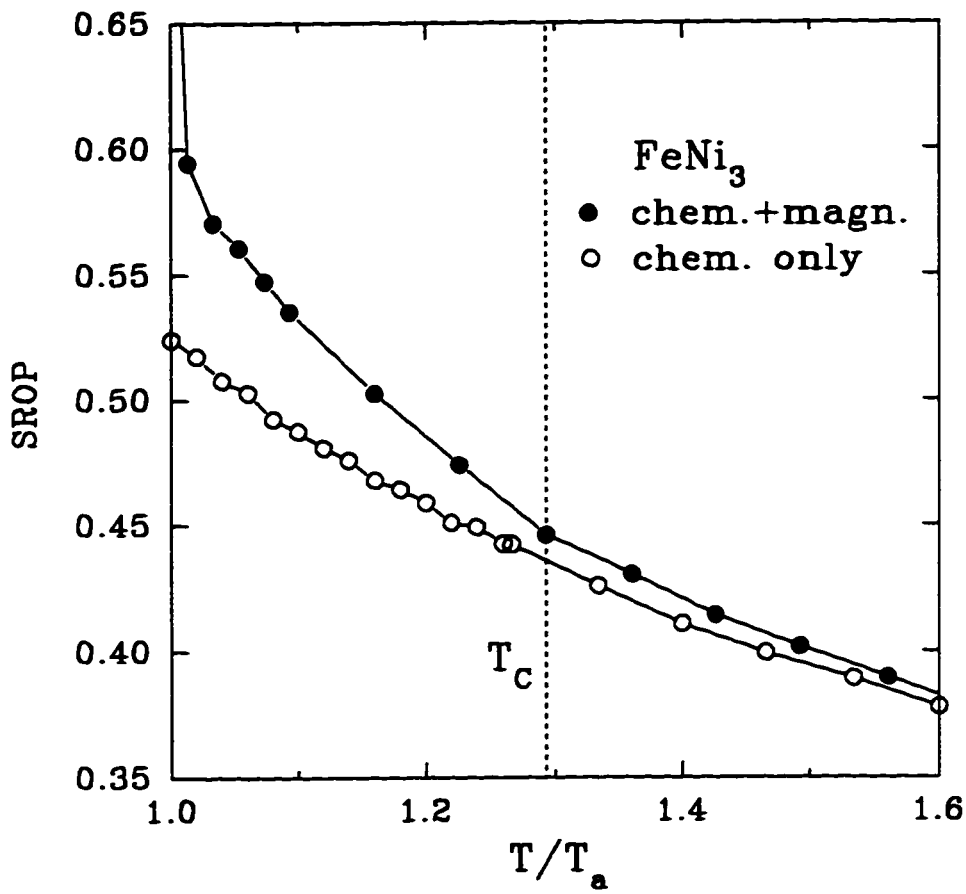

Figure 21.15 : MC simulated equilibrium chemical SROP versus T/T_a(equil) for $FeNi_3$ calculated either with chemical interactions only (open circles) or with both chemical and magnetic interactions (filled circles). The position of T_C(equil) is shown by a vertical dashed line.

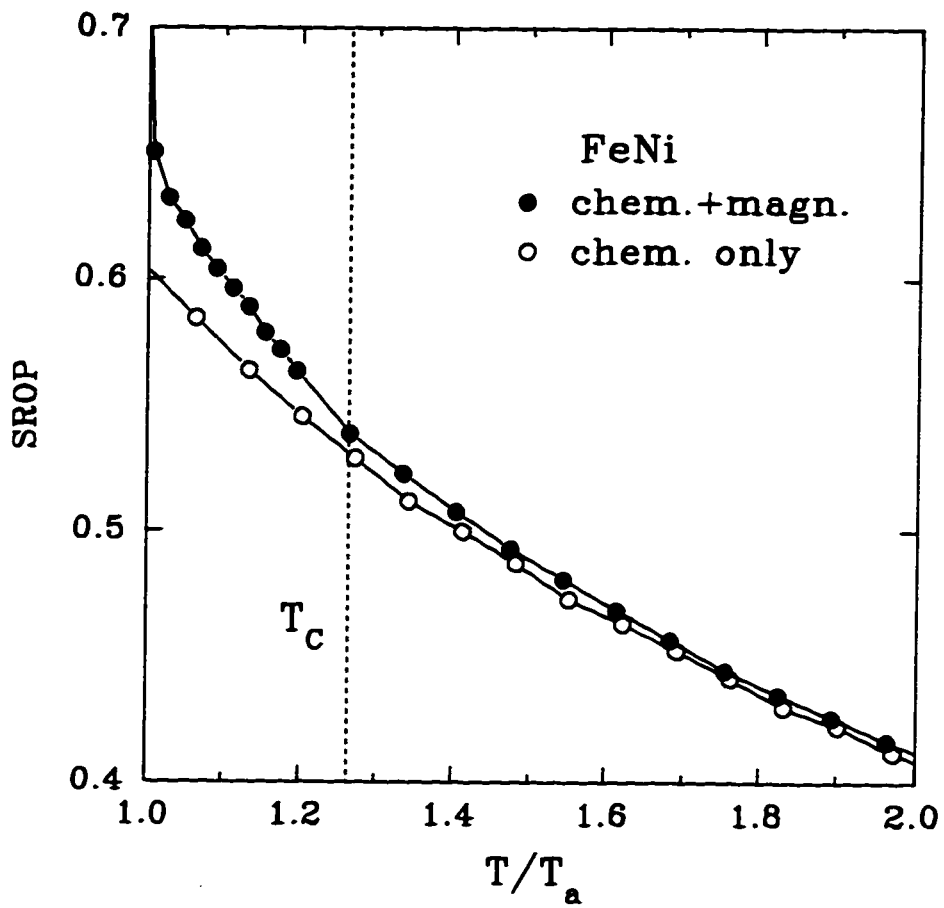

Figure 21.16 : MC simulated equilibrium chemical SROP versus T/T_a(equil) for FeNi calculated either with chemical interactions only (open circles) or with both chemical and magnetic interactions (filled circles). The position of T_C(equil) is shown by a vertical dashed line.

Chapter 22. GENERAL PREDICTIONS WITH COMBINED CHEMICAL AND MAGNETIC INTERACTIONS

We now diverge a little from the specific cases of $FeNi_3$, FeNi, and Fe_3Ni alloys in order to consider some interesting additional predicted phenomena that arise when chemical and magnetic interactions act simultaneously. In particular, we examine how the general behaviour depicted in Fig.21.8 is affected by including the magnetic interactions.

Typical results are shown in Fig.22.1. We find that, for a given set of magnetic exchange parameters, the differential bond energy parameter $U \equiv 2U_{FeNi} - U_{FeFe} - U_{NiNi}$ is again a valid parameter in that, for each alloy, T_a(equil) is a function only of U, not of the particular values of U_{FeNi}, U_{FeFe}, and U_{NiNi}. By comparing with Fig.21.8, we note several new features in Fig.22.1: $FeNi_3$ and Fe_3Ni have different chemical ordering temperatures and the T_a versus U curves are no longer linear and no longer intersect the origin. Also, the T_a(equil) versus U curves (Fig.22.1) approach the MC T_a(chem) versus U curves (Fig.21.8) as U increases. The latter behaviour is expected because as U increases, for fixed magnetic exchange parameters, the chemical component of the change in energy per exchange in the atomic positions of an Fe-Ni pair becomes much larger than the magnetic component.

The special case of Fe_3Ni stoichiometry is discussed below. The fact that, for $FeNi_3$ and FeNi stoichiometries, the T_a(equil) versus U curves intersect the U = 0 axis at positive T_a(equil) values means that the magnetic interactions induce chemical order in these systems, that have no chemical bond energy preference for chemical order.

This is shown for $FeNi_3$ stoichiometry in Fig.22.2 where, although U = 0, T_C(equil) = 140 K. The chemical order-disorder transition does not cause a break in the

magnetization because at temperatures well below T_C(equil) (or T_C(random) or T_C(ordered)) the chemically random and ordered states have the same (saturation) moment per atom. By comparison, the break seen in Fig.21.12 (or Fig.21.13) arises from the combined facts that T_a(equil) $\sim$ T_C(equil) and T_C(random) $\neq$ T_C(ordered), such that, as the temperature is increased through T_a(equil), the magnetization (or $< S >$) at T_a(equil) goes from one corresponding to a large T_C ($\sim$ T_C(ordered)) to one corresponding to a smaller T_C ($\sim$ T_C(random)).

Also, a U = 0 system with chemical only interactions has chemical long and short range order parameters of zero at all non-zero temperatures, however, Fig.22.2 shows that our U = 0 $FeNi_3$ system with magnetic interactions has significant chemical short range order up to T_C(equil) and non-zero values of the chemical SROP even above T_C(equil). Here, the chemical SROP is clearly correlated to $< S >$, dropping more rapidly when $< S >$ drops as T_C(equil) is approached. As with U $\neq$ 0 systems (Figs. 21.15 and Fig.21.16), the chemical SROP is non-zero above T_C(equil) because of magnetic short range order, although the simulated behaviour is somewhat imprecise here due to finite size effects that cause $|< S >|$ to be non-zero above T_C(equil).

Fig.22.3 shows an analogous situation for the FeNi U = 0 case where a T_a(equil) = 130 K is induced by the magnetism. In addition, we have found that it is possible to induce a T_a(equil) > 0 and significant chemical short range order to high temperatures up to $T_C \sim T_C$(equil) in systems that, from a chemical only perspective, would phase separate (U > 0). This suggests that real systems could be found that are miscible below a magnetic ordering temperature and phase separate above the magnetic ordering temperature.

Finally, we describe the more complicated case of Fe_3Ni stoichiometry with U $\sim$ 0. Here additional interesting features are expected because, due to magnetic frustration, the saturation moments per atom are very different for the chemically ordered and disordered states (Fig.21.5). Indeed, at U = 0, the chemically ordered state is not stabilized by the magnetism at any temperature, such that T_a is not defined. At T_C = 0 K, a completely segregated (Fe and Ni phase separated state) leads to lower total energy than either a chemically ordered or disordered state with

equilibrated spin structure. The ground state seems to be a complicated (possibly compositionally modulated or banded) segregated state. This also holds for small negative U, up to U $\sim$ -50 K where segregated and ordered states have about the same energies at T = 0 K. At U = -100 K, a stable chemically ordered ground state is found but the higher temperature behaviour is ambiguous with T_a being difficult to locate. Normal behaviour, such as that depicted in Fig.22.2 and Fig.22.3, is recovered at U = -200 K, which is the last point shown on the graph (Fig.22.1).

Although more work is needed, that is beyond the scope of the present paper, the case of Fe_3Ni stoichiometry shows that magnetism can induce phase separation in a system whose chemical only interactions would give rise to miscibility. Even if they occur at low temperatures, such phenomena could potentially be observed in slowly cooled meteorites (e.g., 1 K/Ma) or by particle irradiation treatments at low temperatures [106].

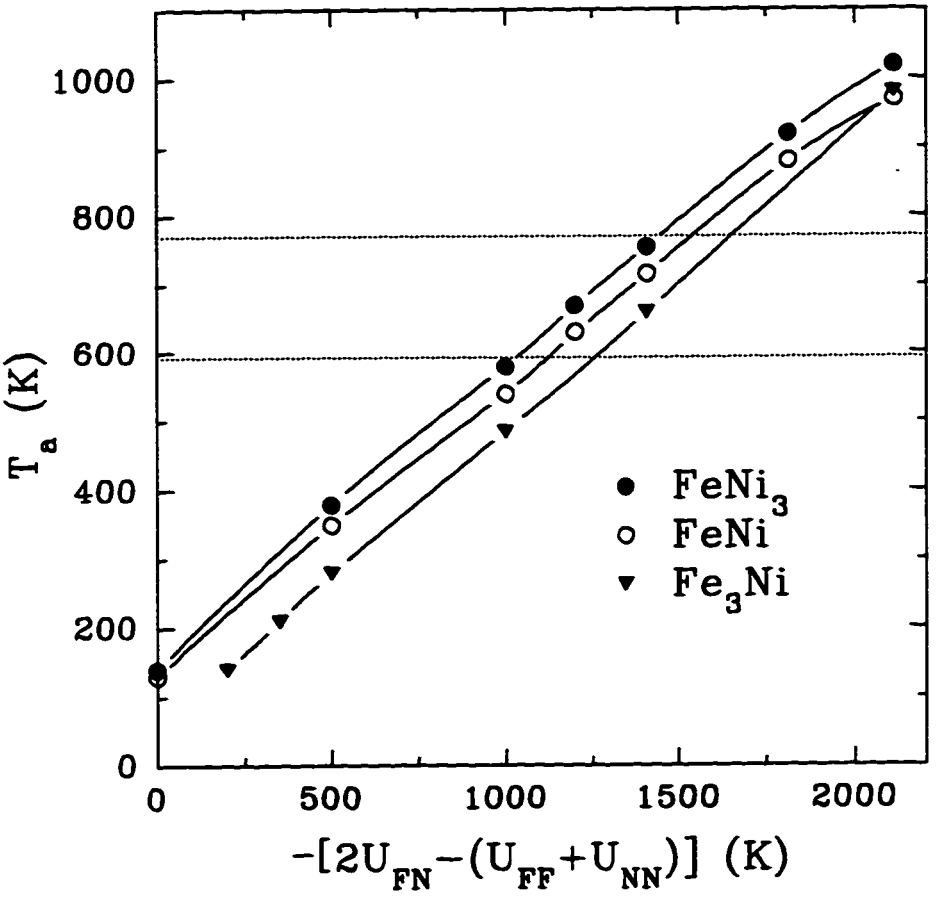

Figure 22.1 : Chemical (or atomic) order-disorder transition temperature, T_a, versus minus the bond energy parameter $U \equiv 2U_{FeNi} - U_{FeFe} - U_{NiNi}$ obtained from MC simulations that combine the chemical and magnetic interactions (with $J_{NiNi} = 700$ K, $J_{FeNi} = 355$ K, and $J_{FeFe} = -25$ K) for $FeNi_3$ (filled circles), FeNi (open circles), and Fe_3Ni (filled triangles). The horizontal lines show the measured T_a values for FeNi (593 K) and $FeNi_3$ (770 K).

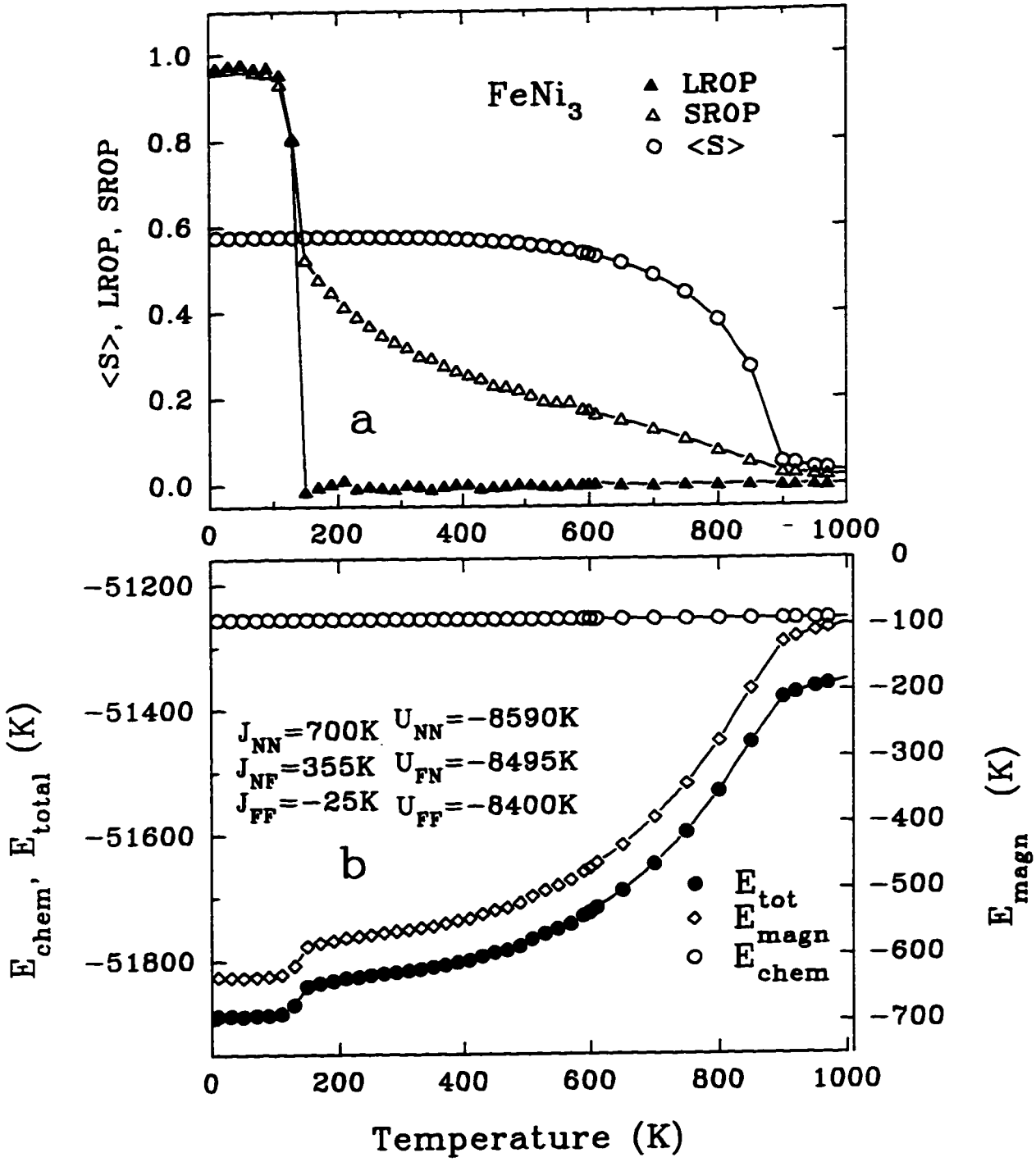

Figure 22.2 : MC simulated crystal chemical and magnetic equilibrium properties, allowing both chemical and magnetic degrees of freedom simultaneously, for $FeNi_3$ with U_{FeNi} adjusted such that U = 0: (a) chemical LROP (filled triangles), chemical SROP (open triangles), and average spin per atom $< S >$ (open circles), as functions of temperature; (b) chemical energy per atom (open circles, left scale), magnetic energy per atom (open diamonds, right scale), and total energy per atom (filled circles, left scale), as functions of temperature.

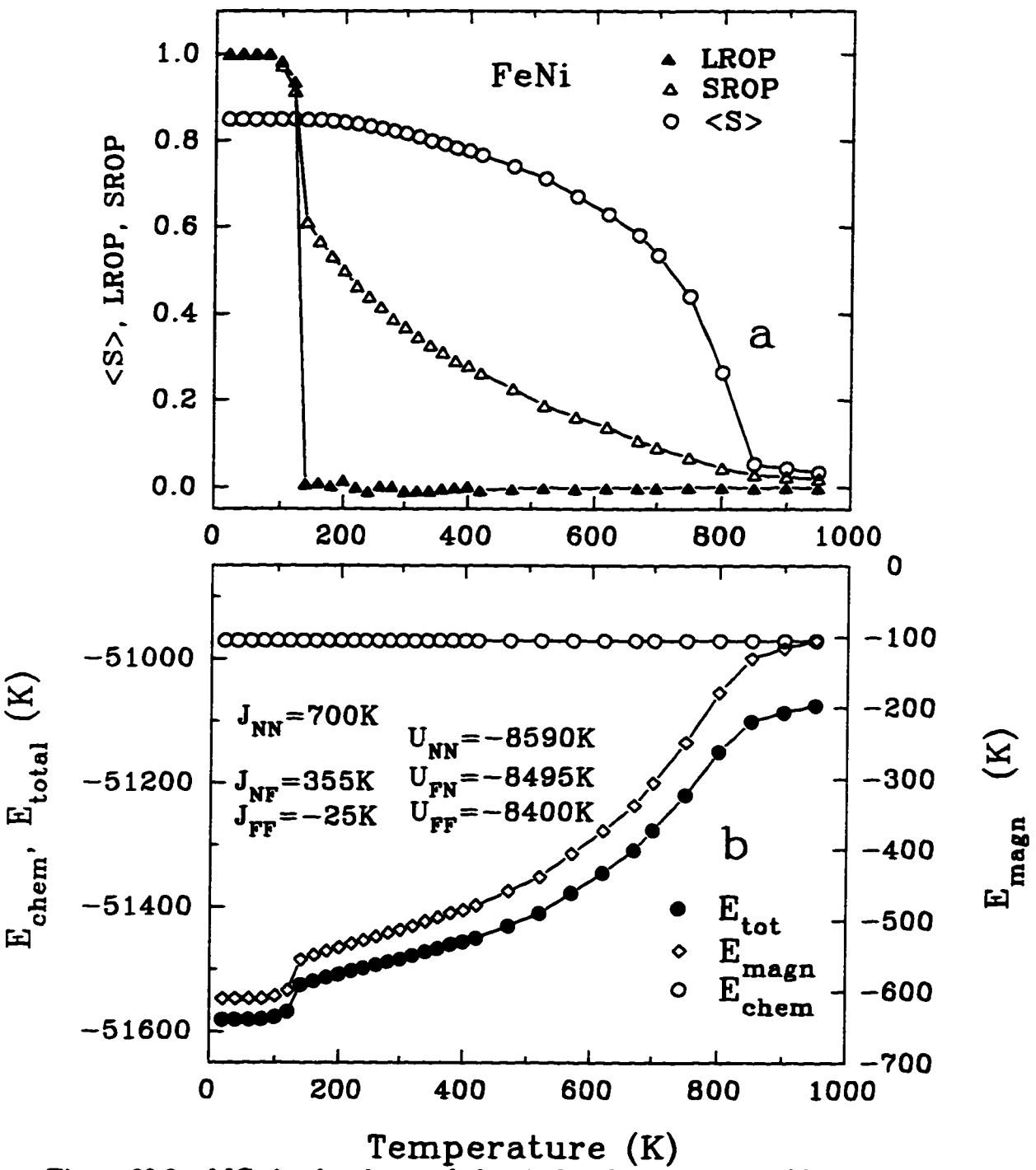

Figure 22.3 : MC simulated crystal chemical and magnetic equilibrium properties, allowing both chemical and magnetic degrees of freedom simultaneously, for FeNi with U_{FeNi} adjusted such that U = 0. The symbols have the same meanings as in Fig.22.2.

Chapter 23. CONCLUSIONS of PART IV

We have shown that in $FeNi_3$, FeNi, and Fe_3Ni alloys, with typical values of the interaction parameters that give agreement with measured properties, it is necessary to include both chemical and magnetic degrees of freedom in simulating the equilibrium properties because, not only does the degree of chemical order affect the magnetism (i.e. saturation moments, Curie points, degree of magnetic order, etc.), but the presence of magnetic interactions also significantly affects the crystal chemical properties (i.e. chemical ordering temperatures, chemical long and short range order parameters, etc.).

Just as chemical order effects on the magnetism can extend to temperatures much greater than the chemical order-disorder transition temperature because of chemical short range order, magnetic effects on the chemical ordering process can extend beyond the magnetic ordering temperature because of magnetic short range order. Above the chemical and magnetic ordering temperatures, the chemical and magnetic interactions continue to be important simultaneously in determining both the chemical and magnetic properties.

What matters is not that the chemical bond energies (U_{ij}) are much larger than the magnetic bond energies ($J_{ij}S_iS_j$) but that the change in chemical energy per atom is comparable in magnitude to the change in magnetic energy per atom, on crossing the chemical order-disorder transition. In the Fe-Ni alloys, which are typical magnetic transition metal compound-forming alloys, the magnetic component to the driving force for chemical order is comparable in magnitude to the chemical bond component.

The results of the present work allow one to make the following suggestions concerning Fe-Ni metallurgy and future work on metallic magnetic alloys in general. In attempting theoretical descriptions of the equilibrium structural phase diagram of Fe-Ni: (1) magnetic interactions must be included, and (2) MFT cannot be used

for either the magnetic degrees of freedom (because of magnetic frustration and magnetic short range order) or the chemical degrees of freedom (because chemical ordering temperatures are over estimated and chemical short range order is ignored).

The present work shows that when the differential chemical bond parameter U is small (or even positive) the magnetic interactions can dominate the chemical ordering processes. New predicted phenomena include: magnetically induced chemical order, magnetically induced chemical segregation, and magnetically driven miscibility/phase-separation transitions. Often, such phenomena will not be observed simply because the chemical equilibration times are too long at the temperatures where they occur. This can be surmounted experimentally by using low temperature particle irradiation as a means of achieving equilibrium (e.g., [106]).

Finally, recent progress has been made in including chemical and magnetic interactions by doing electronic structure calculations to examine chemical short range order at high temperatures [126]. With such elaborate calculations, it is difficult to include certain important realistic effects such as chemical disorder-induced local lattice deformation, whereas, it would be relatively easy to combine MC simulations such as ours with molecular dynamics to include: local strain, atomic vibrations, and various defects. Clearly phenomenological simulations will remain valid alternatives to ab initio calculations for some time with such complicated systems.

Chapter 24. CONCLUSION OF THE THESIS

In this thesis we report on macroscopic and microscopic magnetic properties of fcc Fe_yNi_{1-y} alloys, obtained by Mössbauer spectroscopy and MC simulations.

Detailed Mössbauer measurements and spectral analyses of fcc Fe-Ni alloys at RT, LNT and LHT show a non-linear composition dependence of the average hyperfine field in the collinear ferromagnetic region ($y \leq 0.45$) and give intrinsic HFDs at all compositions and temperatures, except at RT with high Fe-content alloys where the HFD analysis is known to break down because of dynamic lineshape effects. We also studied the effects of residual atomic (i.e. chemical) order by using samples synthesized with various quenching rates.

We proposed a new microscopic hyperfine field vector model that relates a site-specific hyperfine field to its on-site atomic moment and to its surrounding atomic moments: $< \vec{H}_k >_T = A < \vec{\mu}_k >_T + B\sum_j < \vec{\mu}_j >_T$, where A is the local field coupling parameter and B is the transferred field coupling parameter. In applying this hyperfine field model and the binomial distribution of chemical environment to hyperfine field data at LHT in the collinear ferromagnetic region, various assumptions about the coupling parameters A and B are proposed and tested to fit the non-linearity of the average hyperfine fields and the corresponding HFDs. Two sets of assumptions are considered most plausible. The first one explains the curvature in the average hyperfine fields as an artifact of $FeNi_3$-type residual short range atomic order. Two constant coupling parameters are obtained from two end members of the collinear ferromagnetic alloys ($y = 0.05$ and 0.45): $A = A_0 = 88$ kOe/μ_B, $B = B_0 = 4.6$ kOe/μ_B. The other attributes the curvature to a conduction electron density dependence of the intrinsic polarization mechanism of the hyperfine field. It requires composition dependent coupling parameters ($A = A_0 + A_1 y$, $B = B_0 + B_1 y$) to fit both the average hyperfine field and the HFDs. The four coupling parameters are obtained from fitting the predicted HFDs to the experimental counterparts: $A_0 =$

89 kOe/μ_B, A_1 = -20 kOe/μ_B and B_0 = 4.4 kOe/μ_B, B_1 = 3.2 kOe/μ_B.

With the obtained coupling parameters, A and B, the model is extended to RT and LNT. The species-specific average atomic moments of Fe and Ni atoms are obtained from fitting the calculated HFDs to the experimental HFDs. This provides a new approach to obtain species-specific magnetic moments. Moreover, it can be used in Fe-rich alloys ($y > 0.45$) where non-collinear ferromagnetism exists and local atomic moment distributions are no longer the same as the binomial atomic distributions. As long as the spin structure is known by MC simulation or by another method, our hyperfine field vector model can be used to calculate the HFDs.

A local moment model ($\mathcal{H} = -\sum J_{ij}\vec{S}_i \bullet \vec{S}_j$) with only three adjustable parameters, J_{ij}, which are the three pair-specific NN exchange constants: J_{NiNi}, J_{FeNi}, and J_{FeFe}, is used to calculate the macroscopic magnetic properties of Fe-Ni alloys by MC simulation with the Ising approximation. We reproduce the main features of the measured magnetic properties (the Curie temperature versus composition, the spontaneous saturation moment versus composition, the spontaneous magnetization versus temperature, the average magnetic moment versus the applied magnetic field and the high field paraprocess susceptibility at T = 0 K). The results suggest that the Fe-Ni system is a strong local moment system, with non-integer but stable moments that persists far above T_C. The model works quantitatively at low Fe concentrations and gives worse agreement at high Fe concentrations. The latter difficulties may be due to several causes within the context of strong local moment magnetism.

Ground state and non-zero temperature spin structures of fcc Fe-Ni alloys are explored by introducing a composition dependent J_{FeFe}, using MC simulations with the local moment model. A combination of our phenomenological hyperfine field model and the thus obtained spin structures provides a new approach to calculate HFDs as functions of composition and temperature.

The proposed hyperfine field vector model with different coupling parameter assumptions (constant and composition dependent) are tested in both the collinear ferromagnetic region and in the Fe-rich alloys (y>0.45), with MC simulations. Detailed comparison of the calculated average hyperfine fields and HFDs to the measured HFDs show the composition dependent coupling parameter models to be superior

in the overall agreement to other (constant coupling parameter) models.

The atomic moment distributions of both Fe and Ni atoms are also calculated by MC simulations, as functions of temperature and composition, and discussed in comparison to the corresponding HFDs. These types of results lead us to a better understanding of the microscopic relationships between atomic moments, local chemical environments, spin structures, thermal effects and corresponding HFDs.

In the last part of the thesis, we study the simultaneous magnetic and chemical order-disorder transitions in fcc $FeNi_3$, FeNi, and Fe_3Ni, by MC simulations. The interplay of the magnetic and chemical interactions are elucidated by calculations (1) with magnetic interactions only, assuming fixed preset degrees of chemical order, (2) with chemical interactions only, and (3) with both magnetic and chemical interactions acting simultaneously.

We found that in $FeNi_3$, FeNi and Fe_3Ni alloys, not only does the degree of chemical order affect the magnetism (i.e. saturation moments, Curie points, degree of magnetic order, etc.), but the presence of magnetic interactions also significantly affects the crystal chemical properties (i.e. chemical ordering temperatures, chemical long- and short-range order parameters, etc.). What matters is not that the chemical bond energies (U_{ij}) are much larger than the magnetic bond energies ($J_{ij}S_iS_j$) but that the change in chemical energy per atom is comparable in magnitude to the change in magnetic energy per atom, on crossing the chemical order-disorder transition. In Fe-Ni alloys, which are typical magnetic transition-metal compound-forming alloys, the magnetic component to the driving force for chemical order is comparable in magnitude to the chemical bond component. Therefore it is necessary to include both chemical and magnetic degree of freedom in simulating the equilibrium properties and in the phase diagram calculation for Fe-Ni alloys.

Finally, considering what we have presented in the thesis, some suggestions can be made for further work.

First, we could extend our phenomenological hyperfine field vector model to see whether this model is applicable to other crystalline metallic alloy sytems. From the proposed polarization mechanism of the hyperfine field, this model should be general to various systems. We could extract the coupling parameters from different

alloy systems to see how the coupling parameters change with the system and the crystal structure. How far from the probe atoms do we need to go in taking the NN moments into account in alloy systems that have different crystal structures? How do interstitial metalloid atoms (such as C, B, N, etc.) affect the coupling parameters? Is the transferred field coupling parameter species dependent, with the other moment bearing transition metal elements (Cr, Mn, and Co) or is the dependence a simple function of the conduction electron density?

The hyperfine field vector model can also be applied to examine the spin structures of other complicated systems such as spin glasses, amorphous alloys, frustrated magnetic systems, etc. By comparing calculated hyperfine fields and HFDs to the measurements, we can test the assumptions used for the spin structure calculation and then understand the magnetic behaviors of the studied system from a microscopic point of view.

We could improve the local moment model to make HFD calculations at finite temperatures in better agreement with the measurements. We have seen (section 18.2) that discrete HFDs at finite temperature are significantly different from what is obtained shown from Mössbauer spectral analysis [48]. We can try one the following, separately: (1) considering the next NN interactions in the local moment model, (2) using the Heisenberg interaction model and, (3) allowing magnetic exchange parameters J_{FeFe} to be temperature dependent. Including these considerations, one at a time, would indicate which factor is the most effective to improve the HFD calculations at finite temperature. This leads to a more realistic model for the Fe-Ni system.

At T close to T_C, more MC simulations would be useful: going to larger sizes and longer MC simulation time. This is to clarify the finite size effect and critical slowing down, when T is close to T_C. Also, one may try new MC algorithms [128, 129] to improve the calculating efficiencies and get rid of the critical slowing down completely.

The work in Part IV leads to new predictions which includes: magnetically induced chemical order, magnetically induced chemical segregation, and magnetically driven miscibility/phase separation transitions. Often, such phenomena will not be

observed simply because the chemical equilibration times are too long at the temperatures where they occur. This can be surmounted experimentally by using low temperature particle irradiation as a means of achieving equilibrium [106].

In this context, other interesting questions are raised about Fe_3Ni and similar Fe-rich fcc transition metal alloys: what is the ground state? Is it atomically segregated? In which type: clustered, banded? or other structural type? By performing particle irradiation of such alloys, we may find new phases or find an approach to reach the phases in these magnetically frustrated and /or chemically unstable (near the fcc/bcc crystal structure transition) alloys. The new materials created in this way could have various practical applications.

References

[1] C. E. Guillaume, C. R. Acad. Sci. Paris 124, 374(1897).

[2] Y. Tanji, J. Phys. Soc. Jpn. 5, 1366(1971).

[3] M. Hsyase, M. Shiga, J. Phys. Soc. Jpn. 34, 925(1973).

[4] J. S. Kouvel and R. H. Wilson, J. Appl. Phys. 32, 435(1961).

[5] L. Patrick, Phys. Rev. 93, 384(1953).

[6] J. M. Leger, C. Loriers-Susse and B. Vodar, Phys. Rev. B 6, 4250(1972).

[7] J. Crangle and G. C. Hallam, Proc. R. Soc. London Ser. A 272, 119(1963).

[8] E. A. Owen, E. L.Yates, and A. H. Sully, Proc. Phys. Soc. 49, 323(1937).

[9] H. Asano, J. Phys. Soc. Jpn. 27, 542(1969).

[10] R. J. Weiss, Proc. Phys. Soc. 82, 281(1963).

[11] M. Matsui, K. Adachi, and S. Chikazumi, J. Appl. Phys. 51, 6319(1980).

[12] S. Chikazumi, J. Magn. Magn. Mater. 10, 113(1979).

[13] J. Mathon and E. P. Wohlfarth, Phys. Status Solidi, 30, 131(1968).

[14] E. P. Wohlfarth, J. Magn. Magn. Mater. 10, 120(1979).

[15] O. Yamada, F. Ono and I. Nakai, Physica B 91, 198(1977).

[16] E.I. Kondorsky, V.L. Sedov, J. Appl. Phys. 31, 331(1960).

[17] L. Kaufman, Acta Met. 7, 575(1959).

[18] C. G. Shull and M. K. Wilkinson, Phys. Rev. 97, 304(1955).

[19] M. F. Collins, R. V. Jones and I. D. Lowde, J. Phys. Soc. Jpn., Vol. 17, Supplement B-III, 19(1962).

[20] O. K. Andersen, J. Madsen, U. K. Poulsen, O. Jepsen and J. Kollar, Physica B 86-88, 249(1977).

[21] A. R. Williams, V. L. Moruzzi and C. D. Gelatt Jr. and J. Kübler, J. Magn. Magn. Mater. 31-34, 88(1983).

[22] V. L. Moruzzi, Phys. Rev. B 41, 6939(1990).

[23] H. Hasegawa, J. Phys. C 14, 2793(1981).

[24] Y. Kakehashi, J. Phys. Soc. Jpn. 50, 2236(1981).

[25] Y. Kakehashi, Phys. Rev. B 38, 474(1988).

[26] D. Wagner, J. Phys. Cond. Mat. 1, 4635(1989).

[27] M. Shiga, in Materials Science and Technology, Ed. R.W. Cahn, P. Haasen, and E.J. Kramer, VCH, Weinheim, Vol. 3B, Part II, 159(1994).

[28] D. G. Rancourt, Physics in Canada, Jan. 3(1989).

[29] E. F. Wasserman, J. Magn. Magn. Mater. 100, 346(1991).

[30] Y. Nakamura, IEEE Trans. Mag. 10, 113(1976).

[31] A. Z. Menshikov, Physica B 161, 1(1989).

[32] P. Gütlich, R. Link and A. Trautwein, Mössbauer Spectroscopy and Transition Metal Chemistry, Inorganic Chemistry Concepts, Springer-Verlag, Vol. 3, 1978.

[33] N. N. Greenwood and T. C. Gibb, Mössbauer Spectroscopy, Chapman and Hall Ltd., London, 1971.

[34] L. Häggström, Report UUIP-851, Uppsala, 1974.

[35] N. Bales, H. Fischer and U. Gonser, Nucl. Instr. and Meth. B9, 201(1985).

[36] R. A. Brand, Nucl. Instr. and Meth. B28, 398(1987).

[37] J. G. Stevens, V. L. Coman, V. E. Stevens,C. R. Boss, Mössbauer Effecet Reference and data Journal, Mössbauer Effect Data Center, 1977-1987.

[38] D. G. Rancourt, Nucl. Instr. and Meth. B44, 199(1989).

[39] B. Window, J. Phys. E: Sci. Instrum. 4, 401(1971).

[40] J. Hesse and A. Rübartsch, J. Phys. E: Sci. Instrum. 7, 526(1974).

[41] D. G. Rancourt and J. Y. Ping, Nucl. Instr. and Meth. B58, 85(1991).

[42] D. G. Rancourt, H. H. A. Smit and R.C. Thiel, J. Magn. Magn. Mater. 66, 121(1987)

[43] M. B. Stearns, Phys. Rev. B 4, 4081(1971).

[44] S. Blügel, H. Akai, R. Zeller, P. H. Dederichs, Phys. Rev. B 35, 3271(1987).

[45] D. A. Shirley, S. S. Rosenblum, E. Matthias, Phys. Rev. B 170, 363(1968).

[46] H. Akai, M. Akai, S. Blügel, B. Drittler, H. Ebert, K. Terakura, R. Zeller, P. H. Dederichs, Progress of Theoretical Physics Supplement, No. 101, 11(1990).

[47] A. Z. Menshikov, J. Magn. Magn. Mater. 10, 205(1979).

[48] M. Shiga, Y. Nakamura J. Magn. Magn. Mater. 40, 319(1984).

[49] T. Miyazaki, Y. Ando and M. Takahashim, J. Magn. Magn. Mater. 60, 219(1986).

[50] U. Gonser, S. Nasu, W. Kappes, J. Magn. Magn. Mater. 10, 244(1979).

[51] H. Ullrich, J. Hesse, J. Mag. Magn. Mater. 45, 315(1984).

[52] D. Rhiger and R. Ingall, Phys. Rev. Lett. 28, 749(1972).

[53] K. Hayashi and N. Möri, Solid State Comm. 38, 1057(1981).

[54] S. Tomiyoshi, H. Yamamoto and H.Watanabe, J. Phys. Soc. Jpn. 30, 1605(1971).

[55] B. Window, J. Appl. Phys. 44, 2853(1973).

[56] J. Hesse, E. Hagen, Hyper. Int. 28, 475(1986).

[57] D. G. Rancourt, Nucl. Instr. and Meth. Vol. B44, 210(1989).

[58] H. R. Rechenberg, Hyper. Int. 54, 683(1990).

[59] J. B. Muller, J. Hesse, Z. Phys. B 54, 35(1983).

[60] M. M. Abd-Elmeguid, U. Hobuss, H. Micklitz, B. Huck and J.Hesse, Phys. Rev. B 35, 4796(1987).

[61] A. Z. Menshikov and E. E. Yurchikov, Sov. Phys. JETP 36, 100(1973).

[62] J. Y. Ping and D.G. Rancourt, J. Magn. Magn. Mater. 103, 285(1992).

[63] D. G. Rancourt, P. Hargraves and G. Lamarch, J. Magn. Magn. Mater. 87, 71(1990).

[64] C. E. Johnson, Proc. Phys. Soc. 81, 1079(1963).

[65] J. W. Drijver and F. van der Woude, Phys. Rev. B 16, 985(1977), 993(1977).

[66] T. E. Cranshaw, J. Phys.: Cond. Mat. 2, 2743(1972).

[67] T. E. Cranshaw, J. Phys. F: Metal Phys. 2, 615(1972).

[68] S. S. Hanna, J. Heberle, G. J. Perlow, R. S. Perston, D. H. Vincent, Phys. Rev. Lett. 4, 513(1960).

[69] U. Erich Z. Physik 227, 25(1969).

[70] M. Shiga, Y. Maeda, Y. Nakamura, J. Phys. Soc. Jpn. 37, 363(1974).

[71] C. L. Chien, D. P. Musser, F. E. Luborsky, J. J. Becker and J. L. Water, Sol. St. Commun. 24, 231(1974).

[72] M. E. Lines, Sol. St. Commun. 36, 457(1980).

[73] B. Fultz, J.W. Morris, Jr. Phys. Rev. B34, 4480(1986).

[74] P. Panissod, J. Durand and J. I. Budnick, Nucl. Instr. and Meth. 199, 99(1982).

[75] B. Fultz, in Mössbauer Spectroscopy Applied to Magnetism and Material Science, Ed. G. J. Long and Fernande Grandjean, Plenum, New York, Vol. 1, 1993.

[76] H. S. Chen and C. E. Miller, Rev. Sci. Instrum. 41, 1237(1970).

[77] P. Hansen, in "Hand-book of magnetic materials", Ed. K. H. J. Buschow, North-Holland, Amsterdam, 1991, p.289.

[78] H. H. Liebermann, in "Amorphous Metallic Alloys", Ed. F. E. Luborsky, Butterworths, London, 1983, p.26.

[79] G. Burns, Solid State Physics, Academic Press, New York, 508(1985).

[80] H. M. Rietveld, J. Appl. Cryst. 2, 65(1969).

[81] J. Arai, Jpn. J. Appl. Phys. 20, 571(1981).

[82] D. G. Rancourt, J. Y. Ping and M. Z. Dang, Can. J. Phys. 70, 1241(1992).

[83] J. Hesse and Chr. Buchal, Int. J. Magn. 5, 11(1973).

[84] W. H. Press, B. P. Flannery, S. A. Teukolsky and W. T. Vetterling, Numerical Recipes, Cambridge University Press, 1986.

[85] R. Barlow, Statistics, Jogn Wiley&Sons, New York, 1989.

[86] T. G. Kollie and C. R. Brooks, Phys. Stat. Sol. 19, 545(173).

[87] M.-Z. Dang and D. G. Rancourt, Phys. Rev.B 53, 2291(1996).

[88] F. James and M. Ross, Computer Physics Communications 10, 343(1975).

[89] R. Ingalls, F. Van Der Woude, G.A. Sawatzky, in Mössbauer Isomers Shifts, Ed. G.K. Shendy, F.E. Wagner, North Holland Publishing Company, 1978, p.605.

[90] Monte Carlo Method in statistical Physics, Ed. K. Binder, Springer-Verlag, 1980.

[91] P. D. Scholten, Phys. Rev. B 32, 345(1985).

[92] M. K. Phani and J. L. Lebowitz, M. H. Kalos and C. C. Tsai, Phys. Rev. Lett. 42, 577(1979).

[93] K. Binder, Phys. Rev. Lett. 45, 811(1980).

[94] J. Merikoski, J. Tomonen and M. Manninen, Phys. Rev. Lett. 66, 938(1991).

[95] B. Dünweg and K. Binder, Phys. Rev. B 36, 6935(1987).

[96] K. Binder, Statics and Dynamics of Alloy Phase Transformations, Ed. P. E. A. Turchi and A. Gonis, Plenum, New York, 1994.

[97] N. Metropolis, A. W. Rosenbluth, M. N. Rosebluth, A. H. Teller, E. Teller, J. Chem. Phys. 21, 1087(1953).

[98] M. Dubé, P. R. L. Heron, and D. G. Rancourt, J. Magn. Magn. Mater. 147, 122(1995).

[99] Physics and Applications of Invar Alloys, Ed. H. Sato, Maruzen Company Ltd., Tokyo, 1978.

[100] F. López-Salinas and D. A. Conteras-Solorio, Revista Mexicana de Fisica 38, 252(1992).

[101] F. Mejía-Lira, Jesús Urĩas and J. L. Morán-López, Phys. Rev. B 24, 5270(1981).

[102] J. M. Sanchez and C. H. Lin, Phys. Rev. B 30, 1448(1984).

[103] D. G. Rancourt and M. Z. Dang, Phys. Rev. B 54, 1(1996).

[104] D. G. Rancourt, S. Chehab, and G. Lamarche, J. Magn. Magn. Mater. 78, 129(1989).

[105] K. B. Reuter, D. B. Williams, and J.I. Goldstein, Metall. Trans. 20A, 719(1988); and references therein.

[106] D.G. Rancourt and R.B. Scorzelli, J. Magn. Magn. Mater. 150, 30(195); and references therein.

[107] T. Takahashi, W.A. Bassett, and H.K. Mao, J. Geophys. Res. 73, 4717(1968).

[108] E. Huang, W.A. Bassett, and M.S. Weathers, J. Geophys. Res. 93, 7741(1988).

[109] H. K. Mao, Y. Wu, L.C. Chen, J.F. Shu, and A.P. Jephcoat, J. Geophys. Res. 95, 21737(1990).

[110] W. J. Carr Jr., Phys. Rev. 85, 590(1952).

[111] M.-Z. Dang, M. Dubé and D.G. Rancourt, J. Magn. Magn. Mater. 147, 133(1995).

[112] D. G. Rancourt, M. Dubé, and P.R.L. Heron, J. Magn. Magn. Mater. 125, 39(1993).

[113] Y.-Y. Chuang, Y.A. Chang, R. Schmid, and J.-C. Lin, Metall. Trans. 17A, 1361(1986).

[114] G. Inden and W. Pepperhoff, Z. Metall. 81, 770(1990).

[115] F. Schmid and K. Binder, J. Phys.: Cond. Mat., 4, 3569(1992).

[116] R. J. Wakelin and E.L. Yates, Proc. Phys. Soc. B, 66, 221(1953).

[117] T. G. Kollie and C.R. Brooks, Phys. Stat. Sol. A, 19, 545(1973).

[118] E. Josso, J. Phys. 12, 399(1951).

[119] Van der Woude, Phys. Rev. Lett., 34, 1026(1975).

[120] J. Paulev D. Dautreppe, J. Laugier, and L. Néel, C. R. Acad. Sci. Paris 254, 1962.

[121] T. Nagata, M. Funaki, and J.A. Danon, in Memoirs of National Institute of Polar Research Special Issue No. 41, Proceedings of the Tenth Symposium on Antarctic Meteorites (National Institute of Polar Research, Tokyo, 1986.

[122] I. A. Abrikosov, O. Erickson, P. Söderlind, H. L. Skriver, and B. Johansson, Phys. Rev. B 51, 1058(1995).

[123] C. Kuhrt and L. Schultz, J. Appl. Phys. 73, 1975(1993).

[124] G. S. Painter, Phys. Rev. Lett. 70, 3959(1993).

[125] C. Kittel, Introduction to Solid State Physics, Wiley, New York, 1986.

[126] J. B. Staunton, D.D. Johnson, and F.J. Pinski, Phys. Rev. B 50, 1450(1994).

[127] D. D. Johnson, J.B. Staunton, and F.J. Pinski, Phys. Rev. B 50, 1473(1994).

[128] U. Wolff, Physic. Rev. Lett.62, 361(1989).

[129] R. H. Swendsen and J. S. Wang, Phys. Rev. Lett. 58, 86(1987).

[130] L. C. Landau and E. M. Lifshiz, Statistical Physics, Chapter 14, Pergamon Press,1989.

[131] Philip C. Clapp and S. C. Moss, Phys. Rev. 171, 754(1965).

Appendix A. TABLE OF CONTENTS OF APPENDICES

Appendix B. Programs used in Part II

Appendix B-1: CARLO8.FOR

```
C-----------------------------------------------------------------
C  THIS PROGRAM IS TO FIND THE AVERAGE ATOMIC MOMENT FOR A BINARY
C  FCC Fe-Ni ALLOY AS A FUNCTION OF TEMPERATURE BY MONTE CARLO METHOD.
C  ATOMS CAN BE SET TO LATTICE IN A RANDOM OR ORDERED STATE DEPEND ON
C  USER'S REQUEST.
C  SOURCE CODE CARLO8.FOR
C-----------------------------------------------------------------

      DOUBLE PRECISION AVSPIN,EPAT
      INTEGER ATOM(10,10,10,4),SPSIGN(10,10,10,4),FEFLAG
      REAL SPIN(2),JK(2,2)
      PARAMETER(N=10)
C     OBTAIN RELEVANT PARAMETERS
      SPIN(1) = 0.3
      SPIN(2) = 1.4
      WRITE (6,'(/,1X,A40)') 'PLEASE ENTER THE FOLLOWING VALUES:   '
1     WRITE (6,'(/,1X,A30)') 'NI CONCENTRATION AT % ?     '
      READ (5,*)CNI

      CNI=CNI/100.
      CFE = 1.0 - CNI

      WRITE (6,'(/,1X,A25)') 'J(NI,NI)/KB IN KELVIN ?   '
      READ (5,*)JK(1,1)
      WRITE (6,'(/,1X,A25)') 'J(NI,FE)/KB IN KELVIN ?   '
      READ (5,*)JK(1,2)
      JK(2,1)=JK(1,2)
      WRITE (6,'(/,1X,A25)') 'J(FE,FE)/KB IN KELVIN ?   '
      READ (5,*)JK(2,2)
      WRITE (6,'(/,1X,A65,/)')' PLEASE ENTER 1 IF ONLY FE ATOMS ARE TO B
     @E FLIPPED, 0 OTHERWISE:              '
      READ (5,*)FEFLAG
      IF(FEFLAG.NE.1)FEFLAG=0
      NTOT = 4*N**3
      OPEN(2,FILE='CLO7.DAT',STATUS='OLD')
      OPEN(10,FILE='CLO7.OUT',STATUS='OLD')
C     PLACE ATOMS RANDOMLY ON LATTICE
      IDUM=-938245
      CNIR = 0.0
```

```
      DO 40 IX = 1,N
DO 30 IY = 1,N
  DO 20 IZ = 1,N
            DO 10 IM = 1,4
               RANNUM=RAN2(IDUM)
               IF(RANNUM.LE.CNI)THEN
                  ATOM(IX,IY,IZ,IM)=1
                  CNIR = CNIR + 1.0
               ELSE
                  ATOM(IX,IY,IZ,IM)=2
               ENDIF
10          CONTINUE
20        CONTINUE
30      CONTINUE
40    CONTINUE

C     TO MAKE THE COMPOSITION EXACTLY SAME AS THE REQUIRED
      DO 500 I=1,1000
        IF(CNIR.NE.CNI*NTOT)THEN
        RANNUM=RAN2(IDUM)
IX=NINT(RANNUM*N+0.5)
        RANNUM=RAN2(IDUM)
IY=NINT(RANNUM*N+0.5)
        RANNUM=RAN2(IDUM)
IZ=NINT(RANNUM*N+0.5)
        RANNUM=RAN2(IDUM)
        IM=NINT(RANNUM*4+0.5)
        IF(CNIR.LT.CNI*NTOT)THEN
           IF(ATOM(IX,IY,IZ,IM).EQ.1)GO TO 500
              ATOM(IX,IY,IZ,IM)=1
              CNIR=CNIR+1
           ELSE
              IF(ATOM(IX,IY,IZ,IM).EQ.2)GO TO 500
                ATOM(IX,IY,IZ,IM)=2
                CNIR=CNIR-1
              END IF
           END IF
500 CONTINUE
      CNIR = CNIR/NTOT
      CFER = 1.0-CNIR
      WRITE(2,501)JK(1,1),JK(1,2),JK(2,2),SPIN(1),SPIN(2),CNIR,NSTEP,
     *            NTOT

501   FORMAT(1X,'J(NI,NI)=',F6.1,'  J(FE,NI)=',F6.1,'  J(FE,FE)=',
     *       F6.1,/,1X,'S(NI)=',F4.1,'  S(FE)=',F4.1,/,' C(NI)=',
     *       F6.3,//,'NUMBER OF TENTATIVE FLIPS PER RUN: ',I6,/,
```

```
     *  'TOTAL NUMBER OF ATOMS ON LATTICE:',I6)

      IF(FEFLAG.EQ.1)THEN
       WRITE(2,'(1X,A40,/)')'ONLY FE ATOMS ARE ALLOWED TO BE FLIPPED'
      ENDIF
C     CHOOSE INITIAL SPIN CONFIGURATION
50    WRITE(6,*)
      WRITE(6,*)'PLEASE CHOOSE AN INITIAL SPIN CONFIGURATION:'
      WRITE(6,*)'    1 = RANDOM'
      WRITE(6,*)'    2 = ALL UP'
      WRITE(6,*)'    3 = ALL NI UP, ALL FE DOWN'
      WRITE(6,*)'    4 = ALL NI UP, ALL FE RANDOM'
      WRITE(6,*)
      READ(5,*)ICONF
      IF(ICONF.EQ.1) GO TO 60
      IF(ICONF.EQ.2) GO TO 70
      IF(ICONF.EQ.3) GO TO 80
      IF(ICONF.EQ.4) GO TO 90
      WRITE(6,*)'YOU MUST ENTER 1, 2, 3 OR 4'
      GO TO 50
C     RANDOM SPIN CONFIGURATION
60    DO 68 IX = 1,N
DO 66 IY = 1,N
  DO 64 IZ = 1,N
    DO 62 IM = 1,4
      RANNUM=RAN2(IDUM)
      IF(RANNUM.LT.0.5)THEN
SPSIGN(IX,IY,IZ,IM)=1
      ELSE
SPSIGN(IX,IY,IZ,IM)=-1
      ENDIF
62          CONTINUE
64        CONTINUE
66      CONTINUE
68    CONTINUE
      WRITE(2,*) ' INITIAL SPIN CONFIGURATION IS RANDOM'
      GO TO 100
C     ALL SPIN UP CONFIGURATION
70    DO 78 IX = 1,N
DO 76 IY = 1,N
  DO 74 IZ = 1,N
    DO 72 IM = 1,4
      SPSIGN(IX,IY,IZ,IM)=1
72          CONTINUE
74        CONTINUE
76      CONTINUE
```

```
78    CONTINUE
      WRITE(2,*)'INITIAL SPIN CONFIGURATION IS ALL UP'
      GO TO 100
C     ALL NI SPIN UP, ALL FE SPIN DOWN
80    DO 88 IX = 1,N
DO 86 IY = 1,N
  DO 84 IZ = 1,N
    DO 82 IM = 1,4
      IF(ATOM(IX,IY,IZ,IM).EQ.1)THEN
SPSIGN(IX,IY,IZ,IM)=1
      ELSE
SPSIGN(IX,IY,IZ,IM)=-1
      ENDIF
82          CONTINUE
84        CONTINUE
86      CONTINUE
88    CONTINUE
      WRITE(2,*)' INITIAL SPIN CONFIGURATION IS ALL NI UP, ALL FE DOWN'
      GO TO 100
C     ALL NI UP, ALL FE RANDOM
90    DO 98 IX = 1,N
DO 96 IY = 1,N
  DO 94 IZ = 1,N
    DO 92 IM = 1,4
      IF(ATOM(IX,IY,IZ,IM).EQ.1)THEN
SPSIGN(IX,IY,IZ,IM)=1
      ELSE
RANNUM=RAN2(IDUM)
IF(RANNUM.LT.0.5)THEN
 SPSIGN(IX,IY,IZ,IM)=1
ELSE
 SPSIGN(IX,IY,IZ,IM)=-1
ENDIF
      ENDIF
92          CONTINUE
94        CONTINUE
96      CONTINUE
98    CONTINUE

      WRITE(2,*)'INITIAL SPIN CONFIGURATION IS ALL NI UP, ALL FE RANDOM'
C     CALCULATE INITIAL TOTAL ENERGY

100   CALL ENERTOT(SPSIGN,ATOM,SPIN,JK,ETOT,N)
      EPAT = ETOT/NTOT

      WRITE(2,511)EPAT
```

```
      WRITE(6,511)EPAT
511    FORMAT(/,1X,'INITIAL ENERGY PER ATOM = ',E10.4)
C     CALCULATE INITIAL AVERAGE SPIN PER ATOM
      CALL SPINTOT(SPSIGN,ATOM,SPIN,TOTSPIN,N)
      AVSPIN = TOTSPIN / NTOT
      WRITE(2,521)AVSPIN
521    FORMAT(/,1X,'INITIAL AVRAGE SPIN PER ATOM = ',F6.3,/)
C-------------------------------------------------------
C APPLY DIFFERENT TEMPERATURES
C-------------------------------------------------------
      DO 888 KKK=10,2000,100
         IF(KKK.LE.610)THEN
            TEMP=KKK*1.
            NSTEP=1500
         ELSE
            TEMP=TEMP+20
            NSTEP=2500
         END IF
      CALL FLIP1(NSTEP,SPSIGN,ATOM,ETOT,TOTSPIN,SPIN,JK,N,FEFLAG,
     *  TEMP, AVSPIN,EPAT)
      WRITE(10,101)TEMP, AVSPIN, EPAT
101    FORMAT(2X,F6.2,1X,F8.5, 1X, F10.2)
888    CONTINUE
END

C     THIS SUBROUTINE CALCULATES THE TOTAL ENERGY OF A FCC BINARY SPIN
C     SYSTEM WITH CYCLIC BOUNDARY CONDITIONS.

      SUBROUTINE ENERTOT(SPSIGN,ATOM,SPIN,JK,ETOT,N)
      DOUBLE PRECISION ETOT,E
      INTEGER ATOM(10,10,10,4),SPSIGN(10,10,10,4),IX,IY,IZ,IM,N
      REAL SPIN(2),JK(2,2)
      ETOT = 0.0
      DO 10 IX = 1,N
DO 8 IY = 1,N
  DO 6 IZ = 1,N
    DO 4 IM = 1,4
            CALL ECALC(SPSIGN,ATOM,IX,IY,IZ,IM,SPIN,JK,E,N)
      ETOT = ETOT + 0.5*E
4           CONTINUE
6         CONTINUE
8       CONTINUE
10    CONTINUE
      RETURN
      END
```

```
C     SUBROUTINE SPINTOT(SPSIGN,ATOM,SPIN,TOTSPIN,N)
C     THIS SUBROUTINE CALCULATES THE TOTAL SPIN OF FCC BINARY SPIN
C     SYSTEM WITH BYCLIC BOUNDARY CONDITIONS.

      SUBROUTINE SPINTOT(SPSIGN,ATOM,SPIN,TOTSPIN,N)
      DOUBLE PRECISION TOTSPIN
      INTEGER ATOM(10,10,10,4),SPSIGN(10,10,10,4),IX,IY,IZ,IM,N
      REAL SPIN(2)
      TOTSPIN = 0.0
      DO 10 IX = 1,N
DO 8 IY = 1,N
  DO 6 IZ = 1,N
    DO 4 IM = 1,4
      TOTSPIN = TOTSPIN + SPIN(ATOM(IX,IY,IZ,IM))*
     *                          SPSIGN(IX,IY,IZ,IM)
4           CONTINUE
6         CONTINUE
8       CONTINUE
10    CONTINUE
      RETURN
      END

C     SUBROUTINE ECALC
C     THIS SUBROUTINE CALCULATES THE INTERACTION ENERGY BETWEEN
C     A GIVEN ATOM AND ITS 12 NEAR NEIGHBOURS IN A FCC BINARY SPIN
C     SYSTEM WITH CYCLIC BOUNDARY CONDITIONS.
C     IT USES SUBROUTINE BOUND

      SUBROUTINE ECALC(SPSIGN,ATOM,IX,IY,IZ,IM,S,JK,E,N)
      DOUBLE PRECISION E
      INTEGER ATOM(10,10,10,4),SPSIGN(10,10,10,4),SI
      REAL S(2),JK(2,2)

      E1 = 0.0
      II=ATOM(IX,IY,IZ,IM)
      SI=SPSIGN(IX,IY,IZ,IM)
      IF(IM.EQ.1)THEN
DO 10 I=2,4
  JJ=ATOM(IX,IY,IZ,I)
        E1 = E1 + S(II)*SI*SPSIGN(IX,IY,IZ,I)*S(JJ)*JK(II,JJ)
10      CONTINUE
CALL BOUND(IX-1,IIX,N)
CALL BOUND(IY-1,IIY,N)
CALL BOUND(IZ-1,IIZ,N)
DO 20 I=2,4,2
  JJ=ATOM(IIX,IY,IZ,I)
```

```
          E1 = E1 + S(II)*SI*SPSIGN(IIX,IY,IZ,I)*S(JJ)*JK(II,JJ)
 20       CONTINUE
 DO 30 I=2,3
   JJ=ATOM(IX,IIY,IZ,I)
          E1 = E1 + S(II)*SI*SPSIGN(IX,IIY,IZ,I)*S(JJ)*JK(II,JJ)
 30       CONTINUE
 DO 40 I=3,4
   JJ=ATOM(IX,IY,IIZ,I)
          E1=E1+S(II)*SI*SPSIGN(IX,IY,IIZ,I)*S(JJ)*JK(II,JJ)
 40       CONTINUE
 JJ=ATOM(IIX,IIY,IZ,2)
         E1=E1+S(II)*SI*SPSIGN(IIX,IIY,IZ,2)*S(JJ)*JK(II,JJ)
 JJ=ATOM(IX,IIY,IIZ,3)
         E1=E1+S(II)*SI*SPSIGN(IX,IIY,IIZ,3)*S(JJ)*JK(II,JJ)
 JJ=ATOM(IIX,IY,IIZ,4)
         E1=E1+S(II)*SI*SPSIGN(IIX,IY,IIZ,4)*S(JJ)*JK(II,JJ)
 GO TO 500
       ENDIF

       IF(IM.EQ.2)THEN
 DO 110 I=3,4
   JJ=ATOM(IX,IY,IZ,I)
          E1=E1+S(II)*SI*SPSIGN(IX,IY,IZ,I)*S(JJ)*JK(II,JJ)
 110      CONTINUE
 JJ=ATOM(IX,IY,IZ,1)
         E1=E1+S(II)*SI*SPSIGN(IX,IY,IZ,1)*S(JJ)*JK(II,JJ)
 CALL BOUND(IX+1,IIX,M)
 CALL BOUND(IY+1,IIY,M)
 CALL BOUND(IZ-1,IIZ,M)
 DO 120 I=1,3,2
   JJ=ATOM(IIX,IY,IZ,I)
          E1=E1+S(II)*SI*SPSIGN(IIX,IY,IZ,I)*S(JJ)*JK(II,JJ)
 120      CONTINUE
 DO 130 I=1,4,3
   JJ=ATOM(IX,IIY,IZ,I)
          E1=E1+S(II)*SI*SPSIGN(IX,IIY,IZ,I)*S(JJ)*JK(II,JJ)
 130      CONTINUE
 DO 140 I=3,4
   JJ=ATOM(IX,IY,IIZ,I)
         E1=E1+S(II)*SI*SPSIGN(IX,IY,IIZ,I)*S(JJ)*JK(II,JJ)
 140      CONTINUE
 JJ=ATOM(IIX,IIY,IZ,1)
         E1=E1+S(II)*SI*SPSIGN(IIX,IIY,IZ,1)*S(JJ)*JK(II,JJ)
 JJ=ATOM(IX,IIY,IIZ,4)
         E1=E1+S(II)*SI*SPSIGN(IX,IIY,IIZ,4)*S(JJ)*JK(II,JJ)
 JJ=ATOM(IIX,IY,IIZ,3)
```

```
        E1=E1+S(II)*SI*SPSIGN(IIX,IY,IIZ,3)*S(JJ)*JK(II,JJ)
GO TO 500
      ENDIF
      IF(IM.EQ.3)THEN
DO 210 I=1,2
  JJ=ATOM(IX,IY,IZ,I)
        E1=E1+S(II)*SI*SPSIGN(IX,IY,IZ,I)*S(JJ)*JK(II,JJ)
210     CONTINUE
JJ=ATOM(IX,IY,IZ,4)
        E1=E1+S(II)*SI*SPSIGN(IX,IY,IZ,4)*S(JJ)*JK(II,JJ)
CALL BOUND(IX-1,IIX,M)
CALL BOUND(IY+1,IIY,M)
CALL BOUND(IZ+1,IIZ,M)
DO 220 I=2,4,2
  JJ=ATOM(IIX,IY,IZ,I)
        E1=E1+S(II)*SI*SPSIGN(IIX,IY,IZ,I)*S(JJ)*JK(II,JJ)
220     CONTINUE
DO 230 I=1,4,3
  JJ=ATOM(IX,IIY,IZ,I)
        E1=E1+S(II)*SI*SPSIGN(IX,IIY,IZ,I)*S(JJ)*JK(II,JJ)
230     CONTINUE
DO 240 I=1,2
  JJ=ATOM(IX,IY,IIZ,I)
        E1=E1+S(II)*SI*SPSIGN(IX,IY,IIZ,I)*S(JJ)*JK(II,JJ)
240     CONTINUE
JJ=ATOM(IIX,IIY,IZ,4)
        E1=E1+S(II)*SI*SPSIGN(IIX,IIY,IZ,4)*S(JJ)*JK(II,JJ)
JJ=ATOM(IIX,IY,IIZ,2)
        E1=E1+S(II)*SI*SPSIGN(IIX,IY,IIZ,2)*S(JJ)*JK(II,JJ)
JJ=ATOM(IX,IIY,IIZ,1)
        E1=E1+S(II)*SI*SPSIGN(IX,IIY,IIZ,1)*S(JJ)*JK(II,JJ)
GO TO 500
      ENDIF

      IF(IM.EQ.4)THEN
DO 310 I=1,3
  JJ=ATOM(IX,IY,IZ,I)
        E1=E1+S(II)*SI*SPSIGN(IX,IY,IZ,I)*S(JJ)*JK(II,JJ)
310     CONTINUE
CALL BOUND(IX+1,IIX,M)
CALL BOUND(IY-1,IIY,M)
CALL BOUND(IZ+1,IIZ,M)
DO 320 I=1,3,2
  JJ=ATOM(IIX,IY,IZ,I)
        E1=E1+S(II)*SI*(SPSIGN(IIX,IY,IZ,I)*S(JJ)*JK(II,JJ))
320     CONTINUE
```

```
      DO 330 I=2,3
        JJ=ATOM(IX,IIY,IZ,I)
      E1=E1+S(II)*SI*(SPSIGN(IX,IIY,IZ,I)*S(JJ)*JK(II,JJ))
      330     CONTINUE
      DO 340 I=1,2
        JJ=ATOM(IX,IY,IIZ,I)
              E1=E1+S(II)*SI*(SPSIGN(IX,IY,IIZ,I)*S(JJ)*JK(II,JJ))
      340     CONTINUE
      JJ=ATOM(IIX,IIY,IZ,3)
              E1=E1+S(II)*SI*(SPSIGN(IIX,IIY,IZ,3)*S(JJ)*JK(II,JJ))
      JJ=ATOM(IIX,IY,IIZ,1)
              E1=E1+S(II)*SI*(SPSIGN(IIX,IY,IIZ,1)*S(JJ)*JK(II,JJ))
      JJ=ATOM(IX,IIY,IIZ,2)
              E1=E1+S(II)*SI*(SPSIGN(IX,IIY,IIZ,2)*S(JJ)*JK(II,JJ))
            ENDIF
      500   E1=-E1
            E=E1
            RETURN
            END


            SUBROUTINE BOUND(I,II,IMAX)
      C     THIS SUBROUTINE VERIFIES IF COORDINATE I IS OUT OF BOUND
      C     IF IT IS, THE CORRECT VALUE IS RETURNED IN II.

            INTEGER I,II,IMAX
            IF(I.EQ.0)THEN
      II=IMAX
      RETURN
            ENDIF
            IF(I.EQ.IMAX+1)THEN
      II=1
      RETURN
            ENDIF
            II=I
            RETURN
            END

      C     THIS SUBROUTINE FLIPS SINGLE SPINS IF THIS REDUCES THE TOTAL
      C     ENERGY OF THE SYSTEM.  SPINS ARE CHOSEN RANDOMLY.
            SUBROUTINE FLIP1(NSTEP,SPSIGN,ATOM,ETOT,TOTSPIN,SPIN,JK,N,
           *                 FEFLAG,TEMP,AVSPIN,EPAT)
            DOUBLE PRECISION DF,DSFF,E,EPAT,EDELTA,AVSPIN,TOTSPIN
            INTEGER ATOM(10,10,10,4),SPSIGN(10,10,10,4),FEFLAG
            REAL SPIN(2),ETOT,JK(2,2),RANNUM
            NTOT=N*N*N*4
```

```
C     INITIALIZATION
      AVSPIN1=0.0
      EPAT1=0.0
      MD=2500
      MO=30
      MM=0
      IDUM=-59823170
      COUNT=0.0
C-----------------------------------------------------------------
C     PERFORM NSTEP MONTE CARLO SIMULATIONS
C-----------------------------------------------------------------
      DO 150 K=1,NSTEP
        DO 120 I = 1,NTOT
          RANNUM=RAN2(IDUM)
          IX = NINT(RANNUM*N+.5)
          RANNUM=RAN2(IDUM)
          IY = NINT(RANNUM*N+.5)
          RANNUM=RAN2(IDUM)
          IZ = NINT(RANNUM*N+.5)
          RANNUM=RAN2(IDUM)
          IM = NINT(RANNUM*4+.5)
C     SKIP FLIP CHECK IF FEFLAG IS SET AND THIS IS A NICKEL ATOM
           IF(FEFLAG.EQ.1.AND.ATOM(IX,IY,IZ,IM).EQ.1)GO TO 100
            CALL ECALC(SPSIGN,ATOM,IX,IY,IZ,IM,SPIN,JK,E,N)
            EDELTA = -2.*E
            DF=DEXP(-EDELTA/TEMP*1.0)
            DSFF=DF/(1.+DF)
            RANNUM = RAN2(IDUM))
             IF(RANNUM.LT.DSFF)THEN
               SPSIGN(IX,IY,IZ,IM) = -SPSIGN(IX,IY,IZ,IM)
               ETOT = ETOT + EDELTA
               TOTSPIN=TOTSPIN+2*SPSIGN(IX,IY,IZ,IM)
     *  *SPIN(ATOM(IX,IY,IZ,IM))
             END IF
100   CONTINUE
120     CONTINUE
C      AFTER REACH THE EQUILIBRIUM STATE
        IF(K.GE.MD)THEN
C      GET RID OF THE CORRELATION
         COUNT=COUNT+1
C      ACCUMULATE THE AVERAGE
           IF(COUNT.GE.MO)THEN
            MM=MM+1
             COUNT=0.
              AVSPIN=TOTSPIN/NTOT
```

```
              AVSPIN1=AVSPIN1+ABS(AVSPIN)
             EPAT1 = EPAT1+ETOT/NTOT
           END IF
      END IF
150   CONTINUE
      AVSPIN=AVSPIN1/NN
      EPAT=EPAT1/NN
      RETURN
      END

      FUNCTION RAN2(IDUM)
      INTEGER IDUM,IM1,IM2,IMM1,IA1,IA2,IQ1,IQ2,IR1,IR2,NTAB,NDIV
      REAL RAN2,AM,EPS,RNMX
      PARAMETER (IM1=2147483563,IM2=2147483399,AM=1./IM1,IMM1=IM1-1,
     * IA1=40014,IA2=40692,IQ1=53668,IQ2=52774,IR1=12211,
     * IR2=3791,NTAB=32,NDIV=1+IMM1/NTAB,EPS=1.2E-7,RNMX=1.-EPS)
INTEGER IDUM2,J,K,IV(NTAB),IY
SAVE IV,IY,IDUM2
DATA IDUM2/123456789/,IV/NTAB*0/,IY/0/
IF (IDUM.LE.0) THEN
IDUM=MAX(-IDUM,1)
IDUM2=IDUM
DO 11 J=NTAB+8,1,-1
K=IDUM/IQ1
IDUM=IA1*(IDUM-K*IQ1)-K*IR1
IF (IDUM.LT.0) IDUM=IDUM+IM1
IF (J.LE.NTAB) IV(J)=IDUM
11      CONTINUE
IY=IV(1)
ENDIF
K=IDUM/IQ1
IDUM=IA1*(IDUM-K*IQ1)-K*IR1
IF (IDUM.LT.0) IDUM=IDUM+IM1
K=IDUM2/IQ2
IDUM2=IA2*(IDUM2-K*IQ2)-K*IR2
IF (IDUM2.LT.0) IDUM2=IDUM2+IM2
J=1+IY/NDIV
IY=IV(J)-IDUM2
IV(J)=IDUM
IF (IY.LT.1) IY=IY+IMM1
RAN2=MIN(AM*IY,RNMX)
RETURN
END

//////////////////////////////////////////////////////////////////////
\\\\\\\\\\\\\\\\\\\\\\\\\\\\\\\\\\\\\\\\\\\\\\\\\\\\\\\\\\\\\\\\\\\\\\\
```

Appendix B-2: MONTE4.FOR

```
C-----------------------------------------------------------------
C     THIS PROGRAM FINDS A FUNDAMENTAL STATE FOR A RANDOM BINARY ALLOY
C     WITH FCC STRUCTURE AT T = 0 K WITH APPLIED FIELD.  A MONTE CARLO
C     METHOD IS USED.
C     SOURCE CODE MONTE4.FOR
C     Subroutines BOUND, SPINTOT, RAN2 are same those used in CARLO8.FOR
C-----------------------------------------------------------------
      DOUBLE PRECISION EPAT,TOTSPIN
      INTEGER ATOM(10,10,10,4),SPSIGN(10,10,10,4)
      INTEGER FEFLAG
      REAL SPIN(2),ETOT,JK(2,2),HAPL
      PARAMETER(N=10)
C     OBTAIN RELEVANT PARAMETERS
      SPIN(1) = 0.3
      SPIN(2) = 1.4
      WRITE (6,'(/,1X,A40)') 'PLEASE ENTER THE FOLLOWING VALUES:       '
1     WRITE (6,'(/,1X,A30)') 'NI CONCENTRATION AT % ?      '
      READ (5,*)CNI
      CNI=CNI/100.
      CFE = 1.0 - CNI
      WRITE (6,'(/,1X,A25)') 'J(NI,NI)/KB IN KELVIN ?   '
      READ (5,*)JK(1,1)
      WRITE (6,'(/,1X,A25)') 'J(NI,FE)/KB IN KELVIN ?   '
      READ (5,*)JK(1,2)
      JK(2,1)=JK(1,2)
      WRITE (6,'(/,1X,A25)') 'J(FE,FE)/KB IN KELVIN ?   '
      READ (5,*)JK(2,2)
      WRITE (6,'(/,1X,A10)') 'NPAS ?       '
      READ (5,*)NPAS
      WRITE (6,'(/,1X,A65,/)')' PLEASE ENTER 1 IF ONLY FE ATOMS ARE TO B
     @E FLIPPED, 0 OTHERWISE:              '
      READ (5,*)FEFLAG
      IF(FEFLAG.NE.1)FEFLAG=0
      NTOT = 4*N**3
      NSTEP = NPAS
      OPEN(2,FILE="MONTE3.DAT",STATUS="OLD")
      OPEN(8,FILE='MONTE3.DDD',STATUS='OLD')
      OPEN(9,FILE='MONTE3.PRO',STATUS='OLD')
      OPEN(10,FILE='MONTE3.OUT',STATUS='OLD')
 C    PLACE ATOMS RANDOMLY ON LATTICE
      IDUM= -382971
      CNIR = 0.0
      DO 40 IX = 1,N
DO 30 IY = 1,N
```

```
      DO 20 IZ = 1,N
        DO 10 IM = 1,4
          CALL RANDOM(RANNUM)
          IF(RANNUM.LT.CNI)THEN
ATOM(IX,IY,IZ,IM)=1
CNIR = CNIR + 1.0
          ELSE
ATOM(IX,IY,IZ,IM)=2
          ENDIF
10          CONTINUE
20        CONTINUE
30      CONTINUE
40    CONTINUE
      CNIR = CNIR/NTOT
      CFER = 1.0-CNIR
      WRITE(2,501)JK(1,1),JK(1,2),JK(2,2),SPIN(1),SPIN(2),CNIR,NSTEP,
     *            NTOT
501   FORMAT(1X,'J(NI,NI)=',F6.1,'  J(FE,NI)=',F6.1,'  J(FE,FE)=',
     *       F6.1,/,1X,'S(NI)=',F4.1,'  S(FE)=',F4.1,/,' C(NI)=',
     *       F6.3,//,'NUMBER OF TENTATIVE FLIPS PER RUN: ',I6,/,
     *  'TOTAL NUMBER OF ATOMS ON LATTICE:',I6)
      IF(FEFLAG.EQ.1)THEN
       WRITE(2,'(1X,A40,/)')'ONLY FE ATOMS ARE ALLOWED TO BE FLIPPED'
      ENDIF
C     CHOOSE INITIAL SPIN CONFIGURATION
50    WRITE(6,*)
      WRITE(6,*)'PLEASE CHOOSE AN INITIAL SPIN CONFIGURATION:'
      WRITE(6,*)'    1 = RANDOM'
      WRITE(6,*)'    2 = ALL UP'
      WRITE(6,*)'    3 = ALL NI UP, ALL FE DOWN'
      WRITE(6,*)'    4 = ALL NI UP, ALL FE RANDOM'
      WRITE(6,*)
      READ(5,*)ICONF
      IF(ICONF.EQ.1) GO TO 60
      IF(ICONF.EQ.2) GO TO 70
      IF(ICONF.EQ.3) GO TO 80
      IF(ICONF.EQ.4) GO TO 90
      WRITE(6,*)'YOU MUST ENTER 1, 2, 3 OR 4'
      GO TO 50
C     RANDOM SPIN CONFIGURATION
60    DO 68 IX = 1,N
DO 66 IY = 1,N
  DO 64 IZ = 1,N
    DO 62 IM = 1,4
              RANNUM=RAN2(IDUM)
      IF(RANNUM.LT.0.5)THEN
```

```
SPSIGN(IX,IY,IZ,IM)=1
      ELSE
SPSIGN(IX,IY,IZ,IM)=-1
      ENDIF
62          CONTINUE
64        CONTINUE
66      CONTINUE
68    CONTINUE
      WRITE(2,*) ' INITIAL SPIN CONFIGURATION IS RANDOM'
      GO TO 100
C     ALL SPIN UP CONFIGURATION
70    DO 78 IX = 1,N
DO 76 IY = 1,N
  DO 74 IZ = 1,N
    DO 72 IM = 1,4
      SPSIGN(IX,IY,IZ,IM)=1
72          CONTINUE
74        CONTINUE
76      CONTINUE
78    CONTINUE
      WRITE(2,*)'INITIAL SPIN CONFIGURATION IS ALL UP'
      GO TO 100
C     ALL NI SPIN UP, ALL FE SPIN DOWN
80    DO 88 IX = 1,N
DO 86 IY = 1,N
  DO 84 IZ = 1,N
    DO 82 IM = 1,4
      IF(ATOM(IX,IY,IZ,IM).EQ.1)THEN
SPSIGN(IX,IY,IZ,IM)=1
      ELSE
SPSIGN(IX,IY,IZ,IM)=-1
      ENDIF
82          CONTINUE
84        CONTINUE
86      CONTINUE
88    CONTINUE
      WRITE(2,*)' INITIAL SPIN CONFIGURATION IS ALL NI UP, ALL FE DOWN'
      GO TO 100
C     ALL NI UP, ALL FE RANDOM
90    DO 98 IX = 1,N
DO 96 IY = 1,N
  DO 94 IZ = 1,N
    DO 92 IM = 1,4
      IF(ATOM(IX,IY,IZ,IM).EQ.1)THEN
SPSIGN(IX,IY,IZ,IM)=1
      ELSE
```

```
CALL RANDOM(RANNUM)
IF(RANNUM.LT.0.5)THEN
 SPSIGN(IX,IY,IZ,IM)=1
ELSE
 SPSIGN(IX,IY,IZ,IM)=-1
ENDIF
      ENDIF
92          CONTINUE
94        CONTINUE
96      CONTINUE
98    CONTINUE
      WRITE(2,*)'INITIAL SPIN CONFIGURATION IS ALL NI UP, ALL FE RANDOM'
C     CALCULATE INITIAL TOTAL ENERGY
100   CALL ENERTOT(SPSIGN,ATOM,SPIN,JK,ETOT,N,EAPL)
      EPAT = ETOT/NTOT
      WRITE(2,511)EPAT
      WRITE(6,511)EPAT
511    FORMAT(/,1X,'INITIAL ENERGY PER ATOM = ',E10.4)
      CALL SPINTOT(SPSIGN,ATOM,SPIN,TOTSPIN,N)
      AVSPIN = TOTSPIN / NTOT
      WRITE(2,521)AVSPIN
521    FORMAT(/,1X,'INITIAL AVRAGE SPIN PER ATOM = ',F6.3,/)
C-------------------------------------------------------------
C       APPLY MAGNETIC FIELD ON THE SYSTEM
C-------------------------------------------------------------
      HAPL=0.
      EAPL=1.1577*HAPL
      DO 888 KKK=1,300,2
         HAPL=KKK-1
         EAPL=1.1577*HAPL
         WRITE(2,111)HAPL
111   FORMAT(1X,'HAPL(TESLA)=',F10.3)
       CALL FLIP1(NSTEP,SPSIGN,ATOM,ETOT,TOTSPIN,SPIN,JK,N,FEFLAG,EAPL
     *,CFER)
       WRITE(10,881)HAPL,TOTSPIN/NTOT
881    FORMAT(2X,F8.2,2X,F8.5)
888   CONTINUE
      END

C     SUBROUTINE ENERTOT(SPSIGN,ATOM,SPIN,JK,ETOT,N,EAPL)
C     THIS SUBROUTINE CALCULATES THE TOTAL ENERGY OF A FCC BINARY SPIN
C     SYSTEM WITH CYCLIC BOUNDARY CONDITIONS.
      SUBROUTINE ENERTOT(SPSIGN,ATOM,SPIN,JK,ETOT,N,EAPL)

      DOUBLE PRECISION ETOT
      INTEGER ATOM(10,10,10,4),SPSIGN(10,10,10,4)
```

```
      REAL SPIN(2),JK(2,2),EAPL
      ETOT = 0.0
      DO 10 IX = 1,N
DO 8 IY = 1,N
  DO 6 IZ = 1,N
    DO 4 IM = 1,4
     CALL ECALC(SPSIGN,ATOM,IX,IY,IZ,IM,SPIN,JK,E,E1,N,EAPL)
      ETOT = ETOT + 0.5*E1-SPSIGN(IX,IY,IZ,IM)
     *              *SPIN(ATOM(IX,IY,IZ,IM))*EAPL
4           CONTINUE
6         CONTINUE
8       CONTINUE
10    CONTINUE
      RETURN
      END

C     SUBROUTINE ECALC
C     THIS SUBROUTINE CALCULATES THE INTERACTION ENERGY BETWEEN
C     A GIVEN ATOM AND ITS 12 NEAR NEIGHBOURS IN A FCC BINARY SPIN
C     SYSTEM WITH CYCLIC BOUNDARY CONDITIONS.
      SUBROUTINE ECALC(SPSIGN,ATOM,IX,IY,IZ,IM,S,JK,E,E1,N,EAPL)
      DOUBLE E,E1,E2
      INTEGER ATOM(10,10,10,4),SPSIGN(10,10,10,4),SI
      REAL S(2),JK(2,2)
      E1 = 0.0
      E2 = 0.0
      II=ATOM(IX,IY,IZ,IM)
      SI=SPSIGN(IX,IY,IZ,IM)
      E2=S(II)*SI*EAPL

      IF(IM.EQ.1)THEN
DO 10 I=2,4
  JJ=ATOM(IX,IY,IZ,I)
  E1 = E1 + S(II)*SI*SPSIGN(IX,IY,IZ,I)*S(JJ)*JK(II,JJ)*0.8617
10      CONTINUE
CALL BOUND(IX-1,IIX,N)
CALL BOUND(IY-1,IIY,N)
CALL BOUND(IZ-1,IIZ,N)
DO 20 I=2,4,2
  JJ=ATOM(IIX,IY,IZ,I)
  E1 = E1 + S(II)*SI*SPSIGN(IIX,IY,IZ,I)*S(JJ)*JK(II,JJ)*0.8617
20      CONTINUE
DO 30 I=2,3
  JJ=ATOM(IX,IIY,IZ,I)
  E1 = E1 + S(II)*SI*SPSIGN(IX,IIY,IZ,I)*S(JJ)*JK(II,JJ)*0.8617
30      CONTINUE
```

```
DO 40 I=3,4
  JJ=ATOM(IX,IY,IIZ,I)
  E1=E1+S(II)*SI*SPSIGN(IX,IY,IIZ,I)*S(JJ)*JK(II,JJ)*0.8617
40      CONTINUE
JJ=ATOM(IIX,IIY,IZ,2)
E1=E1+S(II)*SI*SPSIGN(IIX,IIY,IZ,2)*S(JJ)*JK(II,JJ)*0.8617
JJ=ATOM(IX,IIY,IIZ,3)
E1=E1+S(II)*SI*(SPSIGN(IX,IIY,IIZ,3)*S(JJ)*JK(II,JJ)*0.8617)
JJ=ATOM(IIX,IY,IIZ,4)
E1=E1+S(II)*SI*SPSIGN(IIX,IY,IIZ,4)*S(JJ)*JK(II,JJ)*0.8617
GO TO 500
      ENDIF

      IF(IM.EQ.2)THEN
DO 110 I=3,4
  JJ=ATOM(IX,IY,IZ,I)
        E1=E1+S(II)*SI*SPSIGN(IX,IY,IZ,I)*S(JJ)*JK(II,JJ)*0.8617
110     CONTINUE
JJ=ATOM(IX,IY,IZ,1)
E1=E1+S(II)*SI*SPSIGN(IX,IY,IZ,1)*S(JJ)*JK(II,JJ)*0.8617
CALL BOUND(IX+1,IIX,N)
CALL BOUND(IY+1,IIY,N)
CALL BOUND(IZ-1,IIZ,N)
DO 120 I=1,3,2
  JJ=ATOM(IIX,IY,IZ,I)
E1=E1+S(II)*SI*SPSIGN(IIX,IY,IZ,I)*S(JJ)*JK(II,JJ)*0.8617
120     CONTINUE
DO 130 I=1,4,3
  JJ=ATOM(IX,IIY,IZ,I)
E1=E1+S(II)*SI*SPSIGN(IX,IIY,IZ,I)*S(JJ)*JK(II,JJ)*0.8617
130     CONTINUE
DO 140 I=3,4
  JJ=ATOM(IX,IY,IIZ,I)
E1=E1+S(II)*SI*SPSIGN(IX,IY,IIZ,I)*S(JJ)*JK(II,JJ)*0.8617
140     CONTINUE
JJ=ATOM(IIX,IIY,IZ,1)
E1=E1+S(II)*SI*SPSIGN(IIX,IIY,IZ,1)*S(JJ)*JK(II,JJ)*0.8617
JJ=ATOM(IX,IIY,IIZ,4)
E1=E1+S(II)*SI*SPSIGN(IX,IIY,IIZ,4)*S(JJ)*JK(II,JJ)*0.8617
JJ=ATOM(IIX,IY,IIZ,3)
E1=E1+S(II)*SI*SPSIGN(IIX,IY,IIZ,3)*S(JJ)*JK(II,JJ)*0.8617
GO TO 500
      ENDIF

      IF(IM.EQ.3)THEN
DO 210 I=1,2
```

```
  JJ=ATOM(IX,IY,IZ,I)
E1=E1+S(II)*SI*SPSIGN(IX,IY,IZ,I)*S(JJ)*JK(II,JJ)*0.8617
210      CONTINUE
JJ=ATOM(IX,IY,IZ,4)
E1=E1+S(II)*SI*SPSIGN(IX,IY,IZ,4)*S(JJ)*JK(II,JJ)*0.8617
CALL BOUND(IX-1,IIX,N)
CALL BOUND(IY+1,IIY,N)
CALL BOUND(IZ+1,IIZ,N)
DO 220 I=2,4,2
  JJ=ATOM(IIX,IY,IZ,I)
E1=E1+S(II)*SI*SPSIGN(IIX,IY,IZ,I)*S(JJ)*JK(II,JJ)*0.8617
220      CONTINUE
DO 230 I=1,4,3
  JJ=ATOM(IX,IIY,IZ,I)
E1=E1+S(II)*SI*SPSIGN(IX,IIY,IZ,I)*S(JJ)*JK(II,JJ)*0.8617
230      CONTINUE
DO 240 I=1,2
  JJ=ATOM(IX,IY,IIZ,I)
E1=E1+S(II)*SI*SPSIGN(IX,IY,IIZ,I)*S(JJ)*JK(II,JJ)*0.8617
240      CONTINUE
JJ=ATOM(IIX,IIY,IZ,4)
E1=E1+S(II)*SI*SPSIGN(IIX,IIY,IZ,4)*S(JJ)*JK(II,JJ)*0.8617
JJ=ATOM(IIX,IY,IIZ,2)
E1=E1+S(II)*SI*SPSIGN(IIX,IY,IIZ,2)*S(JJ)*JK(II,JJ)*0.8617
JJ=ATOM(IX,IIY,IIZ,1)
E1=E1+S(II)*SI*SPSIGN(IX,IIY,IIZ,1)*S(JJ)*JK(II,JJ)*0.8617
GO TO 500
      ENDIF

      IF(IM.EQ.4)THEN
DO 310 I=1,3
  JJ=ATOM(IX,IY,IZ,I)
E1=E1+S(II)*SI*SPSIGN(IX,IY,IZ,I)*S(JJ)*JK(II,JJ)*0.8617
310      CONTINUE
CALL BOUND(IX+1,IIX,N)
CALL BOUND(IY-1,IIY,N)
CALL BOUND(IZ+1,IIZ,N)
DO 320 I=1,3,2
  JJ=ATOM(IIX,IY,IZ,I)
E1=E1+S(II)*SI*(SPSIGN(IIX,IY,IZ,I)*S(JJ)*JK(II,JJ)*0.8617)
320      CONTINUE
DO 330 I=2,3
  JJ=ATOM(IX,IIY,IZ,I)
        E1=E1+S(II)*SI*(SPSIGN(IX,IIY,IZ,I)*S(JJ)*JK(II,JJ)*0.8617)
330      CONTINUE
DO 340 I=1,2
```

```
  JJ=ATOM(IX,IY,IIZ,I)
E1=E1+S(II)*SI*(SPSIGN(IX,IY,IIZ,I)*S(JJ)*JK(II,JJ)*0.8617)
340     CONTINUE
JJ=ATOM(IIX,IIY,IZ,3)
E1=E1+S(II)*SI*(SPSIGN(IIX,IIY,IZ,3)*S(JJ)*JK(II,JJ)*0.8617)
JJ=ATOM(IIX,IY,IIZ,1)
E1=E1+S(II)*SI*(SPSIGN(IIX,IY,IIZ,1)*S(JJ)*JK(II,JJ)*0.8617)
JJ=ATOM(IX,IIY,IIZ,2)
E1=E1+S(II)*SI*(SPSIGN(IX,IIY,IIZ,2)*S(JJ)*JK(II,JJ)*0.8617)
      ENDIF
500   E1=-E1
      E2=-E2
      E=(E1+E2)
      RETURN
      END

C     SUBROUTINE FLIP1
C     THIS SUBROUTINE FLIPS SINGLE SPINS IF THIS REDUCES THE TOTAL
C     ENERGY OF THE SYSTEM.  SPINS ARE CHOSEN RANDOMLY.

      SUBROUTINE FLIP1(NSTEP,SPSIGN,ATOM,ETOT,TOTSPIN,SPIN,JK,N,
     @        FEFLAG,EAPL,CFER)
      DOUBLE PRECISION ETOT, TOTSPIN,EDELTA
      INTEGER ATOM(10,10,10,4),SPSIGN(10,10,10,4)
      INTEGER FEFLAG
      REAL SPIN(2),JK(2,2)
      NTOT=N*N*N*4
      AVSPIN1=0.0
      EPAT1=0.0
      ND=1000
      NO=20
      NN=0
      COUNT=0
      IDUM=-3852619
C     PERFORM NSTEP MONTE CARLO SIMULATIONS
      DO 150 K=1,NSTEP
       DO 120 I = 1,NTOT
        RANNUM=RAN2(IDUM)
IX = NINT(RANNUM*N+.5)
        RANNUM=RAN2(IDUM)
IY = NINT(RANNUM*N+.5)
        RANNUM=RAN2(IDUM)
IZ = NINT(RANNUM*N+.5)
        RANNUM=RAN2(IDUM)
IM = NINT(RANNUM*4+.5)
```

```
C     SKIP FLIP CHECK IF FEFLAG IS SET AND THIS IS A NICKEL ATOM

IF(FEFLAG.EQ.1.AND.ATOM(IX,IY,IZ,IM).EQ.1)GO TO 100
 CALL ECALC(SPSIGN,ATOM,IX,IY,IZ,IM,SPIN,JK,E,E1,N,EAPL)
 EDELTA = -2.*E
         IF(EDELTA.LT.0.0)THEN
   SPSIGN(IX,IY,IZ,IM) = -SPSIGN(IX,IY,IZ,IM)
   ETOT = ETOT + EDELTA
   TOTSPIN=TOTSPIN+2*SPSIGN(IX,IY,IZ,IM)
     *  *SPIN(ATOM(IX,IY,IZ,IM))
 END IF
100 CONTINUE
120    CONTINUE
C     AFTER REACH EQULIBRIUM
       IF(K.GT.NO)THEN
C     GET RID OF THE CORRELATION
       COUNT=COUNT+1
C     ACCUMULATE THE AVERAGE
          IF(COUNT.GE.ND)THEN
             COUNT=0.
             WRITE(2,541)TOTSPIN/NTOT
             WRITE(2,551)ETOT/NTOT
          END IF
       END IF
150   CONTINUE
541   FORMAT(1X,'FINAL AVSPIN = ',F6.3)
551   FORMAT(1X,'FINAL ENERGY PER ATOM= ',E10.4)
      WRITE(8,*)EAPL/1.1577,AVSPIN,EPAT
C    LAST CHECK TO SEE ALL ATOMS ARE AT THE GROUND STATE
      DO 160 IX=1,N
       DO 159 IY=1,N
        DO 158 IZ=1,N
         DO 157 IM=1,4
         IF(FEFLAG.EQ.1.AND.ATOM(IX,IY,IZ,IM).EQ.1)GO TO 200
 CALL ECALC(SPSIGN,ATOM,IX,IY,IZ,IM,SPIN,JK,E,E1,N,EAPL)
 EDELTA = -2.*E
 ETT1=ETOT
         IF(EDELTA.LT.0.0)THEN
   SPSIGN(IX,IY,IZ,IM) = -SPSIGN(IX,IY,IZ,IM)
   ETOT = ETOT + EDELTA
   TOTSPIN=TOTSPIN+2*SPSIGN(IX,IY,IZ,IM)
     *  *SPIN(ATOM(IX,IY,IZ,IM))

             CALL ENERTOT(SPSIGN,ATOM,SPIN,JK,ETOT,N,EAPL)
              IF(ETOT.GT.ETT1)THEN
                SPSIGN(IX,IY,IZ,IM)=-SPSIGN(IX,IY,IZ,IM)
```

```
              TOTSPIN=TOTSPIN+2.*SPSIGN(IX,IY,IZ,IM)
              ETOT=ETT1
            END IF
          END IF
200     CONTINUE
157     CONTINUE
158     CONTINUE
159     CONTINUE
160     CONTINUE
      WRITE(2,542)TOTSPIN/NTOT
      WRITE(2,552)ETOT/NTOT
542   FORMAT(1X,'FINAL AVSPINB = ',F6.3)
552   FORMAT(1X,'FINAL ENERGYB PER ATOM= ',E10.4)
      RETURN
      END
```

Appendix C. Programs used in Part III

Apendix C-1: AVMNTO.FOR

```
C-----------------------------------------------------------------
C     THIS PROGRAM CALCULATES SITE-SPECIFIC THERMAL AVERAGE MOMENT
C     IN A RANDOM BINARY ALLOY WITH FCC STRUCTURE AS A FUNCTION OF
C     TEMPERATURE.  A MONTE CARLO METHOD IS USED.
C     SOURCE CODE AVMNTO.FOR
C-----------------------------------------------------------------
      IMPLICIT DOUBLE PRECISION (A-H,O-Z)
      INTEGER ATOM(10,10,10,4),SPSIGN(10,10,10,4)
      INTEGER FEFLAG
      REAL SPIN(2),JK(2,2),RANNUM
      DIMENSION SS(10,10,10,4),PRO(25),H(25),HFI(10,10,10,4)
      PARAMETER(N=10)
C     OBTAIN RELEVANT PARAMETERS
      SPIN(1) =1.0
      SPIN(2) = 1.0
      OPEN(5,file='AVMNT.PAR')
      READ (5,*)CNI
      READ(5,*)TEMP
      CNI=CNI/100.
      CFE = 1.0 - CNI
      READ (5,*)JK(1,1)
      READ (5,*)JK(1,2)
      JK(2,1)=JK(1,2)
      READ (5,*)JK(2,2)
      READ (5,*)FEFLAG
      IF(FEFLAG.NE.1)FEFLAG=0
      NTOT = 4*N**3
      OPEN(2,FILE ='AVMNT.DAT', STATUS='OLD')
      OPEN(8,FILE='AVMNT.DOD',STATUS='OLD')
      OPEN(9,file='AVMNT.PRO')
      OPEN(10,FILE='AVMNT.OUT',STATUS='OLD')
C     PLACE ATOMS RANDOMLY ON LATTICE
      IDUM=-637419
      CNIR = 0.0
      DO 40 IX = 1,N
DO 30 IY = 1,N
  DO 20 IZ = 1,N
    DO 10 IM = 1,4
      RANNUM=RAN2(IDUM)
```

```
       IF(RANNUM.LE.CNI)THEN
ATOM(IX,IY,IZ,IM)=1
CNIR = CNIR + 1.0
      ELSE
ATOM(IX,IY,IZ,IM)=2
             ENDIF
10          CONTINUE
20         CONTINUE
30       CONTINUE
40     CONTINUE
      DO 500 I=1,1500
IF(CNIR.NE.CNI*NTOT)THEN
RANNUM=RAN2(IDUM)
IX=NINT(RANNUM*N+0.5)
RANNUM=RAN2(IDUM)
IY=NINT(RANNUM*N+0.5)
RANNUM=RAN2(IDUM)
IZ=NINT(RANNUM*N+0.5)
RANNUM=RAN2(IDUM)
IM=NINT(RANNUM*4+0.5)
IF(CNIR.LT.CNI*NTOT)THEN
IF(ATOM(IX,IY,IZ,IM).EQ.1)GO TO 500
   ATOM(IX,IY,IZ,IM)=1
   CNIR=CNIR+1
ELSE
 IF(ATOM(IX,IY,IZ,IM).EQ.2)GO TO 500
   ATOM(IX,IY,IZ,IM)=2
     CNIR=CNIR-1
 END IF
END IF
500    CONTINUE
       CNIR = CNIR/NTOT
       CFER = 1.0-CNIR
       WRITE(2,501)JK(1,1),JK(1,2),JK(2,2),SPIN(1),SPIN(2),CNIR,NSTEP,
     * NTOT
501    FORMAT(1X,'J(NI,NI)=',F6.1,'  J(FE,NI)=',F6.1,'  J(FE,FE)=',
     *         F6.1,/,1X,'S(NI)=',F4.1,'  S(FE)=',F4.1,/,' C(NI)=',
     *         F6.3,//,'NUMBER OF FLIP PER ATOM',I6,/,
     *  'TOTAL NUMBER OF ATOMS ON LATTICE:',I6)

       IF(FEFLAG.EQ.1)THEN
       WRITE(2,'(1X,A40,/)')'ONLY FE ATOMS ARE ALLOWED TO BE FLIPPED'
       ENDIF
C      CHOOSE INITIAL SPIN CONFIGURATION
50     WRITE(6,*)
       WRITE(6,*)'PLEASE CHOOSE AN INITIAL SPIN CONFIGURATION:'
```

```
      WRITE(6,*)'    1 = RANDOM'
      WRITE(6,*)'    2 = ALL UP'
      WRITE(6,*)'    3 = ALL NI UP, ALL FE DOWN'
      WRITE(6,*)'    4 = ALL NI UP, ALL FE RANDOM'
      READ(5,*)ICONF
      IF(ICONF.EQ.1) GO TO 60
      IF(ICONF.EQ.2) GO TO 70
      IF(ICONF.EQ.3) GO TO 80
      IF(ICONF.EQ.4) GO TO 90
C     RANDOM SPIN CONFIGURATION

60    DO 68 IX = 1,N
DO 66 IY = 1,N
  DO 64 IZ = 1,N
    DO 62 IM = 1,4
      RANNUM=RAN2(IDUM)
      IF(RANNUM.LT.0.5)THEN
SPSIGN(IX,IY,IZ,IM)=1
      ELSE
SPSIGN(IX,IY,IZ,IM)=-1
      ENDIF
62          CONTINUE
64        CONTINUE
66      CONTINUE
68    CONTINUE
      WRITE(2,*) ' INITIAL SPIN CONFIGURATION IS RANDOM'
      GO TO 100
C     ALL SPIN UP CONFIGURATION
70    DO 78 IX = 1,N
DO 76 IY = 1,N
  DO 74 IZ = 1,N
    DO 72 IM = 1,4
      SPSIGN(IX,IY,IZ,IM)=1
72          CONTINUE
74        CONTINUE
76      CONTINUE
78    CONTINUE
      WRITE(2,*)'INITIAL SPIN CONFIGURATION IS ALL UP'
      GO TO 100
C     ALL NI SPIN UP, ALL FE SPIN DOWN
80    DO 88 IX = 1,N
DO 86 IY = 1,N
  DO 84 IZ = 1,N
    DO 82 IM = 1,4
      IF(ATOM(IX,IY,IZ,IM).EQ.1)THEN
SPSIGN(IX,IY,IZ,IM)=1
```

```
      ELSE
SPSIGN(IX,IY,IZ,IM)=-1
      ENDIF
82          CONTINUE
84        CONTINUE
86      CONTINUE
88    CONTINUE
      WRITE(2,*)' INITIAL SPIN CONFIGURATION IS ALL NI UP, ALL FE DOWN'
      GO TO 100
C     ALL NI UP, ALL FE RANDOM
90    DO 98 IX = 1,N
DO 96 IY = 1,N
  DO 94 IZ = 1,N
    DO 92 IM = 1,4
      IF(ATOM(IX,IY,IZ,IM).EQ.1)THEN
SPSIGN(IX,IY,IZ,IM)=1
      ELSE
RANNUM=RAN2(IDUM)
IF(RANNUM.LT.0.5)THEN
 SPSIGN(IX,IY,IZ,IM)=1
ELSE
 SPSIGN(IX,IY,IZ,IM)=-1
ENDIF
      ENDIF
92          CONTINUE
94        CONTINUE
96      CONTINUE
98    CONTINUE

      WRITE(2,*)'INITIAL SPIN CONFIGURATION IS ALL NI UP, ALL FE RANDOM'
C     CALCULATE INITIAL TOTAL ENERGY
100   CALL ENERTOT(SPSIGN,ATOM,SPIN,JK,ETOT,N)
      EPAT = ETOT/NTOT
      WRITE(2,511)EPAT
511    FORMAT(/,1X,'INITIAL ENERGY PER ATOM = ',E10.4)
C     CALCULATE INITIAL AVERAGE SPIN PER ATOM
      CALL SPINTOT(SPSIGN,ATOM,SPIN,TOTSPIN,N)
      AVSPIN = TOTSPIN / NTOT
      WRITE(2,521)AVSPIN
      WRITE(6,521)AVSPIN
521    FORMAT(/,1X,'INITIAL AVRAGE SPIN PER ATOM = ',F6.3,/)
C-------------------------------------------------------------
C CALCULATE SITE SPEFIC THERMAL AVERAGE MOMENT AT T
C-------------------------------------------------------------
AVSSFE=0.
       WRITE(2,111)TEMP
```

```
AVSSNI=0.
        NSTEP=100000
      WRITE(9,*)INT((1.-CNIR)*NTOT)
      WRITE(2,*)INT((1.-CNIR)*NTOT)
111   FORMAT(1X,'TEMP=',F8.3)
       CALL FLIP1(NSTEP,SPSIGN,ATOM,ETOT,TOTSPIN,SPIN,JK,N,FEFLAG,
     *TEMP,AVSPIN,AVE,SS)
      DO 18 IX = 1,N
DO 17 IY = 1,N
  DO 16 IZ = 1,N
    DO 14 IM = 1,4
           WRITE(2,202)SS(IX,IY,IZ,IM),ATOM(IX,IY,IZ,IM)
202     FORMAT(1X,F8.5,1X,I4)
        IF(ATOM(IX,IY,IZ,IM).EQ.2)THEN
   AVSSFE=AVSSFE+SS(IX,IY,IZ,IM)
        ELSE
   AVSSNI=AVSSNI+SS(IX,IY,IZ,IM)
END IF
14 CONTINUE
16 CONTINUE
17 CONTINUE
18 CONTINUE
WRITE(2,22)TEMP, AVSSFE/(CFER*NTOT), AVSSNI/(CNIR*NTOT)
22      FORMAT(1X,'TEMP=',F5.1,'AVMFe=',F8.5,'AVMNi=',F8.5)
        WRITE(2,501)JK(1,1),JK(1,2),JK(2,2),SPIN(1),SPIN(2),CNIR,NSTEP,
     @ NTOT
C888 CONTINUE
        RETURN
        END


C     SUBROUTINE FLIP1 TO GET SITE-SPECIFIC THERMAL AVERAGE ATOMIC MOMENT
C     SINGLE FLIP IS USED.  SPINS ARE CHOSEN RANDOMLY.

      SUBROUTINE FLIP1(NSTEP,SPSIGN,ATOM,ETOT,TOTSPIN,SPIN,JK,N,
     @        FEFLAG,TEMP,AVSPIN,EPAT,SS)

      IMPLICIT DOUBLE PRECISION (A-H,O-Z)
      INTEGER ATOM(10,10,10,4),SPSIGN(10,10,10,4),FEFLAG
      REAL SPIN(2),JK(2,2),RANNUM
      DIMENSION SS(10,10,10,4)

      NTOT=N*N*N*4
      IDUM=-4736185
      MD=3000
      MO=20
```

```
      AVSPIN1=0.
      EAV1=0.
      DO 168 IX=1,N
DO 166 IY=1,N
  DO 164 IZ=1,N
    DO 162 IM=1,4
   SS(IX,IY,IZ,IM)=0.0
162      CONTINUE
164    CONTINUE
166  CONTINUE
168    CONTINUE
       NN=0
      COUNT=0.0
      DO 150 K=1,NSTEP
       DO 120 I = 1,NTOT
RANNUM=RAN2(IDUM)
IX = NINT(RANNUM*N+.5)
RANNUM=RAN2(IDUM)
IY = NINT(RANNUM*N+.5)
RANNUM=RAN2(IDUM)
IZ = NINT(RANNUM*N+.5)
RANNUM=RAN2(IDUM)
IM = NINT(RANNUM*4+.5)
IF(FEFLAG.EQ.1.AND.ATOM(IX,IY,IZ,IM).EQ.1)GO TO 100
          CALL ECALC(SPSIGN,ATOM,IX,IY,IZ,IM,SPIN,JK,E,N)
          EDELTA = -2.*E
          DF=EXP(-EDELTA/TEMP)
          DSFF=DF/(1.+DF)
    RANNUM=RAN2(IDUM)
           IF(RANNUM.LT.DSFF)THEN
             SPSIGN(IX,IY,IZ,IM) = -SPSIGN(IX,IY,IZ,IM)
     ETOT = ETOT + EDELTA
     TOTSPIN=TOTSPIN+2*SPSIGN(IX,IY,IZ,IM)
     *  *SPIN(ATOM(IX,IY,IZ,IM))
   END IF
100 CONTINUE
120 CONTINUE
C      WAIT TILL THE SYSTEM REACH THE EQUILIBRIUM STATE
IF(K.GE.3000)THEN
  COUNT=COUNT+1
C        GET RID OF THE CORRELATION AND ACCUMULATE THE AVERAGE
   IF(COUNT.GE.20)THEN
              NN=NN+1
      COUNT=0.
    EAV1=EAV1+ETOT/NTOT
    AVSPIN1=AVSPIN1+ABS(TOTSPIN/NTOT)
```

```
      DO 68 IX1 = 1,N
DO 66 IY1 = 1,N
  DO 64 IZ1 = 1,N
    DO 62 IM1 = 1,4
   SS(IX1,IY1,IZ1,IM1)=SS(IX1,IY1,IZ1,IM1)+
     *SPSIGN(IX1,IY1,IZ1,IM1)*SPIN(ATOM(IX1,IY1,IZ1,IM1))
62          CONTINUE
64        CONTINUE
66      CONTINUE
68    CONTINUE
        END IF
END IF
150    CONTINUE
       DO 268 IX = 1,N
   DO 266 IY = 1,N
  DO 264 IZ = 1,N
    DO 262 IM = 1,4
   SS(IX,IY,IZ,IM)=SS(IX,IY,IZ,IM)/NN
262      CONTINUE
264    CONTINUE
266  CONTINUE
268    CONTINUE
       AVSPIN=AVSPIN1/NN
       EPAT=EAV1/NN
       RETURN
       END
////////////////////////////////////////////////////////////////////
\\\\\\\\\\\\\\\\\\\\\\\\\\\\\\\\\\\\\\\\\\\\\\\\\\\\\\\\\\\\\\\\\\\\\

Appendix C-2: AVHNT1.FOR
C-----------------------------------------------------------
C  THIS PROGRAM CALCULAT THE HYPERFINE FIELD FOR EACH SITE OF THE
C  LATTICE FOR A GIVEN SPIN STRUCTURE USING OUR HF MODEL
C  SOURCE CODE AVHNT1.FOR
C-----------------------------------------------------------
       INTEGER ATOM(10,10,10,4)
       REAL SS(10,10,10,4),HFI(10,10,10,4)
       PARAMETER(N=10)
NTOT=N*N*N*4
       OPEN(5,FILE='CL07.DAT',STATUS='OLD')
       OPEN(8,FILE='CL07.PRO',STATUS='OLD')
       OPEN(2,FILE='CL07.OUT',STATUS='OLD')
C-----------------------------------------------------
       AVSSFE=0.
AVSSNI=0.
READ(5,*)NFE
```

```
WRITE(8,*)NFE
C       GET THE COUPLING PARAMETERS
IF((1.0*NFE/NTOT).LE.0.45)THEN
          Y=NFE*1.0/(NTOT*1.0)
         ELSE
  Y=0.45
END IF
A=89.17-20*Y
B=4.4015+3.146*Y
A=87.96
B=4.62
C    READ THE SITE SPECIFIC ATOMIC MOMENTS
      DO 18 IX = 1,N
DO 17 IY = 1,N
  DO 16 IZ = 1,N
    DO 14 IM = 1,4
     READ(5,*)SS(IX,IY,IZ,IM),ATOM(IX,IY,IZ,IM)
14     CONTINUE
16    CONTINUE
17       CONTINUE
18      CONTINUE
C     CALCULATE HF VALUE FOR EACH SITE USING THE HF MODEL
      DO 28 IX = 1,N
       DO 26 IY = 1,N
        DO 24 IZ = 1,N
         DO 22 IM = 1,4
           IF(ATOM(IX,IY,IZ,IM).EQ.2)THEN
     AVSSFE=AVSSFE+SS(IX,IY,IZ,IM)
     CALL HFTRAN(ATOM,IX,IY,IZ,IM,N,SS,HFT)
     HFI(IX,IY,IZ,IM)=A*2.*SS(IX,IY,IZ,IM) + 2.*B*HFT
       WRITE(8,*)HFI(IX,IY,IZ,IM)
   ELSE
     AVSSNI=AVSSNI+SS(IX,IY,IZ,IM)
   END IF
22    CONTINUE
24   CONTINUE
26  CONTINUE
28 CONTINUE
* WRITE(2,202) AVSSFE/NFE, AVSSNI/((NTOT-NFE)*1.)
202      FORMAT('AVMFe=',F8.5,'AVMNi=',F8.5)
888 CONTINUE
        RETURN
        END

C      SUBROUTINE HFTRAN IS TO CALCULATE THE TRANSFERRED HF
       SUBROUTINE HFTRAN(ATOM,IX,IY,IZ,IM,N,SS,HFT)
```

```
      INTEGER ATOM(10,10,10,4)
      REAL SS(10,10,10,4)

   HFT=0.
   IF(IM.EQ.1)THEN
   DO 50 I=2,4
    HFT=HFT+SS(IX,IY,IZ,I)
50      CONTINUE
CALL BOUND(IX-1,IIX,N)
CALL BOUND(IY-1,IIY,N)
CALL BOUND(IZ-1,IIZ,N)
DO 51 I=2,4,2
 HFT=HFT+SS(IIX,IY,IZ,I)
51      CONTINUE
DO 52 I=2,3
  HFT=HFT+SS(IX,IIY,IZ,I)
52      CONTINUE
DO 53 I=3,4
HFT=HFT+SS(IX,IY,IIZ,I)
53      CONTINUE
 HFT=HFT+SS(IIX,IIY,IZ,2)
 HFT=HFT+SS(IX,IIY,IIZ,3)
 HFT=HFT+SS(IIX,IY,IIZ,4)
  END IF
  IF(IM.EQ.2)THEN
  DO 650 I=3,4
 HFT=HFT+SS(IX,IY,IZ,I)
650         CONTINUE
 HFT=HFT+SS(IX,IY,IZ,1)
CALL BOUND(IX+1,IIX,N)
CALL BOUND(IY+1,IIY,N)
CALL BOUND(IZ-1,IIZ,N)
DO 651 I=1,3,2
 HFT=HFT+SS(IIX,IY,IZ,I)
651     CONTINUE
DO 652 I=1,4,3
HFT=HFT+SS(IX,IIY,IZ,I)
652     CONTINUE
DO 653 I=3,4
 HFT=HFT+SS(IX,IY,IIZ,I)
653 CONTINUE
 HFT=HFT+SS(IIX,IY,IIZ,3)
 HFT=HFT+SS(IX,IIY,IIZ,4)
 HFT=HFT+SS(IIX,IIY,IZ,1)
GO TO 600
END IF
```

```
IF(IM.EQ.3)THEN
  DO 750 I=1,2
  HFT=HFT+SS(IX,IY,IZ,I)
750     CONTINUE
 HFT=HFT+SS(IX,IY,IZ,4)
CALL BOUND(IX-1,IIX,N)
CALL BOUND(IY+1,IIY,N)
CALL BOUND(IZ+1,IIZ,N)
DO 751 I=2,4,2
HFT=HFT+SS(IIX,IY,IZ,I)
751     CONTINUE
DO 752 I=1,4,3
HFT=HFT+SS(IX,IIY,IZ,I)
752     CONTINUE
DO 753 I=1,2
HFT=HFT+SS(IX,IY,IIZ,I)
753     CONTINUE
HFT=HFT+SS(IIX,IIY,IZ,4)
HFT=HFT+SS(IX,IIY,IIZ,1)
HFT=HFT+SS(IIX,IY,IIZ,2)
GO TO 600
END IF

 IF(IM.EQ.4)THEN
    DO 850 I=1,3
    HFT=HFT+SS(IX,IY,IZ,I)
850     CONTINUE
CALL BOUND(IX+1,IIX,N)
CALL BOUND(IY-1,IIY,N)
CALL BOUND(IZ+1,IIZ,N)
DO 851 I=1,3,2
HFT=HFT+SS(IIX,IY,IZ,I)
851     CONTINUE
DO 852 I=2,3
HFT=HFT+SS(IX,IIY,IZ,I)
852     CONTINUE
DO 853 I=1,2
HFT=HFT+SS(IX,IY,IIZ,I)
853     CONTINUE
HFT=HFT+SS(IIX,IIY,IZ,3)
HFT=HFT+SS(IX,IIY,IIZ,2)
HFT=HFT+SS(IIX,IY,IIZ,1)
END IF
600 RETURN
END
```

```
////////////////////////////////////////////////////////////////
\\\\\\\\\\\\\\\\\\\\\\\\\\\\\\\\\\\\\\\\\\\\\\\\\\\\\\\\\\\\\\\\\\
Appendic C-3: HFDSIM.FOR

C-------------------------------------------------------------
C  PROGRAM TO SIMULATE THE MOSSBAUER SPECTRUM FOR A CALCULATED HFD
C  ASSUMING THAT CS AND QS ARE BOTH ZERO, HEIGHT RATIO 3:2:1
C  SOURCE CODE: HFDSIM.FOR
C-------------------------------------------------------------
        DIMENSION X(512),Y(512),HFI(9001),PROB(9001)
        OPEN(2,FILE='HFDSIM.FLD',STATUS='OLD')
OPEN(3,FILE='CL07.PRO',STATUS='OLD')
READ(3,*)NO
DO 100 K=1,NO
READ(3,*)H
HFI(K)=H
PROB(K)=1./NO
100 CONTINUE
NDATA=512
        WRITE(2,*)NDATA
        DO 300 I=1,NDATA
        X(I)=-8.+0.032*(I-1.)
        CALL LORENZ(X(I),YT,HFI,PROB,NO)
        Y(I)=YT
        WRITE(2,'(1X,F10.7,2X,F9.2)')X(I),Y(I)
300     CONTINUE
        END

      SUBROUTINE LORENZ(X,YT,HFI,PROB,NO)
      DIMENSION CC(6),CQ(6),CH(6),HT(6),HFI(9001),PROB(9001)
      DATA CQ/0.5,-0.5,-0.5,-0.5,-0.5,0.5/
      DATA CH/-2.37545,-1.37545,-0.37545,0.37545,1.37545,2.37545/
        BG=200000.
        CS=0.0
CS1=-0.0
        QS=0.
QS1=-0.
        YTHE=0.
       CC(1)=3.
       CC(2)=2.
        CC(3)=1.
        CC(4)=1.
        CC(5)=CC(2)
        CC(6)=CC(1)
C CALCULATE HYPERFINE FIELDS OF DIFFERENT CLUSTERS
C       input hff into te lorenz line shape
```

```
        YTH=0.
YTHE=0.
       HT(3)=30000.
       HT(2)=HT(3)*CC(2)
       HT(1)=HT(3)*CC(1)
       HT(4)=HT(3)
       HT(5)=HT(2)
       HT(6)=HT(1)
       GAMMA=.1
DO 20 I=1,NO
         DO 10 J=1,6
          H=HT(J)
  HZEM=ABS(HFI(I)*0.006757)
          OMEGA=(CS+CS1*HZEM)+CQ(J)*(QS+QS1*HZEM)+CH(J)*HZEM
          XX=X-OMEGA
          TM1=GAMMA*GAMMA
          TM2=XX*XX
          TM3=TM2+TM1
          TM4=TM3*TM3
          TM5=TM1/TM3
          YTH=YTH+H*TM5*PROB(I)
10       CONTINUE
C         YTHE=YTHE+YTH*PROB(I)
20 CONTINUE
        YT=BG-YTH
        RETURN
      END
////////////////////////////////////////////////////////////////
\\\\\\\\\\\\\\\\\\\\\\\\\\\\\\\\\\\\\\\\\\\\\\\\\\\\\\\\\\\\\\\\\\
```

Appendix C-4: READHF.FOR

```
C-------------------------------------------------------------
C PROGRAM TO READ THE CALCULATED HF VALUES AND BIN THE DATA TO HFD
C   SOURCE CODE: READHF.FOR
C-------------------------------------------------------------
      IMPLICIT DOUBLE PRECISION (A-H,O-Z)
      DIMENSION H(100),PRO(100)
      OPEN(1,FILE='CL07.PRO', STATUS='OLD')
      OPEN(2,FILE='HFD.OUT', STATUS='OLD')
TOT=0.
HAV=0.
DO 5 I=1,100
H(I)=0.
PRO(I)=0.
5 CONTINUE
```

```
VARIAN=0.
READ(1,*)NDATA
       DO 50 J=1,NDATA
        READ(1,*)HI
VARIAN=VARIAN+HI**2
HAV=HAV+ABS(HI)/NDATA
C     CHOOSE THE BIN WIDTH
DT=10
DO 40 K=1,501,DT
 I=INT((K-1.)/DT+1.)
 IF(ABS(HI).GE.K-1.AND.ABS(HI).LT.(K+DT-1))THEN
*      H(I)=H(I)+ABS(HI)
    PRO(I)=PRO(I)+1.
 END IF
40 CONTINUE
50     CONTINUE
SDD=SQRT(VARIAN/NDATA-(HAV**2))
        DO 15 KK=1,100
        WRITE(2,*)((KK-1)*DT+DT/2.),PRO(KK)/(NDATA*DT)
TOT=TOT+PRO(KK)/NDATA
15      CONTINUE
WRITE(2,*)SDD,TOT,SDD,HAV
RETURN
       END
```

Appendix D. Programs used in Part IV

Appendix D-1: CARLO4D.FOR

```
C-----------------------------------------------------------------
C  THIS PROGRAM CALCULATE THE LROP FOR A RANDOM BINARY ALLOY
C  WITH FCC STRUCTURE AS A FUNCTION OF TEMPERATURE USING MC METHOD.
C  SOURCE CAODE: CARLO4D.FOR
C  subroutines BOUND, RAN2 are given in Appendex B-1
C-----------------------------------------------------------------
      INTEGER ATOM(10,10,10,4)
      REAL UK(2,2),E,EDELTA
      PARAMETER(N=10)

C     OBTAIN RELEVANT PARAMETERS
      WRITE (6,'(/,1X,A40)') 'PLEASE ENTER THE FOLLOWING VALUES:       '
1     WRITE (6,'(/,1X,A30)') 'NI CONCENTRATION AT % ?      '
      READ (5,*)CNI

      CNI=CNI/100.
      CFE = 1.0 - CNI
      WRITE (6,'(/,1X,A25)') 'UK(NI,NI)/KB IN KELVIN ?   '
      READ (5,*)UK(1,1)
      WRITE (6,'(/,1X,A25)') 'UK(NI,FE)/KB IN KELVIN ?   '
      READ (5,*)UK(1,2)
      UK(2,1)=UK(1,2)
      WRITE (6,'(/,1X,A25)') 'UK(FE,FE)/KB IN KELVIN ?   '
      READ (5,*)UK(2,2)
      WRITE (6,'(/,1X,A10)') 'MPAS ?       '
      READ (5,*)MPAS

      MTOT = 4*N**3
      MSTEP = MPAS
      OPEN(1,FILE="CARLO4.PRO",STATUS="OLD")
      OPEN(2,FILE="CARLO4.DAT",STATUS="OLD")
      OPEN(3,FILE='CARLO4.OUT',STATUS='OLD')
      IDUM= -381792
      CNIR = 0.0
CFER=0.0
C     PACE THE ATOM ON LATTICE IN ORDERED STATE
      DO 40 IX = 1,N
DO 30 IY = 1,N
  DO 20 IZ = 1,N
```

```
    DO 10 IM = 1,4
C             IF (IM.EQ.1.OR.IM.EQ.2)THEN
               IF(IM.EQ.1)THEN
                 ATOM(IX,IY,IZ,IM)=2
                 CFER = CFER + 1.0
      ELSE
                 ATOM(IX,IY,IZ,IM)=1
       CMIR=CMIR+1
      ENDIF
10          CONTINUE
20        CONTINUE
30       CONTINUE
40     CONTINUE
       CMIR=CMIR/NTOT
      PRINT*,CMIR
CFER=1.-CMIR
      WRITE(2,501)UK(1,1),UK(1,2),UK(2,2),CMIR,NSTEP,NTOT

501   FORMAT(1X,'J(MI,MI)=',F7.1,'  J(FE,MI)=',F8.1,'  J(FE,FE)=',
     @        F8.1,/,1X,' C(MI)=',
     @       F6.3,//,'NUMBER PER RUN: ',I6,//,
     @  'TOTAL NUMBER OF ATOMS ON LATTICE:',I6,/)

C     CALCULATE INITIAL TOTAL ENERGY
        CALL PROBCK1(ATOM,IX,IY,IZ,IM,N,CFER,NFER,ALOP)
      CALL PROBCK2(ATOM,IX,IY,IZ,IM,N,CFER,NFER,OP2)
      CALL ENERTOT(ATOM,UK,ETOT,N)
      EPAT = ETOT/NTOT
      WRITE(2,511)EPAT
      WRITE(6,511)EPAT
511    FORMAT(//,1X,'INITIAL ENERGY PER ATOM = ',E10.4)
C     START FLIPPING THE SPINS ONE BY ONE
C=============================================================
C      CALCULATE THE ORDERED PARAMETER AT DIFFERENT TEMPERATURES
C=============================================================
      DO 1000 MM=50,1400,50
        AVOP=0.
        NSTEP=2500
        IF(MM.LE.510)THEN
TEMP=MM+1.
ELSE
        TEMP=TEMP+15.
        END IF
        CALL FLIPB(NSTEP,ATOM,ETOT,UK,N,TEMP)
C       CALCULATE THE INITIAL LONG RANGE ORDER PARAMETER
        CALL PROBCK1(ATOM,IX,IY,IZ,IM,N,CFER,NFER,ALOP)
```

```
        EPAT = ETOT/NTOT
        WRITE(2,551)EPAT
        WRITE(6,551)EPAT
551     FORMAT(/,1X,'FINAL ENERGY PER ATOM= ',E10.4)
AOP=0.
SOP=0.
EP=0.
NNN=0
NUM=0
C       ACCUMULATE LORP AND SORP FOR THE AVERAGE
        DO 950 II=1,2000
        CALL FLIPB(1,ATOM,ETOT,UK,N,TEMP)
NUM=NUM+1
EPATM=ETOT/NTOT
        IF(NUM.GE.20)THEN
NNN=NNN+1
        CALL PROBCK1(ATOM,IX,IY,IZ,IM,N,CFER,NFER,ALOP)
CALL PROBCK2(ATOM,IX,IY,IZ,IM,N,CFER,NFER,OP)
AOP=AOP+ALOP
SOP=SOP+OP
EP=EP+EPATM
NUM=0
END IF
950 CONTINUE
WRITE(6,223)TEMP,AOP/NNN,SOP/NNN,EP/NNN
223 FORMAT(1X,'T=',F6.1,1X,'LOP=',F8.6,2X,
     *  'SOP=',F8.6,1X,'EPAT=',F8.1)
WRITE(2,223)TEMP,AOP/NNN,SOP/NNN,EP/NNN
WRITE(3,*)TEMP,AOP/NNN,SOP/NNN,EP/NNN
CR=AOP/NNN
1000    CONTINUE
        RETURN
33 STOP
        END

C       SUBROUTINE FLIPB TO SWAP TWO ATOMS IF THE SWAP LOWER THE TOTAL ENERGY
        SUBROUTINE FLIPB(NSTEP,ATOM,ETOT,UK,N,TEMP)
        INTEGER ATOM(10,10,10,4)
        REAL ETOT,TEMP,UK(2,2)
DOUBLE PRECISION DF,DSFF
        NTOT=4*N**3
IDUM =-492037
DO 220 J=1,NSTEP
         DO 110 I=1,NTOT
           RANNUM=RAN2(IDUM)
           IX1= NINT(RANNUM*N+0.5)
```

```
            RANNUM=RAN2(IDUM)
            IY1 = NINT(RANNUM*N+0.5)
            RANNUM=RAN2(IDUM)
    IZ1 = NINT(RANNUM*N+0.5)
    RANNUM= RAN2(IDUM)
    IM1= NINT(RANNUM*4+0.5)
    RANNUM=RAN2(IDUM)
            IX2=NINT(RANNUM*N+0.5)
    RANNUM=RAN2(IDUM)
            IY2=NINT(RANNUM*N+0.5)
    RANNUM=RAN2(IDUM)
            IZ2=NINT(RANNUM*N+0.5)
    RANNUM=RAN2(IDUM)
            IM2=NINT(RANNUM*4+0.5)
IF(ATOM(IX1,IY1,IZ1,IM1).EQ.ATOM(IX2,IY2,IZ2,IM2))GO TO 110
        CALL ECALC(ATOM,IX1,IY1,IZ1,IM1,UK,E,N)
        E11=E
        CALL ECALC(ATOM,IX2,IY2,IZ2,IM2,UK,E,N)
        E12=E
E1=E11+E12
        IF(ATOM(IX1,IY1,IZ1,IM1).EQ.1)THEN
           ATOM(IX1,IY1,IZ1,IM1)=2
     ATOM(IX2,IY2,IZ2,IM2)=1
           CALL ECALC(ATOM,IX1,IY1,IZ1,IM1,UK,E,N)
           E21=E
   CALL ECALC(ATOM,IX2,IY2,IZ2,IM2,UK,E,N)
           E22=E
   E2=E21+E22
   EDELTA=E2-E1
   DF=DEXP(-EDELTA/TEMP)
   DSFF=DF/(1.+DF)
   RANNUM=RAN2(IDUM)
   IF(RANNUM.LT.DSFF)THEN
        ETOT=ETOT+EDELTA
     ELSE
      ATOM(IX1,IY1,IZ1,IM1)=1
      ATOM(IX2,IY2,IZ2,IM2)=2
   ENDIF
  ELSE
  ATOM(IX1,IY1,IZ1,IM1)=1
  ATOM(IX2,IY2,IZ2,IM2)=2
  CALL ECALC(ATOM,IX1,IY1,IZ1,IM1,UK,E,N)
  E21=E
  CALL ECALC(ATOM,IX2,IY2,IZ2,IM2,UK,E,N)
  E22=E
  E2=E21+E22
```

```
          EDELTA=E2-E1
  DF=DEXP(-EDELTA/TEMP)
          DSFF=DF/(1.+DF)
        RANNUM=RAN2(IDUM)
          IF(RANNUM.LT.DSFF)THEN
            ETOT=ETOT+EDELTA
          ELSE
   ATOM(IX1,IY1,IZ1,IM1)=2
   ATOM(IX2,IY2,IZ2,IM2)=1
          END IF
END IF
110     CONTINUE
220 CONTINUE
          RETURN
          END

C     SUBROUTINE ENERTOT

C     THIS SUBROUTINE CALCULATES THE TOTAL ENERGY OF A FCC BINARY SPIN
C     SYSTEM WITH CYCLIC BOUNDARY CONDITIONS.
C     IT USES SUBROUTINE ECALC

      SUBROUTINE ENERTOT(ATOM,UK,ETOT,N)

      INTEGER ATOM(10,10,10,4),IX,IY,IZ,IM,N
      REAL UK(2,2),ETOT,E

      ETOT = 0.0

      DO 10 IX = 1,N
DO 8 IY = 1,N
  DO 6 IZ = 1,N
    DO 4 IM = 1,4
     CALL ECALC(ATOM,IX,IY,IZ,IM,UK,E,N)
      ETOT = ETOT + 0.5*E
4           CONTINUE
6         CONTINUE
8       CONTINUE
10    CONTINUE
      RETURN
      END

C     SUBROUTINE ECALC
C     THIS SUBROUTINE CALCULATES THE INTERACTION ENERGY BETWEEN
C     A GIVEN ATOM AND ITS 12 NEAR NEIGHBOURS IN A FCC BINARY SPIN
C     SYSTEM WITH CYCLIC BOUNDARY CONDITIONS.
```

```
      SUBROUTINE ECALC(ATOM,IX,IY,IZ,IM,UK,E,N)
      INTEGER ATOM(10,10,10,4)
      REAL UK(2,2),E
      II=ATOM(IX,IY,IZ,IM)
E=0.0
      IF(IM.EQ.1)THEN
DO 10 I=2,4
  JJ=ATOM(IX,IY,IZ,I)
  E = E + UK(II,JJ)
10      CONTINUE
CALL BOUND(IX-1,IIX,N)
CALL BOUND(IY-1,IIY,N)
CALL BOUND(IZ-1,IIZ,N)
DO 20 I=2,4,2
  JJ=ATOM(IIX,IY,IZ,I)
  E = E + UK(II,JJ)
20      CONTINUE
DO 30 I=2,3
  JJ=ATOM(IX,IIY,IZ,I)
  E = E + UK(II,JJ)
30      CONTINUE
DO 40 I=3,4
  JJ=ATOM(IX,IY,IIZ,I)
  E=E+UK(II,JJ)
40      CONTINUE
JJ=ATOM(IIX,IIY,IZ,2)
E=E+UK(II,JJ)
JJ=ATOM(IX,IIY,IIZ,3)
E=E+UK(II,JJ)
JJ=ATOM(IIX,IY,IIZ,4)
E=E+UK(II,JJ)
ENDIF

      IF(IM.EQ.2)THEN
E=0.0
DO 110 I=3,4
  JJ=ATOM(IX,IY,IZ,I)
E=E+UK(II,JJ)
110     CONTINUE
JJ=ATOM(IX,IY,IZ,1)
E=E+UK(II,JJ)
CALL BOUND(IX+1,IIX,N)
CALL BOUND(IY+1,IIY,N)
CALL BOUND(IZ-1,IIZ,N)
DO 120 I=1,3,2
```

```
  JJ=ATOM(IIX,IY,IZ,I)
E=E+UK(II,JJ)
120      CONTINUE
DO 130 I=1,4,3
  JJ=ATOM(IX,IIY,IZ,I)
E=E+UK(II,JJ)
130      CONTINUE
DO 140 I=3,4
  JJ=ATOM(IX,IY,IIZ,I)
E=E+UK(II,JJ)
140      CONTINUE
JJ=ATOM(IIX,IIY,IZ,1)
E=E+UK(II,JJ)
JJ=ATOM(IX,IIY,IIZ,4)
E=E+UK(II,JJ)
JJ=ATOM(IIX,IY,IIZ,3)
E=E+UK(II,JJ)
ENDIF

      IF(IM.EQ.3)THEN
E=0.0
DO 210 I=1,2
  JJ=ATOM(IX,IY,IZ,I)
E=E+UK(II,JJ)
210      CONTINUE
JJ=ATOM(IX,IY,IZ,4)
E=E+UK(II,JJ)
CALL BOUND(IX-1,IIX,M)
CALL BOUND(IY+1,IIY,M)
CALL BOUND(IZ+1,IIZ,M)
DO 220 I=2,4,2
  JJ=ATOM(IIX,IY,IZ,I)
E=E+UK(II,JJ)
220      CONTINUE
DO 230 I=1,4,3
  JJ=ATOM(IX,IIY,IZ,I)
E=E+UK(II,JJ)
230      CONTINUE
DO 240 I=1,2
  JJ=ATOM(IX,IY,IIZ,I)
E=E+UK(II,JJ)
240      CONTINUE
JJ=ATOM(IIX,IIY,IZ,4)
E=E+UK(II,JJ)
JJ=ATOM(IIX,IY,IIZ,2)
E=E+UK(II,JJ)
```

```
JJ=ATOM(IX,IIY,IIZ,1)
E=E+UK(II,JJ)
        ENDIF

        IF(IN.EQ.4)THEN
E=0.0
DO 310 I=1,3
JJ=ATOM(IX,IY,IZ,I)
E=E+UK(II,JJ)
310     CONTINUE
CALL BOUND(IX+1,IIX,N)
CALL BOUND(IY-1,IIY,N)
CALL BOUND(IZ+1,IIZ,N)
DO 320 I=1,3,2
  JJ=ATOM(IIX,IY,IZ,I)
E=E+UK(II,JJ)
320     CONTINUE
DO 330 I=2,3
  JJ=ATOM(IX,IIY,IZ,I)
E=E+UK(II,JJ)
330     CONTINUE
DO 340 I=1,2
  JJ=ATOM(IX,IY,IIZ,I)
E=E+UK(II,JJ)
340     CONTINUE
JJ=ATOM(IIX,IIY,IZ,3)
E=E+UK(II,JJ)
JJ=ATOM(IIX,IY,IIZ,1)
E=E+UK(II,JJ)
JJ=ATOM(IX,IIY,IIZ,2)
E=E+UK(II,JJ)
ENDIF
500     CONTINUE
        END

C    SUBROUTINE PROBCK1 IS TO CALCULATE THE LONG RANGE ORDER PARAMETER
C    OF THE ALLOY FOR A GIVEN STATE
        SUBROUTINE PROBCK1(ATOM,IX,IY,IZ,IN,N,CFER,NFER,ALOP)
INTEGER N,IX,IY,IZ,IN,ATOM(10,10,10,4)
NTOT=4*N**3
NFER=0
NNIR=0
CNIR=1.- CFER
DO 900 IZ=1,N
   DO 800 IY=1,N
     DO 700 IX=1,N
```

```
      DO 600 IM=1,4
                IF(ATOM(IX,IY,IZ,IM).EQ.2)THEN
                  IF(IM.EQ.1)THEN
C                 IF(IM.EQ.1.OR.IM.EQ.2)THEN
C                  NNIR=NNIR+1
                  NFER=NFER+1
            END IF
          END IF
600     CONTINUE
700    CONTINUE
800   CONTINUE
900 CONTINUE

C          ALOP=(NFER*2./(CFER*NTOT))-1.
           ALOP=(NFER*4./(CFER*NTOT)-1.)/3
C          ALOP=(NFER*4./(CNIR*NTOT)-1.)/3
 RETURN
 END

C       SUBROUTINE PROBCK2 IS TO CALCULATE THE SHORT RANGE ORDER
C       PARAMETER OF THE ALLOY FOR A GIVEN STATE
       SUBROUTINE PROBCK2(ATOM,IX,IY,IZ,IM,N,CFER,NFER,SOP)
        INTEGER ATOM(10,10,10,4)
        REAL PP1(13,2),PP2(13,2),N1(2)
 NTOT=4*N**3
     DO 2 IN=1,13
       DO 4 JO=1,2
              PP1(IN,JO)=0.
4 CONTINUE
2       CONTINUE
DO 900 IZ=1,N
   DO 800 IY=1,N
     DO 700 IX=1,N
       DO 600 IM=1,4
              DO 500 NAM=1,2
               N1(NAM)=0
               IF (ATOM(IX,IY,IZ,IM).EQ.NAM)THEN
  IF(NAM.EQ.1)THEN
                   IDT=2
           ELSE
           IDT=1
          END IF
  IF(IM.EQ.1)THEN
  DO 50 I=2,4
   IF(ATOM(IX,IY,IZ,I).EQ.IDT) THEN
   N1(NAM)=N1(NAM)+1
```

```
   END IF
50      CONTINUE
CALL BOUND(IX-1,IIX,N)
CALL BOUND(IY-1,IIY,N)
CALL BOUND(IZ-1,IIZ,N)
DO 51 I=2,4,2
IF(ATOM(IIX,IY,IZ,I).EQ.IDT)THEN
   N1(NAM)=N1(NAM)+1
       END IF
51      CONTINUE
DO 52 I=2,3
IF(ATOM(IX,IIY,IZ,I).EQ.IDT)THEN
   N1(NAM)=N1(NAM)+1
END IF
52      CONTINUE
DO 53 I=3,4
IF(ATOM(IX,IY,IIZ,I).EQ.IDT)THEN
 N1(NAM)=N1(NAM)+1
 END IF
53      CONTINUE
IF(ATOM(IIX,IIY,IZ,2).EQ.IDT) THEN
  N1(NAM)=N1(NAM)+1
END IF
IF(ATOM(IX,IIY,IIZ,3).EQ.IDT)THEN
 N1(NAM)=N1(NAM)+1
END IF
IF(ATOM(IIX,IY,IIZ,4).EQ.IDT)THEN
  N1(NAM)=N1(NAM)+1
END IF
DO 311 MM=1,13
IF(N1(NAM)+1.EQ.MM)THEN
PP1(MM,NAM)=PP1(MM,NAM)+1
END IF
311     CONTINUE
END IF

  IF(IM.EQ.2)THEN
    DO 650 I=3,4
            IF(ATOM(IX,IY,IZ,I).EQ.IDT) THEN
               N1(NAM)=N1(NAM)+1
    END IF
650      CONTINUE
        IF(ATOM(IX,IY,IZ,1).EQ.IDT)THEN
          N1(NAM)=N1(NAM)+1
END IF
CALL BOUND(IX+1,IIX,N)
```

```
CALL BOUND(IY+1,IIY,N)
CALL BOUND(IZ-1,IIZ,N)
DO 651 I=1,3,2
        IF(ATOM(IIX,IY,IZ,I).EQ.IDT)THEN
           N1(NAM)=N1(NAM)+1
        END IF
651     CONTINUE
DO 652 I=1,4,3
        IF(ATOM(IX,IIY,IZ,I).EQ.IDT)THEN
           N1(NAM)=N1(NAM)+1
END IF
652     CONTINUE
DO 653 I=3,4
        IF(ATOM(IX,IY,IIZ,I).EQ.IDT)THEN
         N1(NAM)=N1(NAM)+1
END IF
653     CONTINUE
        IF(ATOM(IIX,IIY,IZ,1).EQ.IDT) THEN
          N1(NAM)=N1(NAM)+1
END IF
        IF(ATOM(IX,IIY,IIZ,4).EQ.IDT)THEN
         N1(NAM)=N1(NAM)+1
END IF
        IF(ATOM(IIX,IY,IIZ,3).EQ.IDT)THEN
          N1(NAM)=N1(NAM)+1
END IF
DO 411 MM=1,13
IF(N1(NAM)+1.EQ.MM)THEN
        PP1(MM,NAM)=PP1(MM,NAM)+1
END IF
411     CONTINUE
END IF

IF(IM.EQ.3)THEN
  DO 750 I=1,2
            IF(ATOM(IX,IY,IZ,I).EQ.IDT) THEN
              N1(NAM)=N1(NAM)+1
            END IF
750     CONTINUE
        IF(ATOM(IX,IY,IZ,4).EQ.IDT)THEN
          N1(NAM)=N1(NAM)+1
END IF
CALL BOUND(IX-1,IIX,N)
CALL BOUND(IY+1,IIY,N)
CALL BOUND(IZ+1,IIZ,N)
DO 751 I=2,4,2
```

```
        IF(ATOM(IIX,IY,IZ,I).EQ.IDT)THEN
           N1(NAM)=N1(NAM)+1
        END IF
751     CONTINUE
DO 752 I=1,4,3
        IF(ATOM(IX,IIY,IZ,I).EQ.IDT)THEN
           N1(NAM)=N1(NAM)+1
END IF
752     CONTINUE
DO 753 I=1,2
        IF(ATOM(IX,IY,IIZ,I).EQ.IDT)THEN
         N1(NAM)=N1(NAM)+1
 END IF
753     CONTINUE
        IF(ATOM(IIX,IIY,IZ,4).EQ.IDT) THEN
          N1(NAM)=N1(NAM)+1
END IF
        IF(ATOM(IX,IIY,IIZ,1).EQ.IDT)THEN
         N1(NAM)=N1(NAM)+1
END IF
        IF(ATOM(IIX,IY,IIZ,2).EQ.IDT)THEN
          N1(NAM)=N1(NAM)+1
END IF
DO 511 MM=1,13
IF(N1(NAM)+1.EQ.MM)THEN
        PP1(MM,NAM)=PP1(MM,NAM)+1
END IF
511     CONTINUE
END IF

  IF(IM.EQ.4)THEN
            DO 850 I=1,3
             IF(ATOM(IX,IY,IZ,I).EQ.IDT) THEN
               N1(NAM)=N1(NAM)+1
      END IF
850         CONTINUE
CALL BOUND(IX+1,IIX,N)
CALL BOUND(IY-1,IIY,N)
CALL BOUND(IZ+1,IIZ,N)
DO 851 I=1,3,2
        IF(ATOM(IIX,IY,IZ,I).EQ.IDT)THEN
           N1(NAM)=N1(NAM)+1
        END IF
851     CONTINUE
DO 852 I=2,3
        IF(ATOM(IX,IIY,IZ,I).EQ.IDT)THEN
```

```
          N1(NAM)=N1(NAM)+1
END IF
852     CONTINUE
DO 853 I=1,2
        IF(ATOM(IX,IY,IIZ,I).EQ.IDT)THEN
          N1(NAM)=N1(NAM)+1
END IF
853     CONTINUE
        IF(ATOM(IIX,IIY,IZ,3).EQ.IDT) THEN
          N1(NAM)=N1(NAM)+1
END IF
        IF(ATOM(IX,IIY,IIZ,2).EQ.IDT)THEN
         N1(NAM)=N1(NAM)+1
END IF
        IF(ATOM(IIX,IY,IIZ,1).EQ.IDT)THEN
          N1(NAM)=N1(NAM)+1
END IF
DO 611 MM=1,13
IF(N1(NAM)+1.EQ.MM)THEN
        PP1(MM,NAM)=PP1(MM,NAM)+1
END IF
611     CONTINUE
        END IF
END IF
500   CONTINUE
600     CONTINUE
700     CONTINUE
800     CONTINUE
900     CONTINUE
AVNAB=0.
DO 1006 LL=1,2
DO 1005 JJ=1,13
AVNAB=AVNAB+(JJ-1)*PP1(JJ,LL)/NTOT
555     FORMAT(1X,'NN PE CLUSTER',2X,I2,2X,F9.1)
1005    CONTINUE
1006 CONTINUE
C           SOP=(AVNAB-6.)/2.
          SOP=(AVNAB-9./2.)*2./3.
         END
```

//

\\\

Appendix D-2: MCMCRT.FOR

```
C-----------------------------------------------------------------
C THIS PROGRAM FINDS A EQUILIBRIUM STATE FOR A ORDERED BINARY ALLOY
```

```
C WITH FCC STRUCTURE AT DIFFERENT TEMPERATURE.  A MONTE CARLO METHOD IS
C USED.  BOTH THE CHEMICAL AND MAGNETIC EXCHANGE INTERACTION ARE TAKEN
C INTO COUNT.  FOUR  POSSIBLE FLIP APPROACHES ARE RANDOMLY SELECTED.
C SOURCE CODE MCMCRT.FOR
C-----------------------------------------------------------------
      IMPLICIT DOUBLE PRECISION (D-E)
      INTEGER ATOM(10,10,10,4),SPSIGN(10,10,10,4),FEFLAG,NY
      REAL SPIN(2),JK(2,2),UK(2,2)
      PARAMETER(N=10)
C     OBTAIN RELEVANT PARAMETERS
      SPIN(1) = 0.3
      SPIN(2) = 1.4
      WRITE (6,'(/,1X,A40)') 'PLEASE ENTER THE FOLLOWING VALUES:       '
1     WRITE (6,'(/,1X,A30)') 'NI CONCENTRATION AT % ?      '
      READ (5,*)CNI
      CNI=CNI/100.
      CFE = 1.0 - CNI
      WRITE (6,'(/,1X,A25)') 'J(NI,NI)/KB IN KELVIN ?   '
      READ (5,*)JK(1,1)
      WRITE (6,'(/,1X,A25)') 'J(NI,FE)/KB IN KELVIN ?   '
      READ (5,*)JK(1,2)
      JK(2,1)=JK(1,2)
      WRITE (6,'(/,1X,A25)') 'J(FE,FE)/KB IN KELVIN ?   '
      READ (5,*)JK(2,2)
      WRITE (6,'(/,1X,A25)') 'U(NI,NI)/KB IN KELVIN ?   '
      READ (5,*)UK(1,1)
      WRITE (6,'(/,1X,A25)') 'U(NI,FE)/KB IN KELVIN ?   '
      READ (5,*)UK(1,2)
      UK(2,1)=UK(1,2)
      WRITE (6,'(/,1X,A25)') 'U(FE,FE)/KB IN KELVIN ?   '
      READ (5,*)UK(2,2)
      WRITE (6,'(/,1X,A65,/)')' PLEASE ENTER 1 IF ONLY FE ATOMS ARE TO B
     @E FLIPPED, 0 OTHERWISE:                '
      READ (5,*)FEFLAG
      IF(FEFLAG.NE.1)FEFLAG=0
      NTOT = 4*N**3
      OPEN(2,FILE="CL07.DAT",STATUS="OLD")
      OPEN(8,FILE='CL07.DOD',STATUS='OLD')
      OPEN(10,FILE='CL07.OUT',STATUS='OLD')
C     PLACE ATOMS RANDOMLY ON LATTICE
       IDUM=-3847152
       CNIR = 0.0
CFER=0.
6      FORMAT(1X,'ITINIAL=',F12.6)
      DO 40 IX = 1,N
DO 30 IY = 1,N
```

```
      DO 20 IZ = 1,N
        DO 10 IM = 1,4
                  IF(IM.EQ.1)THEN
                  ATOM(IX,IY,IZ,IM)=1
                  CNIR=CNIR+1
                  ELSE
                  ATOM(IX,IY,IZ,IM)=2
                 END IF
10              CONTINUE
20            CONTINUE
30          CONTINUE
40        CONTINUE

          CNIR = CNIR/NTOT
          CFER=1.0-CNIR

          WRITE(2,501)JK(1,1),JK(1,2),JK(2,2),SPIN(1),SPIN(2),CNIR,NTOT
WRITE(2,502)UK(1,1),UK(1,2),UK(2,2)
501       FORMAT(1X,'J(NI,NI)=',F6.1,'  J(FE,NI)=',F6.1,'  J(FE,FE)=',
     @            F6.1,/,1X,'S(NI)=',F4.1,'  S(FE)=',F4.1,/,' C(NI)=',
     @            F6.3,/, 'TOTAL NUMBER OF ATOMS ON LATTICE:',I6)
502       FORMAT(1X,'U(NI,NI)=',F9.2, 'U(FE,NI)=',F9.2, 'U(FE,FE)=',
     @            F9.2)
          IF(FEFLAG.EQ.1)THEN
           WRITE(2,'(1X,A40,/)')'ONLY FE ATOMS ARE ALLOWED TO BE FLIPPED'
          ENDIF
C         GET A SEED FOR RANDOM NUMBER GENERATOR
C         CHOOSE INITIAL SPIN CONFIGURATION

50        WRITE(6,*)
          WRITE(6,*)'PLEASE CHOOSE AN INITIAL SPIN CONFIGURATION:'
          WRITE(6,*)'    1 = RANDOM'
          WRITE(6,*)'    2 = ALL UP'
          WRITE(6,*)'    3 = ALL NI UP, ALL FE DOWN'
          WRITE(6,*)'    4 = ALL NI UP, ALL FE RANDOM'
          WRITE(6,*)

          READ(5,*)ICONF

          IF(ICONF.EQ.1) GO TO 60
          IF(ICONF.EQ.2) GO TO 70
          IF(ICONF.EQ.3) GO TO 80
          IF(ICONF.EQ.4) GO TO 90
C         RANDOM SPIN CONFIGURATION
60        DO 68 IX = 1,N
DO 66 IY = 1,N
```

```
  DO 64 IZ = 1,N
    DO 62 IM = 1,4
              RANNUM=RAN2(IDUM)
      IF(RANNUM.LT.0.5)THEN
SPSIGN(IX,IY,IZ,IM)=1
      ELSE
SPSIGN(IX,IY,IZ,IM)=-1
      ENDIF
62          CONTINUE
64        CONTINUE
66      CONTINUE
68    CONTINUE
      WRITE(2,*) ' INITIAL SPIN CONFIGURATION IS RANDOM'
      GO TO 110
C     ALL SPIN UP CONFIGURATION
70    DO 78 IX = 1,N
DO 76 IY = 1,N
  DO 74 IZ = 1,N
    DO 72 IM = 1,4
      SPSIGN(IX,IY,IZ,IM)=1
72          CONTINUE
74        CONTINUE
76      CONTINUE
78    CONTINUE
      WRITE(2,*)'INITIAL SPIN CONFIGURATION IS ALL UP'
      GO TO 110

C     ALL NI SPIN UP, ALL FE SPIN DOWN
80    DO 88 IX = 1,N
DO 86 IY = 1,N
  DO 84 IZ = 1,N
    DO 82 IM = 1,4
      IF(ATOM(IX,IY,IZ,IM).EQ.1)THEN
SPSIGN(IX,IY,IZ,IM)=1
      ELSE
SPSIGN(IX,IY,IZ,IM)=-1
      ENDIF
82          CONTINUE
84        CONTINUE
86      CONTINUE
88    CONTINUE
      WRITE(2,*)' INITIAL SPIN CONFIGURATION IS ALL NI UP, ALL FE DOWN'
      GO TO 110

C     ALL NI UP, ALL FE RANDOM
90    DO 96 IX = 1,N
```

```
DO 96 IY = 1,N
  DO 94 IZ = 1,N
    DO 92 IM = 1,4
      IF(ATOM(IX,IY,IZ,IM).EQ.1)THEN
SPSIGN(IX,IY,IZ,IM)=1
      ELSE
                RANNUM=RAN2(IDUM)
 IF(RANNUM.LT.0.5)THEN
 SPSIGN(IX,IY,IZ,IM)=1
 ELSE
 SPSIGN(IX,IY,IZ,IM)=-1
ENDIF
      ENDIF
92          CONTINUE
94        CONTINUE
96      CONTINUE
98    CONTINUE

      WRITE(2,*)'INITIAL SPIN CONFIGURATION IS ALL NI UP, ALL FE RANDOM'
C     CALCULATE INITIAL TOTAL ENERGY
110   CALL ENERTOT(SPSIGN,ATOM,SPIN,JK,ETOT,ECT,EMT,N,UK)
      EPAT = ETOT/NTOT
      WRITE(2,511)EPAT
      WRITE(6,511)EPAT
511    FORMAT(/,1X,'INITIAL ENERGY PER ATOM = ',E10.4)

C     CALCULATE INITIAL AVERAGE SPIN PER ATOM
      CALL SPINTOT(SPSIGN,ATOM,SPIN,TOTSPIN,N)
      AVSPIN = TOTSPIN / NTOT
      WRITE(2,521)AVSPIN
      WRITE(6,521)AVSPIN
521    FORMAT(/,1X,'INITIAL AVRAGE SPIN PER ATOM = ',F6.3,/)
       CALL PROBCK1(ATOM,IX,IY,IZ,IM,N,CFER,ALOP)
       CALL PROBCK2(ATOM,IX,IY,IZ,IM,N,CFER, SOP)
       WRITE(2,203)ALOP,SOP
        WRITE(6,203)ALOP,SOP
203     FORMAT(/,'LOP=',F6.4,2X,'SOP=',F6.4)
C-------------------------------------------------------------
C     CALCULATE MAGNETIC AND CHEMICAL ORDER PARAMETERS AT DIFFERENT C
C     TEMPERATURES USING MONTE CARLO METHOD
C-------------------------------------------------------------
      WRITE(8,*)CFER
      TEMP=0.0
      DO 999 KKK=5,1550,10
      AVSPIN=0.
      AVE=0.
```

```
      NN=0
      NO=0
      AVLP=0.
      AVSP=0.
      AVEC=0.
      AVEM=0.
      AVE2=0.
       NSTEP=5500
        NEQ=2500
      IF(TEMP.LE.510)THEN
        TEMP=KKK*1.
        ELSE
      IF(TEMP.GT.510.AND.TEMP.LE.710)THEN
         NSTEP=3500
         NEQ=2500
        TEMP=TEMP+50.
        END IF
      WRITE(2,111)TEMP
      WRITE(6,111)TEMP
C     FLIP SPINS FIRST
      CALL FLIPS(500,SPSIGN,ATOM,ETOT,TOTSPIN,SPIN,JK,N,
     *                FEFLAG,TEMP)
111   FORMAT(1X,'TEMP(K)=',F8.3)
C     PERFORM NSTEP MONTE CARLO SIMULATIONS
        DO 888 J=1,NSTEP
         DO 777 L=1,NTOT
         RANNUM=RAN2(IDUM)
 IX1= NINT(RANNUM*N+0.5)
         RANNUM=RAN2(IDUM)
         IY1 = NINT(RANNUM*N+0.5)
         RANNUM=RAN2(IDUM)
 IZ1 = NINT(RANNUM*N+0.5)
         RANNUM=RAN2(IDUM)
   IM1= NINT(RANNUM*4+0.5)
         RANNUM=RAN2(IDUM)
 IX2=NINT(RANNUM*N+0.5)
         RANNUM=RAN2(IDUM)
 IY2=NINT(RANNUM*N+0.5)
         RANNUM=RAN2(IDUM)
 IZ2=NINT(RANNUM*N+0.5)
         RANNUM=RAN2(IDUM)
         IM2=NINT(RANNUM*4+0.5)

        IF(ATOM(IX1,IY1,IZ1,IM1).EQ.ATOM(IX2,IY2,IZ2,IM2))GO TO 777
         CALL ECALCB(ATOM,IX1,IY1,IZ1,IM1,UK,EB1,N)
         CALL ECALCM(SPSIGN,ATOM,IX1,IY1,IZ1,IM1,SPIN,JK,EM1,N)
```

```
      E11=EB1+EM1
      CALL ECALCB(ATOM,IX2,IY2,IZ2,IM2,UK,EB2,N)
      CALL ECALCM(SPSIGN,ATOM,IX2,IY2,IZ2,IM2,SPIN,JK,EM2,N)
      E12=EB2+EM2
      E1=E11+E12
      ISIGN1=SPSIGN(IX1,IY1,IZ1,IM1)
      ISIGN2=SPSIGN(IX2,IY2,IZ2,IM2)
      RANNUM=RAN2(IDUM)

C     RANDOMLY CHOOSE THREE WAYS OF FLIP+SWAP TWO ATOMS
C     FIRST BOTH SPINS DO NOT FLIP WHEN THEY SWAP
C     SECOND ONLY ONE SPIN IS FLIPPED WHEN THEY SWAP
C     BOTH SPINS FLIP WHEN THEY SWAP
      IL=NINT(RANNUM*3.+0.5)
      IF(IL.EQ.1)GO TO 100
      IF(IL.EQ.2)THEN
       MY=0
       IF(IM1.EQ.2)THEN
       IX1P=IX1+0.5
       IY1P=IY1+0.5
       IZ1P=IZ1
       END IF
       IF(IM1.EQ.3)THEN
        IY1P=IY1+0.5
        IZ1P=IZ1+0.5
        IX1P=IX1
        END IF
         IF(IM1.EQ.4)THEN
          IX1P=IX1+0.5
          IZ1P=IZ1+0.5
          IY1P=IY1
         END IF
       IF(IM2.EQ.2)THEN
       IX2P=IX2+0.5
       IY2P=IY2+0.5
       IZ2P=IZ2
       END IF
       IF(IM2.EQ.3)THEN
        IY2P=IY2+0.5
        IZ2P=IZ2+0.5
        IX2P=IX2
        END IF
         IF(IM2.EQ.4)THEN
          IX2P=IX2+0.5
          IZ2P=IZ2+0.5
         IY2P=IY2
```

```
            END IF
           IF(IM1.EQ.1)THEN
           IX1P=IX1
           IY1P=IY1
           IZ1P=IZ1
           END IF
           IF(IM2.EQ.1) THEN
           IX2P=IX2
           IY2P=IY2
           IZ2P=IZ2
           END IF

           R=SQRT(1.*(IX2P-IX1P)**2+(IY2P-IY1P)**2+(IZ2P-IZ1P)**2)
           IF((R-1./SQRT(2.)).LT.0.001)THEN
            NY=1
            END IF
            GO TO 200
            END IF

           IF(IL.EQ.3)GO TO 400

100       SPSIGN(IX1,IY1,IZ1,IM1)=ISIGN2
          SPSIGN(IX2,IY2,IZ2,IM2)=ISIGN1
         IF(ATOM(IX1,IY1,IZ1,IM1).EQ.1)THEN
           ATOM(IX1,IY1,IZ1,IM1)=2
           ATOM(IX2,IY2,IZ2,IM2)=1
         CALL ECALCB(ATOM,IX1,IY1,IZ1,IM1,UK,EB21,N)
         CALL  ECALCM(SPSIGN,ATOM,IX1,IY1,IZ1,IM1,SPIN,JK,EM21,N)
         E21=EB21+EM21
         CALL ECALCB(ATOM,IX2,IY2,IZ2,IM2,UK,EB22,N)
         CALL ECALCM(SPSIGN,ATOM,IX2,IY2,IZ2,IM2,SPIN,JK,EM22,N)
         E22=EB22+EM22
         E2=E21+E22
         EDELTA=E2-E1
         DF=EXP(-EDELTA/TEMP)
         DSPF=DF/(1.+DF)
          RANNUM=RAN2(IDUM)
            IF(RANNUM.LT.DSPF)THEN
              ETOT=ETOT+EDELTA
            ELSE
      ATOM(IX1,IY1,IZ1,IM1)=1
      ATOM(IX2,IY2,IZ2,IM2)=2
      SPSIGN(IX1,IY1,IZ1,IM1)=ISIGN1
      SPSIGN(IX2,IY2,IZ2,IM2)=ISIGN2
            END IF
         ELSE
```

```
    ATOM(IX1,IY1,IZ1,IM1)=1
    ATOM(IX2,IY2,IZ2,IM2)=2
CALL ECALCB(ATOM,IX1,IY1,IZ1,IM1,UK,EB,N)
       CALL  ECALCM(SPSIGN,ATOM,IX1,IY1,IZ1,IM1,SPIN,JK,EM,N)
E21=EB+EM
CALL ECALCB(ATOM,IX2,IY2,IZ2,IM2,UK,EB,N)
       CALL ECALCM(SPSIGN,ATOM,IX2,IY2,IZ2,IM2,SPIN,JK,EM,N)
E22=EB+EM
E2=E21+E22
       EDELTA=E2-E1
       DF=DEXP(-EDELTA/(TEMP*1.0))
       DSFF=DF/(1.+DF)
       RANNUM=RAN2(IDUM)
          IF(RANNUM.LT.DSFF)THEN
           ETOT=ETOT+EDELTA
          ELSE
           ATOM(IX1,IY1,IZ1,IM1)=2
           ATOM(IX2,IY2,IZ2,IM2)=1
       SPSIGN(IX1,IY1,IZ1,IM1)=ISIGN1
       SPSIGN(IX2,IY2,IZ2,IM2)=ISIGN2
       END IF
       END IF
       GO TO 777
200      SPSIGN(IX1,IY1,IZ1,IM1)=-ISIGN2
         SPSIGN(IX2,IY2,IZ2,IM2)=ISIGN1
         IF(ATOM(IX1,IY1,IZ1,IM1).EQ.1)THEN
         ATOM(IX1,IY1,IZ1,IM1)=2
         ATOM(IX2,IY2,IZ2,IM2)=1
          CALL ECALCB(ATOM,IX1,IY1,IZ1,IM1,UK,EB1,N)
         CALL ECALCM(SPSIGN,ATOM,IX1,IY1,IZ1,IM1,SPIN,JK,EM1,N)
        E21=EB1+EM1
       CALL ECALCB(ATOM,IX2,IY2,IZ2,IM2,UK,EB2,N)
       CALL ECALCM(SPSIGN,ATOM,IX2,IY2,IZ2,IM2,SPIN,JK,EM2,N)
           E22=EB2+EM2
           E2=E21+E22
           IF(NY.EQ.0)THEN
           EDELTA=E2-E1
           ELSE
           EDELTA=E2-E1-2.*JK(1,2)*0.3*1.4*ISIGN1*ISIGN2
           END IF
          DF=DEXP(-EDELTA/TEMP)
           DF=DEXP(-EDELTA/TEMP)
           DSFF=DF/(1.+DF)
           RANNUM=RAN2(IDUM)
            IF(RANNUM.LT.DSFF)THEN
                ETOT=ETOT+EDELTA
```

```
                TOTSPIN=TOTSPIN+2.*SPSIGN(IX1,IY1,IZ1,IM1)
     *           *SPIN(ATOM(IX1,IY1,IZ1,IM1))
              ELSE
                 ATOM(IX1,IY1,IZ1,IM1)=1
                 ATOM(IX2,IY2,IZ2,IM2)=2
               SPSIGN(IX1,IY1,IZ1,IM1)=ISIGN1
               SPSIGN(IX2,IY2,IZ2,IM2)=ISIGN2
              ENDIF
             ELSE
ATOM(IX1,IY1,IZ1,IM1)=1
                 ATOM(IX2,IY2,IZ2,IM2)=2

        CALL ECALCB(ATOM,IX1,IY1,IZ1,IM1,UK,EB1,N)
        CALL ECALCM(SPSIGN,ATOM,IX1,IY1,IZ1,IM1,SPIN,JK,EM1,N)
        E21=EB1+EM1
        CALL ECALCB(ATOM,IX2,IY2,IZ2,IM2,UK,EB2,N)
        CALL ECALCM(SPSIGN,ATOM,IX2,IY2,IZ2,IM2,SPIN,JK,EM2,N)
        E22=EB2+EM2
        E2=E22+E21
        IF(NY.EQ.0)THEN
        EDELTA=E2-E1
        ELSE
         EDELTA=E2-E1-2.*JK(1,2)*0.3*1.4*ISIGN1*ISIGN2
           END IF
        DF=DEXP(-EDELTA/TEMP)
        DSFF=DF/(1.+DF)
        RANNUM=RAN2(IDUM)
             IF(RANNUM.LT.DSFF)THEN
       ETOT=ETOT+EDELTA
              TOTSPIN=TOTSPIN+2.*SPSIGN(IX1,IY1,IZ1,IM1)
     *         *SPIN(ATOM(IX1,IY1,IZ1,IM1))
ELSE
ATOM(IX1,IY1,IZ1,IM1)=2
        ATOM(IX2,IY2,IZ2,IM2)=1
         SPSIGN(IX1,IY1,IZ1,IM1)=ISIGN1
         SPSIGN(IX2,IY2,IZ2,IM2)=ISIGN2
END IF
        END IF
        GO TO 777
400      SPSIGN(IX1,IY1,IZ1,IM1)=-ISIGN2
         SPSIGN(IX2,IY2,IZ2,IM2)=-ISIGN1
             IF(ATOM(IX1,IY1,IZ1,IM1).EQ.1)THEN
             ATOM(IX1,IY1,IZ1,IM1)=2
             ATOM(IX2,IY2,IZ2,IM2)=1
          CALL ECALCB(ATOM,IX1,IY1,IZ1,IM1,UK,EB21,N)
          CALL  ECALCM(SPSIGN,ATOM,IX1,IY1,IZ1,IM1,SPIN,JK,EM21,N)
```

```
            E21=EB21+EM21
         CALL ECALCB(ATOM,IX2,IY2,IZ2,IM2,UK,EB22,N)
         CALL ECALCM(SPSIGN,ATOM,IX2,IY2,IZ2,IM2,SPIN,JK,EM22,N)
            E22=EB22+EM22
     E2=E21+E22
            EDELTA=E2-E1
            DF=DEXP(-EDELTA/TEMP)
            DSFF=DF/(1.+DF)
            RANNUM=RAN2(IDUM)
           IF(RANNUM.LT.DSFF)THEN
C           IF(EDELTA.LT.0.)THEN
           ETOT=ETOT+EDELTA
           TOTSPIN=TOTSPIN+2.*SPSIGN(IX1,IY1,IZ1,IM1)
     *                    *SPIN(ATOM(IX1,IY1,IZ1,IM1))
     *     +2.*SPSIGN(IX2,IY2,IZ2,IM2)*SPIN(ATOM(IX2,IY2,IZ2,IM2))
  ELSE
ATOM(IX1,IY1,IZ1,IM1)=1
ATOM(IX2,IY2,IZ2,IM2)=2
          SPSIGN(IX2,IY2,IZ2,IM2)=ISIGN2
          SPSIGN(IX1,IY1,IZ1,IM1)=ISIGN1
          ENDIF
ELSE
ATOM(IX1,IY1,IZ1,IM1)=1
ATOM(IX2,IY2,IZ2,IM2)=2
         CALL ECALCB(ATOM,IX1,IY1,IZ1,IM1,UK,EB,N)
         CALL  ECALCM(SPSIGN,ATOM,IX1,IY1,IZ1,IM1,SPIN,JK,EM,N)
   E21=EB+EM
         CALL ECALCB(ATOM,IX2,IY2,IZ2,IM2,UK,EB,N)
         CALL ECALCM(SPSIGN,ATOM,IX2,IY2,IZ2,IM2,SPIN,JK,EM,N)
   E22=EB+EM
   E2=E21+E22
           EDELTA=E2-E1
         DF=DEXP(-EDELTA/TEMP)
         DSFF=DF/(1.+DF)
         RANNUM=RAN2(IDUM)
          IF(RANNUM.LT.DSFF)THEN
C          IF(EDELTA.LT.0.)THEN
          ETOT=ETOT+EDELTA
  TOTSPIN=TOTSPIN+2.*SPSIGN(IX1,IY1,IZ1,IM1)
     *                    *SPIN(ATOM(IX1,IY1,IZ1,IM1))
     *     +2.*SPSIGN(IX2,IY2,IZ2,IM2)*SPIN(ATOM(IX2,IY2,IZ2,IM2))
ELSE
   ATOM(IX1,IY1,IZ1,IM1)=2
   ATOM(IX2,IY2,IZ2,IM2)=1
        SPSIGN(IX1,IY1,IZ1,IM1)=ISIGN1
        SPSIGN(IX2,IY2,IZ2,IM2)=ISIGN2
```

```
        ENDIF
       END IF
777    CONTINUE
        IF(J.GT.2500)THEN
            NN=NN+1
           IF(NN.GT.30)THEN
         CALL PROBCK1(ATOM,IX,IY,IZ,IM,N,CPER,ALOP)
         CALL PROBCK2(ATOM,IX,IY,IZ,IM,N,CPER,SOP)
         CALL ENERTOT(SPSIGN,ATOM,SPIN,JK,ETOT2,ECT,EMT,N,UK)
           NO=NO+1
           NN=0
          AVSPIN=AVSPIN+ABS(TOTSPIN/NTOT)
          AVLP=AVLP+ALOP
           AVSP=AVSP+SOP
           AVEM=AVEM+EMT/NTOT
           AVEC=AVEC+ECT/NTOT
           AVE=AVE+ETOT/NTOT
            ETOT=ECT+EMT
            END IF
             END IF
       WRITE(10,*)NSTEP, TOTSPIN/NTOT,ALOP,SOP,ETOT2/NTOT
888     CONTINUE
       WRITE(10,*)TEMP,AVSPIN/NO,AVLP/NO,AVSP/NO,AVE/NO,
     * AVEC/NO,AVEM/NO
541    FORMAT(1X,'FINAL AVSPIN = ',F6.3)
551    FORMAT(1X,'FINAL ENERGY PER ATOM= ',E10.4)
        WRITE(2,571)TEMP,AVSPIN/NO,AVLP/NO,AVSP/NO,AVE/NO
571    FORMAT(1X,F5.1,2X,F7.4,2X,F10.1,2X,F6.4)
999    CONTINUE
       RETURN
       END

C      SUBROUTINE ENERTOT
C      THIS SUBROUTINE CALCULATES THE TOTAL ENERGY OF A FCC BINARY SPIN
C      SYSTEM WITH CYCLIC BOUNDARY CONDITIONS.
C      IT USES SUBROUTINE ECALC

       SUBROUTINE ENERTOT(SPSIGN,ATOM,SPIN,JK,ETOT,ECT,EMT,N,UK)
       IMPLICIT DOUBLE PRECISION (D-E)
       INTEGER ATOM(10,10,10,4),SPSIGN(10,10,10,4)
       REAL UK(2,2),JK(2,2),SPIN(2)
       ECT=0.
       EMT=0.
       NTOT=4*N**3
       DO 10 IX = 1,N
DO 8 IY = 1,N
```

```
      DO 6 IZ = 1,N
        DO 4 IM = 1,4
         CALL ECALCB(ATOM,IX,IY,IZ,IM,UK,EB,N)
                  ECT=ECT+EB*0.5
          CALL ECALCM(SPSIGN,ATOM,IX,IY,IZ,IM,SPIN,JK,EM,N)
                  EMT=EMT+EM*0.5
4               CONTINUE
6             CONTINUE
8           CONTINUE
10        CONTINUE
          ETOT=(ECT+EMT)
          RETURN
          END
```